

Nano for Biomimetics and Biomaterials

Guest Editors: Il-Kwon Oh, Anchal Srivastava, In-Kyu Park,
and Michael Z. Hu





Nano for Biomimetics and Biomaterials

Journal of Nanomaterials

Nano for Biomimetics and Biomaterials

Guest Editors: Il-Kwon Oh, Anchal Srivastava, In-Kyu Park,
and Michael Z. Hu



Copyright © 2014 Hindawi Publishing Corporation. All rights reserved.

This is a special issue published in "Journal of Nanomaterials." All articles are open access articles distributed under the Creative Commons Attribution License, which permits unrestricted use, distribution, and reproduction in any medium, provided the original work is properly cited.

Editorial Board

Katerina E. Aifantis, Greece
Nageh K. Allam, USA
Margarida Amaral, Portugal
Xuedong Bai, China
Lavinia Balan, France
Enrico Bergamaschi, Italy
Theodorian Borca-Tasciuc, USA
C. Jeffrey Brinker, USA
Christian Brosseau, France
Xuebo Cao, China
Shafiq Chowdhury, USA
Kwang-Leong Choy, UK
Cui ChunXiang, China
M. A. Correa-Duarte, Spain
Shadi A. Dayeh, USA
Claude Estourns, France
Alan Fuchs, USA
Lian Gao, China
Russell E. Gorga, USA
Hongchen Chen Gu, China
Mustafa O. Guler, Turkey
John Zhanhu Guo, USA
Smrati Gupta, Germany
Michael Harris, USA
Zhongkui Hong, China
Michael Hu, USA
David Hui, USA
Y.-K. Jeong, Republic of Korea
Sheng-Rui Jian, Taiwan
Wanqin Jin, China
Rakesh K. Joshi, UK
Zhenhui Kang, China
Fathallah Karimzadeh, Iran
Alireza Khataee, Iran
Do Kyung Kim, Republic of Korea
Alan K. T. Lau, Hong Kong
Burtrand Lee, USA
Benxia Li, China
Jun Li, Singapore
Xing-Jie Liang, China
Shijun Liao, China
Gong Ru Lin, Taiwan
J. -Y. Liu, USA
Tianxi Liu, China
Songwei Lu, USA
Daniel Lu, China
Jue Lu, USA
Ed Ma, USA
Gaurav Mago, USA
Santanu K. Maiti, India
Sanjay R. Mathur, Germany
Vikas Mittal, United Arab Emirates
Weihai Ni, Germany
Sherine Obare, USA
Atsuto Okamoto, Japan
Abdelwahab Omri, Canada
Edward Andrew Payzant, USA
Kui-Qing Peng, China
Anukorn Phuruangrat, Thailand
Mahendra Rai, India
Suprakas Sinha Ray, South Africa
Ugur Serincan, Turkey
Huaiyu Shao, Japan
Donglu Shi, USA
Vladimir Sivakov, Germany
Marinella Striccoli, Italy
Bohua Sun, South Africa
Saikat Talapatra, USA
Nairong Tao, China
Titipun Thongtem, Thailand
Somchai Thongtem, Thailand
Alexander Tolmachev, Ukraine
Valeri P. Tolstoy, Russia
Tsung-Yen Tsai, Taiwan
Takuya Tsuzuki, Australia
Raquel Verdejo, Spain
Mat U. Wahit, Malaysia
Shiren Wang, USA
Yong Wang, USA
Ruibing Wang, Canada
Cheng Wang, China
Zhenbo Wang, China
Jinquan Wei, China
Ching-Ping Wong, Hong Kong
Xingcai Wu, China
Guodong Xia, Hong Kong
Zhi Li Xiao, USA
Ping Xiao, UK
Shuangxi Xing, China
Yangchuan Xing, USA
N. Xu, China
Doron Yadlovker, Israel
Yingkui Yang, China
Khaled Youssef, USA
Kui Yu, Canada
William W. Yu, USA
Haibo Zeng, China
Tianyou Zhai, Japan
Renyun Zhang, Sweden
Bin Zhang, China
Yanbao Zhao, China
Lianxi Zheng, Singapore
Chunyi Zhi, Hong Kong

Contents

Nano for Biomimetics and Biomaterials, Il-Kwon Oh, Anchal Srivastava, In-Kyu Park, and Michael Z. Hu
Volume 2014, Article ID 485642, 1 page

A Facile Nanodelivery Platform Based on Functionalized Hyperbranched Poly(ether-ester) for Individualized Antitumor Drugs: Pingyangmycin as a Model, Xing-ai Jin, Yan-wu Li, Guo-lin Li, Shao-hua Lv, Ying-qun Liu, and Li-min Mao
Volume 2014, Article ID 601272, 10 pages

Nanostructural Colouration in Malaysian Plants: Lessons for Biomimetics and Biomaterials, S. Zaleha M. Diah, Salmah B. Karman, and Ille C. Gebeshuber
Volume 2014, Article ID 878409, 15 pages

A Dual-Functional [SBA-15/Fe₃O₄/P(N-iPAAM)] Hybrid System as a Potential Nanoplatfor for Biomedical Application, Andreza de Sousa, Karynne Cristina de Souza, Paula Maria da Silva Leite, Ricardo Geraldo de Sousa, and Edésia Martins Barros de Sousa
Volume 2014, Article ID 293624, 10 pages

Characterization of the Casein/Keratin Self-Assembly Nanomicelles, Su Xiao-Zhou, Wang Hong-Ru, and Huang Mian
Volume 2014, Article ID 183815, 7 pages

Nanopigmented Acrylic Resin Cured Indistinctively by Water Bath or Microwave Energy for Dentures, L. S. Acosta-Torres, M. C. Arenas, R. E. Nuñez-Anita, F. H. Barceló-Santana, C. A. Álvarez-Gayosso, J. Palacios-Alquisira, J. de la Fuente-Hernández, Marcos Cajero-Juárez, and V. M. Castaño
Volume 2014, Article ID 198572, 8 pages

A New Method for Fabrication of Nanohydroxyapatite and TCP from the Sea Snail *Cerithium vulgatum*, O. Gunduz, Y. M. Sahin, S. Agathopoulos, B. Ben-Nissan, and F. N. Oktar
Volume 2014, Article ID 382861, 6 pages

Cationic Gelatin Nanoparticles for Drug Delivery to the Ocular Surface: *In Vitro* and *In Vivo* Evaluation, Ching-Li Tseng, Ko-Hua Chen, Wen-Yu Su, Yen-Hsien Lee, Chi-Chang Wu, and Fen-Huei Lin
Volume 2013, Article ID 238351, 11 pages

Development of Antibiotics Impregnated Nanosized Silver Phosphate-Doped Hydroxyapatite Bone Graft, Waraporn Suvannapruk, Faungchat Thammarakcharoen, Phetrung Phanpiriya, and Jintamai Suwanprateeb
Volume 2013, Article ID 542584, 9 pages

Iron Oxide Magnetic Nanoparticles: Characterization and Toxicity Evaluation by *In Vitro* and *In Vivo* Assays, Alina Mihaela Prodan, Simona Liliana Iconaru, Carmen Steluta Ciobanu, Mariana Carmen Chifiriuc, Mihai Stoicea, and Daniela Predoi
Volume 2013, Article ID 587021, 10 pages

Electrospun Hyaluronan-Gelatin Nanofibrous Matrix for Nerve Tissue Engineering, Hau-Min Liou, Lih-Rou Rau, Chun-Chiang Huang, Meng-Ru Lu, and Fu-Yin Hsu
Volume 2013, Article ID 613638, 9 pages

Investigation of the *In Vitro* Degradation of a Novel Polylactide/Nanohydroxyapatite Composite for Artificial Bone, Jianghong Huang, Jianyi Xiong, Jianquan Liu, Weimin Zhu, and Daping Wang
Volume 2013, Article ID 515741, 10 pages

A Study on the Effect of Plasma Treatment for Waste Wood Biocomposites, MiMi Kim, Heung Soo Kim, and Joong Yeon Lim
Volume 2013, Article ID 138083, 6 pages

Water Absorption and Diffusion Characteristics of Nanohydroxyapatite (nHA) and Poly(hydroxybutyrate-co-hydroxyvalerate-) Based Composite Tissue Engineering Scaffolds and Nonporous Thin Films, Naznin Sultana and Tareef Hayat Khan
Volume 2013, Article ID 479109, 8 pages

Editorial

Nano for Biomimetics and Biomaterials

Il-Kwon Oh,¹ Anchal Srivastava,² In-Kyu Park,³ and Michael Z. Hu⁴

¹ Graphene Research Center, School of Mechanical, Aerospace and Systems Engineering, Division of Ocean Systems Engineering, Korea Advanced Institute of Science and Technology (KAIST), 335 Gwahak-ro, Yuseong-gu, Daejeon 305-701, Republic of Korea

² Department of Physics, Banaras Hindu University, Varanasi 221005, India

³ Department of Biomedical Sciences, Chonnam National University, 300 Yongbong-dong, Buk-gu, Gwang-Ju 500-757, Republic of Korea

⁴ Oak Ridge National Laboratory, 4500N, A34, MS 6181, Oak Ridge, TN 37831-6181, USA

Correspondence should be addressed to Il-Kwon Oh; ikoh@kaist.ac.kr

Received 3 April 2014; Accepted 3 April 2014; Published 29 June 2014

Copyright © 2014 Il-Kwon Oh et al. This is an open access article distributed under the Creative Commons Attribution License, which permits unrestricted use, distribution, and reproduction in any medium, provided the original work is properly cited.

This special issue has been considered as a necessary technology which can overcome the limitations and problems of other modern technologies and lead to a new industrial revolution. The future promise of nanotechnology depends on its high multidisciplinary nature and shared knowledge and information from various fields which can be merged and used to evolve as a revolutionary new technology. Considering the potential impact of nanotechnology on future industry, many countries are investing huge research funds and resources in the field of nanotechnology as one of their top research priorities.

The aim of the special issue is to share the novel knowledge covering the state of the art on biomimetics and nanobiomaterials providing an overview on their potential applications in the industrial, biomedical, and robotic fields. The research topics covered in the special issue include bioinspired materials, devices, structures, and graphene-based materials. The special issue will present current status of the fields of biomimetics and biomaterials. This special issue will be a necessary platform for ongoing studies between researchers from different areas (chemistry, physics, biology, medicine, engineering, robotics, etc.) within biomimetic and biomaterial technologies.

We hope that this special issue reflects the current state of nanotechnology for biomimetics and biomaterials and will be a useful reference for researchers working in this research field.

Acknowledgment

The guest editors and other colleagues from various institutions offered invaluable support for peer-reviewing and the successful completion of this special issue. We sincerely thank all reviewers and authors of this special issue.

*Il-Kwon Oh
Anchal Srivastava
In-Kyu Park
Michael Z. Hu*

Research Article

A Facile Nanodelivery Platform Based on Functionalized Hyperbranched Poly(ether-ester) for Individualized Antitumor Drugs: Pingyangmycin as a Model

Xing-ai Jin,¹ Yan-wu Li,² Guo-lin Li,^{3,4} Shao-hua Lv,^{3,4} Ying-qun Liu,¹ and Li-min Mao³

¹ Department of Pediatrics, College of Stomatology, Harbin Medical University, 23 Youzheng Street, Harbin 150001, China

² Department of Periodontology, College of Stomatology, Harbin Medical University, 23 Youzheng Street, Harbin 150001, China

³ Department of Oral and Maxillofacial Surgery, College of Stomatology, Harbin Medical University, 23 Youzheng Street, Harbin 150001, China

⁴ State Key Laboratory of Metal Matrix Composites, School of Chemistry and Chemical Engineering, Shanghai Jiao Tong University, 800 Dongchuan Road, Shanghai 200240, China

Correspondence should be addressed to Li-min Mao; hrbmlm@126.com

Received 14 December 2013; Revised 18 February 2014; Accepted 7 March 2014; Published 26 June 2014

Academic Editor: In-Kyu Park

Copyright © 2014 Xing-ai Jin et al. This is an open access article distributed under the Creative Commons Attribution License, which permits unrestricted use, distribution, and reproduction in any medium, provided the original work is properly cited.

Nanodelivery of antitumor drugs is a new treatment mode for cancer. The aim of this investigation was to construct and evaluate a facile nanodelivery platform for individualized antitumor drugs based on functionalized hyperbranched poly(ether-ester)s. Poly(ether-ester)s, as a kind of hyperbranched polymers, have received extensive attention. Three terminal-functionalized (OH-, NH₂- and COOH-) hyperbranched poly(ether-ester)s were prepared and characterized by dynamic light scattering and attenuated total reflectance Fourier transform infrared spectroscopy. The relationship between chemical terminal variation and physical surface charges was investigated. Biocompatibility of these polymers was confirmed by methyl tetrazolium assays and scanning electron microscopy. As a model drug, pingyangmycin has antitumor and antiangiogenic effects. In the paper, pingyangmycin was mixed with carboxyl-modified hyperbranched poly(ether-ester) through ionic binding. Polymer-mixed pingyangmycin exhibited significant inhibition of HN-6 head and neck cancer human cells *in vitro*. These studies demonstrate that functionalized hyperbranched (ether-ester)s can be exploited as a facile nanodelivery platform for antitumor therapy.

1. Introduction

Although nanodelivery of antitumor drugs has numerous advantages, such as improved solubility [1], accurate targeting [2–5], increased permeability of tumor vasculature to macromolecules, and decreased lymphatic drainage from the tumor; the complicated techniques involved in nanodelivery development have impeded individualized nanodelivery of numerous antitumor drugs. Even dendritic polymers, which have been used for nanodelivery for years, involve complicated techniques and high costs associated with the crystal architecture [6, 7].

Over the past two decades hyperbranched polymers have received a great deal of attention [8–10]. Since the first intentional preparation of hyperbranched polymers, many types have been synthesized, including polyimide, polyether, poly-

methacrylate, polyphenylene, poly(ether ketone), polyester, and polyurethane [11]. As a novel generation of dendritic polymers, hyperbranched polymers (HBP), which have characteristic incomplete branching and irregular dimensions, provide a facile substitute for the preparation and screening of nanocarriers. Distinct from their linear analogues, hyperbranched polymers have structures and topologies similar to dendrimers and possess some strikingly superior material properties [9, 10]. Due to their low dispersity and excellent biocompatibility and biodegradability [1, 12–16] hyperbranched polymers have been applied in the field of pharmaceutical delivery. In our previous studies, hyperbranched poly(ether-ester) (HPPEE) was prepared, characterized [17, 18], and applied as a nanocarrier of antitumor drug [1, 19]. In the present study, a series of terminal-functionalized derivatives were established based on the HPPEE backbone, thus

providing a facile platform for optimization of individualized antitumor drug delivery. Pingyangmycin is a water-soluble glycopeptide produced by *Streptomyces pingyangensis*. It is chemically similar to bleomycin with antitumor and antiangiogenic effects. In this paper pingyangmycin is used as an example to assess the efficacy of this nanodelivery platform.

2. Materials and Methods

2.1. Synthesis of End-Functionalized HPEE Derivatives. A suspension of potassium hydride (KH, Aldrich) in mineral oil (30% in weight) was placed in a dry preweighed 100 mL Schlenk flask under nitrogen. The mineral oil was removed by three extractions with tetrahydrofuran (THF), which was added to the flask by syringe. Completely dried KH (0.58 g, 14.46 mmol) was added to 40 mL dimethyl sulfoxide (DMSO) and tetra (ethylene glycol) (TTEG; 5.62 g, 28.92 mmol) (Aldrich, ShangHai). The solution was stirred for 30 min to form the alcoholate potassium. Subsequently, glycidyl methacrylate (GMA; 4.12 g, 29.98 mmol) (Sigma, USA) was added and polymerization was conducted for 24 h at 80°C. The resultant mixture was precipitated in 1000 mL of acetone/diethyl ether (v/v 1/4) and then redissolved in methanol and neutralized by filtration over cation-exchange resin. The polymer was precipitated twice from methanol solution into cold diethyl ether and subsequently dried under vacuum at 50°C for 24 h. The purified HPEE-OH was obtained as a highly viscous polymer. For HPEE-NH₂ synthesis, 2 g of HPEE-OH was dissolved into 25 mL of DMF. Fmoc-glycine (2.97 g, 10 mmol), dicyclohexylcarbodiimide (DCC; 4.13 g, 20 mmol), 4-dimethylaminopyridine (DMAP; 0.61 g, 5 mmol), and hydration p-toluene sulfonic acid (PTSA; 0.95 g, 5 mmol) were added to the solution. The mixture was dissolved in 20% piperidine to remove fmoc-protected groups. For HPEE-COOH synthesis, 1 g HPEE-OH was dissolved in 15 mL dichloromethane (CH₂Cl₂) under moderate stirring at room temperature. When it was completely dissolved, 1 g of succinic anhydride and 360 μ L dried piperidine were added to the flask under the same conditions. For comparison and confirmation purposes, the nonbiodegradable structural analogue hyper-branched poly(ether) (HPE) and its functionalized derivatives were concurrently synthesized and analyzed (details are provided in Supplementary Material available online at <http://dx.doi.org/10.1155/2014/601272>). The same synthesis protocols were used for preparation of HPE and its functionalized derivatives.

2.2. Characterization. Nuclear magnetic resonance (NMR): ¹H NMR spectra of the polymers were recorded on an Advanced III 400 M spectrometer (Bruker, Germany) in D₂O as the solvent. Fourier infrared spectra were measured on an EQUINOX55 (Bruker, Germany). Respective potentials were tested using NaCl titrant (25°C, 100 mmol/L, pH = 7) on Malvern Instruments Zetasizer 2000. Dynamic light scattering (DLS) was assessed on Zetasizer Nano S (Malvern Instruments Ltd., Malvern, Worcestershire, UK) at 25°C.

2.3. Cell Cultures. NIH/3T3 normal cells (a mouse embryonic fibroblast cell line) were cultured in DMEM supplemented with 10% FBS and antibiotics (50 units/mL penicillin and

50 units/mL streptomycin) at 37°C in a humidified atmosphere containing 5% CO₂. After 48 h logarithmic growth the attached cells were collected by enzymatic digestion (0.25% pancreatin and 0.02% EDTA) for further assay. HN-6 cancer cells (a human head and neck squamous carcinoma cell line) were cultured in PRMI-1640 supplemented with 10% FBS and antibiotics (200 units/mL penicillin and 50 units/mL streptomycin) at 37°C in a humidified atmosphere containing 5% CO₂. Using enzymatic digestion (0.25% pancreatin and 0.02% EDTA), cells were passaged with a 1:3 ratio every 2-3 days for numerous cell generations.

2.4. In Vitro MTT Assay for Cytotoxicity Assessment. *In vitro* cytotoxicity of a serial dilution of polymer solution against NIH/3T3 cells was measured by the MTT viability assay. Synthesized HPEE-OH, HPEE-NH₂, and HPEE-COOH were compared with their structural analogues (HPE-OH, HPE-NH₂, and HPE-COOH). All solutions were dissolved in PBS with serial dilutions of 0.001 mg/mL, 0.01 mg/mL, 0.1 mg/mL, 1 mg/mL, and 10 mg/mL. The same concentration series of dextran and PEI were also prepared as negative and positive controls, respectively. NIH/3T3 cells were seeded into 96-well plates at a seeding density of 4.0×10^3 cells per well in 50 μ L. After 24 h of incubation, the culture medium was removed and replaced with 50 μ L polymer solution at different concentrations. After treatment with polymers for 24 h, 48 h, and 96 h, 20 μ L of 5 mg/mL MTT stock solution in PBS was added to each well. After addition of 200 μ L DMSO to each well and shaking for 5–10 min, the absorbance was measured at a wavelength of 490 nm using BioTek SynergyH4. Cytotoxicity was determined by the absorbance relative to the blank control.

The *in vitro* inhibitory effect of pingyangmycin-mixed polymers against HN-6 cells was also evaluated by MTT assay. After incubation of HN-6 cells (8.0×10^3 cells/well) for 24 h, the culture medium was removed and replaced with 200 μ L of medium containing pingyangmycin-mixed polymer. Pingyangmycin was tested at serial concentrations of 0.01, 0.1, 1.0, 10, and 100 μ g/mL.

2.5. Surface Morphological Features of 3T3 Cells. 3T3 cells (2×10^5 /mL) were separately cultured with solutions of three end-modified HPEE derivatives and three end-modified HPE analogues. To strengthen the results, each polymer was tested at low concentration (10 μ g/mL) and high concentration (1 mg/mL) and the corresponding data were compared. Cells that were simultaneously incubated with HPEE derivatives for 1 h are shown in Figure 4(a) (low concentration subgroup) and Figure 4(b) (high concentration subgroup). At the same time, two control experiments were performed: polyethyleneimine (PEI), an accepted cell toxicant, was used as a positive control and dextran with polymer structure was used as a negative control. Normal 3T3 cells incubated with PBS are also shown as a blank control. Cells of each subgroup were collected and fixed with 2.5% glutaraldehyde for 24 h. Morphological features of the cell surface were observed by scanning electron microscopy (SEM) (FEI Corp. USA).

2.6. Self-Assembly of Pingyangmycin-Mixed Micelle Preparation. Based on pingyangmycin's physical and chemical

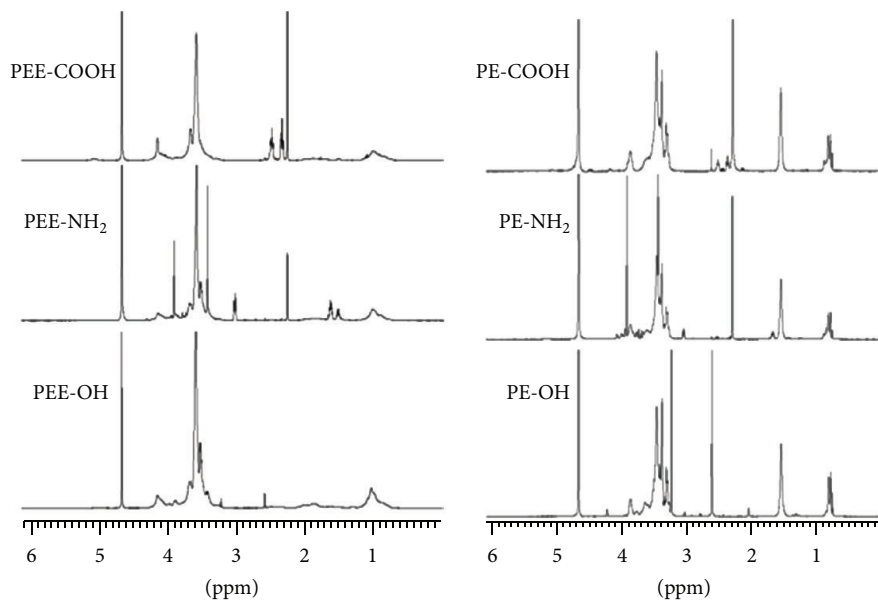


FIGURE 1: Comparison of ^1H NMR spectra between three PEE-derivatives and three PE-analogues.

characteristics, anionic carboxyl-functionalized HPEE was selected for preparation of micelles. Two functionalized mixtures (HPEE: carboxyl = 1:1 or 1:1.02) were separately added to 10 mL ultrapure water. Pingyangmycin (Bolai Pharmacy Company, China) was then added to each flask with increasing polymer/pingyangmycin ratios of 1:1, 1:2, 1:3, 1:4, and 1:5. All mixtures were stirred at room temperature for 24 h to form a transparent aqueous solution.

2.7. Visualization of Self-Assembled Micelles by Transmission Electron Microscopy. Prepared micelle samples that had been dried for 24 h in a vacuum were observed by transmission electron microscopy (TEM) (JEOL2010) at 200 KV.

3. Results

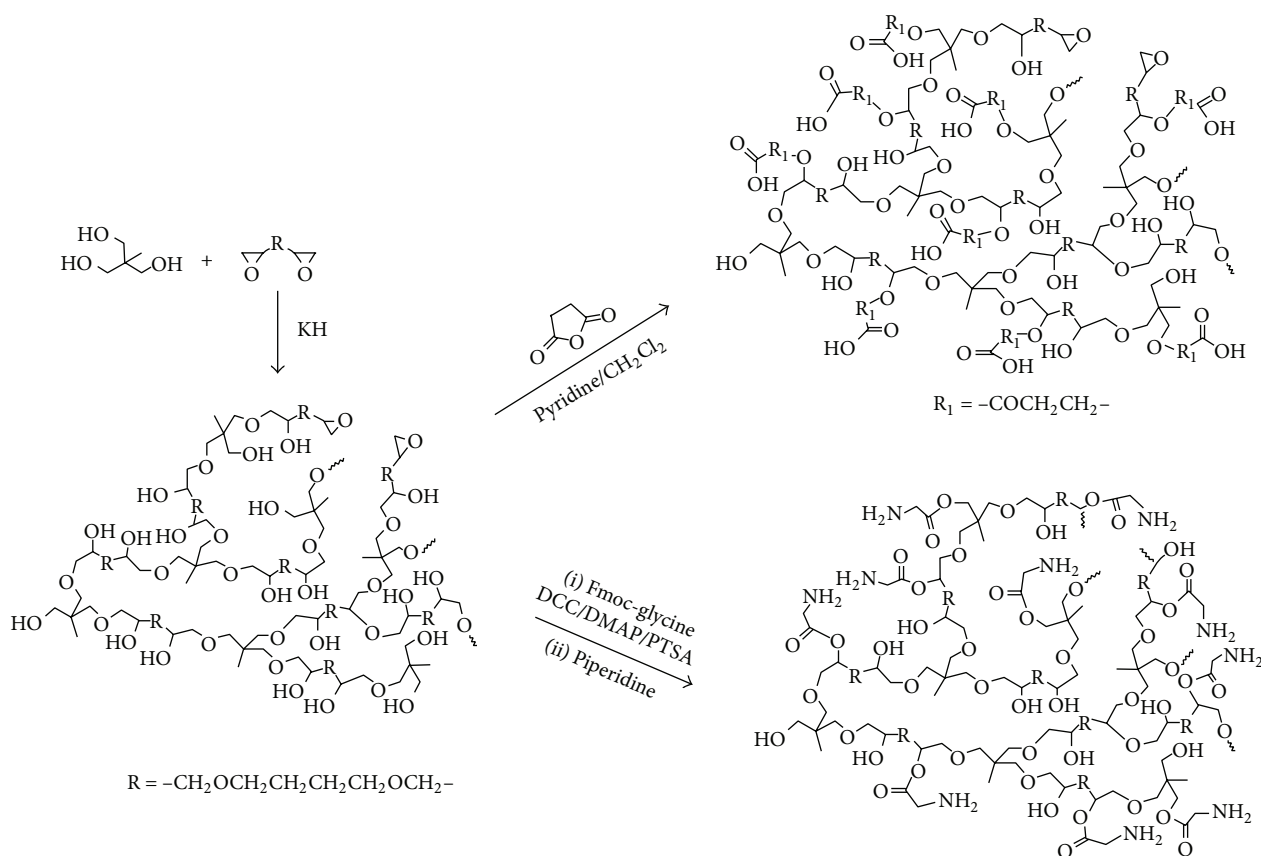
3.1. Synthesis of End-Modified Hyper-Branched Poly(ether-ester)/HPEE Derivatives. Characterization of the HPEE backbone has been intensively documented in a previous study [20], therefore terminal-modified hyper-branched poly(ether-ester)s could be easily synthesized based on the HPEE backbone according to Scheme 1. Supplemental data address the scheme for preparing structure-matched HPE derivatives.

3.2. Characterization of Functionalized Hyper-Branched Poly(ether-ester)s/HPEE by ^1H NMR. According to the quantitative ^1H NMR spectrum of HPEE (Figure 1, Left), the shift of methyl protons was found to be 1.05 ppm. The backbone of HPEE was observed at 1.80–2.10 ppm and revealed a spectrum of $-\text{CH}_2-\text{CH}(\text{CH}_2-)-\text{O}-$ or $-\text{CH}_2-\text{C}(\text{CH}_3)-$ structural subunits. A proton peak of methine adjacent to alcohol oxygen and methylene adjacent to ether oxygen was observed at 4.2–3.3 ppm. Novel peaks could be observed at 2.50 ppm ($-\text{OCOCH}_2\text{CH}_2\text{COOH}-$) and 2.30 ppm ($-\text{OCOCH}_2\text{CH}_2\text{COOH}-$) after the carboxyl

group was grafted onto HPEE. When a glycine residue ($-\text{OCOCH}_2\text{NH}_2-$) was grafted onto HPEE, a novel 3.9 ppm peak that indicated the methylene proton from the amino group could be observed. Similar variation of ^1H NMR peak-to-terminal could be observed when the same terminals were added to the HPE backbone (Figure 1, Right). The degree of ($-\text{OCH}_2\text{CH}_2\text{CH}_2\text{CH}_2\text{O}-$) in HPE was found to be 1.59 ppm. ^1H NMR distributions were 0.70–0.85/17–4.12 ppm (hydroxyl protons), 0.70–0.85 ppm (methyl protons), and 3.15–3.70 ppm (methylene and methane adjacent to ether oxygen and alcohol oxygen).

3.3. Fourier Transform Infrared (FT-IR) Spectra of the Poly(ether-ester) Derivatives. FT-IR spectra of PEE-OH, PEE-NH₂ and PEE-COOH are shown in Figure 2 (Left). Characteristic ether bond and ester bond absorption bands were shown at 1100 cm^{-1} and 1725 cm^{-1} , respectively. A band at 1668 cm^{-1} could be seen after grafting of amidogen, whereas the 1557 cm^{-1} band could only be seen after the carboxyl group was grafted. For comparison purposes, FT-IR spectra of HPE-analogues are also shown in the same figure (Figure 2, Right). Similarly, the 1100 cm^{-1} FTIR band in the top HPE-OH figure was produced by asymmetric stretching vibration originating from C–O–C groups. An amidogen absorption band at 1660 cm^{-1} and a carbonyl absorption band at 1740 cm^{-1} appeared when $-\text{NH}_2$ was polymerized into HPE-OH. For HPE-COOH, the carbonyl and carboxyl bands could be observed at 1730 cm^{-1} and 1555 cm^{-1} , respectively.

3.4. Correlation between Surface Potentials and Terminal Groups. Surface charge varied with chemical terminal functionalization, thus reflecting an interrelationship between physical and chemical variations. As shown in Table 1, the negative potential carried by hydroxyl on the surface of



SCHEME 1: End-functionalization between HPEE and amino group/carbonyl group.

PEE changed to a positive charge when the hydroxyl was replaced by amidogen; conversely, the negative potential of PEE-OH decreased to a more negative value when hydroxyl was replaced by carboxyl. The PE analogues exhibited similar variation in charge-terminal relationships.

3.5. In Vitro Cytotoxicity against 3T3 Cells. The results of MTT assays for 3T3 cells following incubation for 24 h, 48 h, and 96 h with various concentrations of the HPEE end-functionalized derivatives are shown in Figure 3. In general, HPEE derivatives demonstrated low cytotoxicity against 3T3 cells. Even 3T3 cells treated with 10 mg/mL HPEE-NH₂, which was predicted to have the greatest cytotoxicity, for a long incubation time of 96 h retained good viability. The experiment was repeated using the HPE analogues at the same concentrations. Similar MTT results were obtained for HPE-derivatives, as shown in Supplementary Data 2.1.

3.6. Visualization of 3T3 Cell Surface Morphological Changes by SEM. Cell surface morphological features were visualized by scanning electron microscopy (SEM). As shown in Figure 4, we observed an extraordinarily smooth surface in normal 3T3 cells, except for a scattering of microvilli and some ruffles at the ends of the pseudopodia. Compared with PBS controls, cells treated with hyperbranched polymers showed notable changes in scattered microvilli and irregular ruffle distributions on cell surfaces that reflected mild adaptation rather than cell injury. None of the cell membranes

lost their integrity during the whole incubation period. As a positive control, severely damaged 3T3 cells cultured in a high concentration of PEI totally lost their fibroblastic shape and the surface topography appeared to be very irregular and destroyed. Similar SEM observations of HPE-derivatives are shown in Supplementary Data 2.1.

3.7. Self-Assembly of Pingyangmycin into Functionalized HPEE. To verify the nanocarrier platform based on HPEE functionalized derivatives for individualized antitumor drug delivery, we used pingyangmycin as a model drug. Based on the physical and chemical characteristics of pingyangmycin, carboxyl-terminated hyperbranched poly(ether-ester) was selected for bioconjugation as shown in Scheme 2.

After screening, the self-assembly protocol was performed. As shown in Figure 5 and Figure 6, successfully conjugated spherical micelles (Sample 3 and Sample 5) with average diameters of 156 ± 9.6 nm (Sample 3/S3) and 173 ± 12.4 nm (Sample 5/S5) were observed by DLS and TEM visualization.

3.8. In Vitro Cytotoxicity of Carboxyl-HPEE-Pingyangmycin Micelles against HN-6 Cells. To evaluate the potential therapeutic efficiency of the carboxyl-terminal-HPEE-pingyangmycin nanocarrier, an *in vitro* MTT assay was performed using HN6 human neck and head carcinoma cells. Both carboxyl-terminated-HPEE-pingyangmycin nanocarriers (S3 and S5) displayed concentration-dependent and time-dependent cytotoxicity as shown in Figure 7. For 24 h

TABLE 1: Correlation between surface potential and end-functionalized polymers.

Delivery vehicle (PEE)	Potential	Comparable analogue (PE)	Potential
PEE-OH	2.1 ± 1.2	PE-OH	-1.3 ± 1.1
PEE-NH ₂	5.4 ± 2.5	PE-NH ₂	4.2 ± 0.8
PEE-COOH	-11.8 ± 3.5	PE-COOH	-11.7 ± 2.2

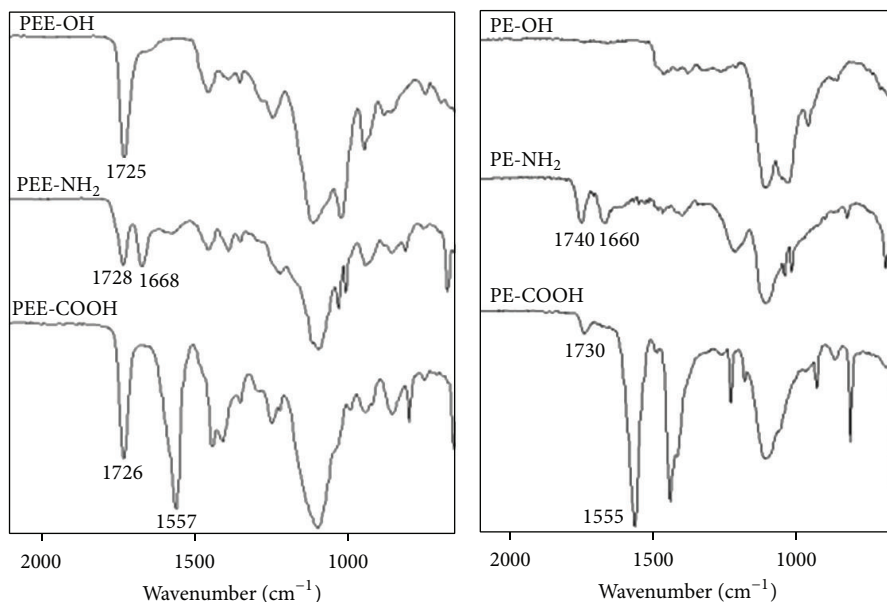


FIGURE 2: Comparison of FT-IR spectra between three PEE-derivatives and three PE-analogues.

treatment, cell viabilities were decreased by 25% for both pingyangmycin alone and pingyangmycin-nanocarrier complexes at concentrations of 0.1 mg/mL to 1 mg/mL. As the concentration increased to 100 mg/mL, cell viabilities significantly reduced. When the time of treatment extended to 48 h, the viability of HN-6 cells was slightly lower than that observed for 24 h treatment.

4. Discussion

Theoretically, a facile platform could be constructed using functionalized hyperbranched polymer derivatives such that a series of nanocarriers could be obtained for optimization of individualized antitumor-drug delivery. Hyperbranched polymers are characterized by three-dimensional cavities with abundant surface terminals and therefore represent an ideal candidate backbone [1, 21–23]. As shown in Scheme 1, ion-transfer polymerization was observed during HPEE terminal functionalization. A hydroxyl group initially reacted with butanedioic anhydride to form a carboxyl group [24, 25]. The carboxyl end then reacted with the glycine that was protected by the 9-carbonyl methoxycarbonyl group to generate an amino group by subsequent esterification [26], after which methoxycarbonyl protection was rapidly removed. Using the facile polymerization procedure presented here, a series of terminal-functionalized polymers were simultaneously prepared. Subsequent studies revealed physical-chemical interrelationships during functionalization. For

confirmation purposes, HPEEs and their HPE structural analogues were simultaneously observed. The similar results confirmed a correlation between physical surface charge and chemical terminal structure; thus, tunable modification of physical charges could be easily achieved by chemical functionalization. Based on this physical-chemical correlation, a tunable nanodelivery platform based on a functionalized HPEE backbone was initially constructed for individualized antitumor drug delivery.

Although good biocompatibility of hyperbranched polymers has been reported [27], the potential cytotoxicity of functionalized HPEE has not been documented. According to the MTT assays, all HPEE derivatives demonstrated excellent biocompatibility even when high concentrations of polymers were used. Furthermore, the biocompatibility of end-modified HPEEs was confirmed by SEM visualization. Previous studies have found that cationic charge of polymers was one of the risk factors for increased cytotoxicity. Due to complicated mechanisms including interactions between cell membranes [28], generation-related clearance [29], and inherent toxicity [30], a strong positive charge of primary amino groups significantly increased the cytotoxicity [28]. Overall, the greatest cytotoxicity of the entire platform was indeed observed for high concentrations of the HPE-NH₂ subgroup, consistent with the previous study. Similarly, mildly enhanced cytotoxicity was observed when the ionic HPEE-COOH subgroup was substituted by the cationic HPEE-NH₂ subgroup. However, relatively good biocompatibility was demonstrated for all HPEE-derivatives in the plat-

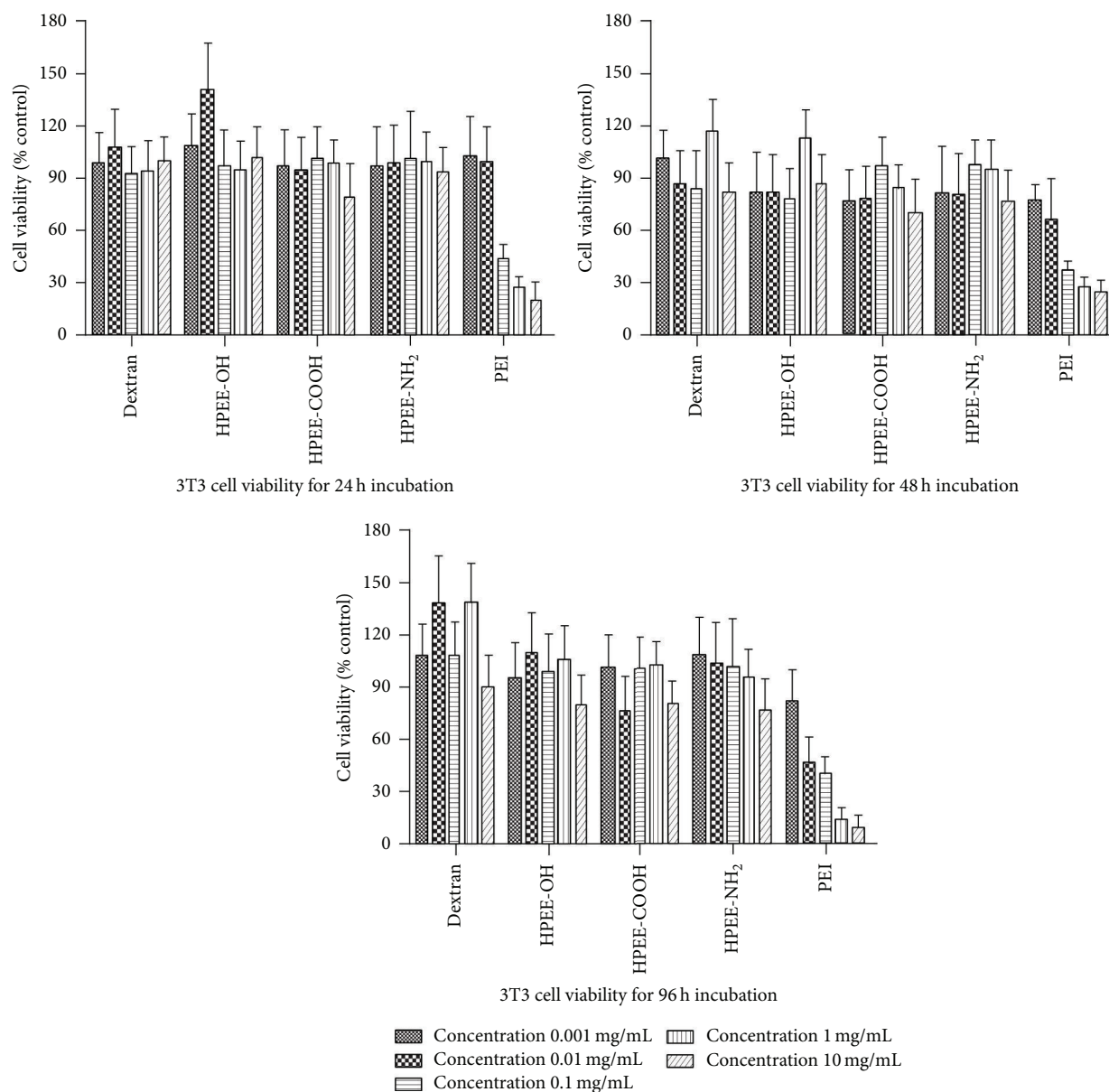


FIGURE 3: 3T3 cell viability following treatment with various concentrations of HPEE-derivatives.

form, including cationic HPEE derivatives despite previous reports of time- and concentration-dependent cytotoxicity of cationic polymers [28]. The mechanism of the reduced cytotoxicity of cationic HPEE functionalization was attributed to scattered surface charge density and the unique uncompleted hyperbranched architecture.

To evaluate potential application of the present nanodelivery platform, an anticancer drug, pingyangmycin (Bleomycin A5), was used as a model agent to assess assembly capability. Pingyangmycin is an antibiotic that was initially isolated from the culture medium of *Streptomyces pingyangensis* spp. in China and has been known for a long time to exhibit significant cytotoxicity to tumor cells [31–34]. Despite its effective antitumor activity, the systemic toxicity and short half-life time of pingyangmycin have largely prevented its widespread clinical application. Therefore, hydrophilic

pingyangmycin has only been used *in situ* to treat head and neck cancers [31–34]. The specific benefits of nanocarriers, such as passive and accurate targeted therapy with decreased systemic toxicity and long circulation [16], could increase the clinical application of pingyangmycin. As shown in Scheme 2, taking into account the amino-bonding surface of pingyangmycin, electrostatic interactions would theoretically be formed between the positive-charged protonated amines of pingyangmycin and the surface carboxyl groups on the oxidized HPEE [35]; therefore, a self-assembled micelle could potentially be constructed in water. Although it is well documented that hyperbranched polymers possess great capability for self-assembly in solution, the issue of interfacial self-assembly and hybrid self-assembly [18, 36–38] and whether and how functionalized HPEE could successfully mix with pingyangmycin was unknown. In addition, some properties

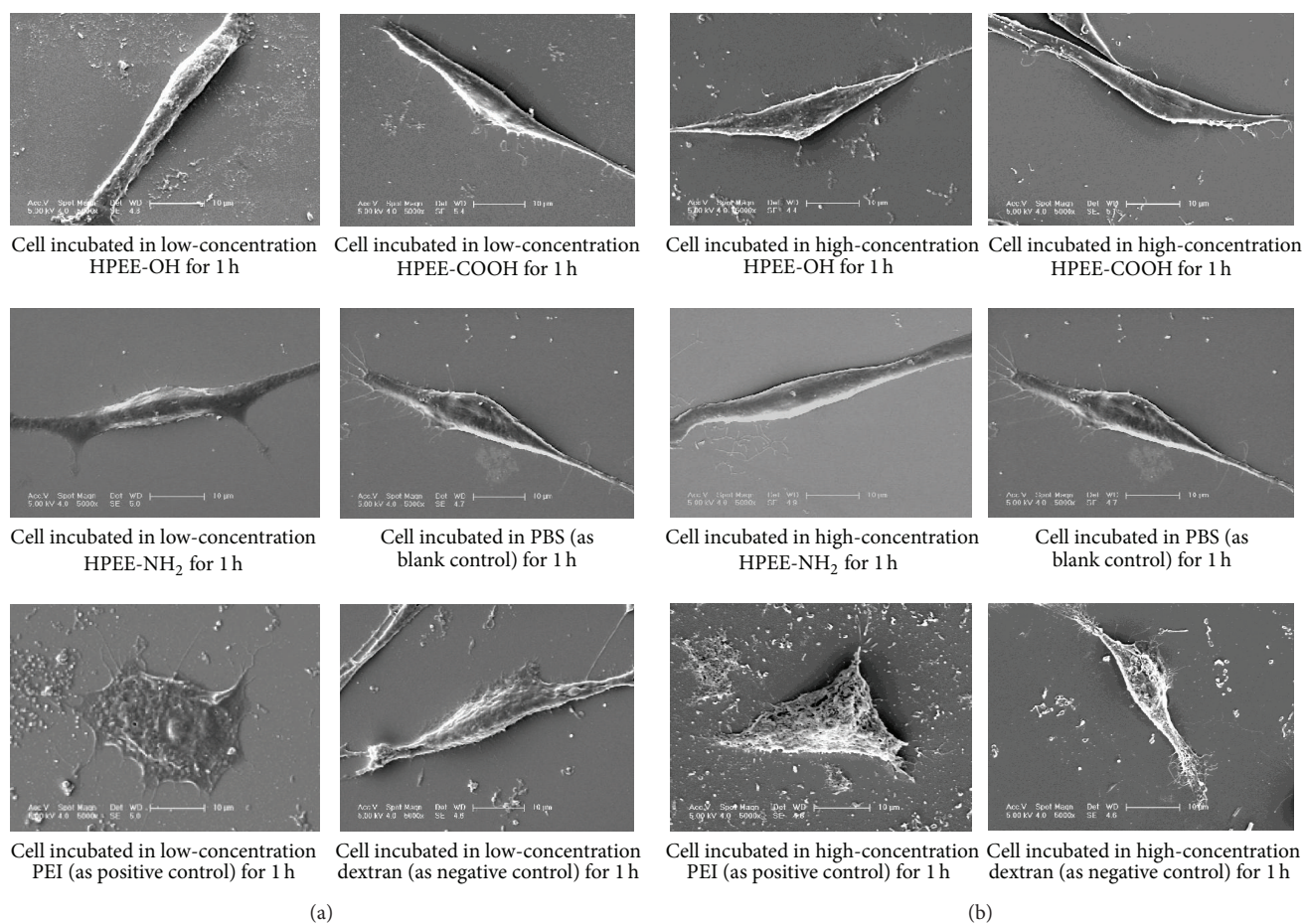
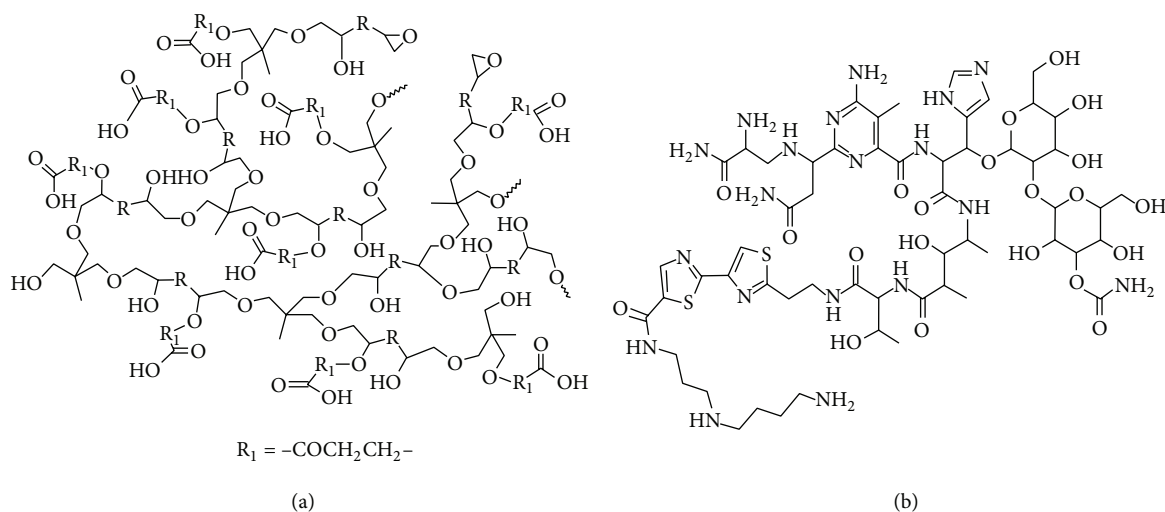


FIGURE 4: (a) SEM visualization of surface morphological features of 3T3 cells following incubation with low concentration (10 $\mu\text{g}/\text{mL}$) of functionalized HPEE-derivatives and controls. (b) SEM visualization of surface morphological features of 3T3 cells following incubation with a high concentration (1 mg/mL) of functionalized HPEE-derivatives and controls.



SCHEME 2: Structure of COOH-HPEE (a) and pingyangmycin (b).

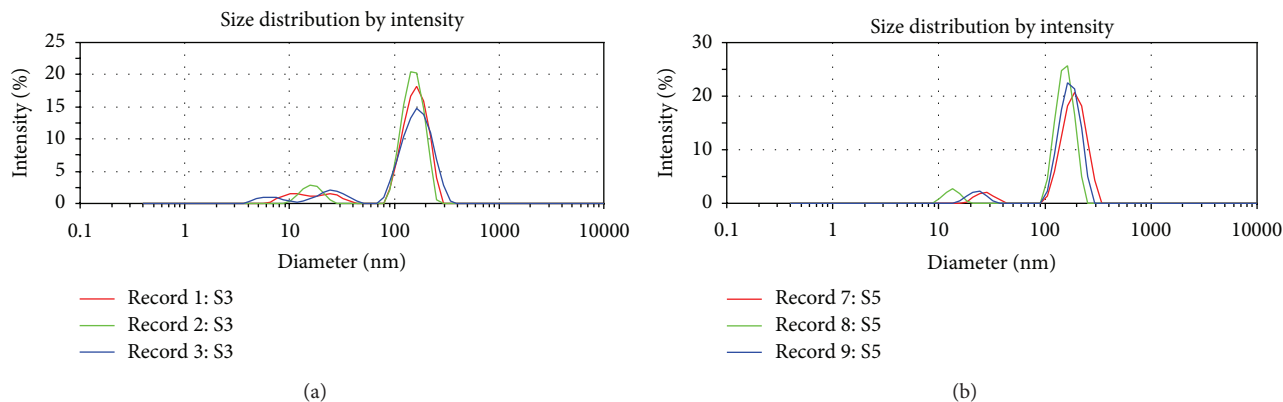


FIGURE 5: (a) Diameter of Sample 3 analyzed by dynamic light scattering assay. (b) Diameter of Sample 5 analyzed by dynamic light scattering assay.

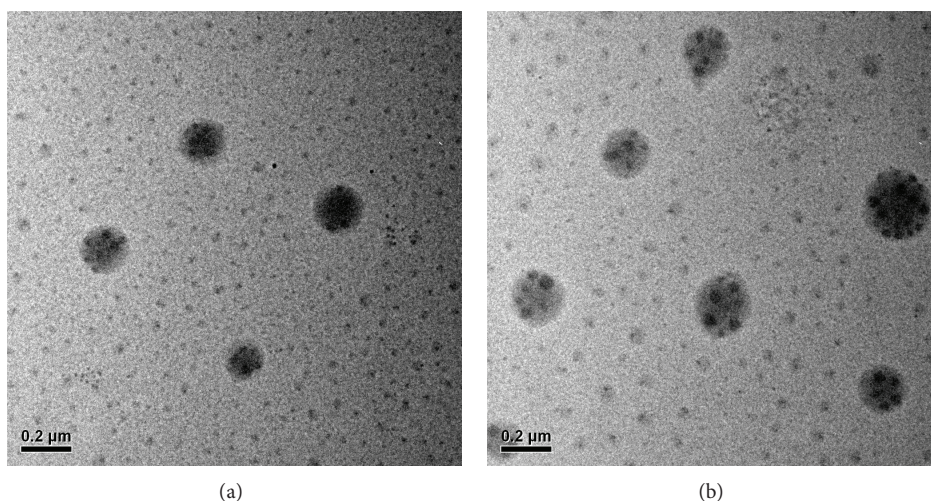


FIGURE 6: Transmission electron microscopy (TEM) visualization of two micelles of pingyangmycin conjugated into carboxyl-terminated HPEE that were successfully self-assembled in water ((a), S3; (b), S5).

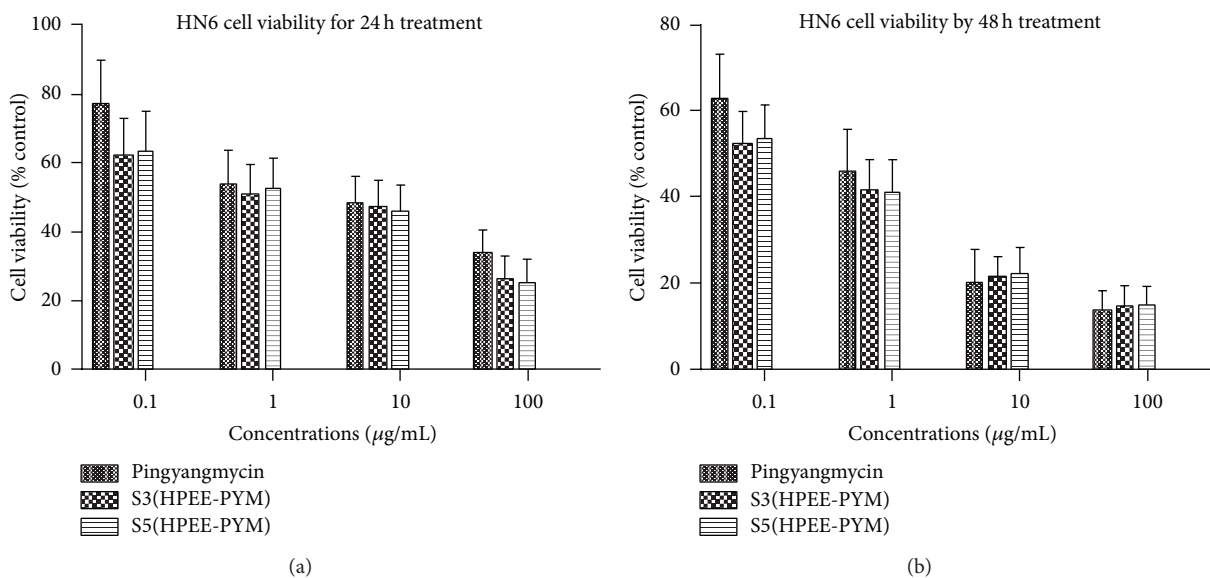


FIGURE 7: (a) HN6 cell viability following treatment with various concentrations of HPEE-pingyangmycin nanocarriers or pingyangmycin alone for 24 h. (b) HN6 cell viability following treatment with various concentrations of HPEE-pingyangmycin nanocarriers or pingyangmycin alone for 48 h.

of hyperbranched polymers have been found to be modulated by terminal-backbone interactions [39]; therefore, confirmation of successful self-assembly was required. For the purpose of comparison, in the present study functionalized HPEE was initially prepared at two different dissolving ratios to give appropriately modified polymer and excessively modified polymer. Accordingly, comparison between these subgroups allowed us to understand the contribution of physical charges. After preparation of functionalized-HPEE with distinct terminal/backbone ratios, pingyangmycin solutions of various concentrations were added for nanocarrier copolymerization. Based on the present results, stable micelles could only be successfully mixed at a ratio of carboxyl-HPEE:pingyangmycin of 5:1, irrespective of terminal/backbone functionalized ratios, suggesting that the terminal-backbone interaction exerted a mild effect on surface charge modification. The polymer: drug ratio meant that one pingyangmycin molecule was appropriately combined with five HPEE-COOH molecules in the water. Notably, numerous multimolecular compounds sized approximately 10 to 50 nm were also observed in the coconjugated solution. The size of these smaller particles was approximately that of HPEE [1], and the particles were considered to be redundant carboxyl-terminal HPEE. The final assembled delivery particles were equivalent to nanoparticles, which can be efficiently taken up by tumor cells due to passive targeting, known as the enhanced permeation and retention (EPR) effect. Therefore, appropriately sized HPEE-pingyangmycin nanocarriers have high potential for targeted antitumor therapy *in vivo*. A previous study revealed that acute cytotoxicity could be eliminated by chemical modification involving replacement of cationic amino-dendrimers on the surface by neutral copolymers [40]. The *in vitro* cytotoxicity of nanocarrier against tumor cells was assessed by MTT assays. Slight differences in tumor cell inhibition were observed between pingyangmycin-HPEE conjugation and pingyangmycin alone, indicating that the HPEE-COOH used in the nanodelivery system based on electrostatic interaction exerted little pharmacological effect, at least in an *in vitro* assay.

5. Conclusions

Due to the facile synthesis and inexpensive costs, individualized nanodelivery systems for antitumor drugs could be optimized using the present platform of functionalized hyperbranched poly(ether-ester)s. Based on the observed relationship between the chemically modified end group and physically variations in surface charge, tunable drug delivery seems easily achievable. After the physical-chemical interrelationship between surface terminal and charge loading of HPEE was revealed, pingyangmycin, a potent antitumor drug, was used as a model drug to assess the HPEE-dependent nanocarrier system. Negative-charged carboxyl-functionalized HPEE was chosen because it was expected to form ionic bonds with the positive-charged pingyangmycin. Mixture between carboxyl-HPEE and pingyangmycin was successfully achieved by self-assembly and confirmed by DLS and TMS. The resultant nanoparticles exhibited promising antitumor cytotoxicity as assessed by MTT assays. The

facile platform presented here provides an attractive pathway for individualized drug delivery based on functionalized-HPEEs.

Abbreviations

HPEE: Hyper-branched poly(ether-ester)
HPE: Hyper-branched poly(ether)
PEE: Poly(ether-ester)
PE: Poly(ether)
HBP: Hyper-branched polymers
PYM: Pingyangmycin.

Conflict of Interests

This work is sponsored by the National Natural Science Foundation of China (20974062) and China Postdoctoral Scientific Foundation (20100470692), Shanghai Jiao Tong University Med-Science Cross Research Foundation (YG2007MS11), and China National Funds for Distinguished Young Scientists (21025417). No conflict of interests has been claimed.

Authors' Contribution

Xing-ai Jin and Yan-wu Li are joint first authors.

References

- [1] G. Li, J. Liu, Y. Pang et al., "Polymeric micelles with water-insoluble drug as hydrophobic moiety for drug delivery," *Biomacromolecules*, vol. 12, no. 6, pp. 2016–2026, 2011.
- [2] D. Colombo, L. Franchini, L. Toma et al., "Anti-tumor-promoting activity of simple models of galactoglycerolipids with branched and unsaturated acyl chains," *European Journal of Medicinal Chemistry*, vol. 40, no. 1, pp. 69–74, 2005.
- [3] O. Schiavon, G. Pasut, S. Moro, P. Orsolini, A. Guiotto, and F. M. Veronese, "PEG-Ara-C conjugates for controlled release," *European Journal of Medicinal Chemistry*, vol. 39, no. 2, pp. 123–133, 2004.
- [4] C. Boulanger, C. di Giorgio, and P. Vierling, "Synthesis of acridine-nuclear localization signal (NLS) conjugates and evaluation of their impact on lipoplex and polyplex-based transfection," *European Journal of Medicinal Chemistry*, vol. 40, no. 12, pp. 1295–1306, 2005.
- [5] A. Kim and J. H. Hong, "Synthesis and antiviral activity of C-fluoro-branched cyclopropyl nucleosides," *European Journal of Medicinal Chemistry*, vol. 42, no. 4, pp. 487–493, 2007.
- [6] B. Guo, Z. Shi, Y. Yao, Y. Zhou, and D. Yan, "Facile preparation of novel peptosomes through complex self-assembly of hyperbranched polyester and polypeptide," *Langmuir*, vol. 25, no. 12, pp. 6622–6626, 2009.
- [7] M. Ji, W. Yang, Q. Ren, and D. Lu, "Facile phase transfer of hydrophobic nanoparticles with poly(ethylene glycol) grafted hyperbranched poly(amido amine)," *Nanotechnology*, vol. 20, no. 7, Article ID 075101, 2009.
- [8] R. Duncan, "Polymer conjugates as anticancer nanomedicines," *Nature Reviews Cancer*, vol. 6, no. 9, pp. 688–701, 2006.
- [9] C. Gao and D. Yan, "Hyperbranched polymers: from synthesis to applications," *Progress in Polymer Science*, vol. 29, no. 3, pp. 183–275, 2004.

- [10] B. Voit, "New developments in hyperbranched polymers," *Journal of Polymer Science A: Polymer Chemistry*, vol. 38, no. 14, pp. 2505–2525, 2000.
- [11] S.-J. Park, K. Li, and F. L. Jin, "Synthesis and characterization of hyper-branched polyimides from 2,4,6-triaminopyrimidine and dianhydrides system," *Materials Chemistry and Physics*, vol. 108, no. 2-3, pp. 214–219, 2008.
- [12] C. Kontoyianni, Z. Sideratou, T. Theodossiou, L. A. Tziveleka, D. Tsiourvas, and C. M. Paleos, "A novel micellar PEGylated hyperbranched polyester as a prospective drug delivery system for Paclitaxel," *Macromolecular Bioscience*, vol. 8, no. 9, pp. 871–881, 2008.
- [13] J. Zou, W. Shi, J. Wang, and J. Bo, "Encapsulation and controlled release of a hydrophobic drug using a novel nanoparticle-forming hyperbranched polyester," *Macromolecular Bioscience*, vol. 5, no. 7, pp. 662–668, 2005.
- [14] S. Chen, X. Z. Zhang, S. X. Cheng, R. X. Zhuo, and Z. W. Gu, "Functionalized amphiphilic hyperbranched polymers for targeted drug delivery," *Biomacromolecules*, vol. 9, no. 10, pp. 2578–2585, 2008.
- [15] W. Daniel, S. E. Stiriba, and F. Holger, "Hyperbranched polyglycerols: from the controlled synthesis of biocompatible polyether polyols to multipurpose applications," *Accounts of Chemical Research*, vol. 43, no. 1, pp. 129–141, 2010.
- [16] Y. Wang, M. Gou, C. Gong et al., "Pharmacokinetics and disposition of nanomedicine using biodegradable PEG/PCL polymers as drug carriers," *Current Drug Metabolism*, vol. 13, no. 4, pp. 338–353, 2012.
- [17] Z. Jia, G. Li, Q. Zhu et al., "Hybrid polymerization of vinyl and hetero-ring groups of glycidyl methacrylate resulting in thermoresponsive hyperbranched polymers displaying a wide range of lower critical solution temperatures," *Chemistry*, vol. 15, no. 31, pp. 7593–7600, 2009.
- [18] Y. Zhou, W. Huang, J. Liu, X. Zhu, and D. Yan, "Self-assembly of hyperbranched polymers and its biomedical applications," *Advanced Materials*, vol. 22, no. 41, pp. 4567–4590, 2010.
- [19] P. Li, G. Zhou, X. Zhu et al., "Photodynamic therapy with hyperbranched poly(ether-ester) chlorin(e6) nanoparticles on human tongue carcinoma CAL-27 cells," *Photodiagnosis and Photodynamic Therapy*, vol. 9, no. 1, pp. 76–82, 2012.
- [20] Z. Jia, H. Chen, X. Zhu, and D. Yan, "Backbone-thermo-responsive hyperbranched polyethers," *Journal of the American Chemical Society*, vol. 128, no. 25, pp. 8144–8145, 2006.
- [21] J. Liu, W. Huang, Y. Pang, X. Zhu, Y. Zhou, and D. Yan, "Hyperbranched polyphosphates for drug delivery application: design, synthesis, and in vitro evaluation," *Biomacromolecules*, vol. 11, no. 6, pp. 1564–1570, 2010.
- [22] H. Zhang, C. Zhao, H. Cao et al., "Hyperbranched poly(amine-ester) based hydrogels for controlled multi-drug release in combination chemotherapy," *Biomaterials*, vol. 31, no. 20, pp. 5445–5454, 2010.
- [23] Y. Xia, Y. Wang, Y. Wang et al., "A tumor pH-responsive complex: carboxyl-modified hyperbranched polyether and cis-dichlorodiammineplatinum(II)," *Colloids and Surfaces B: Biointerfaces*, vol. 88, no. 2, pp. 674–681, 2011.
- [24] I. J. Majoros, A. Myc, T. Thomas, C. B. Mehta, and J. R. Baker Jr., "PAMAM dendrimer-based multifunctional conjugate for cancer therapy: synthesis, characterization, and functionality," *Biomacromolecules*, vol. 7, no. 2, pp. 572–579, 2006.
- [25] Y. Luo and G. D. Prestwich, "Synthesis and selective cytotoxicity of a hyaluronic acid-antitumor bioconjugate," *Bioconjugate Chemistry*, vol. 10, no. 5, pp. 755–763, 1999.
- [26] Y. B. Lim, S. M. Kim, H. Suh, and J. S. Park, "Biodegradable, endosome disruptive, and cationic network-type polymer as a highly efficient and nontoxic gene delivery carrier," *Bioconjugate Chemistry*, vol. 13, no. 5, pp. 952–957, 2002.
- [27] R. S. Kumar, S. Arunachalam, V. S. Periasamy, C. P. Preethy, A. Riyasdeen, and M. A. Akbarsha, "DNA binding and biological studies of some novel water-soluble polymer-copper(II)-phenanthroline complexes," *European Journal of Medicinal Chemistry*, vol. 43, no. 10, pp. 2082–2091, 2008.
- [28] D. Fischer, Y. Li, B. Ahlemeyer, J. Krieglstein, and T. Kissel, "In vitro cytotoxicity testing of polycations: influence of polymer structure on cell viability and hemolysis," *Biomaterials*, vol. 24, no. 7, pp. 1121–1131, 2003.
- [29] J. C. Roberts, M. K. Bhalgat, and R. T. Zera, "Preliminary biological evaluation of polyamidoamine (PAMAM) Starburst dendrimers," *Journal of Biomedical Materials Research*, vol. 30, no. 1, pp. 53–65, 1996.
- [30] N. Malik, R. Wiwattanapatapee, R. Klopsch et al., "Dendrimers: relationship between structure and biocompatibility in vitro, and preliminary studies on the biodistribution of 125I-labelled polyamidoamine dendrimers in vivo," *Journal of Controlled Release*, vol. 65, no. 1-2, pp. 133–148, 2000.
- [31] X. Meisheng, "Histopathologic study of esophageal squamous cell carcinoma treated preoperatively with pingyangmycin," *Chinese Medical Journal*, vol. 92, no. 5, pp. 343–348, 1979.
- [32] K. W. Tai, Y. C. Chang, L. S. S. Chou, and M. Y. Chou, "Cytotoxic effect of pingyangmycin on cultured KB cells," *Oral Oncology*, vol. 34, no. 3, pp. 219–223, 1998.
- [33] K. Adriane, J. Huang, G. Ding, J. Chen, and Y. Liu, "Self assembled magnetic PVP/PVA hydrogel microspheres; magnetic drug targeting of VX2 auricular tumours using pingyangmycin," *Journal of Drug Targeting*, vol. 14, no. 4, pp. 243–253, 2006.
- [34] P. Chen, B. Liu, and M. Hu, "The effect of hydroxycamptothecin and pingyangmycin on human squamous cell carcinoma of the tongue," *Oncology Letters*, vol. 5, no. 3, pp. 947–952, 2013.
- [35] M. L. Chen, M. L. Chen, X. W. Chen, and J. H. Wang, "Functionalization of MWNTS with hyperbranched PEI for highly selective isolation of BSA," *Macromolecular Bioscience*, vol. 10, no. 8, pp. 906–915, 2010.
- [36] Y. Shi, C. Tu, R. Wang, J. Wu, X. Zhu, and D. Yan, "Preparation of CdS nanocrystals within supramolecular self-assembled nano-reactors and their phase transfer behavior," *Langmuir*, vol. 24, no. 20, pp. 11955–11958, 2008.
- [37] Y. Zhou and D. Yan, "Supramolecular self-assembly of amphiphilic hyperbranched polymers at all scales and dimensions: progress, characteristics and perspectives," *Chemical Communications*, no. 10, pp. 1172–1188, 2009.
- [38] H. Jin, W. Huang, X. Zhu, Y. Zhou, and D. Yan, "Biocompatible or biodegradable hyperbranched polymers: from self-assembly to cytomimetic applications," *Chemical Society Reviews*, vol. 41, no. 18, pp. 5986–5997, 2012.
- [39] L. Song, C. Tu, Y. Shi et al., "Controlling the optical properties of hyperbranched conjugated polyazomethines through terminal-backbone interactions," *Macromolecular Rapid Communications*, vol. 31, no. 5, pp. 443–448, 2010.
- [40] N. A. Stasko, C. B. Johnson, M. H. Schoenfisch, T. A. Johnson, and E. L. Holmuhamedov, "Cytotoxicity of polypropylenimine dendrimer conjugates on cultured endothelial cells," *Biomacromolecules*, vol. 8, no. 12, pp. 3853–3859, 2007.

Review Article

Nanostructural Colouration in Malaysian Plants: Lessons for Biomimetics and Biomaterials

S. Zaleha M. Diah,¹ Salmah B. Karman,^{1,2} and Ille C. Gebeshuber^{1,3}

¹ Institute of Microengineering and Nanoelectronics, Universiti Kebangsaan Malaysia (UKM), 43600 Bangi, Selangor, Malaysia

² Department of Biomedical Engineering, Faculty of Engineering, University of Malaya, 50603 Kuala Lumpur, Malaysia

³ Institute of Applied Physics, Vienna University of Technology, Wiedner Hauptstraße 8-10/134, 1040 Vienna, Austria

Correspondence should be addressed to Ille C. Gebeshuber; gebeshuber@iap.tuwien.ac.at

Received 3 September 2013; Revised 10 February 2014; Accepted 10 February 2014; Published 14 April 2014

Academic Editor: Il-Kwon Oh

Copyright © 2014 S. Zaleha M. Diah et al. This is an open access article distributed under the Creative Commons Attribution License, which permits unrestricted use, distribution, and reproduction in any medium, provided the original work is properly cited.

Plant tissues include leaves, flower petals, and fruits. These can provide us with variety of design inspirations. Biomimetics allows us to learn from nature and transfer the knowledge we gain from studying sophisticated and amazing biological structures, materials and processes to engineering and the arts. The microstructures of morphology and anatomy of plant tissue have potential applications in technology through bioinspired design, which can mimic the properties found in nature or use them as inspiration for alternative applications. Many applications have been developed as a result of studying physical properties of plant tissues. Structural colours, for example, have been applied in the design of thin films both with regard to single or multilayer thin film interference, scattering, and diffraction gratings. Iridescent, metallic, or greyish colouration found naturally in plants is the result of physical structures or physical effects and not pigmentation. Phenotypical appearance of plants with structural colouration in tropical Malaysia is correlated with environmental parameters such as location (shady understory rainforest, sunny conditions) and altitude (highlands, lowlands). Various examples of bioinspired technical innovations with structural colours highlight the importance of inspiration by structural colours in living nature.

1. Introduction

Ornamental plants are commercially popular. They are attractive and help to relieve stress. Beautiful plants and/or flowers make houses, restaurants, and offices more attractive. In the process of photosynthesis, plants produce the oxygen we need to breathe and absorb the carbon dioxide that we exhale, using it as their own source of food. Plant diversity is broad and a variety of patterns, colours, and types can be found in nature. Furthermore, plants can also represent a source of inspiration for nanoscience and nanotechnology.

Some plants produce nanostructures that yield colouration, either in the visible range or in the UV range that is only visible to certain species of insects. The nanostructures employed to achieve this colouration serve various functions in plants; for example, they make them even more attractive,

deter herbivores, and help in light management (e.g., UV protection or focusing of light on the chloroplasts). Acquiring a detailed understanding of these structural colours can help scientists and engineers to develop new materials that offer similar tailored properties while remaining benign and sustainable. A number of engineering devices and applications have been developed based on the mechanisms of structural colour production that are observed in nature. Examples of these include thin-film multilayers and photonic crystals, which are both formed in nanoscale structures.

Understanding nanostructures for colouration in plants and their correlation with the respective function can yield increased appreciation of the structure-function relationship in such functional nanostructures and could potentially inspire nanoscientists and nanotechnologists to develop more integrated, multifunctional applications that are both biodegradable and benign.

Colour is a property of both the colour of the object (body colour) and the perception of the observer. Structural colouration is caused by the interaction of light with minuscule structures with spatial dimensions of some hundreds of nanometers (i.e., the wavelength of visible light) or less, down to some tens of nanometers. Iridescent colour is colour that changes according to the angle from which it is viewed and everyday examples of this can be seen in the appearance of DVDs, CDs, and soap bubbles. Iridescent colouration is not caused by pigmentation but is an optical effect. Studies on structural colours date back to the seventeenth century, when the earliest scientific description of structural colours appeared in “*Micrographia*,” written by Robert Hooke in 1665. As early as 1704 in his book “*Opticks*,” Sir Isaac Newton had already related iridescence to optical interference: “*The finely colour'd feathers of some birds, and particularly those of the peacocks' tail, do in the very same part of the feather appear of several colours in several positions of the eye, after the very same manner that thin plates were found to do.*” Following his work, a plethora of articles and books that examined structural colours in organisms were published (see Kinoshita 2008 and the references therein) [1]. In Malaysia (formerly known as Malaya) pioneering research on structural colours in tropical understory plants was conducted by Lee and Lowry [2]. Professor David W. Lee was, at that time, a lecturer at the Faculty of Science, University of Malaya. We will discuss this in more detail in Section 2.

2. Plants with Nanostructural Colouration in Malaysia

2.1. Some Basic Information on Plants

2.1.1. The Anatomy and Morphology of Plants. Plants, just like animals, have parts that provide specific structures and functions; however, their way of life is much different to that of animals. Animals run, walk, hop, and move to get their food and protect themselves, their offspring, and mates. Plants produce their own food through the process of photosynthesis, and they use colourful flowers, exhibit a variety of leaf patterns and colours that attract pollinators, and produce a variety of fruits. Some plant cells have lens structures that interact with light in a manner that influences the reflection and absorption properties of the cell surface [3]. Plant tissues, including leaves, flower petals, and fruits, have their own distinct functions. The leaf functions as an optical organ in plants and uses a complex tissue organization that facilitates the distribution of light to tissues according to their differing physiological requirements for light in photosynthesis, while at the same time facilitating appropriate levels of gas exchange and water and nutrient delivery to those tissues. Figure 1 presents the anatomy of a leaf in terms of the structures through which the plant interacts with light (Figure 1). Pigmentation, both by chlorophylls and accessory pigments, makes an important contribution to these optical properties, as also does the distribution of air spaces, which cause optical scattering and path-lengthening effects. A consequence of these physical properties is that

the actual absorption of electromagnetic radiation by a leaf is significantly different from the absorbance spectrum of chlorophyll in solution. The packaging of pigments into organelles (as with chlorophylls and carotenoids) leads to sieving effects that increase light capture in the regions of the greatest absorbance by these pigments. The path-lengthening effect of air spaces in tissues promotes much greater absorption of electromagnetic radiation in normally weakly absorbed wavelengths. Plant cells have dimensions of $\sim 50 \mu\text{m}$, and the shapes and distributions of cells profoundly influence the optical properties of the leaves and other plant organs.

Optical properties in plant tissues were first studied in 1917 by Richard Willstätter and Arthur Stoll [3] (Nobel Prize to Willstätter in 1915). They published a model of the optics of a leaf. Their model considered complex patterns of internal reflectance within the leaf and disclosed how this was impacted by odd cell angles and accompanying air spaces. As a result of the presence of chlorophyll all plant leaves are basically green; however, some of them appear in other colours. Furthermore, leaves have variegation patterns that are highly influenced by cell division patterns at early growth [4]. Plant cells have a specialized anatomy and morphology that make them function properly and for survival. In this respect, it is worth briefly examining the components of plant cells. Cellulose is secreted by the cytoplasm and forms the cell wall. Cellulose has interesting optical properties: its refractive index is higher than that of water and depends on the angle at which light passes through the layer and the degree of absorption of water. If cellulose is fully moist, it may have a reflective index as great as 1.40. The cell wall becomes rigid and protects the plant from the loss of water due to drought. Inside the cytoplasm is the nucleus, where genetic information is stored, transcribed, and then translated into products that run the cell and the whole organism. Besides that, cells also have other organelles, such as chloroplasts, the sites of photosynthesis [5, 6]. Mitochondria are found in both animal and plant cells. Some plants have characteristic iridescent colouration, especially in tropical understory forests. The parts that are of interest exhibit iridescent colouration [2, 5, 7–9] and/or metallic lustre [10] in leaves, fruits [11, 12], and flowers [13]. Examples of iridescent leaves include *Begonia rex*, *B. pavonina*, *Selaginella willdenowii*, and *Danaea nodosa*. The occurrence of iridescence (change of the colouration according to the angle from which it is viewed) is always an indication of nanostructures responsible for the colour rather than the pigmentation itself [1]. Early studies on silvery plants with metallic lustre were performed on peas [14], tomatoes [15], and marrow [16, 17]. The physical basis and detailed phenomena will be discussed later in Section 2.2.

2.1.2. Iridescence in Plants in Malaysia. Plants with iridescent properties are generally found in shaded forests and tropical latitudes and are associated with lowland and vegetated environments. In Malaysia, these plants adapt to the shady, humid conditions of the forest understory. Blue-green iridescent plants are widely distributed across tropical

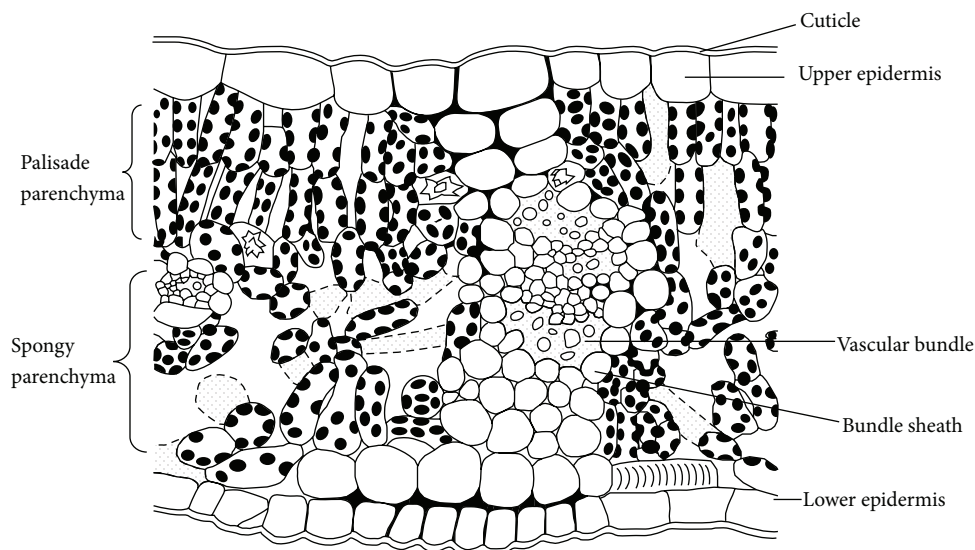


FIGURE 1: Typical anatomy of a leaf structure. A leaf contains a waxy cuticle, an epidermal cell as a cover for the upper and lower surface. Function of each tissue: the cuticle repels water, prevents rapid desiccation, acts as a selective filter in reflecting harmful ultraviolet light, and allows the absorption of visible light for photosynthesis. Epidermis cells are specially adapted for light absorption. In some plants the pigmentation is located in the mesophyll cell, immediately beneath the palisade layer. Figure modified from [6].

Southeast Asia and Africa and some iridescent plants belong to the pteridophytes genus *Selaginella* (Selaginellaceae). Among the common species and predominant blue iridescent plants is *Selaginella willdenowii* (peacock fern, Malay name “pakis merak”). Besides, *S. willdenowii* blue iridescent plants include *Begonia pavonina* (Begoniaceae), *Diplazium tomentosum* (Athyriaceae), *Danaea nodosa* (Marattiaceae), *Lindsaea lucida* (Lindsaeaceae), and *Phyllagathis rotundifolia* (Melastomataceae). 52 native species of *Begonia* are known in Peninsular Malaysia and over 1500 species are recorded in wild tropical and subtropical Asia, Africa, and America. The native species of *Begonia*, which is characterised by leaves that sometimes have a bluish tinge, include *B. alpina*, *B. carnosula*, *B. integrifolia*, and *B. thaipingensis* [18]. A species with green iridescence is the cave moss *Schistostega pennata* (Schistostegaceae), which can be found in shady and dark places near the cave entrance at the Batu Caves near Kuala Lumpur [7]. The colour of many understory tropical rainforest plants can be described as iridescent because of the intensity and metallic quality [7] of their colouring and the fact that they appear to change colour when viewed from different angles. Iridescent leaves generally distribute the reflected granules on epidermal cells, for example, in the case of *S. willdenowii* (Figure 2). Green iridescence occurs via the refraction of diffused light onto specially oriented chloroplasts by lens-shaped cells, while blue occurs when, for example, a thin film acts as an interference filter in or on the epidermis [7]. Iridescence can span two or more different colours and can appear in regions of the spectrum that are visible to a variety of animals including ultraviolet (UV) [19] or the range visible for humans [20]. There is a distinct need for researchers to complete further studies of the phenomenon of iridescence in plant aspects such as structures, functions, distribution, and behaviours.

Iridescent or structural colour phenomena are not limited to leaves but can also be found in fruits and flower petals. However, at present, plants found in Malaysia only exhibit an iridescent effect on their leaves. Several structural fruit colourations with brilliant blue iridescence have been reported for *Elaeocarpus angustifolius* (Elaeocarpaceae) [21, 22], *Delarbrea michieana* (Araliaceae) [12], and *Polia condensata* (Commelinaceae) [11]. *D. michieana* is a small understory tree that is endemic of the tropical region of Queensland, Australia. Vukusic and Stavenga [20] investigated the structural colouration of this species.

2.1.3. Phylogenetics of Plants: Genotype and Phenotype. The physical appearance of an organism is phenotypic, while its internal coding is genotypic. A single genotype can produce different phenotypes in different environments; that is, seeds from the same plant might very well yield completely different looking offspring plants, with the nanostructures responsible for colouration varying according to environmental parameters such as altitude and light intensity. The patterns in plants, for example, those found in a leaf, are under genetic control and may involve different mechanisms for controlling pigments and structure. This fundamental property of organisms is known as phenotypic plasticity. Recent intensive study has shown that plants are plastic for a remarkable array of ecologically important traits, ranging from diverse aspects of morphology and physiology to anatomy, developmental and reproductive timing, breeding system, and offspring developmental patterns. Comparative, quantitative genetics and molecular approaches are leading to new insights into the adaptive nature of plasticity, its underlying mechanisms, and its role in the ecological distribution and evolutionary



FIGURE 2: Iridescent plants. *Selaginella willdenowii* leaf (a), Figure © one of authors (SZMD). Surface details of *S. willdenowii* leaf (b), showing the sites of its unusual colour production. Figure from [23] Permission pending.

diversification of plants [24]. We suggest performing studies on phenotypical variations of nanostructures yielding colouration. Such studies shall give important insights into the function of the respective nanostructures and facilitate understanding of the structure-function relationship and related biomimetics.

Inheritance is the acquisition of traits that are genetically transmitted from parents to offspring. In individual cells, information that controls the division of cells and the formation of tissues, organs, and the complete organism is maintained in the nuclei. Nucleic acids are very large structures that include DNA (deoxyribose nucleic acid) and RNA (ribose nucleic acid) and are composed of four nucleotides (adenine, thymidine, cytosine, and guanine, but in RNA guanine is replaced with uracil). The nucleotides follow a specific sequence in this basic information and have a double helix structure. Each sequence of nucleotides contains information for the production of a unit of heritance or a gene. Nucleic acids are the main constituents of the genes that contain hereditary information within long polymers at specific locations on chromosomes. However, it is possible that the alteration of genes may occur at an individual level and will be expressed in the form of different characteristics in a trait such as flower colour and leaf shape. These are known as alleles. Gregor Mendel established the laws of expression of genes and alleles in the nineteenth century through *Mendel's Principles of Heredity* or *Mendelian Inheritance* and he found that some alleles are dominant in their expression while others are recessive. Afterwards, Mendel found many exceptions to the rules governing the inheritance for combining genes and alleles [5]. For example, it would be interesting to compare the nanostructures of the peacock begonia when grown in different conditions and start to correlate the structure and function from such investigations. In such a way, templates for the transfer of such colours to engineering could be generated [25]. Despite recent developments in molecular genetics in terms of understanding gene action, still little is known about the physiology of colouration. Greater knowledge is needed about the developmental and

physiological constraints that either induce or block the production of pigments [26]. Existing research on phylogenetics and physiology of coloration in plants is much less common than that on animals. Lee et al. [12] examined the phylogenetics of two different taxa of the family Araliaceae, namely, *Delarbraea* and *Mackinlaya*. Genetic diversity and variation in *Begonia* species was studied by Matolweni et al. [27].

2.1.4. Distribution and Environmental Factors (Biotic and Abiotic): Understory and Nonunderstory Forest. Individual organisms live in different habitats and localities. They can be modified or altered by development, physiology, and life history according to environmental conditions. Physical environmental conditions, such as water availability, humidity, temperature, soil chemistry, light exposure, and locality, affect the distribution, pattern, and abundance of plant species.

Light Condition. Plant growth in the understory rainforest is much different to that in the open air or with direct exposure to sunlight. In shaded areas, the light intensity is less and can be only 3–5% of the fully sun-exposed value [5].

Elevation. The majority of plants that are found at high elevations are covered with hairs or wax that protect them against the increased light intensity. Furthermore, some of the plants found in these conditions are capable of converting the sun's light rays into heat (with the help of red pigments) [5].

Tropical rainforests with their high humidity and low light intensity provide a rather specific environment for the herbaceous ground flora. Here, many iridescent plants can be found. In most cases, the iridescence of the leaves and fruits is in the blue and blue-green range of the light spectrum. The first study on the physical basis and ecological significance of iridescence in plants, on *Selaginella willdenowii* (changing the colouration of the top of its leaves from green to blue and back to green when viewed at different angles), was conducted by

Lee and Lowry [2] and revisited in Thomas et al. [28]. According to these authors, iridescent leaves are mainly found in shaded tropical rain forest: when growing in sunlight, their iridescence was lost [2, 28]. Recent research on the structural colours found in plants and other nonanimals (summarized by Gebeshuber and Lee, 2012) [29] indicates that the most common mechanisms in plants that cause structural colouration are multilayer interference and diffraction gratings [29]. Multilayer interference is found predominantly in shade-plant leaves, suggesting a role either in photoprotection or in optimizing the capture of photosynthetically active light (Lee 2007 and references therein) [5]. Diffraction gratings may be a common feature of petals, such as those found on tulips or hibiscus.

Structural colours may be surprisingly frequent in the plant kingdom, and still much remains to be discovered about their distribution, development, and function [19]. The scattering of light yields, for example, the blue appearance of the needles of the blue spruce, and photonic crystals yield interesting and beautiful effects in high altitude plants such as Edelweiss or in viruses and diatoms. Cholesteric liquid crystals might be the reason for the structural colouration in some Malaysian iridescent understory tropical fern species such as *Danaea nodosa*, the necklace fern *Lindsaea lucida*, and *Diplazium tomentosum*. Gebeshuber and Lee [29] also described a multitude of plants and other nonanimals where the nanostructural origin of the colouration effects has not yet been described and/or identified. There might be very interesting nanoscience waiting in some of these organisms and some surprises too! In animals, the interaction of light with the nanostructures of biological tissue produces iridescence either via thin-film interference, multilayer interference, scattering, diffraction, or photonic crystals [1].

2.2. Colouration in Plants

2.2.1. Principles of Colouration. Colour is a property of both the coloured object and the perception of the observing animals or people [19]. According to Mott (1893), the colours of animals and plants have three causes: (1) physical causes such as diffraction and interference from striated surfaces, as in some iridescent feathers and shells; (2) pigments whose function seems to be especially to give colour; (3) the molecular structure of the tissues themselves [30]. Colouration in organisms is normally caused by pigments (chemical) or optical effects (structural) or a combination of both. In plants, the majority of colouration is produced by a variety of pigments such as anthocyanin, flavonoids, and carotenoids. In chemical colours, light is selectively reflected, absorbed, and transmitted. Pigments reflect the wavelengths of light that produce a certain colour and absorb the other wavelengths. While in structural colours, the incident light is reflected, scattered, and deflected on structures with negligible energy exchange between material and the light, resulting in strong and shining colouration [1]. Plants that have waxy coverings are whitish blue [5], for example, the *Schima wallichii* conifer tree. Shaded lowland tropical rainforests are home to various species with leaves that have blue-green iridescence.



FIGURE 3: Iridescent plant. A tropical Asian understory herb, *Mapania caudata*. The colour comes from nanoparticles of biogenic silica. Image from <http://bioserv.fiu.edu/~leed/research.html>. Figure reproduced with permission.

Begonia species have a variety of natural foliar variegated patterns that include leaf structure and pigment-related variegation [31]. The silvery spots that are sometimes present in *Begonia* are not caused by pigments but by increased air-filled cells. These spots on the leaves mimic insect's eggs, preventing butterflies from laying eggs on these leaves because "it is already taken by other insects." *B. pavonina* is found in altitudes above 1,000 meters in hill forests such as those found in the Cameron Highlands, Malaysia. Zhang et al. [10] studied the metallic appearance of *B. rex*. The leaves of this species have two regions that reflect light: spotted patterns and polygonal patterns. They showed that the polygonal patterns influence the metallic colour. Interior air spaces are the most important factors in the formation of the polygonal pattern [10].

Some benthic marine algae produce blue to violet iridescence. The moss *Schistostega* shows iridescence in the golden-green part of the spectrum [31]. Surprisingly, for colouration in certain plants, the presence of nanoparticles of biogenic silica provides the basis for the colour; an example for this is the tropical Asian understory herb, *Mapania caudata* (Figure 3), and two Malaysian tropical rainforest herbs, *Diplazium crenatoserratum* and *Phyllagathis rotundifolia* (Figure 4). In 1975, Lee and Lowry published an article in the journal *Nature* on their research regarding the brilliant iridescent blue in *Selaginella*, which is caused by structure, not pigments. They found that the leaves lose their colour when immersed in water but that the blue colour reappears when the leaves are dried [2]. Prior to their research little was understood about the iridescent phenomena found in plants.

2.2.2. Pigmentation (Chemical Colours). Pigmentation phenomena are associated with the most fundamental elements of organic life. The colour of tissue or pigments depends on the portion of white light that is reflected from them. Sunlight is white light, and after it hits objects it is partly reflected and partly absorbed [30]. The majority of colouration observed in plants stems from pigmentation. In chemical colours, light is selectively reflected, absorbed, and transmitted. The production of colours occurs when pigments reflect certain wavelengths of light and absorb other wavelengths [29]. Some



FIGURE 4: Iridescent plants. Two Malaysian tropical rainforest herbs, *Diplazium crenatoserratum* (on top) and *Phyllagathis rotundifolia* (underneath). Image from <http://bioserv.fiu.edu/~leed/research.html>. Figure reproduced with permission.

sepals (basic parts of a flower, below the petals) change their colours under different cultivation conditions, such as in *Hydrangea macrophylla*. The colour changes in this species from colourless in the early stages of development to blue and then green and finally red during senescence. This is due to a change in anthocyanin biosynthesis [13]. Pigmentation colours occur when light is absorbed in materials. Illuminating light in materials such as pigments, dyes, and metals interacts with electrons within the materials and excites them to a higher state, by virtue of the energy consumption of light [1]. The blue colour in fruits and flowers is mainly caused by modified anthocyanins.

2.2.3. Structural Colours. Studies on structural colour can be traced back to the development of electromagnetic theory by Maxwell 1873 [32], followed by electromagnetic waves by Hertz 1884 [33] and the upgrading of the electromagnetic theory by Lord Rayleigh 1917 [34]. This was, in turn, augmented by the research on surface colours that was completed by Walter 1895 [35] and Michelson 1911 [36], finally resulting in the affirmation of the principle of the concept. Structural colours are normally observed in nature in various animals, plants, and microorganisms. Famous examples of this phenomenon include wings of butterflies (such as *Morpho* sp., *Parides* sp.), peacocks feathers, and beetle carapaces. In plants with structural colouration, chloroplast extraction shows only green chlorophyll and a few carotenoid pigments. The anthocyanins that form the blue colour are not present [5, 37]. Various physical mechanisms are responsible for the production of structural colour in plant leaves, fruits, and others (for overview, see Table 1).

Many iridescent colours in plants are produced by multilayer thin-film interference, diffraction gratings, and scattering (Tyndall scattering) [8] (see Section 3.1). These mechanisms are associated with distinct colouration appearance properties such as tuneable colours that change according to the viewing angle [38] and retroreflection properties [39]. Structural colours are involved in functions such as display and defence, photoprotection, and photoreception. Detailed characteristics, mechanism, and functions of structural colour phenomena for some species of plants were reviewed by Glover and Whitney [19].

2.2.4. Functions and Potential Applications. Colours serve a multitude of functions in nature. Animals use them mainly for signalling, mimicry, mating choice, and protection. Structural colour in plants attracts pollinators and helps to protect and these colour functions are primarily found in flowers and leaves. Fruits may attract animals like birds and mammals, which then disperse the seeds. Structural colour may be related to significant functional biology and the physiology of plants. Structural colouration is relatively permanent and generally does not bleach in the same way that pigment colours do. A piece of the fruit from *Pollicia condensata* that was collected in Ghana in 1974 and kept dried as a herbarium specimen in the herbarium of the Royal Botanic Gardens, Kew, United Kingdom, ever since still retains its brilliant blue colour [11]. In *Selaginella willdenowii*, lamellae are observed, which might serve as functional antireflective coating, reflecting light in short wavelengths and enhancing the absorption of light at longer wavelengths through destructive interference [2]. Iridescent blue leaves might also function to protect leaves via photoinhibition when exposed to high light levels [37].

Plants that are coloured by pigmentation are regularly used for body decoration purposes; for example, henna (*Lawsonia inermis*) is used to colour hands [5] and hair. Plants are also utilized for many other vital purposes, such as the provision of food, medical treatments, and dyeing of cloth. Further details about the application and biomimetics of structural colour will be discussed in Section 4.

3. Relationship between Nanotechnology and Optical Properties

3.1. Light, Vision, and Colour

3.1.1. Light Perception and Optical Properties. Colours undergo changes throughout the day, and these changes are a function of the amount of light that is available. Daytime is dominated by bright and clear colours; however, this ceases to be the case when the weather is overcast or cloudy. During nights, the surroundings are colourless and dark and the light source comes from the moon or artificial lighting. Humans and animals are dependent upon light as a vital sensory signal, while plants are dependent upon light for their growth and physiological responses. Plants capture light as a source of energy and depend on it for survival. Colour is regarded as a visual perception property that corresponds to humans. Human beings are unable to perceive iridescence in flowers; however, honey bees are attracted to flowers for that very reason and this culminates in them collecting nectar. The understanding of the interaction between plants and light and how animals perceive this interaction as form and colour is called light perception phenomena [5].

Light can be defined as an electromagnetic wave that contains particles of energy [40]. Light perception is always related to light propagation, incident light, light reflection, refraction, transmission, and absorption. Light propagating from one medium to another can be reflected or refracted by a surface or interface. The characteristics of the reflected

TABLE 1: Noncomprehensive list of physical mechanisms that yield iridescence in plants, with examples and functions [29].

Physical mechanism	Visual appearance	Examples	Function
Thin film interference	Iridescent blue. Interference within the peridium, a 200 nm transparent layer in fungi.	Slime mold <i>Diachea leucopodia</i>	Photoprotection
Multilayer interference	Iridescent blue leaves. Various layers on the surface, each layer less than 100 nm thick.	Peacock fern <i>Selaginella willdenowii</i> , <i>S. uncinata</i> , <i>Diplazium crenatoserratum</i> (Figure 4), <i>D. tomentosum</i> , <i>Lindsaea lucida</i> , <i>Danaea nodosa</i> , and <i>Trichomanes elegans</i>	Photoprotection
	Iridescent blue leaves. Modified chloroplast structures (iridoplasts) with many layers and each layer less than 100 nm thick.	Peacock begonia <i>Begonia pavonina</i> , <i>Phyllagathis rotundifolia</i> (Figure 4), and <i>P. griffithii</i>	Photoprotection
	Iridescent red. Multilayer system with 17 electron opaque and translucent layers between ten and a few hundred nanometers thick.	Algae <i>Iridaea</i>	Byproduct of wear-protection mechanism
Diffraction gratings	Petals iridescence. Diffractive optics. Surface striated one micrometer apart.	<i>Hibiscus trionum</i> , <i>Tulipa kolpakowskiana</i>	Blue, green, and yellow structural colouration in hibiscus: structural colouration in tulips in the UV part of the spectrum (not visible to people, visible for bees).
Scattering	Microscopic air spaces in surface hairs (trichomes) that reflect the light. Epicuticular wax structures.	Blue spruce <i>Picea pungens</i>	Preferential scattering of short wavelengths and enhanced reflectance of UV.
Photonic crystals	Iridescence in fruits. Iridosomes (secreted by epidermis cells of fruits, partly cellulosic situated inside cell wall), multilayer system arranged in 3D structure.	Blue quandong <i>Elaeocarpus angustifolius</i> syn. <i>E. grandis</i>	Absorption of UV light, photoprotection, display and defence.
	Internal structure of hollow hairs acts as a 2D photonic crystal (optical fiber with photonic crystal cladding).	Edelweiss <i>Leontopodium nivale</i> subsp. <i>alpinum</i>	
	Iridescent blue fruit. Multilayers in cell walls of epicarp [11].	<i>Pollia condensata</i>	Curved micro-Bragg reflector, used for display and defence.
Cholesteric liquid crystals	Modified chloroplasts with helicoidal structures.	Fern <i>Danaea nodosa</i>	

or refracted light are dependent on the optical properties of the respective surfaces or interfaces. The optical properties of surfaces are determined by their structure and morphology [41]. Note that, in the terminology of solid-state physics, “structure” refers to the geometrical arrangement of atoms in a crystal lattice, while “morphology” refers to the macroscopic shape of a surface. This usage of the term structure is different to the usage of structure in “structural colours,” where it relates to micro- and nanometer-sized features that yield colouration or metallic effects [42].

Snell’s law [41] can be used to understand the reflection and refraction of light (Figure 5). These phenomena occur on every surface and interface in this world. The structural colours of many animals and plants are generated by the reflection and refraction of incident light on nanostructured surfaces of periodic biological multilayers [43]. Structural

properties, such as surface condition, multilayer thickness, number of multilayers, and refractive index, are the main factors that contribute to the quality of the reflected or refracted colours. A smooth surface can produce specular reflections, while rough surfaces will produce diffuse reflections [40].

3.1.2. Structural Colour Mechanisms. The physical phenomena involved in producing structural colour in nature and engineering are identified as follows: thin-film interference, multilayer thin film, diffraction gratings, and scattering.

Thin-Film Interference. Interference is described by superposition of two or more waves [40]. When two or more waves overlap, the displacements of waves at any point and any instant in time are combined. For the overlapping condition where the two waves are coherent, the sum of

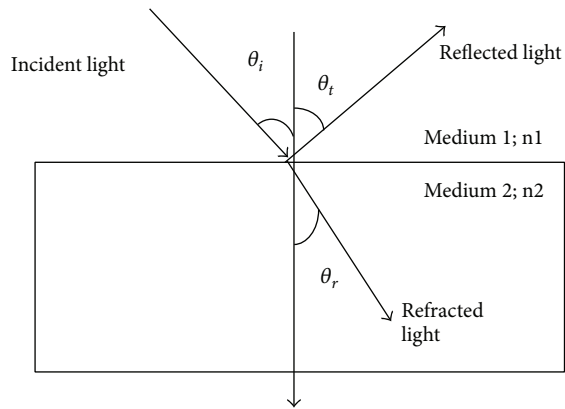


FIGURE 5: The principle of Snell's law.

the two waves will produce constructive interference. In contrast, destructive interference is described by the situation where cancellation or partial cancellation of individual wave amplitudes occurs. The structural colours of many biological tissues, especially in plants, are produced by interference in multilayer thin films [44]. Thin-film interference occurs when the incident light is reflected from its upper and lower surfaces [40]. The incident light that reaches the upper surface is partly reflected and partly transmitted into the thin film. The transmitted light that reaches the lower surface of the thin film is partly reflected. The constructively or destructively interfering reflected light beams will reach the retina of the eye (Figure 6).

Colours produced from thin-film interference are not very bright in most cases and examples include soap bubble colours and colours from oil films on water or gas sheets [43]. Increasing the number of layers results in a multilayer that can produce much more intense, brilliant colours.

Multilayer Interference. The colour produced by this phenomenon is caused by sharp periodic boundaries in the refractive index [11]. The multilayer could be from liquid, solid, or gaseous material [43]. The sparkling metallic lustre in the leaves of *Begonia rex* has been mimicked to improve colouration technology. The metallic effect in these leaves is formed by light reflection off the surface and the interior of the leaves [10]. The formation of the light reflection from the interior is associated with the interior structure of the leaf and is impacted by cell density and the arrangement of air spaces. The anatomical structure of the leaf shows stacked layers of cells, where each layer is one cell thick, in the interior of the leaf. A different type of cell with different cell density forms every second layer. Through this structure the plant establishes a multilayer system.

Diffraction Grating. The diffraction effect is defined by the interference of many light waves around an obstacle [33]. It can also be caused by single or multiple slits, which represent obstacles. The diffraction pattern depends on the width,

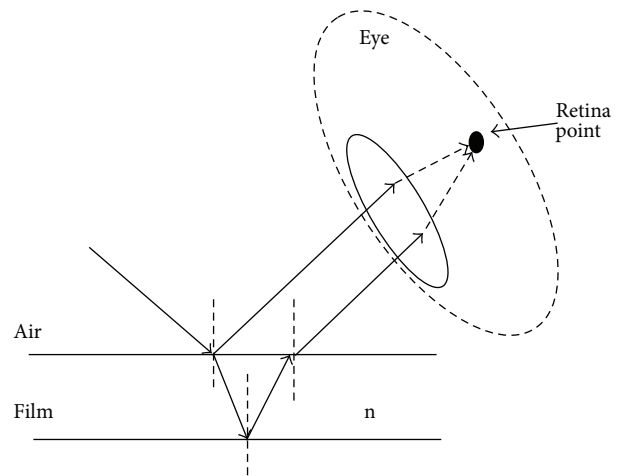


FIGURE 6: Thin-film interference (modified from [33]).

number of slits, and distance between the centres of the adjacent slits. The colouration resulting from light interacting with diffraction gratings depends on the width and separation of the slits/obstacles [40]. A diffraction grating produces rainbow colours that are strongly dependent on incident angle (e.g., DVDs, CDs). Some diffraction patterns can be observed through a microscope but not with the naked eye [44]. Diffraction gratings in plants were discovered pretty late. Whitney and coworkers (2009) published a paper on colour-generating diffraction grating-like structures on the surface of petals of *Hibiscus trionum* in Science [45]. Nowadays, we know that diffraction gratings occur regularly in flowering plants.

Scattering. The scattering phenomena that yield structural colouration in plants can either be coherent or incoherent [29]. Due to the constructive relationship between the two scattered waves, coherent scattering produces strong colours. The destructive relationship between the scattered waves produces weak colours in incoherent scattering phenomena. Two types of scattering phenomena occur in plants: Mie and Tyndall scattering. Mie scattering is a scattering phenomenon that is caused by particles that are larger than the wavelength, while Tyndall scattering is caused by particles that are smaller than the wavelength. Whereas the blue colour of the sky is produced by Rayleigh scattering, the Mie scattering produces the white colour of the clouds [40]. The high concentration of water particles in the clouds allows the scattering of all wavelengths of light, which results in the white colour of clouds. The fat globules in fine suspension of milk scatter the light in all ranges of wavelengths, resulting in the white colour of the milk. A milk solution that has low concentrations of fat globules will be perceived as blue, due to the fact that blue is scattered more than red. Tyndall scattering phenomena occur in blue spruce and are also producing a blue hue in banana leaves [29].

TABLE 2: Engineering applications that use structural colour based optical devices.

Physical mechanism	Device structure	Engineering application	References
Multilayer interference	Multilayer thin film	Coating	[46]
Multilayer interference	Self-assembled nanocrystalline cellulose film	Humidity sensor	[47]
Multilayer interference	Multilayer flakes	Coating/painting	[48]
Multilayer interference	Multilayer thin film	Solar collector	[49]
Multilayer interference	Multilayer structure	Solar collector	[50]
Multilayer interference	Multilayer thin film structure	Antireflection coatings for solar cells	[51]
Multilayer interference	Polypeptide-based LB film	Display system	[52]
Multilayer interference	Elastic optical multilayer fibre	Colouration	[53]
Multilayer interference	Multilayer structure	Interference filters	[54]
Multilayer interference	Multilayer structure	Interference filter	[55]
Photonic structure	Photonic crystals	Temperature tuneable photonic crystals	[56]
Photonic structure	Photonic heterostructures	Colour filter	[57]
Photonic structure	Photonic crystals	Calorimetric sensor	[58]
Photonic structure	Photonic crystals	Antibody detection	[59]
Diffraction grating	Metal-dielectric multilayer	Colour shift	[60]
Photonic structure	Photonic crystals	Blast exposure sensor	[61]

4. Production of Nanostructures for Colouration

4.1. Existing Products or Devices. As summarized in Table 1, the mechanisms involved in the generation of structural colouration in the plant kingdom consist of thin-film/multilayer interference, scattering, diffraction gratings, and photonic structures. In engineering applications, multilayer interference is associated with thin-film technology, while photonic crystals are generally used to produce photonic band gap (PBG) devices [58].

Besides being used for colouration purposes, devices that incorporate structural colour are used for applications such as coatings, sensors, fuel cells, and certain types of display systems (Table 2).

Man-made structural colour is obtained via the manipulation of the optical properties of thin-film multilayers and photonic crystals, such as layer thickness and refractive indices. Multilayer thin films consist of several layers alternately stacked one above the other. The improvement of layer-by-layer (LBL) deposition and fabrication techniques allows the development of multilayer thin films that offer various kinds of optical properties [62].

Photonic crystals (PCs) are materials that have a periodic modulation in their refractive index. This can be used to produce intense visible colours through coherent Bragg diffraction [63, 64]. Photonic crystals are divided into three categories: one-dimensional, two-dimensional, and three-dimensional structures [64]. These three structures differ in terms of periodic modulation of the permittivity. These periodic modulations occur in one-dimensional, two-dimensional, and three-dimensional structures at one, two, and three directions of the medium, respectively. Due to this modulation, photonic crystal structures show similar optical

properties as systems known from solid state physics, with photonic bands.

A discussion on the multilayer and 3D photonic crystal structures used in tuneable colour devices for application in coatings, for decoration, sensors, and display systems is provided in Sections 4.1.1–4.1.4. Although the mimicking of plant structures in developing such devices is not mentioned in most of the reviewed papers, due to the applied mechanisms, some of them might very well be inspired by structural colouration in plants. The majority of engineering devices are designed in simpler ways than the related plant structures [53].

4.1.1. Multilayer Based Colouration

Multilayer Based Colouration for Coatings. Hirayama et al. [46] proposed multilayer film based coatings for illumination models for objects. The film's primary reflection and refraction multilayer structure was used to coat smooth and rough surfaces by using multilayer film ray tracers (MFRT). The illumination models used in this study were made of silicon, coated with three layers: a dielectric-silver-dielectric multilayer or a dielectric-gold-dielectric multilayer. A better rendering illumination model was obtained in this study, where the rough surface model showed clearer iridescent colour than the smooth surface.

Yasuda et al. [48] developed novel $\text{TiO}_2/\text{SiO}_2$ multilayered flakes without cores for application as interference flakes that exhibit structural colours. These multilayered flakes were proposed to improve effect pigment coating in terms of coating thickness reduction (note that the technical term "effect pigments" refers to colouration without actual pigments, but with structures alone. However, this

term is established and generally used, so we also use it, although we state that it is structures that are responsible for the colouration, not pigments). In this study, seven layers of $\text{TiO}_2/\text{SiO}_2$ sol-gel route multilayers were developed for high/low refractive index layers for interference effects on flakes for decorative paint. This multilayer reflected cyan and orange and transmitted red and light blue colour.

Future tuneable structurally coloured fabrics could be realized through the bioinspired design of multilayer based soft photonic fibres, as proposed by Kolle et al. [53]. Inspired by the structure of the seed coating found in *Margaritaria nobilis* fruits, band-gap tuneable elastic multilayer fibres were developed by forming a bilayer of two elastomeric dielectrics, polydimethylsiloxane (PDMS) and polystyrene-polyisoprene triblock copolymer (PSPI) on a silicon substrate. This bilayer was then rolled up onto the glass fibre to form a multilayer cladding with a diameter of $\sim 15 \mu\text{m}$. Removing the glass fibre from the rolled-up multilayer allows mechanical deformation, resulting in tuning of the band gap and spectral blue-shift, with brilliant colours.

Multilayer Based Colouration for Solar Collectors. Schüler et al. simulated the development of a multilayer based coloured solar thermal collector [49, 65]. The issue of colour of solar thermal collectors for buildings is important due to architectural limitation of black solar thermal collectors. A colour reflecting cover glass was proposed in this study as a means of achieving better appearance without interrupting the energy absorption of the solar thermal collector system. The study was conducted through simulation of an International Commission on Illumination (CIE) (CIE is a short form of International Commission on Illumination in French: Commission Internationale de l'Éclairage [66]) based colour coordinated approach on at least two designs, two layered systems and three layered systems designs. From this study, the two-layered design was proposed as a means of creating a colourful reflection in the visible spectral region and a region of antireflection. The three-layered design was proposed as a means of creating a strong enhancement of the reflectance peak.

Wu et al. [50] fabricated titanium-aluminium nitride (Ti-AlN) multilayer based solar thermal collectors. Five colours, namely, black, purple, yellowish green, red, and yellowish orange, were obtained by variation in layer number and thickness of the Ti-AlN multilayer that was fabricated through magnetron sputtering.

Selj et al. [51] proposed a clear coloured, highly efficient solar cell with multilayer antireflection coatings. The use of a multilayer antireflection coating in this study had benefits, not only as an antireflection coating but also as a coloured coating. The multilayer antireflection layer was made of SiN_x and silicon oxide via plasma-enhanced chemical vapour deposition (PECVD) and nanoporous silicon methods. The colours resulting from the multilayer antireflection layers prepared using the PECVD method produced a red, green, and blue. Using nanoporous silicon methods, the colours obtained were green, red, purple, and orange. Through nanoporous silicon methods, the thickness and refractive

index of the layer could be controlled to obtain the desired colour.

Multilayer Based Colouration for Sensing. Zhang et al. [47] developed a self-assembled nanocrystalline cellulose-based chiral nematic multilayer film that changed colour with humidity. The film had a helical twist axis of periodic layer structures that acted as multidomain Bragg reflectors. A multilayer that was constructed using a nematic-type phase structure that possessed self-aligned rod-shape molecules was used to obtain the long-range directional order with regard to parallel long axes [67]. Through the sorption and desorption of water by the film due to reaction to the humidity, the layer thickness changed and thereby also the colour. The iridescent colour produced was blue to green in the dry state and red to orange in the wet state.

Multilayer Based Colouration for Display. Structural colouration has also been used in the development of chameleon-like display systems, as proposed by Kinoshita et al. [52]. The display system was formed by polypeptide multilayers based on Langmuir-Blodgett (LB) films [62]. Kinoshita et al. developed the LB film by transferring the poly (γ -hexyl-L-glutamate) (PHeLG) multilayer onto the silicon substrate in a number of layers up to 160 with a thickness of 1.6 nm per layer. Stacks with different thickness of such PHeLG multilayers produced different colours: 40–50 layers produced brown, 60–70 layers produced dark blue, 80–100 layers produced light blue, yellow was obtained when the number of layers was 120, and red-purple was obtained at 160 layers. The reflective VIS spectra of multilayers produce different interference colors depending on the number of layers.

Multilayer Based Interference Filters. Multilayer polymeric interference reflectors were reviewed by Nevitt and Weber [54]. They found that the desired polymeric interference reflector with the desired optical properties could be obtained by controlling the thickness and structural uniformity of the polymeric multilayer stacks. One popular product that possesses this kind of structure is the narrow-band visible comb filter that is used on a 3D display system. Asghar et al. [55] modelled multilayer thin-film interference-based broad-band-pass filters. The structural modelling was performed by layer-matching the quarter-wave-thick layers in low, medium, and high refractive indices over the visible spectrum. The proposed multilayer based broad-band-pass filter was utilized to transmit visible spectra in a smooth manner, while suppressing the unwanted peak of the spectrum.

4.1.2. Photonic Structure-Based Colouration. Wang and Zhang [58] reviewed the tuneable structural colour of calorimetric sensors using photonic crystals (PCs). One-dimensional (1D) and three-dimensional (3D) photonic crystals are mostly found in plants and always used for such artificial sensing systems. 1D photonics crystals are more popular than 3D crystals as a result of the fact that they incorporate an inherently simple photonic structure. The 1D and 3D photonic crystal-based artificial sensing systems reviewed by Wang and Zhang were vapour and

solvent sensors, temperature sensors, ion and pH sensors, and pressure sensors.

Liu et al. [56] developed the sol-gel inverse opal structure-based temperature tuneable photonic band gap crystals for a temperature sensor. A change in temperature changes the liquid-vapour phase that fills the cavities of the inverse opal film and this precipitates the change of the refractive index. They found that changing the refractive index of the inverse opal film shifted the photonic band gap, which consequently resulted in a colour shift.

The inverse opal structure film-based labelling of free specific detection of immunoglobulin G antibody (IgG) by using nanoporous hydrogel photonic crystals was proposed by Choi et al. [59]. Using the proposed sensor, the IgG concentration level could be determined via the naked eye by looking for changes in colour. In this study, 10 mg/mL IgG concentration was indicated by a colour change from green to dark orange. The proposed sensor made a simple and cost-effective process fabrication possible.

The heterostructures of 1D photonic crystal-based three-color filters were developed by Li et al. [57]. This photonic crystal incorporates defect layers that contain Si/MgF₂ multilayer films. The thickness of the defect layer was altered to restrict certain wavelengths of light from entering the photonic crystal band gap. The restricted light in that wavelength was reflected and correspondingly appeared in colour. Li et al. [57] successfully obtained a blue-green-red colour filter, with high transmission rates.

A structural colour-based display system could also be developed via photonic ink (P-Ink) technology, which is comprised of photonic crystals. This system was developed by Wang et al. [63], who utilized the changes of applied current and voltage in order to reflect a certain band of colour. They found that every single P-Ink material was capable of reflecting all of the spectral colours in the visible range. The colour switching that occurred in the system was caused by the expansion and contraction of the cross-linked electroactive polymer network.

4.1.3. Diffraction Grating-Based Colouration. A colour filter based on the reflection resonance of metal-dielectric-metal trilayered structures was proposed by Chen and Liu [60]. The design of the filter mainly focused upon adjusting the thickness and refractive indices of the middle layer. Red, green, and blue colours were expected to emanate from this filter.

4.1.4. Effect Pigment-Based Colouration. The iridescent effect in flower petals is generated by a diffraction grating mechanism in combination with pigments. This phenomenon entails that the diffraction grating might enhance the pigment-based colouration in the flower petals. In colouration technology, the effect that the pigment technology has is similar to the iridescent effect found in flower petals.

The progress of effect pigment technology was reviewed in detail by Maile et al. [68]. The effect pigments associated with special effect colours like angle-dependent ones is in high demand in today's industries and consumer product

markets. Effect pigments are structured platelets. There are three types: (a) substrate-free effect pigments structure, (b) effect pigments with layer and substrate structure, and (c) multilayer effect pigments without substrate structure (note that what is denoted as pigment here actually refers to structures, but, as described above, because the name "effect pigment" is well introduced and widely accepted, we use it here too).

4.2. Development, Modelling, and Fabrication. As described in Section 4.1, the fabrication process represents an important step towards obtaining a multilayer thin film, a photonic crystal, or a diffraction grating with the desired optical properties. The development of optical structures that are used in various applications within this review consisted of many approaches, such as mathematical modelling, simulations, and fabrication. Potential fabrication methods for biomimetic animal-inspired optical materials were reviewed by Yu et al. [69]. The methods proposed could be divided into two approaches: a biotemplate-based approach and a nonbiotemplate approach. The first approach could be used to produce a structure or an inverse template, while the artificial analogue of the structure could be obtained via the second approach. The fabrication techniques that are involved are atomic layer deposition, nanoimprinting, and the electron beam lithography process, all of which are well-established techniques that are regularly used to fabricate animal-inspired biomimetic optical materials. The fabrication of some photonic crystal structures based on calorimetric sensors was systematically reviewed by Wang and Zhang [58].

Through mathematical modelling, the structural colour of a plant bioinspired multilayer thin-film model is always determined using the Fresnel formula, along with reflection and transmittance phenomena theory [48]. The fabrication techniques used in the development of the plant bioinspired multilayer thin film are sol-gel coating [48, 49, 56], spin coating [53], plasma enhanced chemical vapor deposition (PECVD), and electrochemical etching, Selj et al. [51].

As stipulated in this section, many applications are made viable through the use of engineering-based multilayer thin film and photonic structural products. Engineering-based application products always apply the reflected or refracted colours, which are the result of the interference phenomena. Due to this requirement, the reflection or refraction features are regarded as crucial in this context. On the other hand, different applications require different optical structures. The desired structures, with certain optical properties, could be obtained via the manipulation of the stacked layer's thickness, the refractive index of each layer, structural uniformity, and the surface condition of the outermost layer of the multilayer. The performance of such optical structure's designs is very much influenced by fabrication techniques. Due to the high cost of the fabrication process, computer simulation and mathematical modelling are popular approaches for initial investigations and designs for complex optical structures [46, 48, 55].

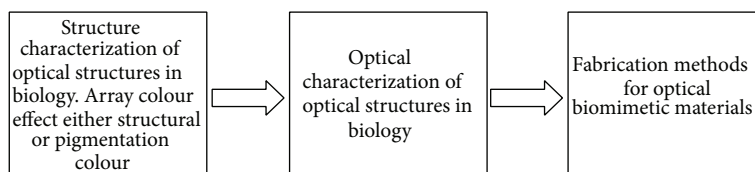


FIGURE 7: Three steps in multidisciplinary concept from nature (organism) to optical biomimetic materials (structural colour) [57].

5. Conclusion and Outlook

5.1. General Ideas in This Paper. The process of studying this subject was intense and the experience resulted in valuable knowledge. Carrying out research involving multidisciplinary fields that includes biology, science, and engineering is difficult, and understanding the key concepts can be challenging; however, its impact is rather significant. The language used in research papers can be difficult to grasp when the work is multidisciplinary in nature. In this context, effective communication plays an important role, so that cost, time, and energy can be optimized. Biology is the study of living organisms and their interactions with the environment and other organisms; however, current engineering that learns from living nature just mimics, imitates, or is bioinspired by a part of that study, mainly mechanisms and materials.

5.2. Biomimetics: Transfer from Nature to Technological Applications

5.2.1. Biology as a Model. Biology represents a large and valuable basis model for technologies and applications. The structural properties of the mechanisms found in leaves, petals, and some fruits prove to be productive in research and biomimicry or bioinspired design. In structural colour, the presence of the thickness of filters/layers and refractive indices is important. The attractive and sometimes really striking structural colours found in animals, plants, and microorganisms have attracted interdisciplinary interest and many scientists and researchers have strived to understand their biological basics and to transfer these into the fields of engineering [70]. Key parameters of structural colours in biological systems that need to be investigated are angle dependence, wavelength dependence, polarization dependence, and system reflectance properties [53].

Natural structural colour phenomena have inspired technologically exploitable features for light and colour manipulation. The nanoscale photonic architecture that is found in iridescent plants formed a key element that is used to produce iridescent colouration in the engineering world. Sometimes the structures used in bioinspired artificial systems neglect many aspects of the complexity found in the related structures of the biological material. For example, the tuneable elastic optical multilayer fibres that were inspired by the *Margaritaria* fruits have much simpler structures than the related structure in nature [53], which, for example, comprises elliptical structures in the periodic layers of the fruit cells.

One always needs to bear in mind the fact that one basic property of the materials and structures of living entities is their multifunctionality, so if it is the intention just to transfer the deep principles of the colouration, then not all structural aspects need to be incorporated in the biomimetic system.

5.2.2. Concept of Biomimetics. Throughout history, nature has inspired various human achievements and has led to the development of effective materials, structures, tools, mechanisms, processes, algorithms, and functions that are advantageous to humankind. The use of nature's designs to solve engineering problems is known as biomimetics. Biomimetics is an interdisciplinary knowledge field that combines biology, technology, and the arts [71] and it has proven promising in the development of emerging MEMS (micro-electromechanical systems). Biomimetics aims to identify the deep underlying principles of materials, structures (including nanostructures), and processes found in living nature and to subsequently transfer knowledge about these phenomena to engineering and the arts. It seeks to apply certain principles from biological systems to technological strategies in order to develop innovative applications. The range of potential uses for biomimetics is enormous and in today's society these include architecture and design and surface and materials technologies as well as sensors, medical engineering, and management [72–74].

Structural colour has inspired researchers to study and understand the step from organisms to biomimetics in related fields such as optical materials. In this proportion, Yu and coworkers summarize biomimetic optical materials by providing a step in optical biomimetic materials (Figure 7) [69]. Nature provided diverse microstructures based on thin-film interference, multilayer interference, diffraction grating, photonic crystals, and light scattering. Optical biomimetics as a multidisciplinary field requires collaboration among biologists, physicists, chemists, and materials scientists.

Glossary

LBL:	Layer-by-layer
IgG:	Immunoglobulin G
Iridescence:	The property of certain surfaces that appear to change colour as the angle of view or the angle of illumination changes

Iridosome:	Secreted by epidermis cell of fruit, partly cellulosic caused situated inside cell wall
Iridoplast:	Modified colourful chloroplast structures of leaf
LB:	Langmuir-Blodgett
MFRT:	Multilayer film raytracers
PBG:	Photonic band gap
PCs:	Photonic crystals
PDMS:	Polydimethylsiloxane
PECVD:	Plasma enhanced chemical vapour deposition
Petal:	Part of a flower
PHeLG:	Poly (γ -hexyl-L-glutamate)
P-Ink:	Photonic ink
lp160ptPSPI:	Polystyrene-polyisoprena triblock polymer
Sepal:	The outmost part in flowering plant
Ti-AIN:	Titanium-aluminium nitride
Understory forest:	Plant life growing beneath the forest canopy without penetrating it to any extent.

Conflict of Interests

The authors declare that there is no conflict of interests regarding the publication of this paper.

Acknowledgment

This work was supported by the Ministry of Higher Education, Government of Malaysia, Project no. FRGS/1/2013/TK02/UKM/01/1.

References

- [1] S. Kinoshita, *Structural Colors in the Realm of Nature*, World Scientific Publishing, River Edge, NJ, USA, 2008.
- [2] D. W. Lee and J. B. Lowry, "Physical basis and ecological significance of iridescence in blue plants," *Nature*, vol. 254, no. 5495, pp. 50–51, 1975.
- [3] R. Willstätter and A. Stoll, *Untersuchungen über die Assimilation der Kohlensäure*, Springer, Berlin, Germany, 1918.
- [4] J. A. Tanno and T. R. Webster, "Variegation in *Selaginella martensii* f. *albovariegata*. I. Expression and inheritance," *Canadian Journal of Botany*, vol. 60, pp. 2375–2383, 1982.
- [5] D. W. Lee, *Nature's Palette: The Science of Plant Color*, The University of Chicago Press, Chicago, Ill, USA, 2007.
- [6] J. D. Mauseth, *Botany: An Introduction to Plant Biology*, Jones and Bartlett, 4th edition, 2009.
- [7] D. W. Lee, "On iridescent plants," *Garden's Bulletin*, vol. 30, pp. 21–29, 1977.
- [8] R. M. Graham, D. W. Lee, and K. Norstog, "Physical and ultrastructural basis of blue leaf iridescence in two neotropical ferns," *The American Journal of Botany*, vol. 80, no. 2, pp. 198–203, 1993.
- [9] K. S. Gould and D. W. Lee, "Physical and ultrastructural basis of blue leaf iridescence in four Malaysian understory plants," *The American Journal of Botany*, vol. 83, no. 1, pp. 45–50, 1996.
- [10] Y. Zhang, T. Hayashi, M. Hosokawa, S. Yazawa, and Y. Li, "Metallic lustre and the optical mechanism generated from the leaf surface of *Begonia rex* Putz," *Scientia Horticulturae*, vol. 121, no. 2, pp. 213–217, 2009.
- [11] S. Vignolini, P. J. Rudall, A. V. Rowland et al., "Pointillist structural color in *Pollia* fruit," *Proceedings of the National Academy Sciences*, vol. 109, no. 39, pp. 15712–15715, 2012.
- [12] D. W. Lee, G. T. Taylor, and A. K. Irvine, "Structural fruit coloration in *Delarbrea michieana* (Araliaceae)," *International Journal of Plant Sciences*, vol. 161, no. 2, pp. 297–300, 2000.
- [13] K. Yoshida, D. Ito, Y. Shinkai, and T. Kondo, "Change of color and components in sepals of chameleon hydrangea during maturation and senescence," *Phytochemistry*, vol. 69, no. 18, pp. 3159–3165, 2008.
- [14] G. A. Marx, "Argenteum (Arg) mutant of *Pisum*: genetic control and breeding behavior," *Journal of Heredity*, vol. 73, no. 6, pp. 413–420, 1982.
- [15] P. E. Grimby and B. J. Thomas, "Silvering, a disorder of the tomato," *Journal of Horticultural Science*, vol. 52, pp. 49–57, 1977.
- [16] Y. Burger, H. S. Paris, H. Nerson, Z. Karchi, and M. Edelstein, "Overcoming the silvering disorder of *Cucurbita*," in *Cucurbit Genetics Cooperative Report*, 1983.
- [17] H. S. Paris, H. Nerson, and Y. Burger, "Leaf silvering of *Cucurbita*," *Canadian Journal of Plant Science*, vol. 67, pp. 593–598, 1987.
- [18] R. Kiew, *Begonias of Peninsular Malaysia*, Natural History Publications (Borneo) Sdn. Bhd, Sabah, Malaysia, 2005.
- [19] B. J. Glover and H. M. Whitney, "Structural colour and iridescence in plants: the poorly studied relations of pigment colour," *Annals of botany*, vol. 105, no. 4, pp. 505–511, 2010.
- [20] P. Vukusic and D. G. Stavenga, "Physical methods for investigating structural colours in biological systems," *Journal of the Royal Society Interface*, vol. 6, no. 2, pp. S133–S148, 2009.
- [21] E. J. H. Corner, *Wayside Trees of Malaya*, Malayan Nature Society, Kuala Lumpur, Malaysia, 3rd edition, 1988.
- [22] D. W. Lee, "Ultrastructural basis and function of iridescent blue colour of fruits in *Elaeocarpus*," *Nature*, vol. 349, no. 6306, pp. 260–262, 1991.
- [23] D. W. Lee, "Iridescent blue plants," *The American Scientist*, vol. 85, no. 1, pp. 56–63, 1997.
- [24] S. E. Sultan, "Phenotypic plasticity for plant development, function and life history," *Trends in Plant Science*, vol. 5, no. 12, pp. 537–542, 2000.
- [25] S. Zobl, T. R. Martin, B. Y. Majlis, T. Schwerte, M. Schreiner, and I. C. Gebeshuber, "Structural colours in the focus of nanoengineering and the arts: survey on state-of-the art developments," in *Proceedings of the 3rd European Conference on Tribology*, Vienna, Austria, 2011.
- [26] S. Lev-Yadun, M. Inbar, I. Izhaki, G. Ne'eman, and A. Dafni, "Colour patterns in vegetative parts of plants deserve more research attention," *Trends in Plant Science*, vol. 7, no. 2, pp. 59–60, 2002.
- [27] L. O. Matolweni, K. Balkwill, and T. McLellan, "Genetic diversity and gene flow in the morphologically variable, rare endemics *Begonia dregei* and *Begonia homonyma* (Begoniaceae)," *The American Journal of Botany*, vol. 87, no. 3, pp. 431–439, 2000.
- [28] K. R. Thomas, M. Kolle, H. M. Whitney, B. J. Glover, and U. Steiner, "Function of blue iridescence in tropical understory plants," *Journal of the Royal Society Interface*, vol. 7, no. 53, pp. 1699–1707, 2010.

- [29] I. C. Gebeshuber and D. W. Lee, "Nanostructures for coloration (organisms other than animals)," in *Springer Encyclopedia of Nanotechnology*, B. Bhushan and M. Nosonovsky, Eds., pp. 1790–1803, Springer, 2012.
- [30] F. T. Mott, "Organic color," *Science*, vol. 21, no. 541, pp. 323–325, 1893.
- [31] C.-R. Sheue, S.-H. Pao, L.-F. Chien, P. Chesson, and C.-I. Peng, "Natural foliar variegation without costs? The case of Begonia," *Annals of Botany*, vol. 109, no. 6, pp. 1065–1074, 2012.
- [32] J. C. Maxwell, *A Treatise on Electricity and Magnetism*, vol. 2, Clarendon Press, Oxford, UK, 1873.
- [33] H. Hertz, "On the relations between Maxwell's fundamental equations of the opposing electromagnetics," *Wiedemann's Annalen*, vol. 23, pp. 84–103, 1884.
- [34] L. Rayleigh, "On the reflection of light from regularly stratified medium," *Proceedings of Royal Society London A*, vol. 93, no. 655, pp. 565–577, 1917.
- [35] B. Walter, *Die Oberflächen- oder Schillerfarben*, Braunschweig, 1895.
- [36] A. A. Michelson, "On metallic colouring in birds and insects," *Philosophical Magazine Series 6*, vol. 21, no. 124, pp. 554–567, 1911.
- [37] D. W. Lee, "Plant tissue optics: micro- and nanostructures," in *Biomimetics and Bioinspiration*, vol. 7401 of *Proceedings of SPIE*, August 2009.
- [38] J. Xu and Z. Guo, "Biomimetic photonic materials with tunable structural colors," *Journal of Colloid and Interface Science*, vol. 406, pp. 1–17, 2013.
- [39] I. Woo, S. Yu, J. S. Lee et al., "Plasmonic structural-color thin film with a wide reception angle and strong retro-reflectivity," *IEEE Photonics Journal*, vol. 4, no. 6, pp. 2182–2188, 2012.
- [40] H. D. Young and R. A. Freedman, *Sears and Zemansky's University Physics: With Modern Physics*, Pearson Addison Wesley, San Francisco, Calif, USA, 11th edition, 2004.
- [41] V. G. Bordo and H. G. Rubahn, *Optics and Spectroscopy at Surfaces and Interfaces*, Wiley-VCH Verlag GmbH & Co.KGAA, Weinheim, Germany, 2005.
- [42] S. Y. Lee and L. Dal Negro, "Angularly independent structural color of nanostructured metal surfaces," in *Proceedings of the 16th International Conference on Optical MEMS and Nanophotonics (OMN '11)*, pp. 25–26, August 2011.
- [43] S. Berthier, *Iridescences : The Physical Colors of Insects*, Springer, New York, NY, USA, 2007.
- [44] J. H. McClendon, "The micro-optics of leaves. I. Patterns of reflection from the epidermis," *The American Journal of Botany*, vol. 71, no. 10, pp. 1391–1397, 1984.
- [45] H. M. Whitney, M. Kolle, P. Andrew, L. Chittka, U. Steiner, and B. J. Glover, "Floral iridescence, produced by diffractive optics, acts as a cue for animal pollinators," *Science*, vol. 323, no. 5910, pp. 130–133, 2009.
- [46] H. Hirayama, K. Kaneda, H. Yamashita, and Y. Monden, "An accurate illumination model for objects coated with multilayer films," *Computers and Graphics*, vol. 25, no. 3, pp. 391–400, 2001.
- [47] Y. P. Zhang, V. P. Chodavarapu, A. G. Kirk, and M. P. Andrews, "Structured color humidity indicator from reversible pitch tuning in self-assembled nanocrystalline cellulose films," *Sensors and Actuators B*, vol. 176, pp. 692–697, 2013.
- [48] T. Yasuda, K. Nishikawa, and S. Furukawa, "Structural colors from TiO₂/SiO₂ multilayer flakes prepared by sol-gel process," *Dyes and Pigments*, vol. 92, no. 3, pp. 1122–1125, 2012.
- [49] A. Schüler, J. Boudaden, P. Oelhafen, E. de Chambrier, C. Roecker, and J.-L. Scartezzini, "Thin film multilayer design types for colored glazed thermal solar collectors," *Solar Energy Materials & Solar Cells*, vol. 89, no. 2-3, pp. 219–231, 2005.
- [50] Y. W. Wu, W. Zheng, L. Lin, Y. Qu, and F. Lai, "Colored solar selective absorbing coatings with metal Ti and dielectric AlN multilayer structure," *Solar Energy Materials & Solar Cells*, vol. 115, pp. 145–150, 2013.
- [51] J. H. Selj, T. T. Mongstad, R. Sondenå, and E. S. Marstein, "Reduction of optical losses in colored solar cells with multilayer antireflection coatings," *Solar Energy Materials & Solar Cells*, vol. 95, no. 9, pp. 2576–2582, 2011.
- [52] T. Kinoshita, S. Hayashi, and Y. Yokogawa, "Preparation of a structural color forming system by polypeptide-based LB films," *Journal of Photochemistry and Photobiology A: Chemistry*, vol. 145, no. 1-2, pp. 101–106, 2001.
- [53] M. Kolle, A. Lethbridge, M. Kreysing, J. J. Baumberg, J. Aizenberg, and P. Vukusic, "Bio-inspired band-gap tunable elastic optical multilayer fibers," *Advanced Materials*, vol. 25, pp. 2239–2245, 2013.
- [54] T. J. Nevitt and M. F. Weber, "Recent advances in multilayer polymeric interference reflector products," *Thin Solid Films*, vol. 532, pp. 106–112, 2013.
- [55] M. H. Asghar, M. B. Khan, and S. Naseem, "Modeling thin film multilayer broad-band-pass filters in visible spectrum," *Czechoslovak Journal of Physics*, vol. 53, no. 12, pp. 1209–1217, 2003.
- [56] Z. Liu, J. Gao, B. Li, and J. Zhou, "Temperature tunable photonic band gap crystals based on liquid-infiltrated inverse opal structure," *Optical Materials*, vol. 35, pp. 1134–1137, 2013.
- [57] H. Li, H. Guan, P. Han, Y. Li, and C. Zhang, "Design for a broad non-transmission band gap of three-color filters using photonic heterostructures," *Optics Communications*, vol. 287, pp. 162–166, 2013.
- [58] H. Wang and K. Q. Zhang, "Photonic crystal structures with tunable structure color as colorimetric sensors," *Sensors*, vol. 13, no. 4, pp. 4192–4213, 2013.
- [59] E. Choi, Y. Choi, Y. H. P. Nejad, K. Shin, and J. Park, "Label-free specific detection of immunoglobulin G antibody using nanoporous hydrogel photonic crystals," *Sensors and Actuators B: Chemical*, vol. 180, pp. 107–113, 2013.
- [60] Y. Chen and W. Liu, "Reflection and color characteristics of tri-layer metal-dielectric structures for generation of distinctive color shifts," *Optik*, vol. 24, pp. 13–16, 2013.
- [61] D. K. Cullen, Y. Xu, D. V. Reneer et al., "Color changing photonic crystals detect blast exposure," *NeuroImage*, vol. 54, no. 1, pp. S37–S44, 2011.
- [62] G. Decher and J. B. Schlenoff, *Multilayer Thin Films: Sequential Assembly of Nanocomposite Materials*, Wiley-VCH Verlag GmbH & Co. KGAA, Weinheim, Germany, 2003.
- [63] H. Wang, F. Kerins, U. Kamp, L. Bonifacio, A. C. Arsenault, and G. A. Ozin, "Photonic-crystal display materials," *Information Display*, vol. 27, no. 7-8, pp. 26–29, 2011.
- [64] I. A. Sukhoivanov and I. V. Guryev, "Photonic crystal optical fibers," *Photonic Crystals*, vol. 152, pp. 127–161, 2010.
- [65] A. Schüler, D. Dutta, E. de Chambrier et al., "Sol-gel deposition and optical characterization of multilayered SiO₂/Ti_{1-x}Si_xO₂ coatings on solar collector glasses," *Solar Energy Materials & Solar Cells*, vol. 90, no. 17, pp. 2894–2907, 2006.
- [66] CIE, "C.B. CIE—International Commission on Illumination CIE Central Bureau," 2014, <http://www.cie.co.at/>.

- [67] J. A. Rego, J. A. A. Harvey, A. L. MacKinnon, and E. Gatdula, "Asymmetric synthesis of a highly soluble "trimeric" analogue of the chiral nematic liquid crystal twist agent Merck S1011," *Liquid Crystals*, vol. 37, no. 1, pp. 37–43, 2010.
- [68] F. J. Maile, G. Pfaff, and P. Reynders, "Effect pigments—past, present and future," *Progress in Organic Coatings*, vol. 54, no. 3, pp. 150–163, 2005.
- [69] K. Yu, T. Fan, S. Lou, and D. Zhang, "Biomimetic optical materials: integration of nature's design for manipulation of light," *Progress in Materials Science*, vol. 58, pp. 825–873, 2013.
- [70] P. Vukusic, "Structural colour: elusive iridescence strategies brought to light," *Current Biology*, vol. 21, no. 5, pp. R187–R189, 2011.
- [71] Y. Bar-Cohen, *Biomimetics: Biologically Inspired Technologies*, CRC Press, Boca Raton, Fla, USA, 2005.
- [72] I. C. Gebeshuber, P. Gruber, and M. Drack, "A gaze into the crystal ball: biomimetics in the year 2059," *Proceedings of the Institution of Mechanical Engineers C: Journal of Mechanical Engineering Science*, vol. 223, no. 12, pp. 2899–2918, 2009.
- [73] I. C. Gebeshuber, *Biomimetics and Nanotechnology*, UKM Press, Penerbit UKM Bangi, Bangi, Malaysia, 2011.
- [74] I. C. Gebeshuber and M. O. Macqueen, "What is a physicist doing in the jungle? Biomimetics of the rainforest," in *Advances in Bionic Engineering*, vol. 461 of *Applied Mechanics and Materials*, pp. 152–162, 2014.

Research Article

A Dual-Functional [SBA-15/Fe₃O₄/P(N-iPAAm)] Hybrid System as a Potential Nanoplatforform for Biomedical Application

Andreza de Sousa,^{1,2} Karynne Cristina de Souza,¹ Paula Maria da Silva Leite,^{1,2}
Ricardo Geraldo de Sousa,² and Edésia Martins Barros de Sousa¹

¹ Serviço de Nanotecnologia, Centro de Desenvolvimento da Tecnologia Nuclear CDTN/CNEN, Avenida Presidente Antônio Carlos, 6.627, Campus da UFMG, Pampulha, 31270-90 Belo Horizonte, MG, Brazil

² Departamento de Engenharia Química, E.E.UFMG, Avenida Presidente Antônio Carlos, 6.627, Campus da UFMG, Pampulha, 31270-90 Belo Horizonte, MG, Brazil

Correspondence should be addressed to Edésia Martins Barros de Sousa; sousaem@cdtn.br

Received 15 November 2013; Revised 7 February 2014; Accepted 23 February 2014; Published 3 April 2014

Academic Editor: Anchal Srivastava

Copyright © 2014 Andreza de Sousa et al. This is an open access article distributed under the Creative Commons Attribution License, which permits unrestricted use, distribution, and reproduction in any medium, provided the original work is properly cited.

The synthesis strategy of a multifunctional system of [SBA-15/Fe₃O₄/P(N-iPAAm)] hybrids of interest for bioapplications was explored. Magnetite nanoparticles coated by mesoporous silica were prepared by an alternative chemical route using neutral surfactant and without the application of any functionalization method. Monomer adsorption followed by *in situ* polymerization initiated by a radical was the adopted procedure to incorporate the hydrogel into the pore channels of silica nanocomposite. Characterization of the materials was carried out by using X-ray diffraction (XRD), Fourier-transform infrared spectroscopy (FTIR), N₂ adsorption, transmission electron microscopy (TEM), and Temperature programmed reduction studies (TPR). Their application as drug delivery system using atenolol as a model drug to assess the influence of the application of low frequency alternating magnetic fields on drug release was evaluated. The structural characteristics of the magnetic hybrid nanocomposite, including the effect of the swelling behavior on heating by the application of an alternating magnetic field, are presented and discussed.

1. Introduction

Ordered mesoporous materials have a number of promising applications in many fields of technology as advanced electronics, catalysis, and nanostructured materials, among others [1–3]. The intrinsic uniform porous structure of this class of compounds with their large specific surface area and pore volume, associated with surface silanol groups, give these materials a significant potential for applications as matrices of many chemical species, such as organic molecules, metals, and polymeric materials. The performance of these materials in many fields of applications depends directly on the silica network porosity. Because of their large pores, high hydrothermal stability, and easy preparation, SBA-15 materials have been considered very promising for hosting and further delivery under appropriate conditions of a variety of molecules of pharmaceutical interest [4].

The delivery of these molecules was once considered impossible, because of the difficulty associated with the diffusion of large molecules through the materials of conventional drug delivery systems. These organic substances are normally very large in size and mesoporous silica is a potential candidate to encapsulate such molecules by utilizing ordered mesopores [5, 6]. Nevertheless, there is one major problem for the mesoporous systems as far as drug release is concerned, that is, the limited control of the drug release whose major mechanism is diffusion [7]. The need to create new materials with optimized, predetermined characteristics has spurred an increasing interest in hybrid materials, especially in organic and inorganic nanocomposites.

For a better release control, some systems can be externally activated to release more drugs when necessary using external forces such as temperature or magnetism [8].

In the case of temperature aging as an external force for diffusion, temperature-responsive hydrogels are a well-studied class of drug delivery systems, as they can respond pronouncedly to temperature changes. Among these stimuli-responsive polymers, temperature-responsive hydrogels such as poly(*N*-isopropylacrylamide) [P(*N*-iPAAm)] [9, 10] exhibits, in water, a phase transition at a lower critical solution temperature (LCST) of approximately 33°C [11]. Below the LCST, the hydrogel incorporates water and swells, whereas the release of water in response to an increase in temperature causes shrinkage. Thus, the development of hybrid functional nanosystems based on silica-[P(*N*-iPAAm)] has drawn much attention to the control of molecular transport, including drug release, because self-regulated delivery allows for drug release when it is needed [5]. Such a thermosensitive polymer with reversible phase transition characteristics is attractive as a polymeric material for the temperature responsive drug release systems [12].

In the case of magnetism, the magnetite nanoparticles can be used to target localized heating *in vivo* when an alternating current (AC) magnetic field is applied, like in the hyperthermia treatment for anticancer therapy due their unique magnetic properties [13]. This treatment consists in dispersing the magnetic nanoparticles in the diseased tissue and applying an alternating magnetic field to cause local heating. Temperature around 43–45°C lysis the tumor cells with no damage to normal cells. However, nonsurface-modified magnetic nanoparticles with a large surface-area-to-volume ratio tend to agglomerate and form large clusters, with the consequent loss of interesting characteristics. Therefore, a suitable coating is essential to prevent such limitations, what can be obtained by using mesoporous silica like SBA-15. For SBA-15/Fe₃O₄, it is possible to obtain magnetite nanoparticles embedded into mesoporous silica, preventing the agglomeration [14]; these coatings provide not only the stability to the nanoparticles in solution but also helps in binding the various biological ligands at the nanoparticle surface for various biomedical applications [15].

Considering a multifunctional system composed by silica/magnetite/gel, a magnetic field with an alternating current (AC) can be used to target localized heating *in vivo* through the magnetohyperthermia treatment for anticancer therapy, which in turn causes a phase change in the host polymer to allow diffusion and release of drugs. In this case, the thermosensitive grafts collapse, opening pathways for an imbedded drug into the system to escape [16]. Thus, an important improvement in cancer therapy would allow two modes of treatment with synergistic effects of magnetic hyperthermia and drug release using a single hybrid system consisting of silica/magnetite/poly(*N*-isopropylacrylamide).

Even though there have been significant advances, studies involving the potential use of responsive hybrids in the area of controlled release of drugs in synergism of magnetohyperthermia are still incipient, many properties of these materials are in the process of analysis, and synthesis procedures are being modified in order to gain greater control over these morphological and structural materials.

In view of the aforementioned, the objective of this study was to investigate the synthesis strategy of a dual-functional system of [SBA-15/Fe₃O₄/P(*N*-iPAAm)] hybrids of interest for bioapplications. Magnetite nanoparticles coated by mesoporous silica were prepared by an alternative chemical route using neutral surfactant and without the application of any functionalization method. Monomer adsorption followed by *in situ* polymerization initiated by a radical was the adopted procedure to incorporate the hydrogel into the pore channels of silica nanocomposite. Subsequently, its physicochemical characteristics were investigated by using different techniques and the drug release profile of the system was studied in the presence of magnetic field-induced heating. In addition, the effects of the gel swelling behavior on heating by the application of an alternating magnetic field were also presented and discussed in terms of drug release and heat generation capacity.

2. Experimental

2.1. Material Synthesis. SBA-15 was synthesized in accordance with the published procedure [17] using Pluronic P123-PEO₂₀PPO₇₀PEO₂₀ (poly(ethylene glycol)-block-poly(propylene glycol)-blockpoly(ethylene glycol), $M_{av} = 5800$, Sigma-Aldrich) as a template in acidic conditions. In a typical experiment, 4 g of triblock copolymer was dissolved in water and HCl (37 wt. % solution) under stirring at 40°C. After 1 h, 8.2 g of tetraethyl orthosilicate (TEOS, Sigma-Aldrich) was added to the solution. After aging under continuous stirring at 100°C, the solids were collected by filtration and dried in air at 40°C. The surfactant was removed by calcination, which was carried out by increasing the temperature to 550°C under nitrogen flow for 2 h and then in O₂ atmosphere for another 1 h. SBA-15/Fe₃O₄ was prepared by adding 4 g of iron oxide precursor (Fe₂(SO₄)₃·6H₂O) before the addition of TEOS in the synthesis of silica SBA-15. The step of surfactant removing was carried out by heating the material in a nitrogen atmosphere at a rate of 5°C min⁻¹ to 550°C. At this temperature the material was kept under nitrogen flow for 8 hours. The nitrogen flow remained constant throughout the heating process and followed up to complete cooling of the sample. The hybrid was prepared using the following procedure: 0.5 g of SBA-15/Fe₃O₄ nanocomposite was added to 3.5 mL solution of 0.245 g of monomer (*N*-isopropylacrylamide—*N*-iPAAm) and 0.005 g of crosslinking agent (N,N,N',N'-methylene-bisacrylamide—MBA). The mixture was transferred to an INNOVA 4200 (150 rpm) shaker and the mixture was continuously purged with nitrogen. The solution was then allowed to polymerize for 24 h in a water bath at 9°C. The obtained multifunctional hybrid material was dried at 60°C for 24 h and subsequently washed to remove the excess monomers, crosslinking agent, initiator, and accelerator. In the washing stage, the material was disaggregated, suspended in water, and continuously stirred. The hybrid was then collected by centrifugation at 3600 rpm for 3 min and dried at 60°C for 24 h. It was designated [SBA-15/Fe₃O₄/P(*N*-iPAAm)] and the gel composition studied was 5 × 1 [7]. The monomer: SBA-15 mass ratio used was 1 : 2 (wt/wt).

2.2. Characterization. The samples were characterized by X-ray diffraction (XRD), Fourier-transform infrared spectroscopy (FTIR), N_2 adsorption, transmission electron microscopy (TEM), and Temperature programmed reduction studies (TPR). Low-angle XRD measurements were obtained using synchrotron radiation with $\lambda = 1.488$ nm. Synchrotron radiation measurements were carried out at the D11A-SAXS beamline of the LNLS (Campinas, Brazil) using a Huber-423 3-circle diffractometer. The high-angle XRD patterns were obtained using a Rigaku Geigerflex-3034 diffractometer with a $Cu-K\alpha$ tube. Specific surface area and pore size distribution were determined by N_2 adsorption using the BET and BJH methods, respectively [18], in Autosorb-Quantachrome Nova 1200. The samples were outgassed for 2 h at $120^\circ C$ before analysis. FTIR measurements were conducted in a Perkin-Elmer 1760-X spectrophotometer in the range $4000-400\text{ cm}^{-1}$ at room temperature using KBr pellets. TEM characterization was performed through a Tecnai-G2-20-FEI 2006 electron microscope with an acceleration potential of 200 kV, of the Microscopy Center of UFMG, Belo Horizonte, Brazil. TPR experiments were performed in a CHEMBET 3000 equipment with 20 mg sample under $25\text{ mL min}^{-1} H_2$ (8%)/ N_2 with heating rate of $5^\circ C\text{ min}^{-1}$.

2.3. Calculations. BET specific surface area, S_{BET} , was calculated from adsorption data in the relative pressure interval $p/p_0 = 0.045-0.25$. A cross-sectional area of 0.162 nm^2 was used for the nitrogen molecule in the BET calculations. The total pore volume, V_p , was calculated from the amount of N_2 adsorbed at the highest p/p_0 ($p/p_0 = 0.99$) [19]. The micropore volume, V_μ , of SBA-15 silica was estimated from nitrogen adsorption data using the α_s plot method [20] in the standard reduced adsorption, α_s , interval from 0.75 to 1 (relative pressure range from 0.15 to 0.40). The external surface area, S_{ext} , was evaluated using an α_s interval from 1.6 to 3.0. The primary mesopore volume, V_{meso} , was estimated as the difference between the total pore volume and the micropore volume. The α_s -plot was analysed by standard reduced adsorption for nonporous hydroxylated silica [21]. The mesopore size distributions were calculated from the adsorption branches of the nitrogen isotherms employing the BJH algorithm.

2.4. Model Drug Adsorption and Delivery Assays. All samples were loaded with atenolol as a model drug as follows: 0.5 g of the powder sample was added to 150 mL of an atenolol solution ($10\text{ mg}\cdot\text{mL}^{-1}$) and shaken for 48 h at $25^\circ C$ (200 rpm). A 3 : 1 weight ratio of atenolol/solid sample was used. Powder atenolol loaded samples were recovered by filtration, washed with distilled water, and left to dry for 24 h at $60^\circ C$. The same procedure was used to load the hybrid with atenolol. Small atenolol loaded sample disks with 7 mm diameter and 2 mm thick were obtained under uniaxial pressure. TGA was performed to evaluate the percentage of atenolol adsorbed by each sample.

The *in vitro* study of release of atenolol from the materials was performed as follows. The release profile was obtained by

soaking nanocomposites [SBA-15/ Fe_3O_4] and hybrid [SBA-15/ Fe_3O_4 /P(*N*-iPAAm)] samples in 30 mL of simulated body fluid (SBF) [22]. The temperature was maintained constant ($37^\circ C$) and the solutions were continually stirred. UV spectrometry (UV-Vis Shimadzu, model 2401) was used to monitor the amount of drug delivered as a function of time. The concentration of atenolol in SBF was found from the intensity of the absorption band at 274 nm.

2.5. Hyperthermia. The capacity of heat generation of the obtained nanocomposites and hybrid system was measured in a custom-designed magnetic-induction hyperthermia chamber. Heating was measured of [SBA-15/ Fe_3O_4] and hybrid [SBA-15/ Fe_3O_4 /P(*N*-iPAAm)] samples dispersed in water with sonication. The sample concentration was $20\text{ mg}\cdot\text{mL}^{-1}$ and the solution was sonicated for 30 min before measurement. A three-loop coil with resonant frequency of 222 kHz was used in the experiments. In order to study the correlation between the applied magnetic field and the AC magnetically induced heating temperature, the heat produced was measured at a fixed frequency in magnetic 126 Oe until the temperature was nearly steady. A digital thermometer was placed above the sample inside the coil and the temperature measurements were taken at the center of the sample. The results were the average of triplicate measurements. Tests have also been performed in pure deionized water without any magnetic material and the temperature increase from this blank sample has been subtracted of the results obtained for the solution.

2.6. Statistical Analysis. The results were calculated and presented as the mean for each group \pm the standard error of the mean (mean \pm SD). Statistical evaluation of the data was performed using analysis of variance (ANOVA), followed by Bonferroni's test (Post hoc), where $P \leq 0.05$ was considered to be statistically significant.

3. Results and Discussion

3.1. Material Characterization. Figure 1 shows the X-ray diffractograms of the pure magnetite prepared via oxidation-precipitation route, and SBA-15/ Fe_3O_4 sample treated at $550^\circ C$. The broad diffraction peak at high angles (Figure 1(a)) at 2θ between 20° and 30° is attributed to the peak of the siliceous material. In addition, several XRD peaks indicate the formation of well-crystallized Fe_3O_4 . The sharp main diffraction peak and other weak diffraction peaks at $2\theta = 30.0^\circ$, 35.4° , 56.9° , and 62.4° , respectively, can be assigned to (220), (311), (511), and (440) reflections, which can be indexed to the spinel structure of pure stoichiometric magnetite (Fe_3O_4) (JCPDS file 19-0629).

SBA-15/ Fe_3O_4 sample has been analyzed by temperature programmed reduction employing H_2 as reducing gas and the results are presented in Figure 2. TPR profile shows mainly three sets of reduction process. The consumption

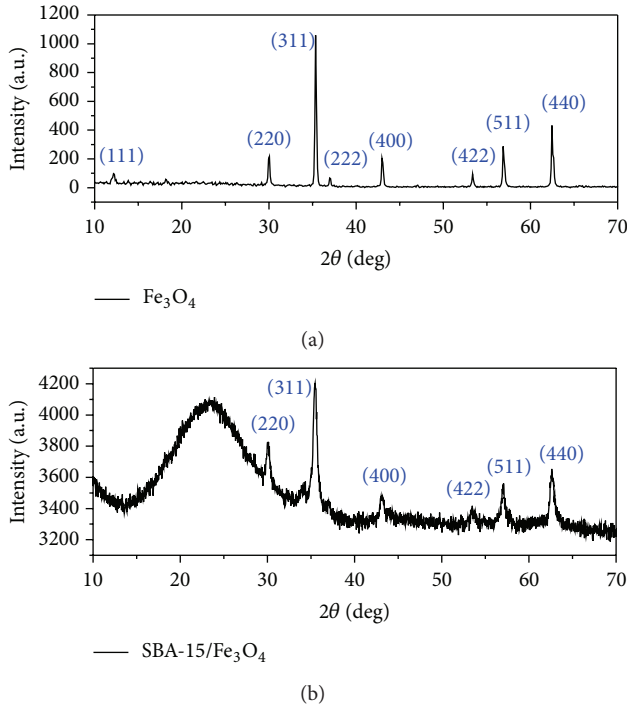


FIGURE 1: X-ray diffraction patterns of the pure magnetite and silica-magnetite nanocomposite.

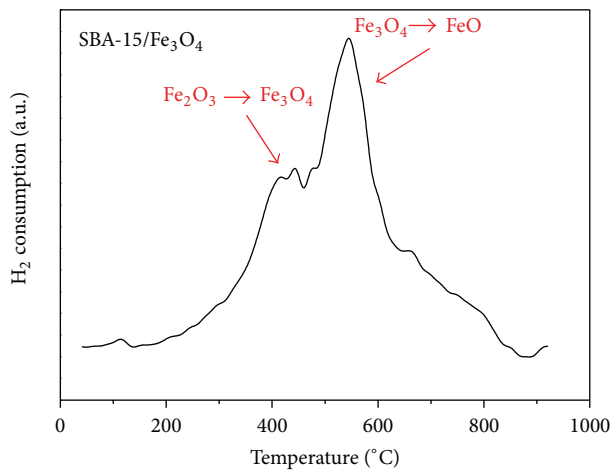
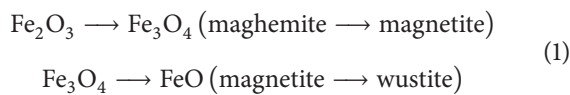


FIGURE 2: TPR profiles of the SBA-15/Fe₃O₄ sample.

profile of H₂ for this sample shows characteristic peaks of reduction transformation of the following phases [23]:



However, the largest nitrogen consumption was observed in the temperature range of 485–650°C, regarding the conversion of magnetite to wustita, confirming the hypothesis that the phase present in higher concentration is magnetite. It is worth mentioning that this sample does not contain ferrisilicate since it has no peaks at temperatures higher

than 700°C that are characteristic of phase transformation of ferrisilicate.

Figures 3(a) and 3(b) show the profile at low angle for SBA-15/Fe₃O₄ and the [SBA-15/Fe₃O₄/P(N-IPAAM)], respectively. The three diffraction peaks of the former, at $2\theta = 0.85^\circ$, 1.51° , and 1.75° , can be indexed as (100), (110), and (200) reflections, respectively, which are typical of hexagonally structured SBA-15 silica with highly ordered mesoporous channels, as reported by Zhao et al. [24]. However, a slight shift of these diffraction peaks to higher 2θ values is identified for [SBA-15/Fe₃O₄/P(N-IPAAM)], Figure 3(b), possibly due to the contraction of the support framework with the formation of the polymer phase in the silica channels. The XRD peaks of SBA-15/Fe₃O₄ can be indexed to a hexagonal lattice structure with $d(100)$ spacing of 9.5 nm and unit cell parameter ($a = 2d/\sqrt{3}$) of 10.94 nm, as reported by Souza et al. [25]. On the other hand, the d spacing of [SBA-15/Fe₃O₄/P(N-IPAAM)] shifted slightly to 9.2 nm, corresponding to a unit cell parameter of 10.62 nm. Despite these small differences in the reflections of the XRD peaks, it is clear that the mesostructure was still ordered after the polymer phase was loaded.

Figure 4 shows the TEM images of the [SBA-15/Fe₃O₄] and [SBA-15/Fe₃O₄/P(N-iPAAM)] hybrid samples. In accordance with the low angle XRD results, the mesoscopic order of the host can be clearly identified in the TEM image of both samples, which shows a well-defined hexagonal arrangement of uniform pores when the incident electron beam was parallel to the main axis of the mesopores (Figure 4(a)), and unidirectional channels, when the electron beam was perpendicular to the channel axis (Figure 4(b)). The Fe₃O₄ nanoparticles appear as dark dot-like objects between the channel walls (Figure 4(c)). These nanoparticles are evenly distributed in the channels with a uniform size, which is close to the pore diameter of SBA-15. Thus, the TEM investigation gives consistent evidence that the ordered structure is preserved in the approach proposed in this work to obtain a nanocomposite and hybrid systems.

Figure 5 shows the FTIR spectra of the SBA-15/Fe₃O₄ and the hybrid [SBA-15/Fe₃O₄/P(N-IPAAM)] samples before and after washing procedure to remove residual monomers. For SBA-15/Fe₃O₄ sample, the infrared spectrum shows absorption bands concerning to fundamental vibrations network of silica. The amount of water in the samples can be monitored by observing the adsorption lines at 3500 and 1640 cm⁻¹, whereas SiOH can be seen as a shoulder at 960 cm⁻¹ for all spectra. The band at about 810 cm⁻¹ is related to the symmetric stretching of the Si–O–Si and the band about 460 cm⁻¹ is related to the vibration mode deformation Si–O–Si. A broad and very intense band in the range 1000 – 1200 cm⁻¹ corresponding to ν Si–O–Si modes of the siliceous matrix of SBA-15 is also present. The spectrum of SBA-15/Fe₃O₄ is dominated by ν O–H modes, presenting a broad and intense band at 3440 cm⁻¹ assigned to hydroxyl groups.

It can be seen in the spectrum of hybrid [SBA-15/Fe₃O₄/P(N-IPAAM)] systems before the washing procedure, bands corresponding to the ν_{C-H} modes of P(N-IPAAM) at 2972 – 2875 cm⁻¹, the bands attributed to isopropyl

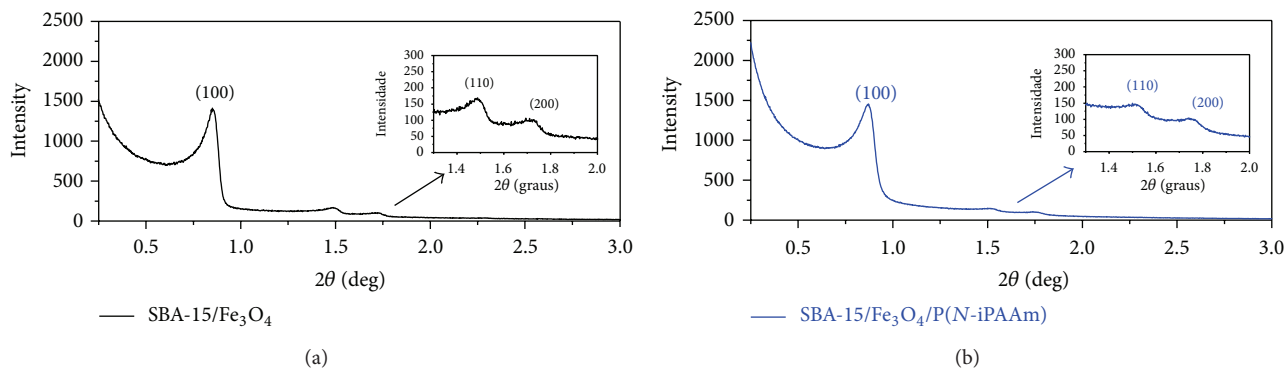


FIGURE 3: X-ray diffraction patterns of small-angle region of (a) SBA-15/Fe₃O₄ and (b) [SBA-15/Fe₃O₄/P(N-iPAAm)].

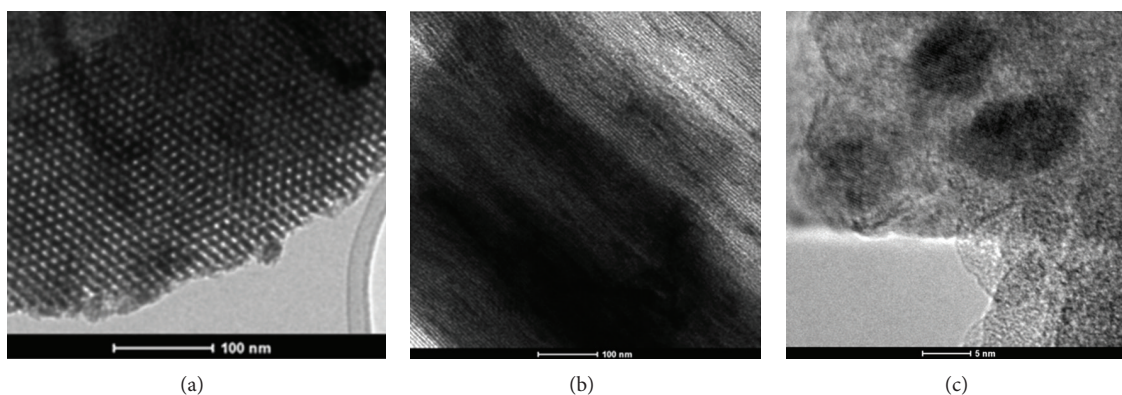


FIGURE 4: Transmission electron micrographs of [SBA-15/Fe₃O₄/P(N-iPAAm)]: (a) viewed along the pore axis, (b) viewed perpendicular to the pore axis, and (c) high resolution images showing the magnetite nanoparticles (dark region) covered by the mesoporous silica of SBA-15/Fe₃O₄.

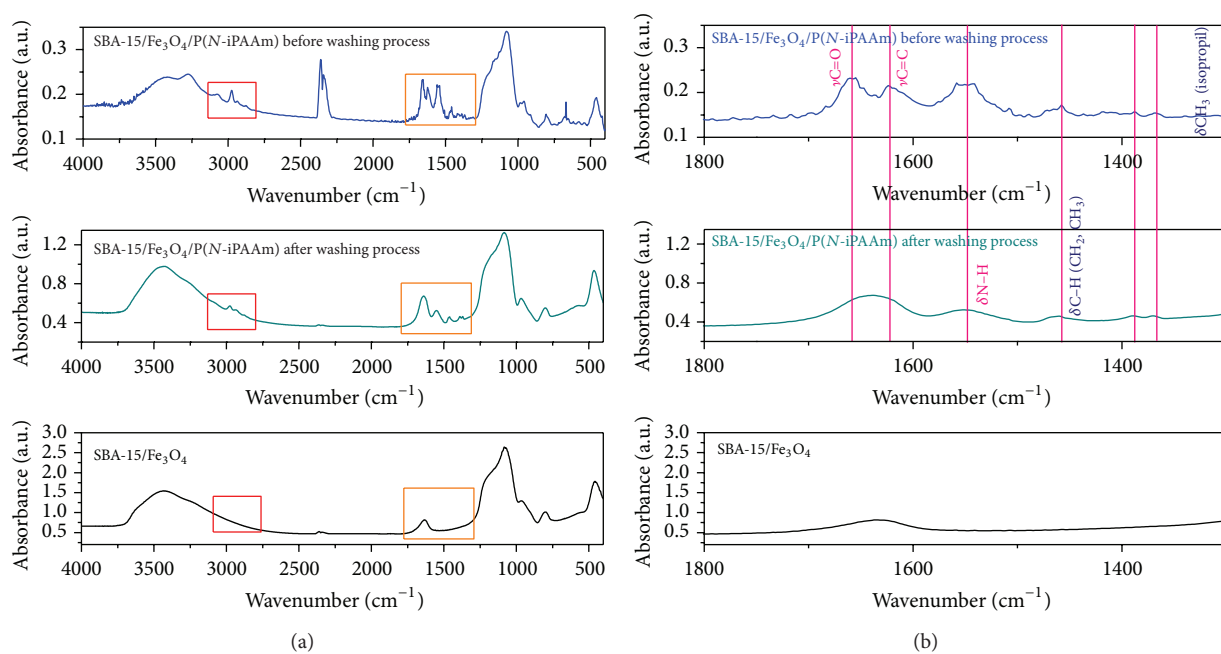


FIGURE 5: (a) FTIR spectra of SBA-15/Fe₃O₄ and [SBA-15/Fe₃O₄/P(N-iPAAm)] before and after the washing procedure to remove the residual monomers. (b) FTIR spectra of SBA-15/Fe₃O₄ and [SBA-15/Fe₃O₄/P(N-iPAAm)] before and after the washing procedure to remove the residual monomers in the expanded scale of 2000–1400 cm⁻¹.

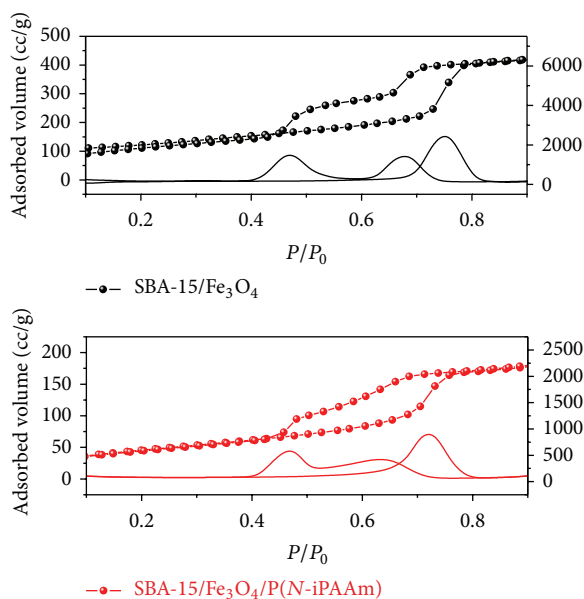


FIGURE 6: N_2 adsorption-desorption isotherms and respective derived curves of SBA-15/Fe₃O₄ and [SBA-15/Fe₃O₄/P(N-iPAAm)] hybrid system.

group are located at 1386 and 1368 cm^{-1} . The band corresponding to the bending vibration of CH₃ is located at 1456 cm^{-1} , while the bands arising from C=O stretching and N-H bending vibrations are observed at 1645 and 1550 cm^{-1} , respectively.

The monomer characteristic bands ($\nu\text{C}=\text{C}$ 1620 cm^{-1} , $\delta\text{CH}_2 = 1409 \text{ cm}^{-1}$, $\delta\text{H}_2\text{C}=\text{C}-$ 1305, and 1325 cm^{-1} , δvinyl group at 990 and 916 cm^{-1}) are not present in the hybrid sample spectra, as can be seen in the scale-expanded FTIR spectrum in the 1800–900 cm^{-1} region (Figure 5(b)). These results prove the presence of P(N-iPAAm) in SBA-15/Fe₃O₄ pores with no other significant synthesis components (monomer, initiator, or accelerator) and demonstrate the successful conversion of the monomers into polymer and the removal of the residual monomers. In addition, the stretching bands of carbonyl groups and N-H bending vibrations from secondary amide around 1648 and 1550 cm^{-1} , respectively, in the spectrum of the sample after washing, are broader compared to the spectrum before washing, likely due to the intramolecular interactions such as hydrogen bond (C=O \cdots HN) which can occur between the polymer chains after the polymerization reaction.

The nitrogen adsorption isotherms for SBA-15/Fe₃O₄ and the [SBA-15/Fe₃O₄/P(N-iPAAm)] hybrid are shown in Figure 6. In both cases, the isotherms were type IV, according to the IUPAC classification, which is associated with the presence of mesopores [19]. These H1 type hysteresis isotherms are related to materials with pores of uniform cross section (e.g., cylindrical or hexagonal). However, these materials exhibit the phenomenon of stepwise desorption, often referred to as blocking phenomenon of pores and is typically associated with the bottle-shaped pores (ink bottle pores) (Figure 6).

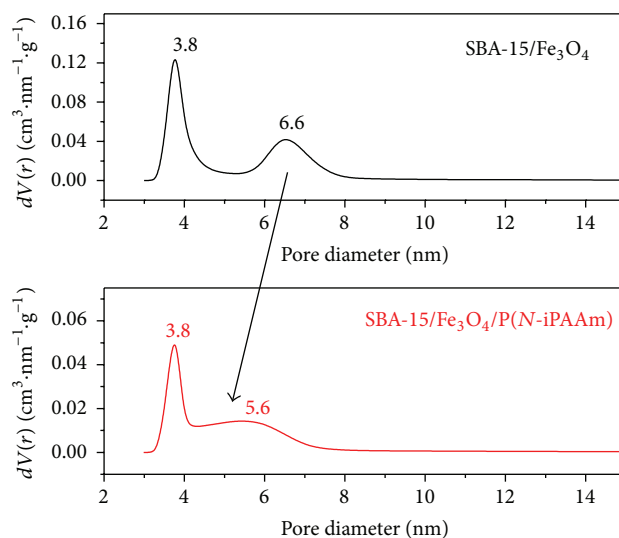


FIGURE 7: Pore size distribution of SBA-15/Fe₃O₄ and [SBA-15/Fe₃O₄/P(N-iPAAm)] hybrid system.

Antochshuk and coauthors [26] attributed this stepwise desorption phenomenon due to the presence of constrictions in the porous structures. According to the authors, in the case of a pore connected to neighboring pores or its surroundings through entrances (constrictions) with diameter smaller than the pore diameter, capillary evaporation from the pore interior is delayed until the capillary evaporation from the constrictions takes place. This phenomenon can be more easily seen in the curves derived from the adsorption and desorption branches (Figure 6). After polymerization, the shape of the hysteresis loop in the N_2 -sorption isotherm displays a broadening suggestive of a reduction in pore size uniformity.

All samples present a bimodal pore size distribution due to the presence of mesopores of different diameters, for example, primary mesopores, secondary, or pores with constrictions. In Figure 7, it is possible to observe two maximum points for SBA-15/Fe₃O₄: one about 6.6 nm, corresponding to the primary mesoporosity, and the second corresponding to a diameter of 3.8 nm equivalent to the secondary mesoporosity. In the hybrid multifunctional, the first maximum point is shifted to lower values of diameter: 5.6 nm and no change were observed in the secondary mesopores, which kept on 3.8 nm.

It can be seen that the pore size distribution is affected by the incorporation of polymeric gel in the SBA-15/Fe₃O₄ sample. After incorporation of the gel, it fills the pores with higher diameters (peaks at 6.6 nm), reducing its statistical contribution and causing a shift of the maximum point for lower values of pore diameter. Notably, the incorporation of the gel does not cause complete filling of the pores of the final material. Even after incorporation of the gel into SBA-15/Fe₃O₄ samples, significant values of surface areas can be observed, which may be convenient to use this material as drug release devices (Table 1).

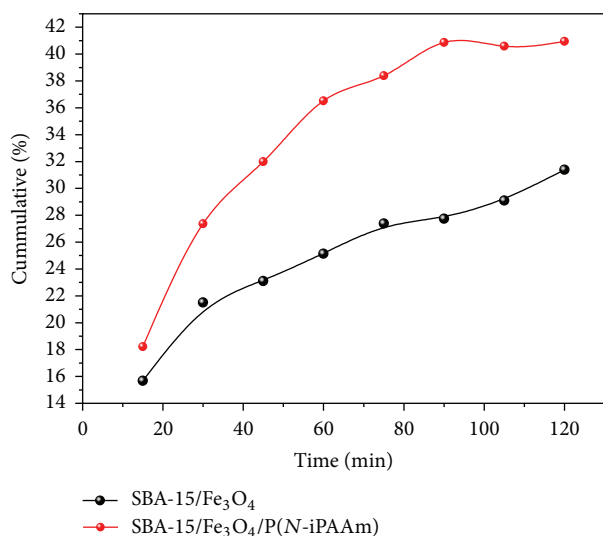


FIGURE 8: Release kinetic profiles of atenolol from SBA-15/Fe₃O₄ and [SBA-15/Fe₃O₄/P(N-iPAAM)] samples.

TABLE 1: N₂ adsorption results.

Sample	S_{BET} (m ² ·g ⁻¹)	V_p (cm ³ /g)	$D_p^{(\text{BJH})}$ (nm)
SBA-15/Fe ₃ O ₄	413	0.76	3.8/6.5
[(SBA-15/Fe ₃ O ₄ /P(N-iPAAM))]	171	0.35	3.8/5.6

Table 1 presents the results of N₂ adsorption, which show the differences in the specific surface area (S_{BET}), pore volume (V_p), and pore diameter (D_p) of the samples. A significant difference was observed for the S_{BET} , V_p , and D_p for SBA-15/Fe₃O₄ and [SBA-15/Fe₃O₄/P(N-iPAAM)] samples, which may indicate the presence of the polymer in the pore structure. Regarding the nitrogen adsorbed volume, it was found that the formation of P(N-iPAAM) into the mesoporous support provoked on a slight decrease in the pore volume and in the pore diameter.

3.2. Atenolol Incorporation and Release Profile Study. *In vitro* atenolol release properties from mesoporous SBA-15/Fe₃O₄ and [SBA-15/Fe₃O₄/P(N-iPAAM)] were investigated as a function of time and are shown in Figure 8. The resulting drug loading into samples was approximately the same, 41 wt% for SBA-15/Fe₃O₄ and 44 wt% for [SBA-15/Fe₃O₄/P(N-iPAAM)], as no statistically significant differences could be observed ($P > 0.05$) in the loading percentage. The release profiles of both samples exhibited no initial burst release effect during the first minutes. However, as can be observed from Figure 8, SBA-15/Fe₃O₄ sample did in fact release a smaller percentage of atenolol than did the hybrid sample. The maximum release level achieved in 2 hours for the SBA-15/Fe₃O₄ sample was 32% and for hybrid system was 43%.

As a result, the presence of the gel increased the amount of drug released, which shows the potential application of this material as a controlled release of drugs. It is relevant

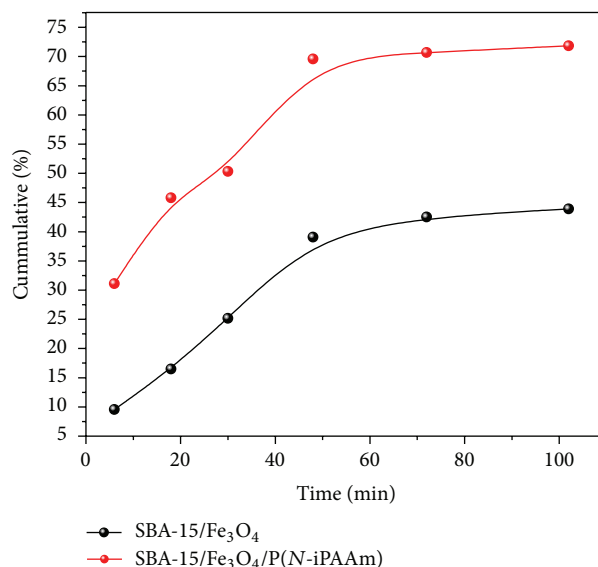


FIGURE 9: Release kinetic profiles of atenolol from SBA-15/Fe₃O₄ and [SBA-15/Fe₃O₄/P(N-iPAAM)] systems in an alternating field.

to mention here that the drug release rate can be enhanced using magnetic field, which would subsequently reduce the period for the drug release. Considering this fact, and in order to evaluate the multifunctionality of the SBA-15/Fe₃O₄ and [SBA-15/Fe₃O₄/P(N-iPAAM)] systems as release device via magnetic hyperthermia treatment, a preliminary test was carried out where the samples were subjected to an external magnetic field over the time. The study was based on the model proposed by Dash and Cudworth [27], in which the application of an alternating magnetic field provokes the vibration of the magnetic particles and the quick release of large quantities of drugs. The measures presented here are designed to assess the influence of the application of low frequency alternating magnetic fields (168 Oe) on drug release [28].

Figure 9 shows the result of this experiment for SBA-15/Fe₃O₄. The presence of magnetic field provokes a heating of the nanocomposite material due to the presence of magnetic particles; thus, the diffusion of atenolol molecules was enhanced by increasing the vibration of the nanoparticles and, consequently, increasing the amount of drug released.

The same behavior can be observed for hybrids systems. Similar to the experiment of release without the influence of the magnetic field, the presence of the gel into the nanocomposite structure increased the amount of drug released, and these results can be explained by the possible interaction of the drugs with the magnetite nanoparticles, maybe due to the incorporation of atenolol into the mesopores, and its interaction with the surface of the magnetic nanoparticles. Moreover, the application of an alternating magnetic field in the hybrid system containing magnetic nanoparticle leads to heat generation, which could drive the swelling transition of the polymer.

Comparing the results obtained during about 100 minutes of both assays (with and without the influence of an external

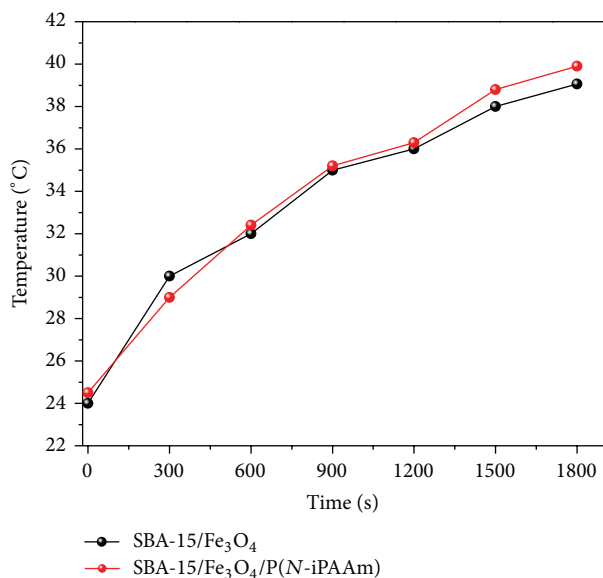


FIGURE 10: Heating induced by magnetic field of SBA-15/Fe₃O₄ and [SBA-15/Fe₃O₄/P(N-iPAAm)] systems.

magnetic field), we can observe that the presence of magnetic field affects the release profile of both samples. Even though there is an increase in the drug release rate for the nanocomposites in the presence of the magnetic field ranging from 32 to 40%, this increase is significantly higher for samples containing the polymer. The analysis of the performance of the hybrid system as a drug delivery device in the presence of alternating magnetic field shows that the release profiles vary from approximately 40 to 70%, indicating that the polymer expanded and consequently presented a lesser barrier to the diffusion of atenolol.

These observations lead us to suggest that the drug release response of hybrid systems depends on temperature and the polymer phase behavior. In this case, a synergistic effect of hyperthermia and controlled drug delivery for a hybrid system composed by the combination of SBA-15, Fe₃O₄ nanoparticles, and P(N-iPAAm) has occurred. To accomplish this assumption, heating generation experiments were performed and discussed below.

3.3. Magnetic Hyperthermia. The saturation magnetization of SBA-15/Fe₃O₄ is 2 emu/g which is much smaller than that of pure bulk magnetite (94 emu/g) [29] because the nanoscale particles form a single magnetic domain that do not communicate/interact due to coating of silica. The magnetic properties obtained by ⁵⁷Fe Mössbauer spectroscopy (not shown) showed that the nanocrystals present superparamagnetic characteristics. The AC magnetic field-induced heating characteristics of the nanocomposite and hybrid system in 20 mg·mL⁻¹ solution were measured to assess its possible application as a hyperthermia agent in an *in vivo*-like environment. Figure 10 shows the time-dependent temperature curves of the pure and hybrid systems for 222 kHz and 126 Oe AC. When the samples were exposed to an AC magnetic

field for 30 min, the temperature ranged from 24 to 39°C and from 24 to 40°C for SBA-15/Fe₃O₄ and [SBA-15/Fe₃O₄/P(N-iPAAm)], respectively, showing no statistically significant differences in the temperature variation.

The measured temperatures of the hybrid system suspension after sonication and under 126 Oe AC magnetic fields after 30 min of assay, presented a ΔT_{\max} of 16°C. For all evaluated samples, ($T + \Delta T_{\max}$) was minor than the recommended hyperthermia treatment temperature, which is reported between 40 and 45°C [30]. At these temperatures, the growth of cancerous cells can be halted and any damage to healthy cells can be avoided by using magnetic nanoparticles with controlled temperatures. It is available treatment when tumors have not metastasized and their locations are known. However, based on such results, it does not mean that the obtained material cannot be used for such application, but the experimental conditions employed to evaluate its heating might be improved.

Thus, a temperature variation of $\Delta T_{\max} = 5\text{--}8^\circ\text{C}$ would be sufficient, based on a body temperature of 37°C. Significant results were obtained in our previous work [25]. Hyperthermia tests have demonstrated a good heating capacity of the powders prepared from SiO₂-Fe₃O₄ nanocomposite, which increased linearly with milling time. In the selected experimental conditions, the measured temperatures of the nanoparticle suspension after sonication and under 168 Oe AC magnetic field increased to 47.5°C after 30 min of assay, presenting a ΔT_{\max} of 24.5°C. The effect of frequency for CoFe₂O₄ nanoparticles dispersed in water on magnetic heating was investigated using a magnetic field of 385 Oe at frequencies of 195, 231, and 266 kHz. The results show that the heating rates diminished with time and reached steady-state temperatures around 30–35°C and ΔT increased linearly with frequency. As a result, heat generation can be controlled in selected magnetic particles by adjusting the magnetic field and frequency [31, 32].

The above results show that the sample prepared in this work is important to be used in a medical application, as drug delivery and magnetic hyperthermia. A critical step in the combined therapy is controlled drug release. Although important, these conclusions need a deeper study of heat generation by adjusting the magnetic field, the frequency, and choosing an appropriated medium with different amounts of materials in order to increase ΔT_{\max} and it is planned for future work. Due to their mesoporous properties we also envisioned that such system might be further investigated as a theranostic device. The *in vivo* experiments will be conducted and reported in the due course.

4. Conclusion

The possibility to prepare hybrid system to be used as nanoplatform for drug delivery and heating agent in hyperthermia was presented and discussed. We developed an easy and direct synthesis route to obtain hybrid functional nanosystems based on responsive polymer synthesized inside the iron nanoparticle/mesoporous silica nanocomposites. The above results show that the composition and morphology

of carrier materials and the external agents are important factors in influencing the drug delivery performance. Drug release was more effective and faster in alternating magnetic field for both systems. However, a direct comparison of these results indicates that the performance of the hybrid system is more affected by the presence of the magnetic field, resulting in a greater release of the drug, as the polymer expanded and consequently presented a lesser barrier to the diffusion of atenolol. Hyperthermia tests have demonstrated that the temperature variation achieved under selected conditions increased linearly with milling time. The maximum temperature obtained is around 40°C inferior to that recommended for hyperthermia treatment. Therefore, the magnetic field amplitude, the frequency, or both of them might be reduced in order to optimize the use of the obtained hybrid system. In spite of this, we have shown that mesoporous silica-coated magnetite nanoparticles containing stimuli-responsive polymers with especial structural and magnetic characteristics and unobstructed pores seem to be promising material for use in biomedical application presenting synergistic effects of hyperthermia and controlled drug delivery.

Conflict of Interests

The authors declare that there is no conflict of interests regarding the publication of this paper.

Acknowledgments

The authors wish to thank FAPEMIG (Fundação de Amparo a Pesquisa do Estado de Minas Gerais), CNPQ (Conselho Nacional de Desenvolvimento Científico e Tecnológico), and CAPES (Comissão Aperfeiçoamento de Pessoal de Nível Superior) for their financial support.

References

- [1] I. W. Hamley, "Nanostructure fabrication using block copolymers," *Nanotechnology*, vol. 14, no. 10, pp. R39–R54, 2003.
- [2] G. J. D. A. A. Soler-Illia, C. Sanchez, B. Lebeau, and J. Patarin, "Chemical strategies to design textured materials: from microporous and mesoporous oxides to nanonetworks and hierarchical structures," *Chemical Reviews*, vol. 102, no. 11, pp. 4093–4138, 2002.
- [3] W. Paul and C. P. Sharma, "Nanoceramic matrices: biomedical applications," *American Journal of Biochemistry and Biotechnology*, vol. 2, p. 41, 2006.
- [4] A. L. Doadrio, E. M. B. Sousa, J. C. Doadrio, J. Pérez Pariente, I. Izquierdo-Barba, and M. Vallet-Regí, "Mesoporous SBA-15 HPLC evaluation for controlled gentamicin drug delivery," *Journal of Controlled Release*, vol. 97, no. 1, pp. 125–132, 2004.
- [5] A. Sousa, K. C. Souza, S. C. Reis et al., "Positron annihilation study of pore size in ordered SBA-15," *Journal of Non-Crystalline Solids*, vol. 354, no. 42–44, pp. 4800–4805, 2008.
- [6] M. Vallet-Regí, "Mesoporous silica nanoparticles: their projection in nanomedicine," *ISRN Materials Science*, vol. 2012, Article ID 608548, 20 pages, 2012.
- [7] A. De Sousa, D. A. Maria, R. G. De Sousa, and E. M. B. De Sousa, "Synthesis and characterization of mesoporous silica/poly(*N*-isopropylacrylamide) functional hybrid useful for drug delivery," *Journal of Materials Science*, vol. 45, no. 6, pp. 1478–1486, 2010.
- [8] G. Vilara, J. Tulla-Puchea, and F. Albericio, "Polymers and drug delivery systems," *Current Drug Delivery*, vol. 9, pp. 1–28, 2012.
- [9] L. M. Geever, M. J. D. Nugent, and C. L. Higginbotham, "The effect of salts and pH buffered solutions on the phase transition temperature and swelling of thermoresponsive," *Journal of Materials Science*, vol. 42, no. 23, pp. 9845–9854, 2007.
- [10] W.-F. Lee and Y.-H. Lin, "Swelling behavior and drug release of NIPAAm/PEGMEA copolymeric hydrogels with different crosslinkers," *Journal of Materials Science*, vol. 41, no. 22, pp. 7333–7340, 2006.
- [11] R. F. S. Freitas and E. L. Cussler, "Temperature sensitive gels as extraction solvents," *Chemical Engineering Science*, vol. 42, no. 1, pp. 97–103, 1987.
- [12] C. S. Biswas, V. K. Patel, N. K. Vishwakarma et al., "Synthesis, characterization, and drug release properties of poly(*N*-isopropylacrylamide) gels prepared in methanol-water cosolvent medium," *Journal of Applied Polymer Science*, vol. 125, no. 3, pp. 2000–2009, 2012.
- [13] S. Kralj, M. Drogenik, and D. Makovec, "Controlled surface functionalization of silica-coated magnetic nanoparticles with terminal amino and carboxyl groups," *Journal of Nanoparticle Research*, vol. 13, no. 7, pp. 2829–2841, 2011.
- [14] L. A. Harris, J. D. Goff, A. Y. Carmichael et al., "Magnetite nanoparticle dispersions stabilized with triblock copolymers," *Chemistry of Materials*, vol. 15, no. 6, pp. 1367–1377, 2003.
- [15] A. K. Gupta and M. Gupta, "Synthesis and surface engineering of iron oxide nanoparticles for biomedical applications," *Biomaterials*, vol. 26, no. 18, pp. 3995–4021, 2005.
- [16] G. Bao, S. Mitragotri, and S. Tong, "Multifunctional nanoparticles for drug delivery and molecular imaging," *Annual Review of Biomedical Engineering*, vol. 15, p. 253, 2013.
- [17] K. C. Souza, G. Salazar-Alvarez, J. D. Ardisson, W. A. A. Macedo, and E. M. B. Sousa, "Mesoporous silica-magnetite nanocomposite synthesized by using a neutral surfactant," *Nanotechnology*, vol. 19, no. 18, Article ID 185603, 2008.
- [18] M. Choi, F. Kleitz, D. Liu, Y. L. Hee, W.-S. Ahn, and R. Ryoo, "Controlled polymerization in mesoporous silica toward the design of organic-inorganic composite nanoporous materials," *Journal of the American Chemical Society*, vol. 127, no. 6, pp. 1924–1932, 2005.
- [19] K. S. W. Sing, "Reporting physisorption data for gas/solid systems with special reference to the determination of surface area and porosity," *Pure and Applied Chemistry*, vol. 57, no. 4, pp. 603–619, 1985.
- [20] A. Sayari, P. Liu, M. Kruk, and M. Jaroniec, "Characterization of large-pore MCM-41 molecular sieves obtained via hydrothermal restructuring," *Chemistry of Materials*, vol. 9, no. 11, pp. 2499–2506, 1997.
- [21] S. J. Gregg and K. S. W. Sing, *Standard Data for Alpha-s Method Comment*, 2nd edition, 1982.
- [22] T. Kokubo, H. Kushitani, S. Sakka, T. Kitsugi, and T. Yamamuro, "Solutions able to reproduce in vivo surface-structure changes in bioactive glass-ceramic A-W3," *Journal of Biomedical Materials Research*, vol. 24, no. 6, pp. 721–734, 1990.
- [23] A. Pineau, N. Kanari, and I. Gaballah, "Kinetics of reduction of iron oxides by H₂. Part I: low temperature reduction of hematite," *Thermochimica Acta*, vol. 447, no. 1, pp. 89–100, 2006.

- [24] D. Zhao, Q. Huo, J. Feng, B. F. Chmelka, and G. D. Stucky, "Nonionic triblock and star diblock copolymer and oligomeric surfactant syntheses of highly ordered, hydrothermally stable, mesoporous silica structures," *Journal of the American Chemical Society*, vol. 120, no. 24, pp. 6024–6036, 1998.
- [25] K. C. Souza, N. D. S. Mohallem, and E. M. B. Sousa, "Mesoporous silica-magnetite nanocomposite: facile synthesis route for application in hyperthermia," *Journal of Sol-Gel Science and Technology*, vol. 53, no. 2, pp. 418–427, 2010.
- [26] V. Antochshuk, M. Kruk, and M. Jaroniec, "Surface modifications of cage-like and channel-like mesopores and their implications for evaluation of sizes of entrances to cage-like mesopores," *Journal of Physical Chemistry B*, vol. 107, no. 43, pp. 11900–11906, 2003.
- [27] A. K. Dash and G. C. Cudworth II, "Therapeutic applications of implantable drug delivery systems," *Journal of Pharmacological and Toxicological Methods*, vol. 40, no. 1, pp. 1–12, 1998.
- [28] K. C. Souza, J. D. Ardisson, and E. M. B. Sousa, "Study of mesoporous silica/magnetite systems in drug controlled release," *Journal of Materials Science: Materials in Medicine*, vol. 20, no. 2, pp. 507–512, 2009.
- [29] B. D. Cullity and C. D. Graham, *Introduction to Magnetic Materials*, IEEE Press Editorial Board, 2nd edition, 2009.
- [30] M. Liangruksa, R. Ganguly, and I. K. Puri, "Parametric investigation of heating due to magnetic fluid hyperthermia in a tumor with blood perfusion," *Journal of Magnetism and Magnetic Materials*, vol. 323, no. 6, pp. 708–716, 2011.
- [31] G. Baldi, G. Lorenzi, and C. Ravagli, "Hyperthermic effect of magnetic nanoparticles under electromagnetic field," *Processing and Application of Ceramics*, vol. 3, p. 103, 2009.
- [32] E. A. Périgo, S. C. Silva, E. M. B. De Sousa et al., "Properties of nanoparticles prepared from NdFeB-based compound for magnetic hyperthermia application," *Nanotechnology*, vol. 23, no. 17, Article ID 175704, 2012.

Research Article

Characterization of the Casein/Keratin Self-Assembly Nanomicelles

Su Xiao-Zhou, Wang Hong-Ru, and Huang Mian

College of Resources and Environment, Shaanxi University of Science and Technology, Xi'an 710021, China

Correspondence should be addressed to Wang Hong-Ru; wanghr@sust.edu.cn

Received 12 September 2013; Revised 16 January 2014; Accepted 19 January 2014; Published 25 February 2014

Academic Editor: Anchal Srivastava

Copyright © 2014 Su Xiao-Zhou et al. This is an open access article distributed under the Creative Commons Attribution License, which permits unrestricted use, distribution, and reproduction in any medium, provided the original work is properly cited.

Complex nanomicelles were made from casein and keratin through electrostatic self-assembly and transglutaminase fixation that was proved to be harmless and green. The complex nanomicelles were characterized by dynamic light scattering, scanning electron microscopy, atomic force microscopy, Fourier transform infrared spectroscopy, differential scanning calorimetry, and steady-state fluorescence. The results show that the complex nanomicelles acquired at the neutral pH in the mass ratio of casein to keratin 4:1 exhibit an anomalous sphere shape with uniform size which the diameter is about 40–70 nm. The complex nanomicelles in solution possess excellent dilution and storage stability due to the fixation and their high ζ -potential (22.8 mV). The complex nanomicelles are relatively hydrophilic and have a good potential for industrial application.

1. Introduction

Molecular self-assembly is the spontaneous association of molecules under equilibrium conditions into stable, structurally well-defined aggregates joined by noncovalent bonds [1]. Self-assembly of biomacromolecules is emerging as a new route to produce novel materials, which can find many applications in biomedical technology and biomaterials technology.

Both casein and keratin have a strong tendency to self-assemble spontaneously into micelles in solution and their spontaneous self-assembly has been studied extensively in recent years [2–7]. Casein has an isoelectric point of 4.6, and it is relatively hydrophobic, making it poorly soluble in water. High glycine-tyrosine keratin from wool has an isoelectric point around 6.5, and it is relatively hydrophilic in water [8, 9]. When these different types of proteins were mixed together, they did not result in precipitation and phase separation. Therefore, the hydrophobic effect and the electrostatic interaction can be employed to reassemble and fabricate the casein/keratin nanomicelles.

The polymer micelles were characterized by their good drug loading capacity, high structural stability, excellent water solubility, and tiny particle size (100 nm or smaller).

Based on these viewpoints, our studies intended for structural stability and nanoparticles have been conducted. Biomaterials used for drug delivery, ecological coating, or cosmetic ingredients with desired properties will be developed based on the complex casein/keratin nanomicelles without toxicity.

2. Materials and Methods

2.1. Materials. Casein (technical grade) was purchased from Sigma Company Ltd. High glycine-tyrosine keratin powder was prepared from wool hydrolysate by stepwise precipitation with acid. All the other reagents used were of analytical grade.

2.2. Preparation of the Complex Nanomicelles. Casein was dispersed in ultrapure water by magnetic stirring at 50°C and then stored at 4°C at least for 10 days. The casein solution (5 mg/mL) was prepared and adjusted to pH 7.0 with 1 M NaOH and 1 M HCl solutions. High glycine-tyrosine keratin powder was put into ultrapure water and solid NaOH was added until the keratin completely dissolved by magnetic stirring. The casein and keratin solutions were then filtrated by millipore filters with 2.0 μ m pore size to get rid of the impurities and microbes. Then the casein and keratin

TABLE 1: Influence of the mass ratio of casein to keratin on the D_h , PDI, and scattering light intensity of the casein/keratin complex nanomicelles.

C/K	D_h (nm)	PDI	Intensity (counts)
1:0	70.85 ± 1.6	0.591 ± 0.04	82.47 ± 12
8:1	65.22 ± 1.4	0.522 ± 0.03	72.26 ± 9
4:1	60.24 ± 1.1	0.425 ± 0.01	96.53 ± 18
2:1	64.55 ± 1.8	0.613 ± 0.06	92.31 ± 11
1:1	50.48 ± 1.5	0.625 ± 0.09	66.89 ± 7
1:2	46.57 ± 0.8	0.611 ± 0.08	75.25 ± 14
1:4	42.15 ± 0.6	0.654 ± 0.07	89.95 ± 12
1:8	48.58 ± 0.8	0.687 ± 0.09	63.25 ± 12
0:1	120.23 ± 2.8	0.712 ± 0.08	60.54 ± 10

Note: C/K represents the casein/keratin nanomicelles. D_h is the hydrodynamic diameters; PDI is the particle dispersion index.

solutions were dispersed with sodium citrate in the mass ratio of protein to sodium citrate 5 : 1. Casein and keratin solutions were then mixed gently under different conditions and kept at 4°C for at least 24 hours to allow the casein and keratin to self-assemble completely. The complex micelles were then fixed by transglutaminase for 1 hour at 50°C and the enzyme was inactivated at 80°C for 10 min.

2.3. Turbidity Measurements. A Shimadzu UV 1705 spectrometer was used for turbidity measurements. Solution was injected into the Quartz cuvettes and the turbidity was detected at 600 nm wavelength.

2.4. Dynamic Light Scattering (DLS) Measurements. Hydrodynamic diameter of the micelles was measured by a Zeta Sizer Nano ZS90 (Malvern Instrument, Worcs, UK) equipped with 4 mW He-Ne Laser. The measurements were performed at a scattering angle of 90° at 25.0 ± 0.1°C. The apparent z -average diameter (D_h), polydispersity index (PDI), and the intensity for z -average were calculated by the Dispersion Technology Software provided by Malvern. The concentration of the micelles for DLS measurements was 5 mg/mL in each sample.

2.5. ζ -Potential Measurements. The ζ -potential was measured on a Zeta Sizer Nano ZS90 (Malvern Instrument, Worcs, UK) by using laser doppler microelectrophoresis. In this technique, an electric field was applied to the micelles, which then moved with a velocity related to their ζ -potential. This velocity was measured using a patented laser interferometric technique called M3-PALS (phase analysis light scattering). This enabled the calculation of electrophoretic mobility. The test was carried out at 25.0 ± 0.1°C. The electrophoresis mobility (U_E) was used to calculate the potential (ζ) by the Henry equation $U_E = 2\epsilon\zeta f(ka)/3\eta$, and ϵ , η , and $f(ka)$ represented, respectively, the dielectric constant, the viscosity of the medium, and Henry's function.

2.6. Scanning Electron Microscopy (SEM) Measurements. Hitachi S-4800 field emission scanning electron microscope was

used to observe the micelles at 1 kV. The micelles were fixed by 2% glutaraldehyde on the silicon surface for at least 30 min in order to keep the micelles primitive form, then washed with deionized water, and dried at the room temperature. Before observation, the specimens were coated with gold.

2.7. Atomic Force Microscopy (AFM) Measurements. AFM samples were prepared by dropping the solution on freshly cleaved mica surface, and then the micelles were fixed by 2% glutaraldehyde for at least 30 min. The samples were washed with deionized water and dried at room temperature. Skiko Atomic force Microscopy SPA400-SPI3800N was used to analyze the micelles in tapping mode.

2.8. Fourier Transform Infrared Spectroscopy Measurements. FT-IR spectra of the complex nanomicelles and the complex nanomicelles fixed by transglutaminase were measured with an Equinox 55 Spectrometer (Bruker). The analysis was performed in triplicate.

2.9. Thermal Analysis. Differential scanning calorimetry (DSC) measurements were performed with an instrument (netzsch STA 409) from room temperature to 400°C at a heating rate of 10°C/min. The complex nanomicelles and the complex nanomicelles fixed by transglutaminase were kept at 105°C for 30 min to get rid of the moisture.

2.10. Steady-State Fluorescence Measurements. The steady-state fluorescence tests were carried out on a fluorescence spectrophotometer Hitachi F-7000. Recrystallized pyrene was dissolved in acetone to prepare a concentration of 2×10^{-5} g/mL stock solution and its final concentration in micelles solution was 2×10^{-7} g/mL for test. Before measurements, the micelles solution was stored at 4°C for 24 hours after the pyrene was added. The excitation and emission wavelength were recorded at the 338 nm, 381 nm, and 373 nm wavelengths.

3. Results and Discussion

3.1. Diameter of the Complex Nanomicelles in Solution. The influence of mass ratio of casein to keratin on complex nanomicelles diameter was investigated at neutral pH. The DLS measurements revealed that the two proteins interacted with each other and formed complex micelles with diameter about 40–65 nm at pH 7.0 (Table 1). It was also found that any of the diameters of the complex nanomicelles in different mass ratio of casein and keratin were smaller than that of either casein micelles or keratin particles. This proved that the two protein particles had a strong hydrophobicity in the reassembly process. The casein micelles and keratin particles dissociated partly when these two proteins mixed together. The keratin peptides competed with casein peptides and bound to the interior sites of the casein micelles and led to the dissociation of the colloidal calcium phosphate (CCP). Table 1 also showed that the diameters of the complex nanomicelles decreased when the keratin content increased, which implied

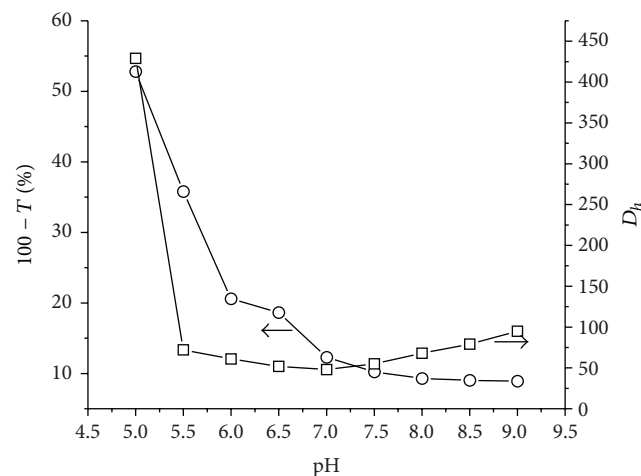


FIGURE 1: Turbidity and diameters of the casein/keratin complex nanomicelles (5 mg/mL) as a result of pH value in the mass ratio of casein to keratin 4 : 1.

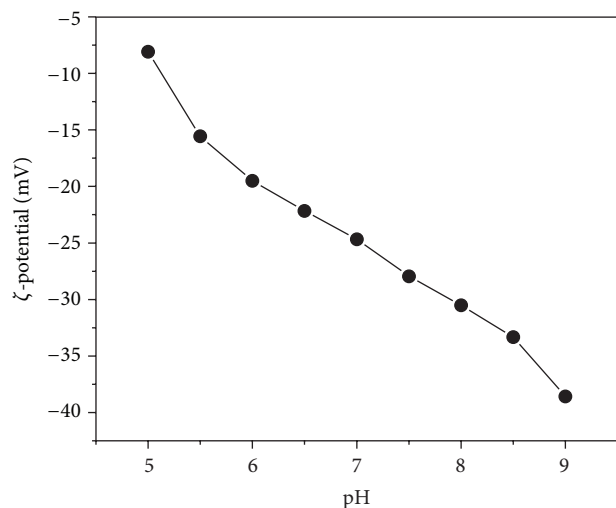


FIGURE 2: ζ-potential of the casein/keratin complex nanomicelles. The micelles were prepared in the mass ratio of casein to keratin 4 : 1 and at pH 5.0–9.0.

that the keratin particles played a major role in nanomicelle dispersion process.

The data in Table 1 also showed that the nanomicelles prepared at neutral pH in mass ratio of casein to keratin 4 : 1 had the highest intensity and relatively narrow PDI. Therefore, the smallest and stable nanomicelles can be obtained at the neutral pH in the mass ratio of casein to keratin 4 : 1, of which the average diameter is 60 nm (Figure 1).

3.2. ζ-Potential of the Complex Nanomicelles. ζ-potential relates to the net charges on the surface of the particles in solution. Figure 2 showed that the absolute value of the ζ-potential of the complex nanomicelles increased with the enhancement of pH value from 5.0 to 9.0 in the mass ratio of 4 : 1. This illustrated that the complex nanomicelles became

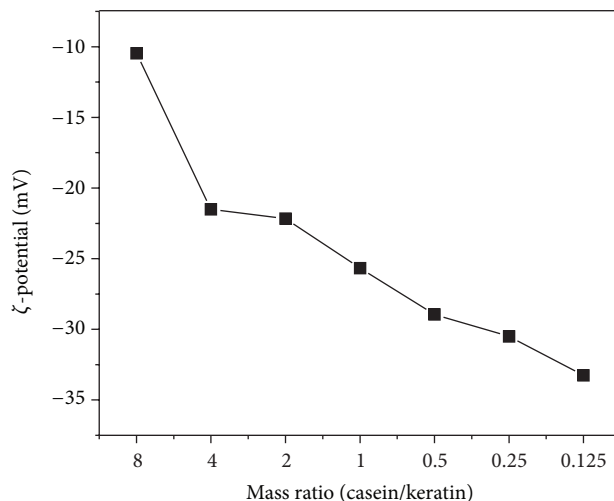


FIGURE 3: ζ-potential of the casein/keratin complex nanomicelles prepared at pH 7.0 in different mass ratios.

stabilized when the solution pH value increased from 5.0 to 9.0.

Figure 3 showed the ζ-potential of the complex micelles in different mass ratios of casein and keratin at neutral pH. The ζ-potential absolute value of the complex micelles increased with the increase of the keratin content. It can be inferred that the introduction of the keratin increased the stability of the complex nanomicelles.

3.3. Morphology of the Complex Nanomicelles. The morphology of the casein/keratin complex nanomicelles was observed by SEM. The samples in Figures 4(a) and 4(b) were from the 100-fold diluted self-assembly solution, and the samples in Figures 4(c) and 4(d) were from the 200-fold diluted self-assembly solution.

Figures 4(a) and 4(c) represented the nanomicelles' image, and Figures 4(b) and 4(d) represented the nanomicelles' image fixed by transglutaminase. The complex nanomicelles made from casein and keratin via self-assembly had a diameter of about 20–40 nm (Figures 4(a) and 4(c)). The fixed complex nanomicelles had a diameter of 40–70 nm (Figures 4(b) and 4(d)). The fixation with transglutaminase led to the enhancement of the micelles' diameter. In addition, two different fold-diluted samples showed almost the same diameter and morphology of the micelles (Figures 4(b) and 4(d)), which indicated that the dilution did not result in the dissociation of the complex nanomicelles, and the complex nanomicelles were stable on dilution. These implied that the crosslinking was formed either in the nanomicelles or between the nanomicelles during the fixation with transglutaminase.

Figure 5 showed the topography image of the fixed complex nanomicelles by the atomic force microscope. The morphology of the nanomicelles was of nearly spherical shape and had a diameter of 40–70 nm. This result was in accordance with the result measured by SEM and DLS. The diameter of the nanomicelles measured in solid state (SEM,

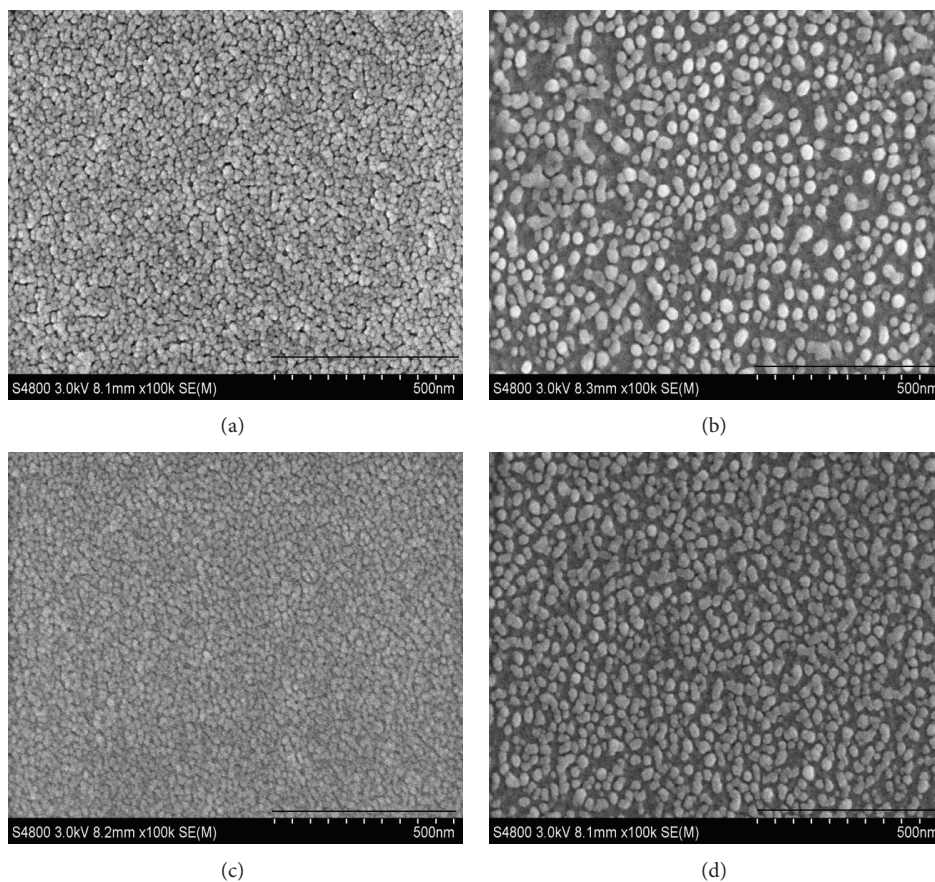


FIGURE 4: SEM images of the casein/keratin complex nanomicelles. (a) and (b) were diluted by 100-fold. (c) and (d) were diluted by 200-fold. (a) and (c) were casein/keratin complex nanomicelles; (b) and (d) were complex nanomicelles treated with transglutaminase (100 k magnification).

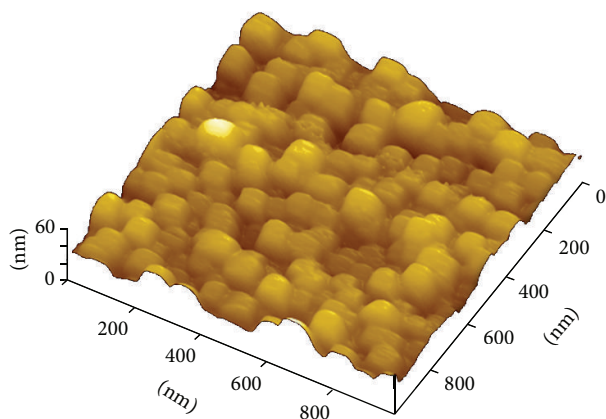


FIGURE 5: AFM images of the fixed casein/keratin complex micelles.

AFM) and in solution (DLS) had no great difference. This is attributed to the unique structure of the nanomicelles and the fixation method.

The FTIR spectrum of the complex nanomicelles showed an absorption band at 1113 cm^{-1} (Figure 6, CK-), but the complex nanomicelles fixed with transglutaminase showed

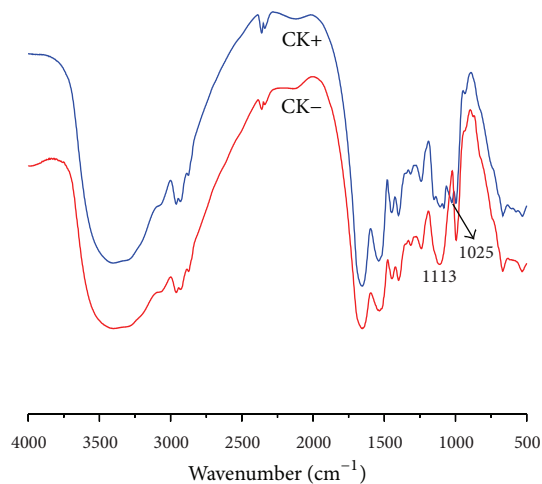


FIGURE 6: FT-IR spectra of the casein/keratin nanomicelles mixtures (CK-) and mixture treated with transglutaminase (CK+).

three absorption bands, respectively, at 1150 cm^{-1} , 1107 cm^{-1} , and 1081 cm^{-1} in the corresponding area (Figure 6, CK+). The absorption in this area is related to the C-N stretching

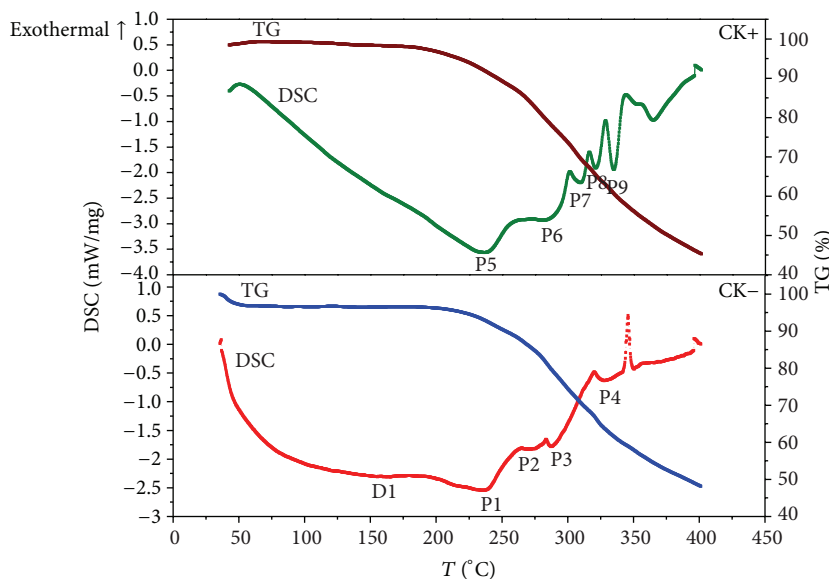


FIGURE 7: DSC thermograms of the casein/keratin nanomicelles mixture (CK-) and mixture treated by transglutaminase (CK+).

vibration of amido bonds. This indicated that some different new amido bonds were formed during the fixation with transglutaminase. Furthermore, the complex nanomicelles fixed with transglutaminase exhibited an additional band at 1025 cm^{-1} (Figure 6, CK+). On the basis of the transglutaminase spectrum (spectrum not shown) it was determined that this band came from the saccharide structure of malt dextrin incorporated into preparation of commercial transglutaminase.

3.4. Thermal Performance of the Complex Nanomicelles. The TG curve and the DSC curve of the complex nanomicelles were shown in Figure 7 (CK-). The wide heat absorption band D1 ($120\text{--}180^\circ\text{C}$) was related to the phase transition of the hydrated casein/keratin crystal. Peak 1 (238°C) corresponded to the cleavage of casein/keratin crystal. Peak 2 (275°C) corresponded to the breakdown of crosslinks ($-s-s-$ bonds, H bonds, and salt links) in keratin. Peak 3 (290°C) corresponded to the rupture of peptide bonds of casein. Peak 4 (330°C) corresponded to the liquefaction and rupture of peptide bond of keratin [10, 11].

The TG curve and the DSC curve of the complex nanomicelles fixed with transglutaminase were shown in Figure 7 (CK+). In Figure 7 (CK+), the wide heat absorption band ($120\text{--}180^\circ\text{C}$) related to the phase transition of the hydrated casein/keratin crystal disappeared, which indicated that the hydration ability of casein/keratin micelles was reduced by the fixation with transglutaminase. The heat absorption related to the breakdown of crosslinks in keratin and peptide bonds in casein appeared at 283°C (peak 6) as a single band, which implied that either the crosslinks or the peptide bonds were altered by the fixation with transglutaminase. The cleavage of casein/keratin crystal was scarcely influenced by the fixation (peak 1, peak 5). Peak 7 (310°C), peak 8 (320°C), and peak 9 (333°C) corresponded to the rupture of

keratin peptide bonds from different components caused by the fixation with transglutaminase.

3.5. Hydrophobicity/Hydrophilicity of the Complex Nanomicelles. Recrystallized pyrene was used as a probe to detect the hydrophobicity and hydrophilicity of casein/keratin complex nanomicelles. The intensity ratio of the first to the third peak (I_1/I_3) in the fluorescence spectrum can reflect the microenvironmental polarity where the probe exists [12]. The greater the value of I_1/I_3 was, the weaker the hydrophobic microenvironment for pyrene was.

Figure 8 showed that the value of I_1/I_3 for the complex nanomicelles was pH sensitive at pH 5.0–9.0. The value of I_1/I_3 of the complex nanomicelles increased with the increase of pH value from 5.0 to 9.0. The complex nanomicelle was more hydrophobic near the isoelectric point of the casein and keratin, which led to the relative lower value of I_1/I_3 . When the pH was increased from 5.0 to 9.0, the micelles' structure became loose because of the increase in electrostatic repulsion and the more hydrophilic group stretched out from the micelles, which led to the relative higher value of I_1/I_3 .

Figure 9 showed that the value of I_1/I_3 for the complex nanomicelles varied as a function of mass ratio. The value of I_1/I_3 of the micelles increased when the value of mass ratio of casein/keratin decreased. When the keratin was added gradually, the micelles disassociated partly and the structure became loose, and the micelles got more hydrophilic relatively.

3.6. Storage Stability of the Complex Nanomicelles. Casein nanomicelles (5 mg/mL) and casein/keratin complex nanomicelles (5 mg/mL, mass ratio 4:1) at neutral pH were prepared separately and their stability was compared during storage at room temperature. The changes in diameters and PDI were showed in Figures 10 and 11. Figure 10 showed

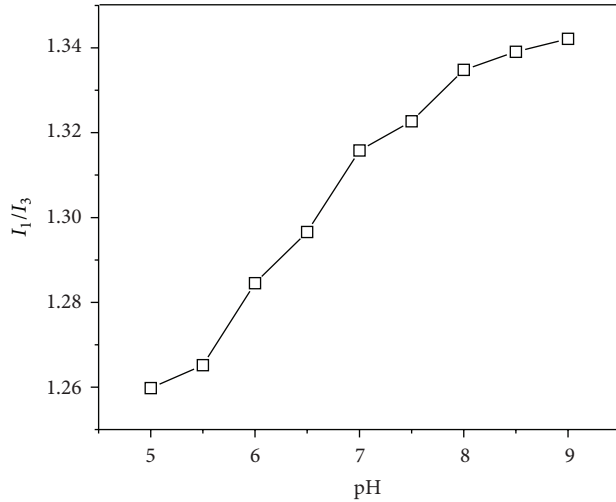


FIGURE 8: I_1/I_3 ratio of pyrene fluorescence for casein/keratin complex nanomicelles solution as functions of pH in the range of 5.0–9.0. The micelles solutions were prepared at pH 7.0 with a protein concentration of 5 mg/mL.

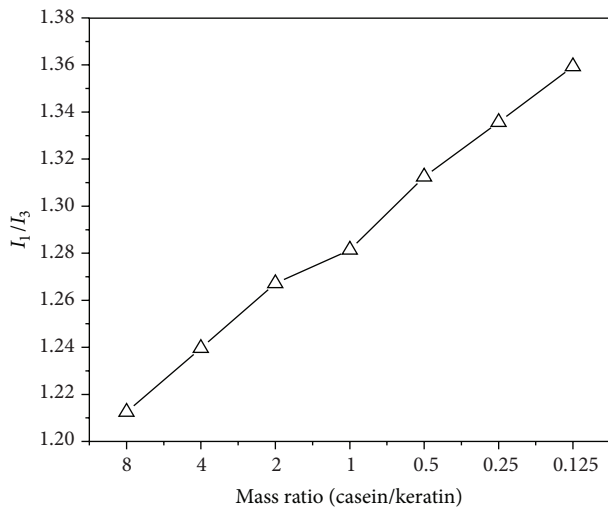


FIGURE 9: I_1/I_3 ratio of pyrene fluorescence for casein/keratin complex nanomicelles solution as functions of mass ratio. The micelles solutions were prepared at pH 7.0 with a protein concentration of 5 mg/mL.

that the value of the diameter for the complex nanomicelles almost was constant during the forty days of storage. On the contrary, casein micelles' diameter increased greatly in this process. The PDI value also exhibited similar result in Figure 11. These indicated that the nanomicelles' stability was improved dramatically when keratin was added. This is because the keratin employed possesses high stability in structure [13] and lower molecular weight with intact secondary structure.

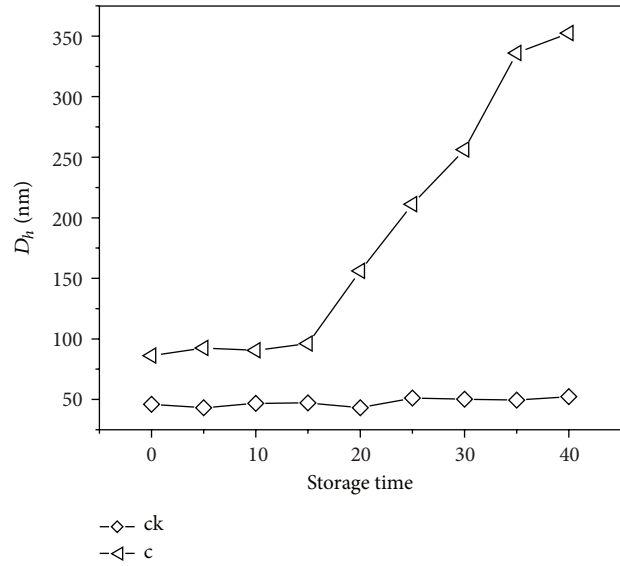


FIGURE 10: Plots of D_h variations for the casein micelles and the casein/keratin complex nanomicelles in the 40-day preservation time. The micelles solutions were prepared at pH 7.0 with a protein concentration of 5 mg/mL.

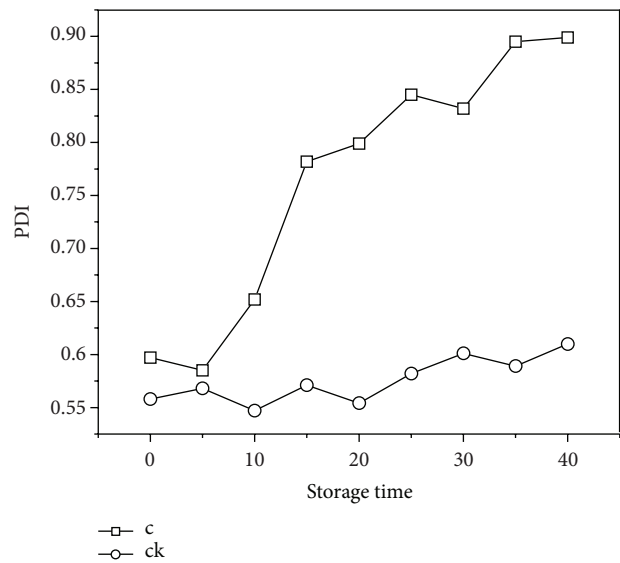


FIGURE 11: Plots of PDI variations for the casein micelles and the casein/keratin complex nanomicelles in the 40-day preservation time. The micelles solutions were prepared at pH 7.0 with a protein concentration of 5 mg/mL.

4. Conclusions

Casein and keratin were used to fabricate complex nanomicelles through electrostatic self-assembly. In this process, no harmful reagents were used. Polydisperse complex nanomicelles can be formed in pH range of 5.0–9.0. Stable complex nanomicelles can be acquired at the neutral pH in the mass ratio of casein to keratin 4:1, and the absolute value of ζ -potential was 22.8 mV. The stable complex nanomicelles

exhibited anomalous sphere shape with uniform size of which the average diameter was about 40–70 nm. The fixation with transglutaminase could enhance the dilution stability and reduce the hydration of the complex nanomicelles to some extent by forming crosslinking in the nanomicelles or between the nanomicelles. The complex nanomicelles were relatively hydrophilic and had good storage stability.

Conflict of Interests

The authors declare that there is no conflict of interests regarding the publication of this paper.

Acknowledgments

This work was financially supported by the Hongliang Research Fund (413118) and Doctor Research Fund of Shaanxi University of Science and Technology (BJ08-15). The material in this work was supported by Jiangsu Yiming Bio-Products Co.

References

- [1] G. M. Whitesides, J. P. Mathias, and C. T. Seto, "Molecular self-assembly and nanochemistry: a chemical strategy for the synthesis of nanostructures," *Science*, vol. 254, no. 5036, pp. 1312–1319, 1991.
- [2] C. G. De Kruif, "Casein micelle interactions," *International Dairy Journal*, vol. 9, no. 3–6, pp. 183–188, 1999.
- [3] C. F. Narambuena, F. S. Ausar, I. D. Bianco, D. M. Beltramo, and E. P. M. Leiva, "Aggregation of casein micelles by interactions with chitosans: a study by Monte Carlo simulations," *Journal of Agricultural and Food Chemistry*, vol. 53, no. 2, pp. 459–463, 2005.
- [4] C. Garnier, C. Michon, S. Durand, G. Cuvelier, J.-L. Doublier, and B. Launay, "Iota-carrageenan/casein micelles interactions: evidence at different scales," *Colloids and Surfaces B*, vol. 31, no. 1–4, pp. 177–184, 2003.
- [5] M. van de Locht, "Reconstitution of microfibrils from wool and filaments from epidermis proteins," *Melliand Textilberichte*, vol. 10, pp. 780–786, 1987.
- [6] P. M. Steinert and M. I. Gullino, "Bovine epidermal keratin filament assembly in vitro," *Biochemical and Biophysical Research Communications*, vol. 70, no. 1, pp. 221–227, 1976.
- [7] H. Thomas, A. Conrads, P. H. Phan, M. van de Locht, and H. Zahn, "In vitro reconstitution of wool intermediate filaments," *International Journal of Biological Macromolecules*, vol. 8, pp. 258–264, 1986.
- [8] J. E. Plowman, "The proteomics of keratin proteins," *Journal of Chromatography B*, vol. 849, no. 1–2, pp. 181–189, 2007.
- [9] L. M. Flanagan, J. E. Plowman, and W. G. Bryson, "The high sulphur proteins of wool: towards an understanding of sheep breed diversity," *Proteomics*, vol. 2, no. 9, pp. 1240–1246, 2002.
- [10] W. Xu, W. Guo, and W. Li, "Thermal analysis of ultrafine wool powder," *Journal of Applied Polymer Science*, vol. 87, no. 14, pp. 2372–2376, 2003.
- [11] B. Purevsuren and Y. Davaajav, "Thermal analysis of casein," *Journal of Thermal Analysis and Calorimetry*, vol. 65, no. 1, pp. 147–152, 2001.
- [12] C. Keyes-Baig, J. Duhamel, S. Fung, and J. Bezaire, "Self-assembling peptide as a potential carrier of hydrophobic compounds," *Journal of the American Chemical Society*, vol. 126, no. 24, pp. 7522–7532, 2004.
- [13] J. Li, Y. Li, L. Li, A. F. T. Mak, F. Ko, and L. Qin, "Preparation and biodegradation of electrospun PLLA/keratin nonwoven fibrous membrane," *Polymer Degradation and Stability*, vol. 94, no. 10, pp. 1800–1807, 2009.

Research Article

Nanopigmented Acrylic Resin Cured Indistinctively by Water Bath or Microwave Energy for Dentures

L. S. Acosta-Torres,¹ M. C. Arenas,¹ R. E. Nuñez-Anita,² F. H. Barceló-Santana,³
C. A. Álvarez-Gayosso,³ J. Palacios-Alquisira,⁴ J. de la Fuente-Hernández,¹
Marcos Cajero-Juárez,² and V. M. Castaño^{5,6}

¹ Escuela Nacional de Estudios Superiores, Unidad León, Licenciatura en Odontología, Universidad Nacional Autónoma de México, Boulevard UNAM No. 2011 Predio el Saucillo y el Potrero, 36969 León, GTO, Mexico

² Facultad de Medicina Veterinaria y Zootecnia, UMSNH, Km. 9.5 Carretera Morelia-Zinapécuaro, Col. La Palma, 58893 Tarímbaro, MICH, Mexico

³ Laboratorio de Materiales Dentales, División de Estudios de Posgrado e Investigación, Facultad de Odontología, Universidad Nacional Autónoma de México, Avenida Universidad No. 3000, Colonia Copilco, 04510 México, DF, Mexico

⁴ Posgrado de la Facultad de Química, Universidad Nacional Autónoma de México, Avenida Universidad No. 3000, Colonia Copilco, 04510 México, DF, Mexico

⁵ Departamento de Ingeniería Molecular de Materiales, Centro de Física Aplicada y Tecnología Avanzada, Universidad Nacional Autónoma de México, Campus Juriquilla, Boulevard Juriquilla No. 3001, 76230 Juriquilla, QRO, Mexico

⁶ Centro de Tecnología Avanzada, (CIATEQ), av. El Retablo 150, 76150 Querétaro, Qro, Mexico

Correspondence should be addressed to M. C. Arenas; carenas@enes.unam.mx

Received 9 July 2013; Revised 25 December 2013; Accepted 27 December 2013; Published 20 February 2014

Academic Editor: Il-Kwon Oh

Copyright © 2014 L. S. Acosta-Torres et al. This is an open access article distributed under the Creative Commons Attribution License, which permits unrestricted use, distribution, and reproduction in any medium, provided the original work is properly cited.

The highlight of this study was the synthesis of nanopigmented poly(methyl methacrylate) nanoparticles that were further processed using a water bath and/or microwave energy for dentures. The experimental acrylic resins were physicochemically characterized, and the adherence of *Candida albicans* and biocompatibility were assessed. A nanopigmented acrylic resin cured by a water bath or by microwave energy was obtained. The acrylic specimens possess similar properties to commercial acrylic resins, but the transverse strength and porosity were slightly improved. The acrylic resins cured with microwave energy exhibited reduced *C. albicans* adherence. These results demonstrate an improved noncytotoxic material for the manufacturing of denture bases in dentistry.

1. Introduction

Poly(methyl methacrylate) (PMMA) is the main commercial acrylic resin used in denture fabrication [1]. Advances in polymer science for denture bases have developed different molding and activation techniques [2]. The heat- and microwave-generated commercial acrylic resins have similar chemical formulations [3], but there are specific components to the curing of resins for each technique. The microwave method for PMMA denture base polymerization has the following advantages: shorter times for curing and for attaining

the plastic phase and less porosity and excellent adaptation of a prosthetic material in contrast to conventional heat-water polymerization. Despite these advantages, this method has limited use in the dentistry field [4].

A few studies regarding the experimental acrylic resin have been reported. In our previous works, spherical particles of an experimental acrylic resin were synthesized by the polymerization suspension technique using sodium alginate or gelatin as suspension agents. A clear PMMA was obtained and the morphology, particle size, thermal behavior, and flexural properties were fully characterized. The result was a

material comparable with the commercial acrylic resins for dentures when the material was processed by a water bath or a microwave technique [5]. Metallic oxide nanoparticles were included in the synthesis as pigments to obtain a pink PMMA that was similar to the gums in color. These nanopigmented PMMA particles were thermopolymerized with the water bath technique, and they presented lower porosity and solubility compared with the clear PMMA [6]. Different types of fibers [7] or silver nanoparticles [8] were added in the nanopigmented PMMA formulation, but the fibers did not change the flexural strength, and the nanoparticles decreased this value, despite an improvement of the antifungal effect against *Candida albicans*.

The nanopigmented PMMA needs to be assessed in all the physical, antimicrobial, and cytocompatible properties when it is processed indistinctively by a water bath and microwave thermopolymerization techniques. These methods do not sacrifice the resin's physicochemical properties and might generate a cheap and nontoxic material. The material needs to be compared with the commercial acrylic resins available for each specific technique. The material was compared with the Lucitone 199 and Acron MC acrylic resins for denture bases that are commercially available for specific water bath and microwave polymerization techniques, respectively.

2. Materials and Methods

Methyl methacrylate (MMA) monomer and benzoyl peroxide (both from Sigma-Aldrich, St. Louis, MO, USA) were used as received. Sodium alginate (Manufacturera-Dental-Continental, Mexico) was used as a suspension agent. Iron oxide and titanium oxide nanoparticles (Fe_2O_3 [R-4511] and TiO_2 [RF-9400] (González-Cano y Compañía, Mexico) were used as pigments. The commercial heat-cured acrylic resins Lucitone 199 (water bath thermopolymerized; Dentsply/Trubyte, York, PA) and Acron MC (GC Lab Technologies, Alsip, IL) were selected for the comparisons.

3. Synthesis of Nanopigmented PMMA Particles

Nanopigmented PMMA, a pink substance similar to the gums, was synthesized by the suspension polymerization technique described in previous work [5]. The brief method was as follows. In a five-neck flask, 200 mL of deionized water, 1.5 g of sodium alginate, 200 g of MMA monomer, and 0.2 g of initiator were mixed with reflux; nitrogen gas was added; the mixture was stirred (1,200 rpm) and heated at 70°C for 2 h. The TiO_2 and Fe_2O_3 nanopigments were dissolved in 30 mL of deionized water and added to the reactor 30 min before the initiator incorporation. Constant stirring throughout the reaction was used to ensure equal distribution of pigments. When the reaction was finished and the PMMA particles had sedimented, they were separated by decantation. The PMMA was washed with deionized water four times until the water was clear to eliminate the nonreactant products. The polymer particles were dried at room temperature.

4. Characterization of Nanopigmented PMMA Particles

The nanopigmented PMMA, Lucitone 199, and Acron MC powders were characterized. Fourier transform infrared (FT-IR) spectroscopy was conducted in a Bruker Vector 33 Instrument using the transmittance technique. The samples were prepared in KBr translucent disks and analyzed with 17 scans in the wavelength region between 400 and 4,000 cm^{-1} .

For scanning electron microscopy (SEM) analysis, the polymer particles were coated with gold by vacuum evaporation, and the observations were carried out with a JSM-6060LV scanning microscope (JEOL, Peabody, MA). The particle size distribution and standard deviation were obtained for each acrylic resin.

5. Water Bath and Microwave Polymerization for Specimen Preparation

To obtain the PMMA specimens, the nanopigmented PMMA powder was separated in two parts to form two experimental groups. Mixtures were prepared with the powders of each group and were collocated in three molds with the following dimensions: 65 × 10 × 2.5 mm, 50 × 0.5 mm, and 10 × 2 mm.

The first group, designated PMMA-wb, was obtained by mixing the PMMA with a MMA monomer (3 : 1) and benzoyl peroxide (1%), packing the mixture into metallic molds, and processing in a water bath for 90 min at 70°C and then for 30 min at 90°C. The second group, designated PMMA-mw, was obtained by mixing the PMMA particles with a MMA monomer (3 : 1) and benzoyl peroxide (1%) and packing the mixture into polyester molds, which was followed by curing with microwave energy at 500 W for 3 min. After the curing process, the molds were cooled at room temperature for 30 min and placed into cold water at 4°C for 30 min before opening the molds.

The commercial acrylic resins Lucitone 199 and Acron MC were cured following the manufacturers' instructions.

The specimens obtained were plates of 65 × 10 × 2.5 mm for the flexural strength and flexural modulus calculations ($n = 10$), discs of 50 × 0.5 mm for the water sorption and solubility tests ($n = 10$), and discs of 10 × 2 mm for the *C. albicans* adherence and cytotoxicity assays ($n = 9$). All the specimens were trimmed with wet abrasive paper of grit 100 and 300 (Fandeli, Mexico) prior to use.

Table 1 summarizes the curing technique, batch number, and viscosity molecular weight of each evaluated acrylic resin. The mentioned molecular weight belongs to the experimental PMMA without the nanopigment particles.

6. Characterization of the Cured Nanopigmented PMMA Specimens

The processed PMMA-wb, PMMA-mw, Lucitone 199, and Acron MC samples were tested as follows.

Thermogravimetric analysis (TGA) was carried out on a fragment of each group of the nanopigmented PMMA cured resins using a thermogravimetric analyzer (TA Instrument

TABLE 1: Summary of processing methods for curing of commercial acrylic resin and experimental PMMA.

Acrylic resin	Processing method	Manufacturer (location)	Viscosity mol wt (g/mol) ^a
Lucitone 199	Water bath cured at 70°C for 90 min and 90°C for 30 min	Dentsply/Trubyte (York, PA)	19×10^{-5}
Acron MC	Microwave cured at 500 W for 3 min	GC (Alsip, IL)	14×10^{-5}
Experimental PMMA	Water bath cured at 70°C for 90 min and 90°C for 30 min; microwave cured at 500 W for 3 min	—	36×10^{-5}

^aThe viscosity molecular weight was reported previously [5].

Q500 V6.3) at a heating rate of 10°C/min up to 900°C in an N₂ atmosphere.

For the characterization of the flexural behavior, the samples were placed in a transverse deflection machine (Mecmesin, Sterling, VA) at 5 N/min until they fractured. The flexural modulus and transverse strength values were obtained using the equations reported previously [5, 6].

For the water sorption and solubility test, 10 discs ($n = 10$) were weighed (reported in mg), placed in a silica gel desiccator, and weighed every 24 h until a constant mass (m_1) was obtained. The discs were placed in distilled water for 7 days at $37 \pm 1^\circ\text{C}$. The discs were then dried and weighed (m_2). The discs were placed in the desiccator again and weighed every 24 h until a constant mass (m_3) was reached. The area (A) of each sample was calculated (reported in cm²). The water sorption (W_s) and solubility (Sl) were calculated according to ADA 12, 1990 [9], as follows: $W_s = (m_2 - m_1)/A$; $Sl = (m_1 - m_3)/A$.

For the porosity test, the fractured plates were adjusted to obtain plates of $30 \times 10 \times 2.5$ mm. They were weighed to obtain their mass, and the volume of each sample was calculated (V_{sp}). The samples were weighed every 24 h and placed in a silica gel desiccator until a constant mass was obtained. The volume of each sample was determined, and the internal porosity (V_{ip}) was calculated as follows:

$$V_{ip} = V_{sp} - \frac{Wa}{(d_r - d_a)}. \quad (1)$$

Wa is the weight of the sample (in g), d_r is the acrylic resin density (1.198 g/cm³), d_a (0.00123 g/cm³) is the Mexico City air density (at $T = 294$ K, 78 kPa), and V_{sp} is the volume of the sample (in cm³).

One of the broken parts from each group after the flexural tests was used to observe the fracture zone by SEM.

The contact angles of the PMMA polymer films have been measured by the spheroidal segment method using a contact angle measurement system [10].

For the biological testing (*C. albicans* adherence and cytotoxicity assays), *C. albicans* strain 90026 (American Type Culture Collection, Manassas, VA) was cultured in 24-well plates at a density of 1×10^5 cells/mL. The PMMA samples were sterilized by exposing both faces to ultraviolet irradiation for 5 min [8, 11]. Each acrylic resin sample was placed in contact with the microorganisms for 24 h, and the samples were removed and washed with distilled water

under stirring conditions. The samples were placed in new 24-well plates, and 100 μL of benzalkonium chloride was added to each sample to extract the adhered *C. albicans* cells. The plate contents were stirred for 15 min, and the samples were removed. A microbial cell viability assay based on luminescent ATP measurements (BacTiter Glo; Promega, Fitchburg, WI) was performed to determine the number of viable cells that had adhered to the composite resins. Briefly, extract aliquots (20 μL each) were mixed with 30 μL of BacTiter Glo reagent in 1.5-mL clear Eppendorf tubes, and the luminescence was recorded after 5 min using a luminometer (Turner Biosystems, Sunnyvale, CA) at an emission wavelength of 590 nm. The relative luminescence intensity, in 10 sec integration periods, was measured in triplicate.

A MTT assay was performed using NIH 3T3 mouse fibroblast-like cells (ATCC No. CRL-1658). The nanopigmented and commercial PMMA samples were sterilized by exposing both faces to ultraviolet irradiation for 5 min. The cells were exposed to acrylic resins specimens, and proliferation was assessed by measuring the reductase enzymatic activity based on the transformation of 3-(4,5-dimethylthiazol-2-yl)-2,5-diphenyltetrazolium bromide (MTT) into the colored, reduced form of MTT [12]. After 24 and 48 h incubation times, the resins were removed, the MTT assay was performed following the manufacturer's instructions (Sigma-Aldrich), and the absorbance was measured in a microplate reader (Bio-Rad 680) at a wavelength of 655 nm.

The viability percentage was calculated as follows: [(optical density of the samples)/(optical density of the control group)] $\times 100$. The control group was cultured without acrylic resins. The samples were analyzed in triplicate, and three independent experiments were performed.

For the statistical analysis, One-Way Analysis of Variance ($P < 0.05$) and Tukey tests were applied for the water sorption, solubility, flexural modulus, transverse strength, porosity, cytotoxicity, and *C. albicans* adherence values.

7. Results and Discussion

7.1. FTIR and Size Distribution of Nanopigmented PMMA. Figure 1 shows the infrared spectrum of the nanopigmented PMMA compared with those of the commercial PMMA resins (Lucitone 199 and Acron MC) in the wavelength range of $4,000 \text{ cm}^{-1}$ to 650 cm^{-1} . All the spectra present similar responses, in which the characteristic peaks of the PMMA were observed [9, 10, 13]. The peaks at $2,950 \text{ cm}^{-1}$ and

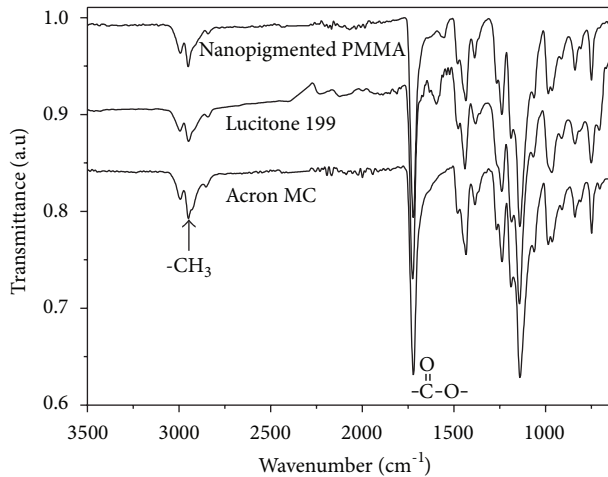


FIGURE 1: Infrared spectra of polymer particles of nanopigmented PMMA, Lucitone 199, and Acron MC showing the main stretching bands of the PMMA molecule.

$1,720\text{ cm}^{-1}$ correspond to the C–H and C=O (ester carbonyl) stretching vibrations, and the band at $1,434\text{ cm}^{-1}$ is due to the C–H bending vibrations. Other peaks at low frequencies, $1,139\text{ cm}^{-1}$, 840 cm^{-1} , and 752 cm^{-1} , are related to the H–C–H stretching vibration, to the O–C–O deformation vibration, and to the puckering vibration of PMMA, respectively. The absence of peaks in the range of $1,680\text{ cm}^{-1}$ to $1,640\text{ cm}^{-1}$ indicates that the MMA monomer was fully polymerized [12].

Despite the similarities in the infrared results for the PMMA samples, the particle sizes were very different according to the SEM results (not shown here). The nanopigmented PMMA particle sizes were between 4.5 and $10\text{ }\mu\text{m}$, and the sizes for Lucitone 199 and Acron MC were in the range of 30 to $60\text{ }\mu\text{m}$ and 60 to $120\text{ }\mu\text{m}$, respectively. Figure 2 shows the distribution of the particles sizes, where the averages for the samples were $16.51\text{ }\mu\text{m} \pm 6.5\text{ }\mu\text{m}$ (nanopigmented PMMA), $32.23\text{ }\mu\text{m} \pm 10.8\text{ }\mu\text{m}$ (Lucitone 199), and $69.69\text{ }\mu\text{m} \pm 23.88\text{ }\mu\text{m}$ (Acron MC).

7.2. Evaluation of Nanopigmented PMMA Cured Using a Water Bath and Microwave Thermopolymerization. The nanopigmented PMMA particles were cured by a water bath and by microwave methods. The thermal stability of the PMMA specimens (PMMA-wb and PMMA-mw, Lucitone and Acron MC) was determined from the thermogram profiles (Figure 3). As shown in Figure 3(a), abrupt reductions in weight at approximately 300°C to 400°C (80 to 98% weight loss) were observed for all specimens, and these were attributed to the complete degradation of the polymer chain. As shown in the inset of Figure 3(a), the profile of PMMA-wb is slightly later than Lucitone 199, indicating a better stability. PMMA-mw is slightly less thermally stable than Acron MC. Based on the derived weight profiles (Figure 3(b)), the two main peaks between 276°C and 285°C (12 to 20% weight loss) and between 364°C and 379°C (80 to 98% weight loss) could be attributed to other components in the commercial

acrylic resins, such as plasticizers, comonomers, or cross-linking agents with different thermal behaviors. The manufacturer specifications of Lucitone 199 mention the presence of ethylene dimethacrylate in its liquid composition, and Acron MC presents a copolymer of poly (methyl methacrylate/ethylacrylate) in the powder formulation. It is clear that microwave energy influences in thermal stability of the nanopigmented PMMA specimens.

In the flexural modulus, there were no statistically significant differences between any of the tested groups ($P > 0.05$). PMMA-wb, Lucitone 199 and Acron MC showed slightly higher transverse strength values than the nanopigmented PMMA processed by microwaves (PMMA-mw) (Table 2), and this value fulfilled the minimum allowed value according to ISO 1567 (65 MPa) [14]. These values are still better compared with those of other commercial acrylic resins [15].

One important property of acrylates is water sorption and release, which allows for dimensional instability, subjecting the material to internal stresses that might result in crack formation and eventually might fracture the denture. The water molecules spread between the macromolecules of the material, forcing them apart and affecting the dimensional behavior and denture stability. Water sorption and solubility of these materials should be as low as possible [16]. In the water sorption test, there was a marked difference. The PMMA-wb had a lower value ($0.27 \pm 0.02\text{ mg/cm}^2$), and Lucitone 199 had a higher value ($0.37 \pm 0.04\text{ mg/cm}^2$). The materials processed by microwave energy had similar results. All the groups were tested for water sorption and solubility according to the ADA number 12-required values [17], which were lower than 0.8 and 0.04 mg/cm^2 , respectively.

The mechanical properties of denture base materials decrease as the solubility increases. One study showed that water bath polymerization results in enhanced mechanical properties. It has been established that the water sorption and solubility of polymers depend on the homogeneity of the material; less water absorbed and less solubility are presented in a homogeneous material [16]. PMMA-wb presented lower porosity than Lucitone 199, but there were no significant differences between the PMMA-mw and Acron MC. The low porosity of PMMA-wb was in accordance with the expected values, and it is important to emphasize that the porosities of all the nanopigmented PMMA specimens were lower than other acrylic resins [18].

After the flexural behavior evaluations, the topographies of the fractured zone of each specimen were examined in transverse sections by SEM (Figure 4). The micrographs showed irregular surfaces in the four acrylic resins, and the morphology changed according to the curing method. A slightly nonhomogeneous surface for PMMA-mw was observed, which was in concordance with the low transverse strength value.

The mechanical properties and wear resistance of denture materials have improved substantially, but their antibacterial properties are still of great interest [19]. In the present study, a *C. albicans* adherence assay was performed. Figure 5(a) shows the results of the adherence assay, in which PMMA-wb and Lucitone 199 resulted in slightly higher values than the

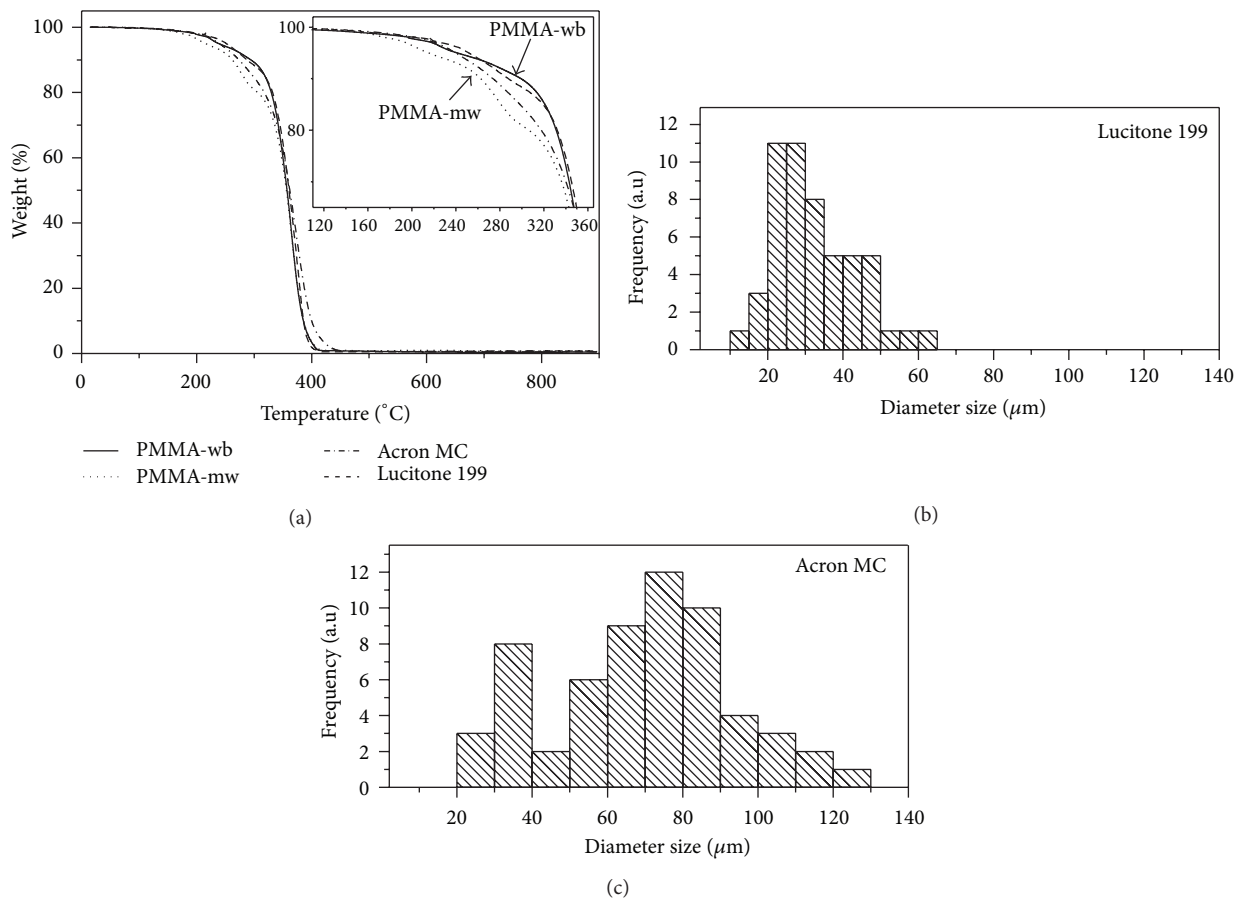


FIGURE 2: Statistical particle size distribution of (a) nanopigmented PMMA compared to the commercial acrylic resins: (b) Lucitone 199 and (c) Acron MC.

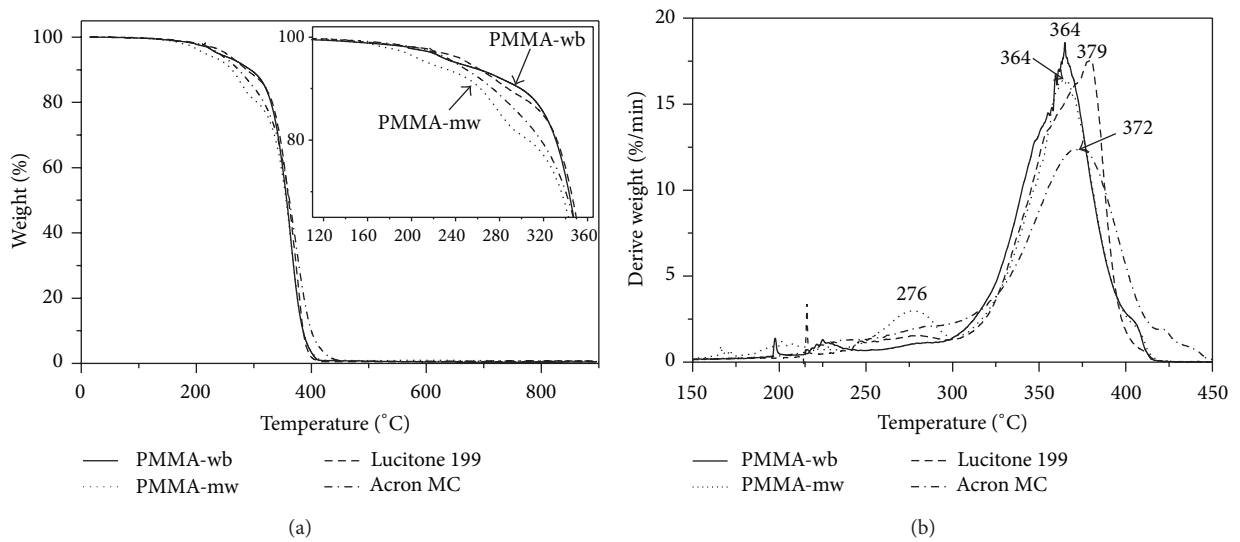


FIGURE 3: (a) TGA profiles and (b) derived weight profiles of PMMA-wb and PMMA-mw compared with the commercial acrylic resins.

TABLE 2: Physical properties of PMMA polymerized by water bath and with microwave energy.

Acrylic resin	Flexural modulus (GPa)	Transverse strength (MPa)	Water sorption (mg/cm ²)	Solubility (mg/cm ²)	Porosity (%)	Contact angle (°)	<i>Candida albicans</i> adherence (×10 ⁵ LRUs)
PMMA-WB	2.5 ± 0.14*	77.6 ± 5.1*	0.27 ± 0.02*	0.03 ± 0.004*	4.6 ± 0.4*	60.29 ± 1.8	5.8 ± 1.3
PMMA-MW	2.5 ± 0.30	68.1 ± 2.8	0.31 ± 0.06	0.04 ± 0.005	5.5 ± 0.5	32.66 ± 7.4	2.6 ± 0.5
Lucitone 199	2.5 ± 0.20 ⁺	78.2 ± 0.2 ⁺	0.37 ± 0.04	0.02 ± 0.010	6.8 ± 1.0 ⁺	36.02 ± 4.4	6.3 ± 2.2
Acron MC	2.5 ± 0.17	75.8 ± 5.1	0.30 ± 0.10	0.04 ± 0.008	5.4 ± 0.4	53.02 ± 3.1	1.6 ± 0.4

*[6]; ⁺[7].

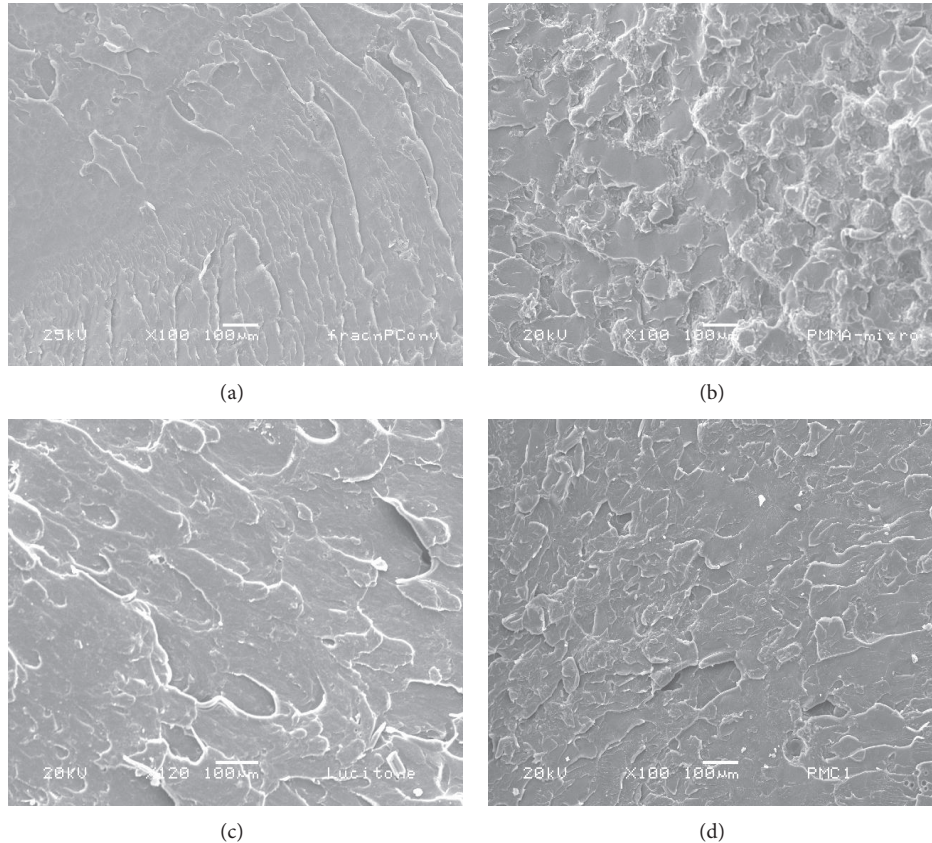


FIGURE 4: SEM images of the fracture zone of (a) PMMA-wb and (b) PMMA-mw compared with the commercial resins (c) Lucitone 199 and (d) Acron MC.

acrylic resins processed by microwave energy (PMMA-mw, Acron MC). Acron MC showed the lowest value, followed by nanopigmented PMMA-mw, which was indicative of a lower *C. albicans* adherence compared with PMMA-wb and Lucitone 199. *C. albicans* possesses various virulence factors, including the capacity to form biofilms, which render antifungal drugs less efficient. *C. albicans* has the ability to form hyphae, which facilitates soft tissue invasion, allowing the microorganisms to hide from the host defense system [20]. It is difficult to avoid the adhesion of pathogenic microorganisms to the surface of dental materials, though some efforts toward this have been made [21]. The exact mechanisms by which *C. albicans* adheres to acrylic surfaces are unknown, but many factors that affect *C. albicans* adherence have been

described, including surface roughness, salivary pellicle formation, hydrophobic property, and electrostatic interactions [22].

The water contact angle was measured to estimate the hydrophobicity of the nanopigmented PMMA and commercial acrylic resins (Table 2). The nanopigmented PMMA-wb specimens presented a high water contact angle and a large amount of *C. albicans*. This is contrary to the references, where the adherence was linearly related to high hydrophobicity [22]. These specimens are composed of small particles and have low porosity, which could influence the *C. albicans* adherence. The Acron MC specimens formed with large particles present low amounts of *C. albicans* and high hydrophobicity. The PMMA-mw and Acron MC specimens

Acrylic resin	<i>Candida albicans</i> adherence ($\times 10^5$ LRUs)
PMMA-wb	5.8 ± 1.3
PMMA-mw	2.6 ± 0.5
Lucitone 199	6.3 ± 2.2
Acron MC	1.6 ± 0.4

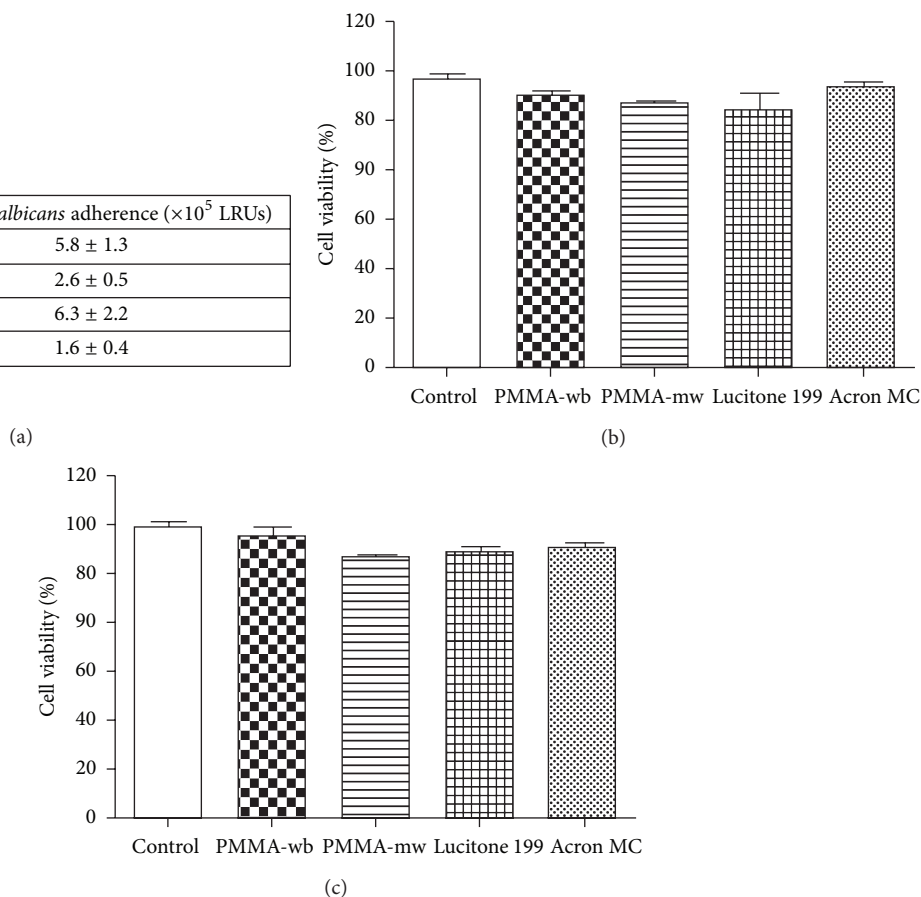


FIGURE 5: The antifungal effects and biocompatibility of PMMA-wb and PMMA-mw. (a) The adherence of *C. albicans* as measured in a luminescent microbial cell viability assay. The luminescence was determined based on light relative units (LRUs). (b) and (c) The viability of NIH 3T3 cells after exposure to materials for 24 and 48 h, respectively.

cured with microwave energy presented similar porosities and a low amount of *C. albicans*, and there was a great difference in the particle sizes.

Cytotoxicity tests were designed to determine how the sample material affected a particular cell type. Figures 5(b) and 5(c) show the results of the cytotoxicity assays for all the groups when they were in contact with mouse fibroblast-like NIH 3T3 cell cultures for 24 and 48 h. The MTT test was used because it is based on an evaluation of mitochondrial function after exposure to potential toxic substances [23]. The results were not statistically significantly different ($P > 0.05$), indicating that the synthesized PMMA and the commercial acrylic resins are nontoxic materials.

Consideration must be given to the relative biocompatibility of all denture base materials. Considerations of the incidence and severity of side effects of denture bases have been included as parts of some general studies on dental materials. Local reactions that have been reported are not severe, and the most common are lichenoid reactions in the oral mucosa and skin reactions such as rashes, dermatitis, and eczematous lesions. These reactions depend on the chemical composition of the materials used and their degradation products, absorption, accumulation, and other factors associated with

leachable substances from the restoration. Another group of side effects are related to cell proliferation. One study showed that a PMMA-based denture base polymer triggered death signals in cell culture [24]. Another study showed that treatment in a water bath postpolymerization reduced the cytotoxicity of Lucitone 550 [25]. In this work, Lucitone 199 and Acron MC were used as controls, representing noncytotoxic resins. The results showed that no significant differences were observed regarding fibroblast cell viability, therefore PMMA-wb and PMMA-mw can be considered biocompatible materials.

8. Conclusions

Nanopigmented PMMA particles were successfully synthesized and cured by a water bath or by microwaves for denture bases. According to results, the particle sizes and the curing process influence the physical properties of the PMMA. The PMMA specimens exhibited good physical and mechanical properties and were noncytotoxic, similar to commercial acrylic resins. These nanopigmented particles will be applied *in vivo* in the denture field in further work.

Conflict of Interests

The authors confirm that they have no conflict of interests regarding the present paper.

Acknowledgments

The authors wish to thank the following individuals for their excellent technical support: Dra. Genoveva Hernández, Dra. Marina Vega, Mtra. Ma. Lourdes Palma Tirado, Q. Carmen Vázquez, Dr. Antonio Gómez Cortés, Miguel A. Arellano Rodríguez, C. D. Rodrigo Hernández-Medina, Daniel Mondragón, Antonio Prado, and L. E. I. Daniel González Espejel.

References

- [1] M. G. Tu, W.-M. Liang, T.-C. Wu, and S.-Y. Chen, "Improving the mechanical properties of fiber-reinforced acrylic denture-base resin," *Materials and Design*, vol. 30, no. 7, pp. 2468–2472, 2009.
- [2] C. Machado, E. Sanchez, S. S. Azer, and J. M. Uribe, "Comparative study of the transverse strength of three denture base materials," *Journal of Dentistry*, vol. 35, no. 12, pp. 930–933, 2007.
- [3] J. S. Moura, W. J. da Silva, T. Pereira, A. A. del Bel Cury, and R. C. M. Rodrigues Garcia, "Influence of acrylic resin polymerization methods and saliva on the adherence of four *Candida* species," *Journal of Prosthetic Dentistry*, vol. 96, no. 3, pp. 205–211, 2006.
- [4] M. J. Azzarri, M. S. Cortizo, and J. L. Alessandrini, "Effect of the curing conditions on the properties of an acrylic denture base resin microwave-polymerised," *Journal of Dentistry*, vol. 31, no. 7, pp. 463–468, 2003.
- [5] L. S. Acosta-Torres, F. H. Barceló-Santana, C. A. Álvarez-Gayosso, and J. Reyes-Gasga, "Synthesis and characterization of poly(methyl methacrylate) polymerized by microwave energy or conventional water bath," *Journal of Applied Polymer Science*, vol. 109, no. 6, pp. 3953–3960, 2008.
- [6] L. S. Acosta-Torres, L. M. López Marín, R. E. Nuñez-Anita, G. Hernández-Padrón, and V. M. Castaño, "Biocompatible metal-oxide nanoparticles: nanotechnology improvement of conventional prosthetic acrylic resin," *Journal of Nanomaterials*, vol. 2011, Article ID 941561, 8 pages, 2011.
- [7] V. Moreno-Maldonado, L. S. Acosta-Torres, F. H. Barceló-Santana, R. D. Vanegas-Lancón, M. E. Plata-Rodríguez, and V. M. Castaño, "Fiber-reinforced nanopigmented poly(methyl methacrylate) as improved denture base," *Journal of Applied Polymer Science*, vol. 126, pp. 289–295, 2012.
- [8] L. S. Acosta-Torres, I. Mendieta, R. E. Nuñez-Anita, M. Cajero-Juárez, and V. M. Castaño-Meneses, "Cytocompatible antifungal acrylic resin containing silver nanoparticles for dentures," *International Journal of Nanomedicine*, vol. 7, pp. 4777–4786, 2012.
- [9] R. W. Walker, L. M. Markillie, A. H. Colotelo et al., "Ultra-violet radiation as disinfection for fish surgical tools," *Animal Biotelemetry*, vol. 1, article 4, pp. 1–11, 2013.
- [10] S. Wei, J. Sampathi, Z. Guo et al., "Nanoporous poly(methyl methacrylate)-quantum dots nanocomposite fibers toward biomedical applications," *Polymer*, vol. 52, no. 25, pp. 5817–5829, 2011.
- [11] V. Di Noto, K. Vezzù, G. A. Giffin, F. Conti, and A. Bertucco, "Effect of high pressure CO₂ on the structure of PMMA: a FT-IR study," *Journal of Physical Chemistry B*, vol. 115, no. 46, pp. 13519–13525, 2011.
- [12] T. L. Tsai, C. C. Lin, G. L. Guo, and T. C. Chu, "Effects of microwave-assisted digestion on decomposition behavior of polymethyl methacrylate (PMMA)," *Materials Chemistry and Physics*, vol. 108, no. 2-3, pp. 382–390, 2008.
- [13] D. Padalia, U. C. Johri, and M. G. H. Zaidi, "Study of cerium doped magnetite (Fe₃O₄:Ce)/PMMA nanocomposites," *Physica B*, vol. 407, no. 5, pp. 838–843, 2012.
- [14] "Dentistry-Denture Base Polymers," ISO 1567, International Organization for Standardization, Geneva, Switzerland, 1999.
- [15] A. Sodagar, M. Z. Kassae, A. Akhavan, N. Javadi, S. Arab, and M. J. Kharazifard, "Effect of silver nano particles on flexural strength of acrylic resins," *Journal of Prosthodontic Research*, vol. 56, pp. 120–124, 2012.
- [16] P. Pfeiffer and E.-U. Rosenbauer, "Residual methyl methacrylate monomer, water sorption, and water solubility of hypoallergenic denture base materials," *Journal of Prosthetic Dentistry*, vol. 92, no. 1, pp. 72–78, 2004.
- [17] ADA-12, "Revised American Dental Association Specification No. 12 for denture base polymers," Reports of Councils and Bureaus/ JADA, 1990.
- [18] C. P. Lai, M.-H. Tsai, M. Chen, H.-S. Chang, and H.-H. Tay, "Morphology and properties of denture acrylic resins cured by microwave energy and conventional water bath," *Dental Materials*, vol. 20, no. 2, pp. 133–141, 2004.
- [19] M. Z. Kassae, A. Akhavan, N. Sheikh, and A. Sodagar, "Antibacterial effects of a new dental acrylic resin containing silver nanoparticles," *Journal of Applied Polymer Science*, vol. 110, no. 3, pp. 1699–1703, 2008.
- [20] C. Messier, F. Epifano, S. Genovese, and D. Grenier, "Inhibition of *Candida albicans* biofilm formation and yeast-hyphal transition by 4-hydroxycordoin," *Phytomedicine*, vol. 18, no. 5, pp. 380–383, 2011.
- [21] L. Zhou, Z. Tong, G. Wu et al., "Parylene coating hinders *Candida albicans* adhesion to silicone elastomers and denture bases resin," *Archives of Oral Biology*, vol. 55, no. 6, pp. 401–409, 2010.
- [22] C. A. Zamperini, A. L. Machado, C. E. Vergani, A. C. Pavarina, E. T. Giampaolo, and N. C. Da Cruz, "Adherence in vitro of *Candida albicans* to plasma treated acrylic resin: effect of plasma parameters, surface roughness and salivary pellicle," *Archives of Oral Biology*, vol. 55, no. 10, pp. 763–770, 2010.
- [23] G. Meriç, J. E. Dahl, and I. E. Ruyter, "Cytotoxicity of silica-glass fiber reinforced composites," *Dental Materials*, vol. 24, no. 9, pp. 1201–1206, 2008.
- [24] M. R. Cimpan, R. Matre, L. I. Cressey et al., "The effect of heat- and auto-polymerized denture base polymers on clonogenicity, apoptosis, and necrosis in fibroblasts: denture base polymers induce apoptosis and necrosis," *Acta Odontologica Scandinavica*, vol. 58, no. 5, pp. 217–228, 2000.
- [25] J. H. Jorge, E. T. Giampaolo, C. E. Vergani, A. L. Machado, A. C. Pavarina, and I. Z. Carlos, "Biocompatibility of denture base acrylic resins evaluated in culture of L929 cells: effect of polymerisation cycle and post-polymerisation treatments," *Gerodontology*, vol. 24, no. 1, pp. 52–57, 2007.

Research Article

A New Method for Fabrication of Nanohydroxyapatite and TCP from the Sea Snail *Cerithium vulgatum*

O. Gunduz,^{1,2} Y. M. Sahin,³ S. Agathopoulos,⁴ B. Ben-Nissan,⁵ and F. N. Oktar^{2,6,7}

¹ Department of Metal Education, Faculty of Technical Education, Marmara University, Kadıköy, 34722 Istanbul, Turkey

² Center for Nanotechnology and Biomaterials Applied & Research, Marmara University, Kadıköy, 34722 Istanbul, Turkey

³ Department of Biomedical Engineering, Faculty of Engineering and Architecture, Istanbul Arel University, Buyukcekmece, 34537 Istanbul, Turkey

⁴ Department of Materials Science and Engineering, University of Ioannina, P.O. Box 1186, 45110 Ioannina, Greece

⁵ Department of Chemistry and Forensic Science, University of Technology Sydney, P.O. Box 123, Broadway, Ultimo, Sydney, NSW 2007, Australia

⁶ Department of Bioengineering, Faculty of Engineering, Marmara University, Kadıköy, 34722 Istanbul, Turkey

⁷ Department of Medical Imaging Techniques, School of Health Related Professions, Marmara University, Tibbiye Street No. 49, Üsküdar, 34688 Istanbul, Turkey

Correspondence should be addressed to O. Gunduz; oguzhan@marmara.edu.tr and F. N. Oktar; foktar@marmara.edu.tr

Received 26 July 2013; Accepted 27 November 2013; Published 2 January 2014

Academic Editor: Il-Kwon Oh

Copyright © 2014 O. Gunduz et al. This is an open access article distributed under the Creative Commons Attribution License, which permits unrestricted use, distribution, and reproduction in any medium, provided the original work is properly cited.

Biphasic bioceramic nanopowders of hydroxyapatite (HA) and β -tricalcium phosphate (TCP) were prepared from shells of the sea snail *Cerithium vulgatum* (Bruguière, 1792) using a novel chemical method. Calcination of the powders produced was carried out at varying temperatures, specifically at 400°C and 800°C, in air for 4 hours. When compared to the conventional hydrothermal transformation method, this chemical method is very simple, economic, due to the fact that it needs inexpensive and safe equipment, because the transformation of the aragonite and calcite of the shells into the calcium phosphate phases takes place at 80°C under the atmospheric pressure. The powders produced were determined using infrared spectroscopy (FT-IR), X-ray diffraction, and scanning electron microscopy (SEM). The features of the powders produced along with the fact of their biological origin qualify these powders for further consideration and experimentation to fabricate nanoceramic biomaterials.

1. Introduction

To date, biomaterials is a rapidly developing interdisciplinary field at the interface of engineering, science, and healthcare industry; its effect on human health related issues is also obvious and recognized all over the world. The global biomaterials device market was estimated as \$115.4 billion in 2008 and is expected to increase to \$252.7 billion in 2014. The largest market share among all biomaterial products belongs to orthopedic biomaterials [1], like hydroxyapatite (HA) materials. With a chemical formula of $\text{Ca}_{10}(\text{PO}_4)_6(\text{OH})_2$, HA is the main inorganic component of bone [2] and tooth [3]. Thus, HA is very popular for implant materials

especially in orthopedic bone surgery [2] and other hard tissue implantations [3], such as in dental and aesthetic surgery.

Powders of HA can be produced with very various chemical techniques, such as precipitation, hydrothermal techniques, hydrolysis of other calcium phosphates, and sol-gel [4] from very pure chemicals or from natural materials. Calcination is another method to fabricate HA from different natural sources, like bone (i.e., human [5], bovine [6], sheep [7], turkey, and chicken) or tooth dentine [8] and enamel [9–11]. In previous work, there are also papers reporting some very interesting sources for HA production, such as crocodile bone [12], deer antler [13], and fish wastes.



FIGURE 1: Typical photos of shells of *Cerithium vulgatum* Bruguère, 1792, Mediterranean [30].



FIGURE 2: Habitation areas for *Cerithium vulgatum* [31].

Hydrothermal methods are very popular to transform various sources with a sea origin, such as cuttlefish bone [14], some oysters [15], and corals [16]. In our more recent studies, we have presented some very simple mechanochemical methods, which can be conducted with a simple hot-plate stirrer and with ultrasonic equipment [17, 18]. Various aragonitic structures, such as cuttlefish bone [19], sea [20] and land snail shells [21], sea urchin shells [17, 18, 20], various mussel shells [19, 22–24], pearl powder [25], corals [16], and calcite from egg shells [26], were successfully transformed into various Ca-phosphate bioceramic powders using these novel mechanochemical methods.

In this work, a novel and simple chemical method was utilised to fabricate nanobiphasic powders of HA and TCP from the shells of a local sea snail, *Cerithium vulgatum* Bruguère, 1792 [27]. The *Cerithium vulgatum* is a species of sea snail, which is a marine gastropod mollusk and also belongs to the family Cerithiidae [28]. Generally the *Cerithium vulgatum* shells are occupied by hermit crabs [29]. The typical shape of these shells is revealed in Figure 1 [30].

2. Materials and Experimental Procedure

Generally, the habitation areas for *Cerithium vulgatum* are all coastal areas of the United Kingdom, Spain, Portugal, Greece, and West of Turkey (Figure 2, [31]). These species can be obtained from the Black Sea in Turkey [32]. Thus, it is not surprising to come across with the empty shells of the sea snail *Cerithium vulgatum* Bruguère by the Marmara Sea, in Turkey, and specifically by the beaches of Princes Islands. However, the collection of the *Cerithium vulgatum* shells is generally difficult by the beaches of Istanbul since their number are quite small and are negligible in comparison to those of other collected shells. The other shells mainly

belong to the species *Nassarius hinniea reticulatus* (this species is overnumbered in these beaches). However, the shells of *Cerithium vulgatum* are easily recognized and separated from the shells of *Nassarius hinniea reticulatus* because the latter ones are much smaller in length and diameter than the former ones and have a brownish color.

Empty shells of a local sea snail (*Cerithium vulgatum* Bruguère, 1792) were taken from a local beach in Princes Islands, Heybeli Island (local beach name; German Beach) in Istanbul, Turkey. No living creatures were used in this study at all. The empty shells were cleaned thoroughly from sand particles and other foreign materials. Then, the shells were dried and crushed into small particles and finally planetary-milled in a porcelain jar. The milled powder was sieved using a 100 μm sieve (i.e., the particle size was $<100 \mu\text{m}$).

A small sample of the fine powder was analyzed using differential thermal and gravimetric analysis (DTA/TGA) to determine the exact CaCO_3 content. Batches of 2 g of powder were suspended in an aqueous solution of distilled water in a conical flask. Then, according to a previous study [33], solution of H_3PO_4 was added in such an amount as to satisfy the stoichiometric molar ratio of Ca/P equal to 1.667 (that corresponds to HA; this sample is hereafter designated as A) or 1.5 (that corresponds to TCP; this sample is hereafter designated as B). Hot-plate stirrer equipment was used with a conical flask in this work. The temperature of the solution was set at 80°C and the reaction took place for 8 h under continuous stirring. After that, the powders were removed from the liquid by filtration and dried at 100°C overnight in an incubator. The dried powders were calcined using an electric furnace (Nabertherm HT 16/17, Lilienthal, Germany) for 4 h in air. The powders of the sample A (i.e., $\text{Ca/P} = 1.667$) and the powders of the sample B (i.e., $\text{Ca/P} = 1.5$) were calcined at 800°C and 400°C , respectively.

To characterize the materials, in either the raw form or the final powders, the following equipment was used. The thermal analysis was determined using DSC-DTA-TG equipment (TA SDT Q600 Protherm). The observation of the microstructure of the samples was observed in a scanning electron microscope (SEM, JEOL JSM 7000F Field Emission Scanning Electron Microscope, equipped with a Hitachi 1000 Tabletop microscope). The crystalline phases developed in the calcined powders were used by X-ray diffraction analysis (Bruker D8 Advance X-ray diffractometer). The Fourier transform infrared (FT-IR) spectra of the produced powders were analyzed in a Bruker ALPHA FT-IR spectrometer.

3. Results and Discussion

The typical microstructure at a fracture surface of the shells is revealed in the low-magnification SEM image of Figure 3. A plate-like structure can be attributed largely to aragonite crystals. The direction of the plates is perpendicular to the outer (upper part in the image) and the inner surfaces of the shell. The outer surface apparently has a less dense structure. Calcite is expected to be concentrated in the outer layer of the shell. The inner layer (lower part in the image) has apparently a denser structure. Usually, the inner part of the

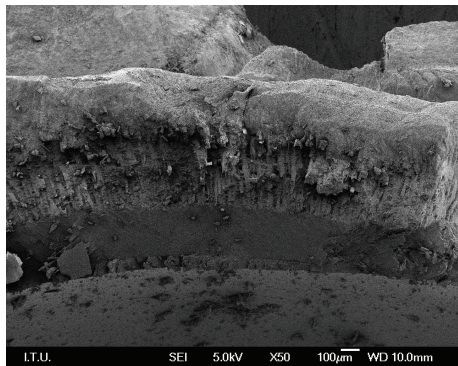


FIGURE 3: Microstructure at fracture surface of *Cerithium vulgatum* shell.

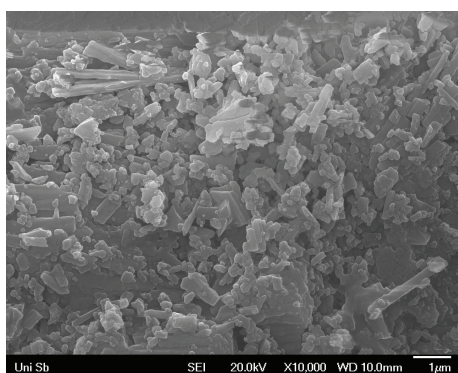


FIGURE 4: SEM image of raw powder after planetary milling and sieving with a sieve of $100\ \mu\text{m}$.

shells is largely made of aragonite. Therefore, the raw powder that was subjected afterwards to transformation into calcium phosphates should involve both the phases of aragonite and calcite, which is observed in all regular shells. But the influence of aragonite-calcite sea conditions on the evolution of biocalcification remained up to now poorly understood [34].

The nanoparticles were spontaneously fabricated after crushing, milling, and sieving, as shown in the SEM image of Figure 4. The powder mainly consisted of prismatic particles with a semirounded shape and nanosize dimensions of about 200 nm. Some elongated rod-like prismatic particles with a length of ca $1\text{--}1.5\ \mu\text{m}$ and a width of ca 200 nm are also observed.

The results of the differential and gravimetric thermal analysis (DTA/TGA) of the raw powders after milling and sieving are plotted in the diagrams of Figure 5. The decomposition of CaCO_3 to CaO was clearly obtained in both curves. These curves confirm that the shell was exclusively consisted of CaCO_3 . Thus, the calculation of the amount of H_3PO_3 solution required to satisfy the demanded Ca/P ratios was possible.

The X-ray analysis of the powders produced after calcination for 4 h in air is shown in the diffractograms of Figure 6(a), for the powder B (Ca/P = 1.5, 400°C), and Figure 6(b), for the powder A (Ca/P = 1.667, 800°C). From

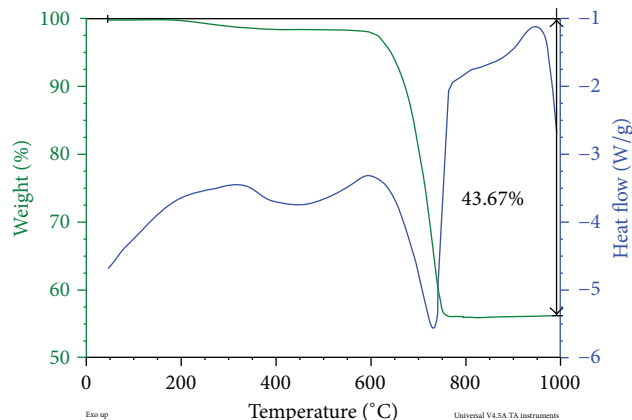


FIGURE 5: Differential and gravimetric thermal analysis (DTA/TGA) of the raw powders (after planetary milling and sieving).

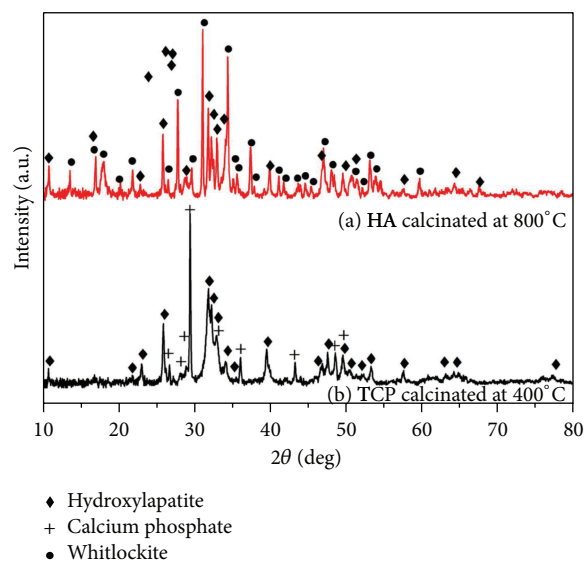


FIGURE 6: X-ray diffractograms of the produced powders after calcination for 4 h in air: (a) powder B (Ca/P = 1.5, 400°C); (b) powder A (Ca/P = 1.667, 800°C).

these diffractograms it is concluded that the transformation of CaCO_3 , in the form of either aragonite or calcite, was completely indicated. In both diffractograms, the phase of HA was clearly observed (JCPDS card 00-009-0432 in sample B and JCPDS card 01-089-4405 in sample A; the differences between the two cards are negligible). The second major phase recorded was TCP ($3\text{CaO}\cdot\text{P}_2\text{O}_5$) in particular β -TCP in the sample B (JCPDS card 00-009-0346) and whitlockite (JCPDS card 00-009-0169) in the sample A. Whitlockite is also known as β -tricalcium phosphate (β -TCP) [35], which is used in treatment of defects of cortical and cancellous bone due to its osteoconductivity and bioresorbability [36].

The findings of the X-ray analysis indicate that the powders produced are biphasic materials, which comprise HA and TCP. It is well known that the best bioceramic materials

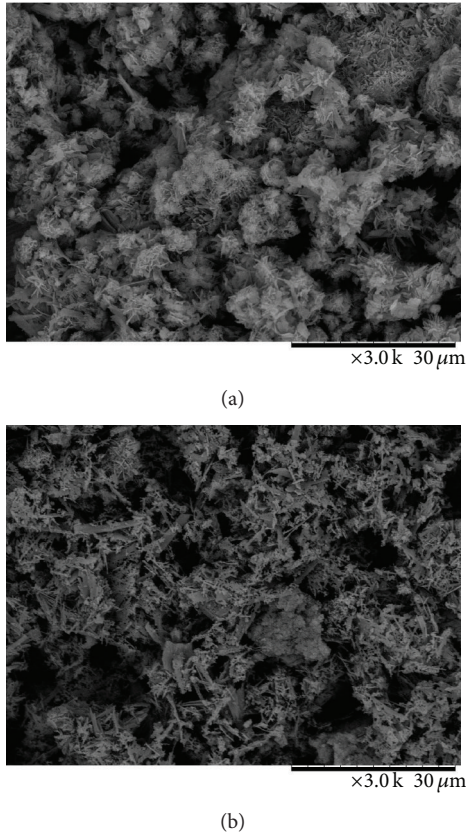
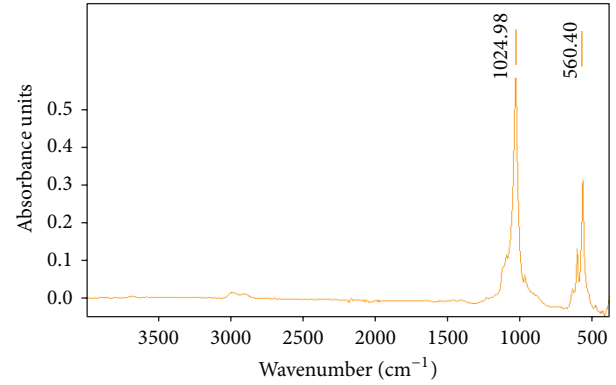


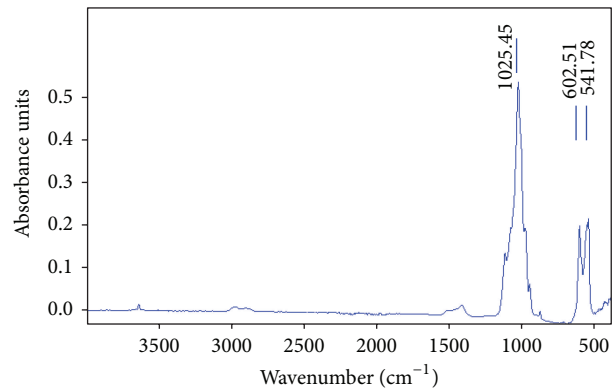
FIGURE 7: Microstructure of the produced powders after calcination for 4 h in air: (a) powder B (Ca/P = 1.5, 400°C); (b) powder A (Ca/P = 1.667, 800°C).

should ideally consist of biphasic materials of HA and β -TCP. In such biphasic biomaterials, β -TCP is the resorbable and osteoconductive [37] component. Usually, resorbable bioceramics are considered as very active and thus they stimulate a faster formation of the newly formed bone. On the other hand, HA presents an excellent biocompatibility and bioactivity.

All the results indicate that the produced powders are very promising materials. However, these good prospects, due to the biphasic crystalline regime of the produced powders, are further enforced because the SEM analysis showed that this production process resulted in the production of nanopowders as well. The characteristic microstructure of the powders produced after calcination for 4 h in air is shown in the SEM images of Figure 7(a), for the powder B (Ca/P = 1.5, 400°C), and Figure 7(b), for the powder A (Ca/P = 1.667, 800°C). The powder B comprises prismatic nanoparticles as well as needle-like nanorods with length of 1.5–3 μ m and diameter of 200 nm. The SEM image of Figure 7(b) for the sample A indicates that this powder is apparently finer than the powder B because there are less prismatic particles; the rod-like (needle-shaped) particles are thinner (with a diameter of ca 150 nm), and formation of apparently loosened agglomerations of nanoparticles was also observed, as revealed in the middle of Figure 7(b).



(a)



(b)

FIGURE 8: FT-IR spectra of the produced powders after calcination for 4 h in air: (a) powder B (Ca/P = 1.5, 400°C); (b) powder A (Ca/P = 1.667, 800°C).

FT-IR spectra of the HA powders in the range 4000–400 cm^{-1} are revealed in Figure 8 for powder B (Ca/P = 1.5, 400°C, Figure 8(a)) and powder A (Ca/P = 1.667, 800°C, Figure 8(b)), after calcination for 4 h in air. They revealed strong vibrations modes at the following wave numbers: 541, 560, 602, 1024, and 1025 cm^{-1} . Absorption bands characteristic of O–P–O bending vibrations can be clearly seen at 541 and 602 cm^{-1} . The powders appear to lack the O–H vibrational bands indicated by the weak peak at 630 cm^{-1} (Figure 8(a)) [38]. The sharp bands at 1024–1025 cm^{-1} correspond to ν_3 asymmetric stretching modes of $(\text{PO}_4)^{3-}$ groups. Moreover, the increase of the calcination temperature to 800°C caused the appearance of the peaks at 1500 and 3700–3500 cm^{-1} . The addition, IR bands in the range of 3700–3500 cm^{-1} (Figure 8(b)) were also observed by Duta et al. [39], which was assigned them to the O–H stretching vibrations of surface P–OH groups. These spectra are in agreement with the XRD results.

4. Conclusions

Using a simple mechanochemical method, biphasic bioceramic nanopowders of hydroxyapatite (HA) and tricalcium phosphate (TCP) were fabricated. It has been indicated that

these nanopowders can be used as bioceramic for graft material. The shell of a regular sea snail from the species *Cerithium vulgatum* was successfully transformed into the target compounds. This new method is very simple, economic, and safe.

Conflict of Interests

The authors declare that there is no conflict of interests regarding the publication of this article.

Acknowledgments

This study was carried out partly with the equipment furnished (between 2007 and 2008) to Marmara University with the support of the Turkish Republic Government Planning Organization in the framework of the Project 2003K120810 “Manufacturing and Characterization of Electro-Conductive Bioceramics.” The authors also acknowledge the very valuable support of the Metallurgical and Materials Engineering Department, Istanbul Technical University, Turkey.

References

- [1] D. Lahiri, S. Ghosh, and A. Agarwal, “Carbon nanotube reinforced hydroxyapatite composite for orthopedic application: a review,” *Materials Science and Engineering C*, vol. 32, no. 7, pp. 1727–1758, 2012.
- [2] M. R. Foroughi, S. Karbasi, and R. Ebrahimi-Kahrizsangi, “Physical and mechanical properties of a poly-3-hydroxybutyrate-coated nanocrystalline hydroxyapatite scaffold for bone tissue engineering,” *Journal of Porous Materials*, vol. 19, no. 5, pp. 667–675, 2012.
- [3] F. N. Oktar, M. R. Demirer, O. Gunduz et al., “Sintering effect on mechanical properties of composites of bovine hydroxyapatite (BHA) and Li_2O ,” *Key Engineering Materials*, vol. 309–311, pp. 49–52, 2006.
- [4] S. J. Roll, *Processing of hydroxyapatite by biomimetic process, a thesis submitted in partial fulfillment of the requirement for the degree of bachelor of technology [M.S. thesis]*, Department of Ceramic Engineering, National Institute of Technology Rourkela, Odisha, India, 2006–2010.
- [5] G. Goller, F. N. Oktar, L. S. Ozyegin, E. S. Kayali, and E. Demirkesen, “Plasma-sprayed human bone-derived hydroxyapatite coatings: effective and reliable,” *Materials Letters*, vol. 58, no. 21, pp. 2599–2604, 2004.
- [6] L. S. Ozyegin, F. N. Oktar, G. Goller, E. S. Kayali, and T. Yazici, “Plasma-sprayed bovine hydroxyapatite coatings,” *Materials Letters*, vol. 58, no. 21, pp. 2605–2609, 2004.
- [7] N. Demirkol, F. N. Oktar, and E. S. Kayali, “Mechanical and microstructural properties of sheep hydroxyapatite (SHA)-niobium oxide composites,” *Acta Physica Polonica A*, vol. 121, no. 1, pp. 274–276, 2012.
- [8] G. Goller and F. N. Oktar, “Sintering effects on mechanical properties of biologically derived dentine hydroxyapatite,” *Materials Letters*, vol. 56, no. 3, pp. 142–147, 2002.
- [9] F. N. Oktar, “Microstructure and mechanical properties of sintered enamel hydroxyapatite,” *Ceramics International*, vol. 33, no. 7, pp. 1309–1314, 2007.
- [10] N. Akyurt, U. Karacayli, M. Yetmez, S. S. Pazarlioglu, and F. N. Oktar, “Microstructure and mechanical properties of sintered sheep enamel-derived hydroxyapatite,” *International Journal of Artificial Organs*, vol. 34, no. 8, p. 700, 2011.
- [11] N. Demirkol, M. Yetmez, U. Karacayli et al., “Mechanical properties of hydroxyapatite-tantalum composites,” *International Journal of Artificial Organs*, vol. 33, p. 468, 2010, (XXXVII Annual ESAO Congress) Skopje, R. Macedonia from 8th to 11th September 2010.
- [12] K. Lewis, U. Boonyang, L. Evans, S. Siripaisarnpipat, and B. Ben-Nissan, “A comparative study of Thai and Australian crocodile bone for use as a potential biomaterial,” *Key Engineering Materials*, vol. 309–311, pp. 15–18, 2006.
- [13] M. Băciuş, G. Băciuş, V. Simon et al., “Investigation of deer antler as a potential bone regenerating biomaterial,” *Journal of Optoelectronics and Advanced Materials*, vol. 9, no. 8, pp. 2547–2550, 2007.
- [14] J. H. G. Rocha, A. F. Lemos, S. Agathopoulos et al., “Scaffolds for bone restoration from cuttlefish,” *Bone*, vol. 37, no. 6, pp. 850–857, 2005.
- [15] A. F. Lemos, J. H. G. Rocha, S. S. F. Quaresma et al., “Hydroxyapatite nano-powders produced hydrothermally from nacreous material,” *Journal of the European Ceramic Society*, vol. 26, no. 16, pp. 3639–3646, 2006.
- [16] B. B. Nissan, A. S. Milev, D. D. Green et al., “Processes for treating coral and coating an object,” US patent no. 2004/0091547 A1, 2004.
- [17] D. Agaogulları, D. Kel, H. Gokce et al., “Bioceramic production from sea urchins,” *Acta Physica Polonica A*, vol. 121, no. 1, pp. 23–26, 2012.
- [18] R. Samur, L. S. Ozyegin, and D. Agaogullari, “Calcium phosphate formation from sea urchin (*brissus Latecarinatus*) via modified mechano-chemical (ultrasonic) conversion method,” *Metallurgija*, vol. 52, pp. 375–378, 2013.
- [19] A. U. Tuyel, E. T. Oner, S. Ozyegin, and F. N. Oktar, “Production and characterization of bioceramic nanopowders of natural-biological origin,” *Journal of Biotechnology*, vol. 131S, p. S-65, 2007.
- [20] M. L. Tamasan, L. S. Ozyegin, F. N. Oktar, and V. Simon, “Characterization of calcium phosphate powders originating from *Phyllacanthus imperialis* and *Trochidae Infundibulum concavus* marine shells,” *Materials Science and Engineering C*, vol. 33, no. 5, pp. 2569–2577, 2013.
- [21] D. Kel, H. Gökçe, D. Bilgiç et al., “Production of natural bioceramic from land snails,” *Key Engineering Materials*, vol. 493–494, pp. 287–292, 2012.
- [22] I. J. Macha, L. S. Ozyegin, J. Chou, R. Samur, F. N. Oktar, and B. Ben-Nissan, “An alternative synthesis method for di calcium phosphate (Monetite) powders from mediterranean mussel (*Mytilus galloprovincialis*) shells,” *Journal of the Australian Ceramic Society*, vol. 49, pp. 122–128, 2013.
- [23] S. Agathopoulos, L. S. Ozyegin, Z. Ahmad et al., “Nanobioceramics production from razor shell,” *Key Engineering Materials*, vol. 493–494, pp. 775–780, 2012.
- [24] F. N. Oktar, U. Tuyel, N. Demirkol et al., “A new safe method to produce bioceramic nano-powders from nacre *verrucosa*,” *International Journal of Artificial Organs*, vol. 33, pp. 467–468, 2010, (XXXVII Annual ESAO Congress) Skopje, R. Macedonia from 8th to 11th September 2010.
- [25] A. U. Tuyel, *Production and characterization of bioceramic nanopowders of natural-biological origin [M.S. thesis]*, Institute

- for Graduate Studies in Pure and Applied Sciences, T.C. Marmara University, 2008.
- [26] D. Kel, U. Karacayli, M. Yetmez, L. S. Ozyegin, E. S. Kayali, and F. N. Oktar, "Hydroxyapatite production with various techniques from sea urchin," *International Journal of Artificial Organs*, vol. 34, p. 700, 2011.
- [27] April 2013, <http://www.marinespecies.org/aphia.php?p=taxdetails&id=139066>.
- [28] April 2012, http://en.wikipedia.org/wiki/Cerithium_vulgatum.
- [29] A. S. Ates, T. Katagan, and A. Kocataş, "Gastropod shell species occupied by hermit crabs (Anomura: Decapoda) along the Turkish coast of the Aegean Sea," *Journal of Zoology*, vol. 31, pp. 13–18, 2007.
- [30] April 2013, http://www.idscaro.net/sci/01_coll/plates/gastro/pl_cerithiidae.1.htm.
- [31] April 2012, <http://www.eu-nomen.eu/portal/taxon.php?GUID=urn:lsid:marinespecies.org:taxname:139066>.
- [32] V. I. Zdun and S. M. Ignat'ev, "Black Sea mollusc, *Cerithium vulgatum* (Gastropoda, Cerithiidae), a new intermediate trematode host," *Parazitologiya*, vol. 14, no. 4, pp. 345–348, 1980.
- [33] L. S. Ozyegin, F. Sima, C. Ristoscu et al., "Sea snail: an alternative source for nano-bioceramic production," *Key Engineering Materials*, vol. 493–494, pp. 781–786, 2012.
- [34] U. Balthasar and M. Cusack, "Aragonite-Calcite seas and evolution of biocalcification," in *Proceedings of the 22nd V.M. Goldschmidt Conference, Earth in Evaluation*, Montreal, Canada, 2012.
- [35] J. J. Song, *An in vitro investigation of the spatial control involved in collagen mineralization [M.S. thesis]*, University of Toronto, 2010.
- [36] S. Sai and K. Fujii, "β-tricalcium phosphate as a bone graft substitut," *Jikeikai Medical Journal*, vol. 52, pp. 47–54, 2005.
- [37] P. Hernigou, X. Roussignol, C. H. Flouzat-Lachaniette, P. Filippini, I. Guissou, and A. Poignard, "Opening wedge tibial osteotomy for large varus deformity with Ceraver TM resorbable beta tricalcium phosphate wedges," *International Orthopaedics*, vol. 34, no. 2, pp. 191–199, 2010.
- [38] A. R. Boyd, B. J. Meenan, and N. S. Leyland, "Surface characterisation of the evolving nature of radio frequency (RF) magnetron sputter deposited calcium phosphate thin films after exposure to physiological solution," *Surface and Coatings Technology*, vol. 200, no. 20–21, pp. 6002–6013, 2006.
- [39] L. Duta, F. N. Oktar, G. E. Stan et al., "Novel doped hydroxyapatite thin films obtained by pulsed laser deposition," *Applied Surface Science*, vol. 265, pp. 41–49, 2013.

Research Article

Cationic Gelatin Nanoparticles for Drug Delivery to the Ocular Surface: *In Vitro* and *In Vivo* Evaluation

Ching-Li Tseng,¹ Ko-Hua Chen,^{2,3,4} Wen-Yu Su,^{2,5,6} Yen-Hsien Lee,^{2,7}
Chi-Chang Wu,¹ and Fen-Huei Lin^{2,5}

¹ Graduate Institute of Biomedical Materials and Tissue Engineering, College of Oral Medicine, Taipei Medical University, No. 250, Wu-Hsing Street, Taipei City 110, Taiwan

² Division of Medical Engineering Research, National Health Research Institutes, No. 35, Keyan Road, Zhunan Town, Miaoli County 350, Taiwan

³ Department of Ophthalmology, Taipei Veterans General Hospital, No. 201, Section 2, Shipai Road, Beitou District, Taipei City 112, Taiwan

⁴ National Yang-Ming University, No. 155, Section 2, Linong Street, Taipei City 112, Taiwan

⁵ Institute of Biomedical Engineering, National Taiwan University, No. 1, Section 1, Ren-ai Road, Taipei City 100, Taiwan

⁶ Institute of Biomedical Engineering and Material Science, Central Taiwan University of Science and Technology, No. 666, Buzih Road, Taichung City 406, Taiwan

⁷ Graduate Institute of Medical Science, College of Medicine, Taipei Medical University, No. 250, Wu-Hsing Street, Taipei City 110, Taiwan

Correspondence should be addressed to Fen-Huei Lin; double@ntu.edu.tw

Received 2 August 2013; Revised 12 November 2013; Accepted 25 November 2013

Academic Editor: Anchal Srivastava

Copyright © 2013 Ching-Li Tseng et al. This is an open access article distributed under the Creative Commons Attribution License, which permits unrestricted use, distribution, and reproduction in any medium, provided the original work is properly cited.

To develop an effective ocular drug delivery carrier, we prepared two different charged gelatin nanoparticles (GPs) and evaluated particle size, surface charge, and morphology. The *in vitro* biocompatibility of GPs was assessed using human corneal epithelium (HCE) cells and *in vivo* safety by administering them as eye drops to New Zealand rabbits. The GPs prepared using type A gelatin were positively charged (GP(+), +33 mV; size, 180.6 ± 45.7 nm). Water-soluble tetrazolium salt (WST)-1 assay showed that both GPs were nontoxic to HCE cells. The fluorescence intensity of HCE cells cultured with cationic GPs conjugated with a fluorescent dye was higher than that of the anionic GP-treated HCE cells. *In vivo* examination showed no serious irritation to the rabbit eyes. Furthermore, corneal thickness and ocular pressure in the eyes of the treated rabbits were similar to those in the eyes of normal rabbits. Microscopic examination of corneal cryosections showed widely distributed fluorescent nanocarriers, from the anterior to the posterior part of the cornea of the GP(+) group, and higher fluorescence intensity in the GP(+) group was also observed. In conclusion, GPs as cationic colloidal carriers were efficiently adsorbed on the negatively charged cornea without irritating the eyes of the rabbits and can be retained in the cornea for a longer time. Thus, GPs(+) have a great potential as vehicles for ocular drug delivery.

1. Introduction

The eye poses unique challenges for drug delivery. The main objective of ocular therapeutics is to provide and maintain adequate concentration of the drug at the target site. Most ocular diseases are treated with topical application of solutions administered as eye drops. The major disadvantages of this dosage form include (i) poor ocular drug bioavailability because of the anatomical and physiological constraints of

the eye that limit drug retention, (ii) pulse-drug entry with high variation in dose, (iii) nasolacrimal duct drainage, which causes systemic exposure, and (iv) poor entrance to the posterior segments of the eye because of the lens-iris diaphragm [1, 2]. The above disadvantages result in clearance of 90% of the eye drops within 2 min, and only 5% of the administered dose permeates to the eye [3].

Most efforts in ocular delivery have been focused on increasing the corneal retention of drugs with the final goal

of improving the efficacy of treatments for different ocular diseases. These attempts include the use of colloidal drug delivery systems such as liposomes [4], nanoparticles [5–8], and nanospheres [9]. The results of different studies showed the potential of nanoparticles for either gene or drug delivery for ophthalmic application. Nanoparticles are able to encapsulate and protect the gene/drug against degradation, improve tolerance, and increase corneal uptake and intraocular half-lives [10]. Gelatin nanoparticles (GPs) were selected for topical delivery because of their unique properties such as biocompatibility and biodegradability [11]. Moreover, the source of gelatin, collagen, which is the major constituent of the corneal stroma, has been used for ophthalmic applications [12].

Although several studies have examined the use of GPs for gene/drug delivery [13–16], few studies have examined the use of GPs for ocular delivery. Vandervoort examined GPs encapsulated pilocarpine or hydrocortisone for topical ophthalmic delivery [17]. Vandervoort characterized the different forms of GPs and reported the rates of drug release from these GPs, but they did not perform *in vitro* or *in vivo* tests. *In vivo* administration of GPs loaded with plasmid DNA showed significantly higher expression of MUC5AC in the conjunctiva than that in untreated controls, and naked plasmid DNA encapsulated in GPs was beneficial for ophthalmic gene delivery [18]. These results show that GPs may be effectively used as vehicles for topical administration to the eyes.

The cornea and conjunctiva possess negative surface charges, and it is expected that cationic colloidal nanoparticles may penetrate through the negatively charged ocular tissues more efficiently than anionic carriers [19]. To determine the importance of these characteristics in the interaction of nanoparticles with the cornea, we prepared GPs with a positive and negative charge for ocular delivery. The GPs with different charge were selected for ocular drug delivery. We examined the particle size, polydispersity index (PDI), shape, and surface charge and cytotoxicity of the GPs. Fluorescently labeled GPs were used in *in vitro* and *in vivo* experiments to observe the distribution of the particles in the eyes of rabbits. In addition, the central corneal thicknesses and intraocular pressure (IOP) of rabbits were also examined to confirm the influence of nanoparticles in rabbit eyes.

2. Materials and Methods

2.1. Reagent and Chemicals. Gelatin type A (derived from porcine skin, bloom 175), gelatin type B (derived from bovine skin, bloom 225), 25% glutaraldehyde (GA) solution, and acetone were purchased from Sigma-Aldrich (MO, USA). Dulbecco's modified Eagle's medium (DMEM)/F12 (1:1), fetal bovine serum (FBS), insulin, trypsin-EDTA, penicillin/streptomycin, and phosphate-buffered saline (PBS) were obtained from Gibco/BRL (MD, USA); epithelial growth factor (EGF) was acquired from Pepro Tech (Rocky Hill, NJ, USA). Tetramethyl rhodamine succinyl (TAMRA-NHS) ester and rabbit anti-zona occludens (ZO-1) polyclonal antibody were obtained from Invitrogen (CA, USA). The Quick Cell

Proliferation Assay Kit II was got from BioVision (CA, USA). A Live/Dead Kit was purchased from Molecular Probes (OR, USA). Single-well cell inserts (PET) were obtained from Millipore (MO, USA). All other chemicals were of reagent grade and obtained from Sigma-Aldrich.

2.2. Preparation of GPs. The GPs were prepared by a two-step desolvation method as described previously with some modifications [20, 21]. Type A and type B gelatin solution (5 wt%) initially underwent desolvation by addition of excess quantity of acetone. Then, the gelatin deposited was redissolved in water. The pH of the type A gelatin solution was adjusted to 2.5 and that of type B was adjusted to 11. Acetone was added in a dropwise manner to form nanoparticles. At the end of the process, 250 μ L of 8% GA solution was used as a crosslinking agent for preparing nanoparticles, and the solution was stirred for 12 h at 1000 rpm. The remaining organic solvent was evaporated using a rotary evaporator (EYELA, Tokyo, Japan), and the resultant nanoparticles were stored at 4°C for further examination.

2.3. Characterization and Measurement of Different Parameters of the GPs. The size and zeta potential of the GPs were analyzed using photon correlation spectroscopy (PCS) and laser Doppler anemometry, respectively, using a Zetasizer, 3000 HS (Malvern Instruments, UK). Each batch was analyzed in triplicate. The morphology of the nanoparticles was obtained by scanning the dried particles deposited on a flat surface with a cantilever probe model AC240 (Olympus, USA) using tapping mode in an atomic force microscope (AFM; Asylum Research, MFP-3DTM, USA).

2.4. Human Corneal Epithelial Cells Culture. The SV40-immortalized human corneal epithelial (HCE) cell line was kindly gifted by Dr. Ko-Hua Chen (Taipei Veterans General Hospital, Taiwan). The HCE cells were cultured in DMEM/F-12 supplemented with 5% FBS, 100 U/mL penicillin, 0.1 mg/mL streptomycin, 10 ng/mL EGF, 0.5% DMSO, and 5 μ g/mL insulin. The cells were cultured at 37°C in a 5% CO₂-95% air atmosphere. Media were changed every other day, and the cells were observed daily under a phase contrast microscope.

2.4.1. Evaluation of Cytotoxicity of GPs. The cytotoxicity of the GPs was examined in the HCE cells using the Quick Cell Proliferation Assay Kit II (BioVision). The cells were seeded onto 96-well plates (5 \times 10³ cells/well) about 16 h before the experiment. The HCE cells were incubated with different concentrations of the GPs (500 to 0.1 μ g/mL) for 2 h. Then, the culture medium was discarded, and 0.2 mL water-soluble tetrazolium-8 (WST-8) working solution was added to each well. WST-8 is reduced by dehydrogenases in the living cells to produce a yellow colored product (formazan). After incubation for 4 h, 100 μ L of the working solution was quantitatively assessed using a SpectraMAXM5 spectrophotometer (Molecular Devices, CA, USA) at a wavelength of 450 nm. The reference wavelength was set at 650 nm. The cells were stained with a live/dead stain (Molecular Probe) to observe

cell viability. The live cells emit green fluorescence, and the dead cells emit red fluorescence. Images were acquired using an inverted fluorescence microscope (Nikon, TiS, Japan) and were analyzed using Nikon NIS Element software.

2.4.2. Evaluation of Transepithelial Electrical Resistance. About 3×10^5 HCE cells/cm² were seeded on PET inserts with a 0.4- μ m pore size (Millipore, MA, USA), and the medium was replenished every other day. Resistance across the insert membrane was measured using the STX2 electrode set (World Precision Instruments [WPI], Florida, USA). The transepithelial electrical resistance (TEER) of cells grown on filters was measured with an epithelial voltohmmeter (EVOM, WPI). Cells were used only if their TEER was more than 100 V/cm². The suspension of GPs (100 μ g/mL) was added into the media of the insert well. The electrode set was inserted in both the chambers for the indicated times. The TEER was calculated from the measured resistance and normalized using the area of the monolayer (ohms per square centimeter). The background TEER of blank insert filters was subtracted from the TEER of the cell monolayers. Chitosan nanoparticles (CNP) were used as the positive control because of their capacity to disrupt the tight intercellular junctions [22]. The size of the CNP was about 180 nm and their zeta potential showed a positive charge (20 mV).

2.4.3. Western Blotting. The HCE cells were lysed to extract the cellular protein, and their absorbance was measured at OD 260/280 nm before use. Equal amounts of protein (approximately 10 μ g) were separated using 6% sodium dodecyl sulfate polyacrylamide gel electrophoresis. Then, the proteins were transferred onto nitrocellulose membrane, and the membranes were blocked in 5% nonfat powdered milk in Tris-buffered saline (TBS) and 0.05% Tween. The membranes were incubated with the primary antibody (ZO-1 at 1:3000 overnight at 4°C) followed by incubation with the appropriate secondary antibodies (horseradish peroxidase [HRP]-conjugated anti-rabbit antibody at 1:10,000 for 1 h at room temperature). α -Tubulin was used as the internal control. Bands were visualized using an enhanced chemiluminescence reagent and exposed to a Fujifilm LAS1000 Intelligent Dark Box and captured digitally.

2.4.4. Cellular Uptake Study. GPs with positive or negative charge were labeled with red fluorescence via being conjugated with TAMRA-NHS ester (Invitrogen) according to the method described by the manufacturer. The concentration of the fluorescent dye (TAMRA) in the GPs (100 μ g/mL) was 0.35 μ g/mL. In addition, we examined the culture medium with the dye concentration equal to that in the aqueous formulation. The fluorescent GPs (100 μ g/mL) were cultured with HCE cells for 2 h; subsequently, the medium was removed, and the cells were washed twice using PBS. Subsequently, 0.2 mL of cell lysis solution (50 mM Tris-HCl, pH 7.6, 300 mM NaCl, and 0.5% Triton X-100) was added to the cell pellets, and they were maintained for 2.5 h on ice with frequent vortexing. Then, the cells lysate was collected into Eppendorf tubes and centrifuged at 12,500 rpm for 20 min.

The cell suspension (100 μ L) was added to a 96-well plate and the OD was measured at an excitation wavelength of 546 nm and an emission wavelength of 576 nm by the microplate spectrophotometer (SpectraMAXM5) under fluorescence mode.

2.5. Preliminary Animal Study. Male New Zealand rabbits weighing 2.5–3.5 kg and with no signs of ocular inflammatory or gross abnormalities were used. The *in vivo* experimental protocol was approved by the Institutional Animal Care and Use Committee of the Taipei Medical University (IACUC Approval No. LAC-100-0165). The animals were housed in standard cages in a light-controlled room and were given food and water *ad libitum*. We used 9 rabbits for measurement at each time point, and during the experiments, the rabbits were allowed to move their heads freely, and their eye movements were not restricted.

2.5.1. In Vivo Tolerance. Positively charged GPs conjugated with the fluorescent dye (GP [+] TAMRA) were used in this study. We administered 50 μ L of sterilized GP(+) TAMRA in the lower conjunctival sac of the right eye of rabbits. The rabbits simultaneously received 50 μ L of TAMRA in PBS in their left eye. The same volume of PBS was administered to another group of rabbits as control. This irritation test was performed using a clinical evaluation scale of 0 (absence) to 3 (highest) of discomfort, discharge, cornea/conjunctival chemosis, or redness as described in Table 2 using a modification of the scoring system established in the 2002 Organization for Economic Cooperation and Development guidelines for ocular irritation testing [4, 23]. The test was performed on 5 eyes of each group; the test was performed in 3 eyes in the PBS-treated (control) group. Each animal was observed and tested at 0.5, 2, 4, and 16 h after instillation.

2.5.2. Clinical Observations. At each study point, we measured the intraocular pressure (IOP) using a Schiottz tonometer (AMANN Ophthalmic Instruments, Liptingen, Germany) calibrated according to the manufacturer's instructions. For determination of IOP, 5 readings were taken on each eye alternating between the left and right eyes, and the mean was calculated [24]. Central corneal thickness (CCT) was determined using an ultrasonic pachymeter (DGH Technology, Exton, PA, USA) with a hand-held solid probe [25]. During the measurements, the probe tip of the pachymeter was held perpendicular to the central cornea. Averages of 10 readings were recorded. An ophthalmic table slit lamp (Topcon Medical Systems Inc., NJ, USA) was used to observe and record the anterior segment. The rabbits were killed 16 h after administration of the eye drops. The eyeballs were harvested and fixed in 3.7% formaldehyde.

2.5.3. Fluorescence Quantification. The rabbits were killed at 0.5, 2, 4, and 16 h after the last instillation. Eyeballs were harvested and cleaned using PBS. Fluorescent GPs in the eyes were quantified using an *in vivo* imaging system (IVIS Imaging System 200 Series; Xenogen, USA). The relative intensity of fluorescence in the eyes was equivalent to the concentration of fluorescent nanoparticles. The fluorescence

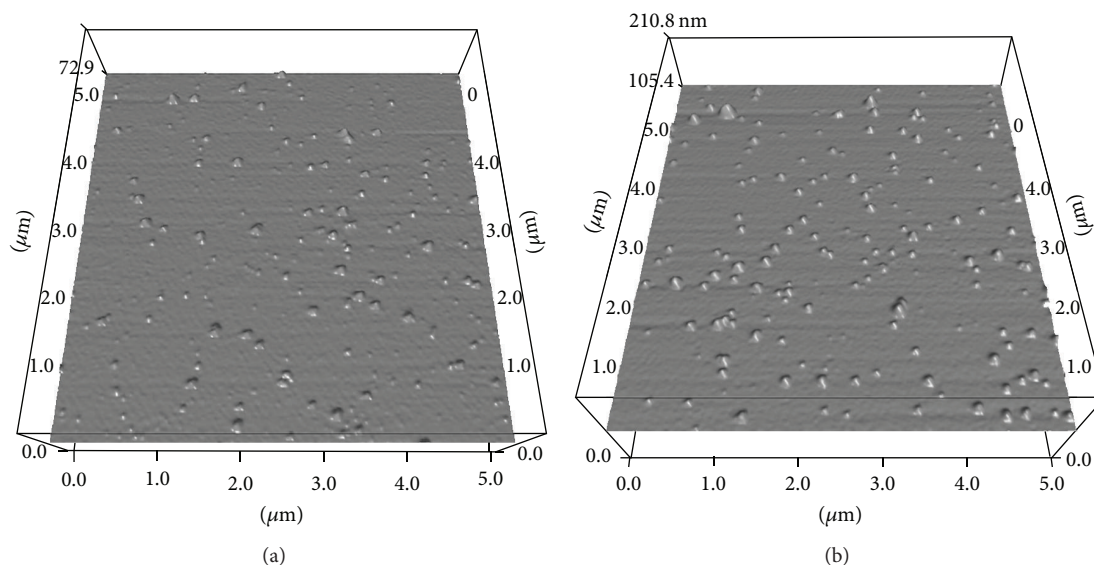


FIGURE 1: Morphology and size of charged GPs with (a) positive or (b) negative charge. Image acquired by atomic force microscopy.

TABLE 1: Size and zeta potential of gelatin nanoparticles ($n = 3$).

	Size (nm)	Zeta (mV)
GPs(+)	180.6 ± 45.7	33.4 ± 10.9
GPs(-)	230.7 ± 84.6	-44.2 ± 7.2

intensity of the PBS-treated group was used as the background value. The quantified area was restricted to the cornea, and the fluorescein signal was calculated ($n = 5$).

2.5.4. Distribution of GPs in the Cornea Observed Using Confocal Laser Scanning Microscopy. After the fluorescence intensity was quantified, the cornea was excised from the eyeball and separated into 2 sections. One section was directly mounted on a glass slide and examined under a microscope without additional processing of the tissue. A 5- μm cryosection was prepared using the other section from the apical to the lateral end of the cornea. All cornea samples were analyzed with a confocal microscope (Nikon, A1, Japan).

2.6. Statistical Analysis. Experiments were performed at least in triplicate, and the results were reported as mean \pm standard deviation (SD). All data were analyzed with the Student's t -test or one-way analysis of variance (ANOVA). Statistical significance was considered at a level of $P < 0.05$.

3. Results and Discussion

In this study, we prepared charged GPs and performed *in vitro* and *in vivo* studies. The rabbit cornea model was used to determine the retention of the cationic GPs because of the similarity of this model with that of the human cornea [10, 26].

3.1. Characterization of GPs. GPs can be prepared using type A or type B gelatin to obtain positively or negatively charged nanocarriers (Table 1). The size of GPs prepared using type

A gelatin was approximately 180.6 ± 45.7 nm. The size of the negatively charged GPs (prepared using type B gelatin) was 230.7 ± 84.6 nm; these nanoparticles were larger and more widely distributed than GPs prepared using type A gelatin. The zeta potential of GPs prepared using type A and type B gelatin was 33.4 ± 10.9 mV and -44.2 ± 7.2 mV (Table 1). The nanoparticles prepared using type A gelatin had a positive surface charge and were abbreviated as GP(+), and those prepared using type B gelatin were negatively charged and were abbreviated as GP(-). The nanoparticles of both types observed under the AFM showed a smooth and ball like structure (Figure 1). The particle size was about 200 nm, which was consistent with the findings of photon correlation spectroscopy (PCS). Type A and type B gelatin were prepared using by different processes by extracting gelatins from collagen [11]. The amount of free carboxyl or amino groups was different in both types of gelatin. At pH 6~7, however, type A gelatin has a positive net charge, while type B gelatin is negatively charged [17, 27]; thus, the zeta potential of these gelatins may also be different. The positively charged GPs (GP+) may have electrostatic attraction with the negatively charged corneal epithelial cells, which is more preferred in ocular drug delivery.

3.2. Cytotoxicity of GPs. An important aspect of the development of new carrier for drug/gene delivery is its safety of interaction with the target cells. The biocompatibility of the newly developed materials should be examined to determine their potential for ophthalmic use. In this study, we evaluated the cytotoxicity of GPs in the HCE cell line by measuring their metabolic activity. The percentage of viable cells in the treated group versus nontreated group (culture medium) is

TABLE 2: Grading system of the macroscopic signs in the *in vivo* tolerance study for the colloidal system tested [23].

Grade	Discomfort	Cornea	Conjunctiva	Discharge	Lids
0	No reaction	No alterations	No alterations	No discharge	No swelling
1	Blinking	Mild opacity	Mild hyperemia Mild edema	Mild discharge without moistened hair	Mild swelling
2	Enhanced blinking Intense tearing Vocalizations	Intense opacity	Intense hyperemia Intense edema Hemorrhage	Intense discharge with moistened hair	Obvious swelling

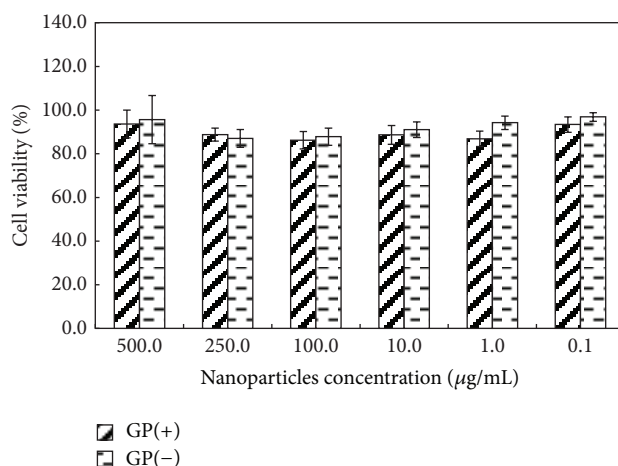


FIGURE 2: Results of WST-1 assays of human corneal epithelium (HCE) cells after incubation with 2 kinds of gelatin nanoparticles for 2 h. (GP+, GPs with positive surface charge; GP-, GPs with negative charge. Data were analyzed using the Student's *t*-test and are presented as mean \pm standard deviation (SD); $n = 6$, * $P < 0.05$).

shown in Figure 2. No significant difference was observed in cell viability even after treatment with 500 $\mu\text{g/mL}$ of GPs for 2 h. The images of HCE cells labeled using the live/dead stain are shown in Figure 3; the live cells emit green fluorescence and the dead cells emit red fluorescence. Large percentage of live cells was observed in the control group (Figure 3(a)), and nearly all the HCE cells were viable after coculturing with GP(+) or GP(-) for 2 h (Figures 3(b) and 3(c)). HCEs were viable and only a few dead cells were observed after culturing with GPs, which indicated that GPs had adequate safety for application to the ocular surface. de la Fuente et al. cultured HCE cells with hyaluronic acid-CNP for 1 h and showed that this treatment had no effect on cell viability [7]. The viability of HCE cells treated with cationized gelatin nanovector hybrid with chondroitin sulfate or dextran sulfate for 72 h was not significantly different from that nontreated HCE cells [18]. These results indicate that GPs are not toxic to HCE cells after short-term or long-term exposure.

3.3. Alteration in the TEER across the Tight Junction in HCE Cells by GPs Treatment. The presence of tight junctions between epithelial cells prevents the flow of the fluids and the movement of molecules and ions between cells [22]. The epithelial membrane provides a significant barrier to the free diffusion of substances from the cornea to the anterior chamber. The barrier integrity of these monolayers can be measured directly by measuring the TEER of HCE cells. The TEER of HCE monolayers cultured with charged GPs

(GP+/GP-) slightly increased to 110% \pm 12.7% (% against initial) and then returned to normal (Figure 4(a)). No significant difference was observed in the TEER of HCE cells treated with GPs(+) or GP(-) after 96 h. However, cells treated with CNP showed a marked decrease in the TEER (70% decrease), which showed that the barrier integrity of the HCE monolayer was changed by CNP treatment. The CNP-treated cells showed loss of ZO-1, but no variation in the 2 GPs groups (Figure 4(b)). Chitosan has been widely used for ocular drug delivery [5, 28–30] because of its mucoadhesive property. Chitosan disrupts the tight intercellular junctions and results in loss of membrane-associated ZO-1, thus increasing the permeability of the epithelium [22]. The anterior part of the eye is constantly exposed to the external environment and thus is vulnerable to a wide range of microorganisms; further, its moist mucosal surface makes the cornea particularly susceptible to attack. The barrier to avoid microorganism invasion depends on the integrity of the tight junctions in the cornea. The tight junctions between the neighboring epithelial cells prevent the free diffusion of hydrophilic molecules across the epithelium by the paracellular route [31]. However, CNP increases the drug concentration in the cornea via intracellular (uptake by the cells) and intercellular (opening the tight intercellular junction) routes [31]. Previous study showed that the tight junction reclosed may be impeded by the unremoved chitosan residue on the surface of the Caco-2 cells [22]. Therefore, a similar phenomenon may be observed in the corneal epithelial cells causing continuously

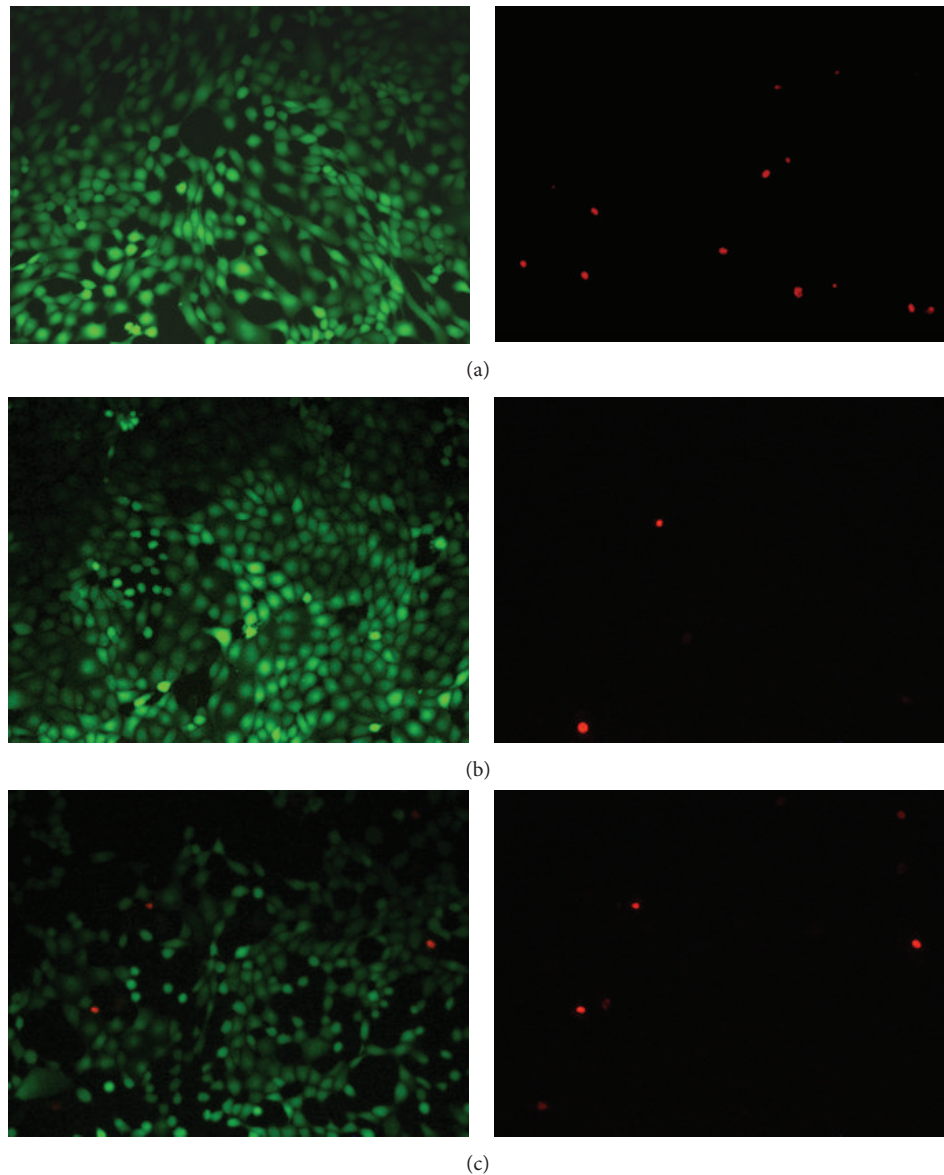


FIGURE 3: Fluorescent photomicrographs of human corneal epithelial (HCE) cells cultured with (a) culture medium, (b) GP(+), and (c) GP(-) at a concentration of $100 \mu\text{g}/\text{mL}$ for 2 h. The polyanionic dye calcein-AM is well retained within the live cells, which produced intense uniform green fluorescence in the live cells. (Magnification: 40x); GP: gelatin nanoparticles.

open of the tight junction. Therefore, a risk for using CNP for ocular drug delivery is increasing the microorganism invasion to the cornea via disruption of cornea tight junction. But, there is no risk for tight junction disruption by GPs.

3.4. Intracellular Content. We examined the intracellular accumulation of the charged GPs in the HCE cells. We examined internalization of fluorescence-labeled GPs by measuring the fluorescence in the cell lysates. Cationic or ionic GPs conjugated with TAMRA were added into the culture medium. The intracellular fluorescence of the cell lysates in the GP(+) group at 10, 30, and 60 min was higher than that of the GP(-) (Figure 5). After 60 min, the OD value of the GP(+) group was much higher than that of the GP(-) group ($P < 0.05$). This finding is consistent with previous study, which showed

that cationic nanoparticles could increase the stability of the nanoparticle system and improve the interaction between the particles and the eye surface and thus increase the transfection efficiency [18, 32].

3.5. Tolerance and Clinical Evaluation. Gelatin is commonly used in the preparation of capsules, and GPs are widely investigated for drug/gene delivery. However, few studies have examined the safety and tolerance of GPs for ocular drug delivery. We performed an irritation test on rabbits after single instillation of $50 \mu\text{L}$ of GPs formulation. The eye treated using PBS was used as a control. Each animal was observed at 0.5, 2, 4, and 16 h after instillation. An index of overall irritation (Table 2) was calculated by summing up the total clinical evaluation scores over the observation time

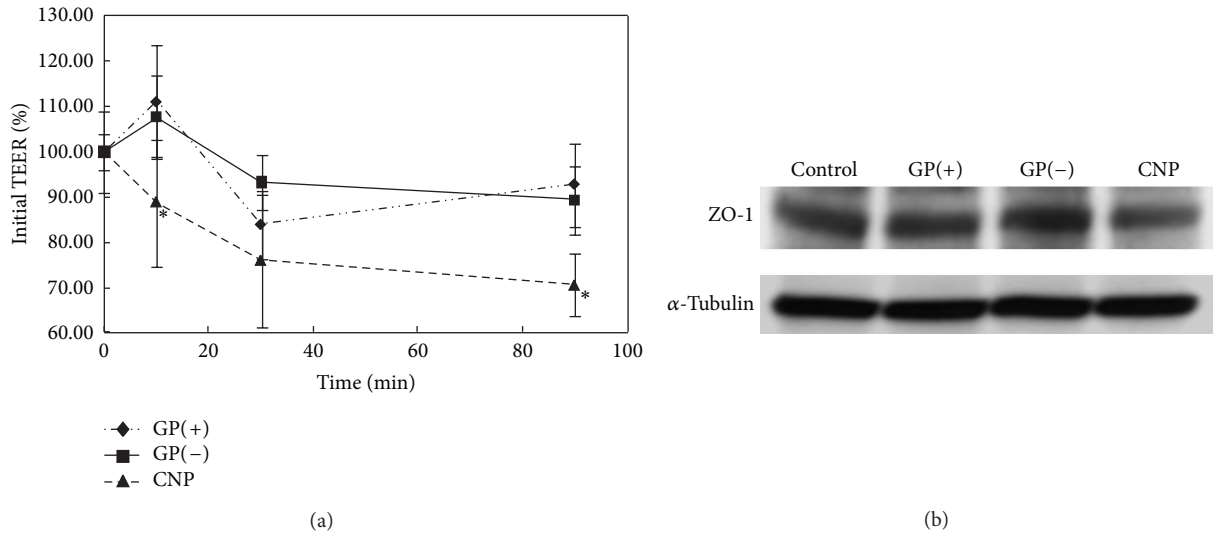


FIGURE 4: The transepithelial electrical resistance (TEER) assay showed recovery of human corneal epithelial (HCE) cell layer barrier after coculturing with gelatin nanoparticles (GPs), but not in chitosan nanoparticles (CNP). $n = 5$ standard error of mean (SEM), $*P < 0.05$. (b) Western blot analysis of zonula occluden-1 (ZO-1) expression in HCE cells after treatment with different nanoparticles.

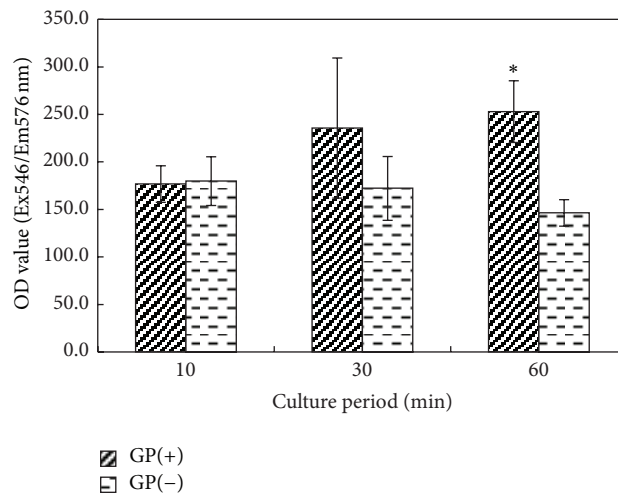


FIGURE 5: Nanoparticles uptaken by the human corneal epithelial (HCE) cells were evaluated by measuring the fluorescence intensity of the cell lysate. $n = 6$ standard error of mean (SEM), $*P < 0.05$.

TABLE 3: Grading system of macroscopic signs in the *in vivo* tolerance study of the gelatin nanoparticles.

Time	Control*		Free TAMRA			GP(+) TAMRA				
	0.5 h	4.0 h	0.5 h	2.0 h	4.0 h	16.0 h	0.5 h	2.0 h	4.0 h	16.0 h
Grade										
Discomfort	0	0	0	0	0	0	0	0	0	0
Cornea	0	0	0	0	0	0	0	0	0	0
Conjunctive	0	0	0	0	1	0	0	0	1	0
Discharge	0	0	0	0	1	0	1	0	0	0

* $n = 3$.

GP: gelatin nanoparticles; TAMRA: tetramethyl rhodamine.

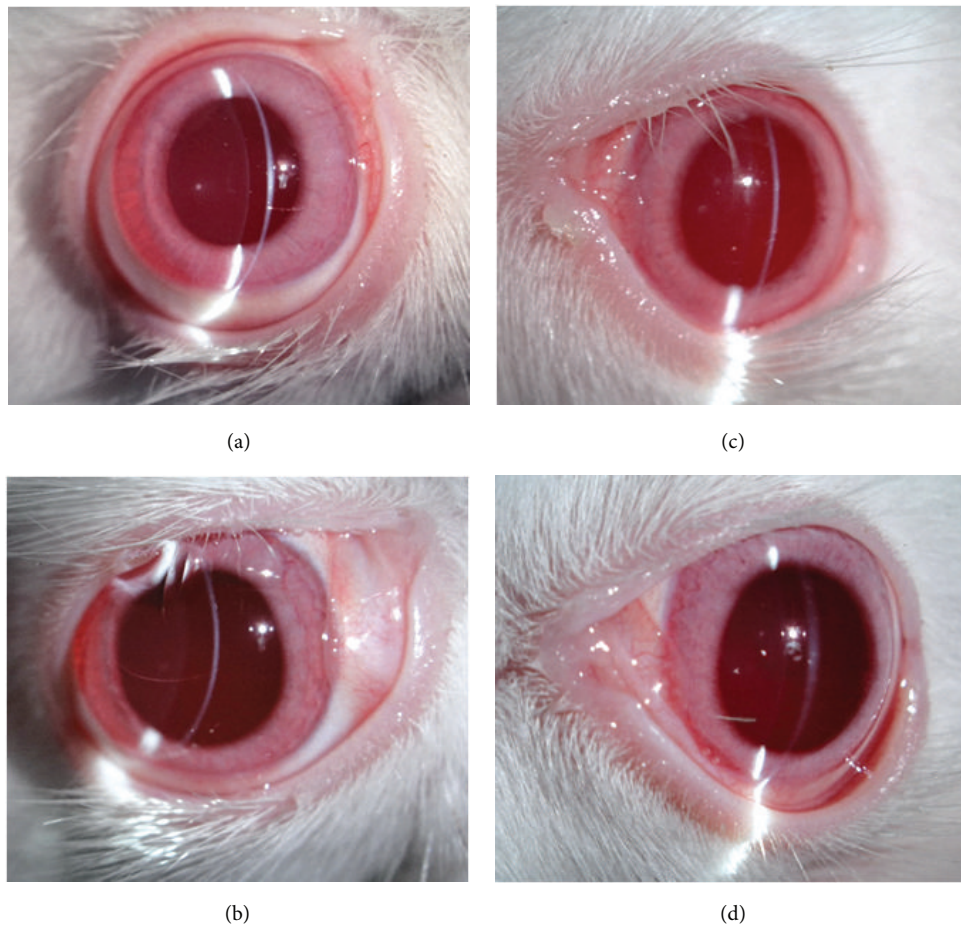


FIGURE 6: The appearance of rabbit eyes topically treated with 100 μL of free tetramethyl rhodamine succinyl (TAMRA) solution: (a) 0.5 h and (b) 16 h after treatment; treated with GP(+)-TAMRA solution (100 μL): (c) 0.5 h and (d) 16 h after the application.

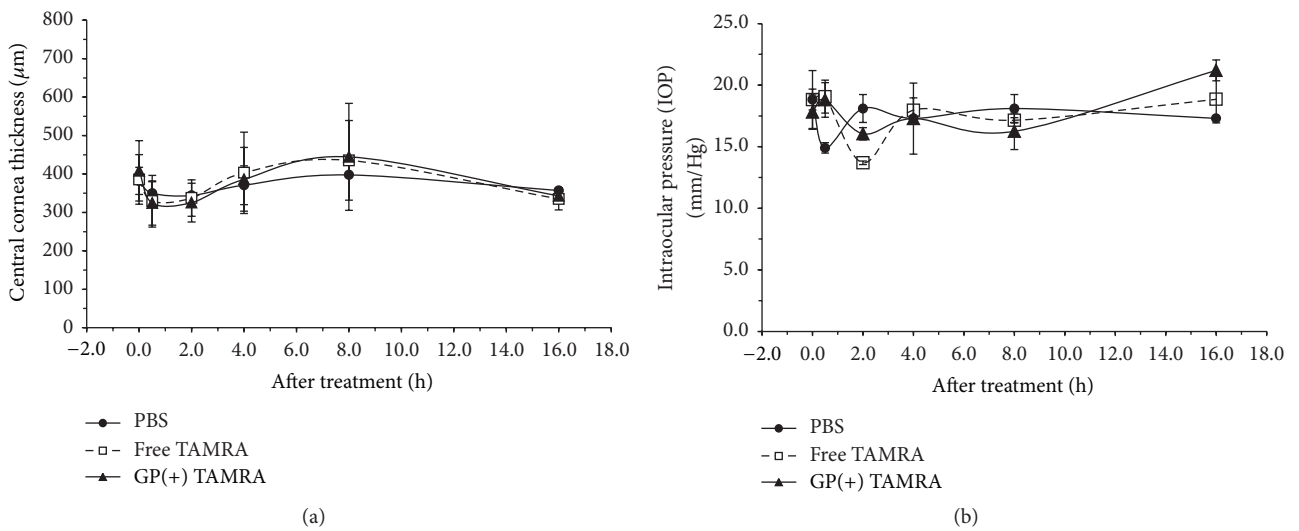


FIGURE 7: (a) Measurements of central corneal thickness (CCT) and (b) intraocular pressure (IOP) after treatment with eye drops containing TAMRA solution or GP(+)-TAMRA. An asterisk indicates statistically significant differences ($*P < 0.05$; $n = 5$) compared to control (PBS-treated rabbits, $n = 3$).

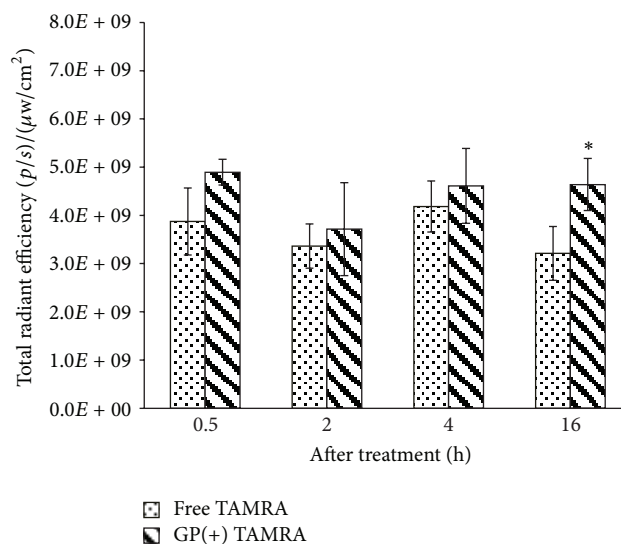


FIGURE 8: *Ex vivo* fluorescence imaging of the eyes of rabbits treated with fluorescent dye for different time periods: (a) TAMRA solution and (b) GP(+ TAMRA. $n = 5$ standard error of mean (SEM), * $P < 0.05$.

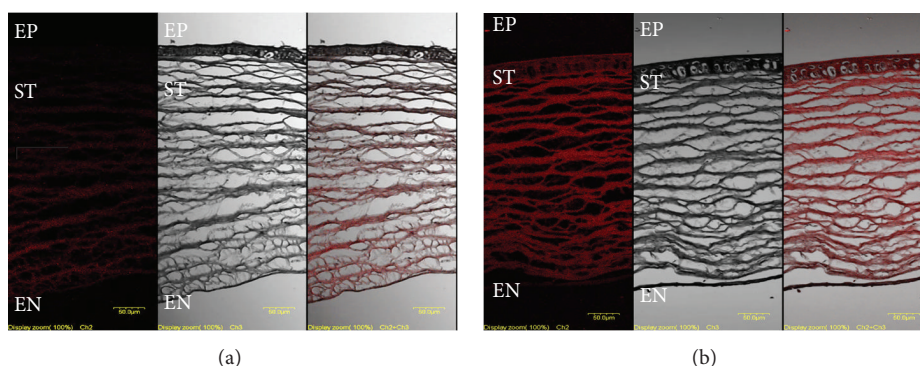


FIGURE 9: ((a), (b)) are images from cryosections of the cornea treated with the free dye and GP(+) fluorescence dye. Free dye: TAMRA/PBS solution; GP(+) dye: GP(+) with TAMRA conjugation (red). Scale bar: 50 μm . EP: corneal epithelium; ST: corneal stroma; EN: corneal endothelium. After treatment for 0.5 h.

points; the results are shown in Table 3. Very slight redness of the conjunctiva was observed in the eyes treated with free TAMRA solution and in GP(+) TAMRA-treated eyes at 4 h, but no chemosis was observed after treatment in other groups and at other time points. No differences were observed in the ocular tissue of rabbits treated with free and GP(+) TAMRA after 0.5 and 16 h (Figure 6). Treatment with GP(+) was safe and caused no irritation to the eyes of the rabbits. Previous studies have shown that the rabbit eye is more sensitive than the human eye and has a longer time for epithelial repair [10, 33]. Therefore, it is reasonable to expect that charged GPs are well tolerated by the human eye.

One of the risk factors involved in eye disease is increased IOP, which leads to apoptosis and loss of retinal ganglion cells [34]. Therefore, we examined the changes in the IOP and corneal thickness after eye drop treatment to confirm the safety of GPs for ocular drug delivery. The effects of instillation of free TAMRA and GP(+) TAMRA eye drops on corneal thickness and IOP in rabbits are shown in Figure 7. Compared to the control groups ($328 \pm 21 \mu m$), the

groups treated with free TAMRA and GP(+) TAMRA eye drops showed a decrease in the corneal thickness after 0.5 h ($297 \pm 4 \mu m$; $292 \pm 6 \mu m$) and 2 h ($304 \pm 5 \mu m$; $290 \pm 5 \mu m$) (Figure 7(a)). After 4 h of treatment, the corneal thickness in the treated group was almost the same as that in the control group. The mean baseline of IOP values ranged from 16 to 20 mmHg (Figure 7(b)). The IOP decreased immediately after treatment with PBS. The IOP returned to the baseline level within 2 h. In addition, the IOP decreased at 2 h even after treatment with free TAMRA and GP(+) TAMRA. However, the IOP in these 2 groups returned to the normal range after 4 h (Figure 7(b)). The corneal thickness and IOP did not change significantly after treatment with GP(+) TAMRA suspension.

3.6. Fluorescence Examination to Determine the Distribution of GPs in the Eyes. The amount of fluorescent nanoparticles in the cornea at different time points acquired using the IVIS spectrum imaging system is shown in Figure 8. The number of fluorescent spots obtained after treatment with

GP(+) TAMRA was greater than that obtained treatment with free TAMRA/PBS at 0.5, 2, 4, and 16 h. The accumulation of the fluorescent dye differed significantly between the free TAMRA and GP(+) TAMRA treated group at 16 h after treatment. After IVIS examination, the cornea was removed and a cryosection was prepared for examination under a confocal microscope. The distribution profile of the fluorescent dye in the cornea of rabbits after administration of the eye drops is shown in Figure 9. The cross-section of the cornea from the epithelium, stroma to endothelium layer, was observed under the same magnification. The cornea treated using the free TAMRA solution showed a weak fluorescent signal located in the posterior region (Figure 9(a)). The cornea treated with GP(+) TAMRA showed a strong fluorescent signal in the entire cornea and (Figure 9(b)). Moreover, the fluorescence quantification of the cornea treated with GP(+) TAMRA increased by 4-fold compared to that treated with TAMRA/PBS solution, which indicated that the dye encapsulated in the GPs could be retained in the cornea for a longer time and was distributed uniformly across the entire cornea. Solid lipid nanoparticles (SLNs) and CNP are retained for a longer time on the corneal surface probably because of their small size, and further characterization of nanoparticles would help in determining the transcorneal absorption [5, 10]. Hyaluronic acid coated poly-3-caprolactone nanospheres achieved high levels of cyclosporine A (CyA) in the cornea, which was 10-fold higher than that was achieved with CyA solution in castor oil [35]. In our study, the levels of GPs in the corneas treated with GP(+) TAMRA were higher than those in the cornea treated with free TAMRA at each time point, which indicated a longer retention time (16 h) of GP(+) TAMRA compared to that of free TAMRA. Our *in vivo* results might be explained on the basis of the prolonged retention in the precorneal area and cornea because of the small size of GP(+) (180 nm) and also in the uptake/internalization of GP(+) into the corneal epithelium.

4. Conclusion

The aim of this study was to confirm whether cationic GPs could be used for topical application, and this was examined in rabbit eyes. Positively charged GPs were prepared with a size of about 180 nm. GPs are nontoxic to HCE cells and had no influence on the tight intercellular junctions. The corneal thickness slightly decreased 0.5 h after treatment and then returned to normal. The IOP showed variation in the normal range after treatment with GPs. GPs showed retention of the fluorescent dye in the cornea for the prolonged period, which is beneficial to maintain the dose in the therapeutic range. Therefore, dye/drug/gene encapsulated in cationic GPs nanoparticles is promising new medicines for ocular disease.

Acknowledgments

This work was supported in part by a grant from the Taipei Medical University Startup Grant (TMU100-AE1-B01) and National Science Council, Taiwan (NSC 101-2221-E-038-002).

References

- [1] V. P. Torchilin and V. S. Trubetsky, "Which polymers can make nanoparticulate drug carriers long-circulating?" *Advanced Drug Delivery Reviews*, vol. 16, no. 2-3, pp. 141-155, 1995.
- [2] E. E. Binstock and A. J. Domb, "Nanoparticles in ocular drug delivery," in *Nanoparticles for Pharmaceutical Applications*, A. J. Domb, Y. Tabata, M. N. V. R. Kumar, and S. Farber, Eds., pp. 367-376, American Scientific Publishers, Valencia, Calif, USA, 2007.
- [3] N. M. Davies, "Biopharmaceutical considerations in topical ocular drug delivery," *Clinical and Experimental Pharmacology and Physiology*, vol. 27, no. 7, pp. 558-562, 2000.
- [4] Y. Diebold, M. Jarrin, V. Sáez et al., "Ocular drug delivery by liposome-chitosan nanoparticle complexes (LCS-NP)," *Biomaterials*, vol. 28, no. 8, pp. 1553-1564, 2007.
- [5] A. M. de Campos, A. Sánchez, and M. J. Alonso, "Chitosan nanoparticles: a new vehicle for the improvement of the delivery of drugs to the ocular surface. Application to cyclosporin A," *International Journal of Pharmaceutics*, vol. 224, no. 1-2, pp. 159-168, 2001.
- [6] J.-L. Bourges, S. E. Gautier, F. Delie et al., "Ocular drug delivery targeting the retina and retinal pigment epithelium using polylactide nanoparticles," *Investigative Ophthalmology & Visual Science*, vol. 44, no. 8, pp. 3562-3569, 2003.
- [7] M. de la Fuente, B. Seijo, and M. J. Alonso, "Novel hyaluronic acid-chitosan nanoparticles for ocular gene therapy," *Investigative Ophthalmology & Visual Science*, vol. 49, no. 5, pp. 2016-2024, 2008.
- [8] E. Başaran, M. Demirel, B. Sirmagül, and Y. Yazan, "Cyclosporine-A incorporated cationic solid lipid nanoparticles for ocular delivery," *Journal of Microencapsulation*, vol. 27, no. 1, pp. 37-47, 2010.
- [9] Y. Kawashima, H. Yamamoto, H. Takeuchi, and Y. Kuno, "Mucoadhesive DL-lactide/glycolide copolymer nanospheres coated with chitosan to improve oral delivery of elcatonin," *Pharmaceutical Development and Technology*, vol. 5, no. 1, pp. 77-85, 2000.
- [10] E. H. Gökçe, G. Sandri, S. Eğrilmez, M. C. Bonferoni, T. Güneri, and C. Caramella, "Cyclosporine A-loaded solid lipid nanoparticles: ocular tolerance and in vivo drug release in rabbit eyes," *Current Eye Research*, vol. 34, no. 11, pp. 996-1003, 2009.
- [11] K. B. Djagny, Z. Wang, and S. Xu, "Gelatin: a valuable protein for food and pharmaceutical industries: review," *Critical Reviews in Food Science and Nutrition*, vol. 41, no. 6, pp. 481-492, 2001.
- [12] M. B. Sintzel, S. F. Bernatchez, C. Tabatabay, and R. Gurny, "Biomaterials in ophthalmic drug delivery," *European Journal of Pharmaceutics and Biopharmaceutics*, vol. 42, no. 6, pp. 358-374, 1996.
- [13] J. O.-H. Sham, Y. Zhang, W. H. Finlay, W. H. Roa, and R. Löbenberg, "Formulation and characterization of spray-dried powders containing nanoparticles for aerosol delivery to the lung," *International Journal of Pharmaceutics*, vol. 269, no. 2, pp. 457-467, 2004.
- [14] G. Kaul and M. Amiji, "Tumor-targeted gene delivery using poly(ethylene glycol)-modified gelatin nanoparticles: in vitro and in vivo studies," *Pharmaceutical Research*, vol. 22, no. 6, pp. 951-961, 2005.
- [15] A. K. Gupta, M. Gupta, S. J. Yarwood, and A. S. G. Curtis, "Effect of cellular uptake of gelatin nanoparticles on adhesion, morphology and cytoskeleton organisation of human fibroblasts," *Journal of Controlled Release*, vol. 95, no. 2, pp. 197-207, 2004.

- [16] C.-L. Tseng, W.-Y. Su, K.-C. Yen, K.-C. Yang, and F.-H. Lin, "The use of biotinylated-EGF-modified gelatin nanoparticle carrier to enhance cisplatin accumulation in cancerous lungs via inhalation," *Biomaterials*, vol. 30, no. 20, pp. 3476–3485, 2009.
- [17] J. Vandervoort and A. Ludwig, "Preparation and evaluation of drug-loaded gelatin nanoparticles for topical ophthalmic use," *European Journal of Pharmaceutics and Biopharmaceutics*, vol. 57, no. 2, pp. 251–261, 2004.
- [18] G. K. Zorzi, L. Contreras-Ruiz, J. E. Párraga et al., "Expression of MUC5AC in ocular surface epithelial cells using cationized gelatin nanoparticles," *Molecular Pharmaceutics*, vol. 8, no. 5, pp. 1783–1788, 2011.
- [19] R. C. Nagarwal, S. Kant, P. N. Singh, P. Maiti, and J. K. Pandit, "Polymeric nanoparticulate system: a potential approach for ocular drug delivery," *Journal of Controlled Release*, vol. 136, no. 1, pp. 2–13, 2009.
- [20] C. J. Coester, K. Langer, H. Von Briesen, and J. Kreuter, "Gelatin nanoparticles by two step desolvation—a new preparation method, surface modifications and cell uptake," *Journal of Microencapsulation*, vol. 17, no. 2, pp. 187–193, 2000.
- [21] C.-L. Tseng and F.-H. Lin, "Preparation of gelatin nanoparticles with EGFR selection ability via biotinylated-EGF conjugation for lung cancer targeting," *Biomedical Engineering: Applications, Basis and Communications*, vol. 20, no. 3, pp. 161–169, 2008.
- [22] J. Smith, E. Wood, and M. Dornish, "Effect of chitosan on epithelial cell tight junctions," *Pharmaceutical Research*, vol. 21, no. 1, pp. 43–49, 2004.
- [23] *Test Guideline 405: Acute Eye Irritation/Corrosion*, Organization for Economic Co-Operation and Development, 2002.
- [24] J.-Y. Lai, "Biocompatibility of chemically cross-linked gelatin hydrogels for ophthalmic use," *Journal of Materials Science: Materials in Medicine*, vol. 21, no. 6, pp. 1899–1911, 2010.
- [25] W. M. Hsu, K. H. Chen, J. Y. Lai, and G. Hsiue, "Transplantation of human corneal endothelial cells using functional biomaterials: poly(N-isopropylacrylamide) and gelatin," *Journal of Experimental & Clinical Medicine*, vol. 5, no. 2, pp. 56–64, 2013.
- [26] P. van der Bijl, A. H. Engelbrecht, A. D. van Eyk, and D. Meyer, "Comparative permeability of human and rabbit corneas to cyclosporin and tritiated water," *Journal of Ocular Pharmacology and Therapeutics*, vol. 18, no. 5, pp. 419–427, 2002.
- [27] S. Young, M. Wong, Y. Tabata, and A. G. Mikos, "Gelatin as a delivery vehicle for the controlled release of bioactive molecules," *Journal of Controlled Release*, vol. 109, no. 1–3, pp. 256–274, 2005.
- [28] A. M. de Campos, Y. Diebold, E. L. S. Carvalho, A. Sánchez, and M. J. Alonso, "Chitosan nanoparticles as new ocular drug delivery systems: in vitro stability, in vivo fate, and cellular toxicity," *Pharmaceutical Research*, vol. 21, no. 5, pp. 803–810, 2004.
- [29] A. E. de Salamanca, Y. Diebold, M. Calonge et al., "Chitosan nanoparticles as a potential drug delivery system for the ocular surface: toxicity, uptake mechanism and in vivo tolerance," *Investigative Ophthalmology & Visual Science*, vol. 47, no. 4, pp. 1416–1425, 2006.
- [30] A. M. de Campos, A. Sánchez, R. Gref, P. Calvo, and M. J. Alonso, "The effect of a PEG versus a chitosan coating on the interaction of drug colloidal carriers with the ocular mucosa," *European Journal of Pharmaceutical Sciences*, vol. 20, no. 1, pp. 73–81, 2003.
- [31] E. Mannermaa, K.-S. Vellonen, and A. Urtti, "Drug transport in corneal epithelium and blood-retina barrier: emerging role of transporters in ocular pharmacokinetics," *Advanced Drug Delivery Reviews*, vol. 58, no. 11, pp. 1136–1163, 2006.
- [32] L. Rabinovich-Guilatt, P. Couvreur, G. Lambert, and C. Dubernet, "Cationic vectors in ocular drug delivery," *Journal of Drug Targeting*, vol. 12, no. 9–10, pp. 623–633, 2004.
- [33] C. M. Hutak and R. B. Jacaruso, "Evaluation of primary ocular irritation: alternatives to the Draize test," in *Ocular Therapeutics and Drug Delivery*, R. Ik, Ed., Technomic Publishing, Lancaster, Pa, USA, 1996.
- [34] L. Guo, S. E. Moss, R. A. Alexander, R. R. Ali, F. W. Fitzke, and M. F. Cordeiro, "Retinal ganglion cell apoptosis in glaucoma is related to intraocular pressure and IOP-induced effects on extracellular matrix," *Investigative Ophthalmology & Visual Science*, vol. 46, no. 1, pp. 175–182, 2005.
- [35] I. Yenice, M. C. Mocan, E. Palaska et al., "Hyaluronic acid coated poly- ϵ -caprolactone nanospheres deliver high concentrations of cyclosporine A into the cornea," *Experimental Eye Research*, vol. 87, no. 3, pp. 162–167, 2008.

Research Article

Development of Antibiotics Impregnated Nanosized Silver Phosphate-Doped Hydroxyapatite Bone Graft

Waraporn Suvannapruk, Faungchat Thammarakcharoen,
Phetrungr Phanpiriya, and Jintamai Suwanprateeb

National Metal and Materials Technology Center (MTEC), 114 Paholyothin Road, Klong 1, Klongluang, Pathumthani 12120, Thailand

Correspondence should be addressed to Jintamai Suwanprateeb; jintamai@mtec.or.th

Received 2 August 2013; Revised 2 October 2013; Accepted 2 October 2013

Academic Editor: In-Kyu Park

Copyright © 2013 Waraporn Suvannapruk et al. This is an open access article distributed under the Creative Commons Attribution License, which permits unrestricted use, distribution, and reproduction in any medium, provided the original work is properly cited.

Nanosized Ag_3PO_4 loaded hydroxyapatite which was prepared by a novel low temperature phosphorization of 3D printed calcium sulfate dihydrate at the nominal silver concentration of 0.001 M and 0.005 M was impregnated by two antibiotics including gentamicin and vancomycin. Phase composition, microstructure, antibiotics loading, silver content, antimicrobial performance, and cytotoxic potential of the prepared samples were characterized. It was found that the fabricated sample consisted of hydroxyapatite as a main phase and spherical-shaped silver phosphate nanoparticles distributing within the cluster of hydroxyapatite crystals. Antibacterial activity of the samples against two bacterial strains (gram negative *P. aeruginosa* and gram positive *S. aureus*) was carried out. It was found that the combination of antibiotics and nanosized Ag_3PO_4 in hydroxyapatite could enhance the antibacterial performance of the samples by increasing the duration in which the materials exhibited antibacterial property and the size of the inhibition zone depending on the type of antibiotics and bacterial strains compared to those contained antibiotics or nanosilver phosphate alone. Cytotoxic potential against osteoblasts of antibiotics impregnated nanosilver phosphate hydroxyapatite was found to depend on the combination of antibiotics content, type of antibiotics, and nanosilver phosphate content.

1. Introduction

Hydroxyapatite is one of calcium phosphate family which is widely used for bone repairs and reconstruction due to its osteoconductive property. Recently, antibiotics impregnated hydroxyapatite which was prepared by a novel low temperature phosphorization route was developed for bone infection treatment by providing local, sustained, and high concentration of antimicrobial agents while also function as a restorable bone graft for new bone formation in the injured area [1, 2]. The advantages of this approach were that it minimized systemic complications which would expose patients to antibiotic levels that often would result in numerous toxic side effects, improved clinical efficacy, and eliminated the need for additional bone grafting. Furthermore, hydroxyapatite prepared by this low temperature process could resorb faster than typically used high temperature sintered hydroxyapatite [3–6] due to its low crystalline nanostructure which is close to that of bone.

Apart from antibiotics, silver ions were known to have inhibitory and antibacterial properties against a broad spectrum of bacterial strains while being relatively low toxic to human cells. Recently, silver nanoparticles have increasingly been used for infection treatment due to its unique properties resulting from the nanoscale features and the ability to rapidly release of several silver species which were seen to improve the treatment efficiency [7–9]. Silver phosphate (Ag_3PO_4) is one form of silver compounds that could be used as a silver source for antibacterial applications due to its advantages compared to other silver compounds including its low solubility in aqueous solutions, its high antibacterial efficiency, and its strong photocatalytic activity under visible light [10, 11]. Recently, we successfully applied a low temperature phosphorization process to *in situ* load nanosilver phosphate into hydroxyapatite structure in a single step which enhances its antibacterial property [12]. It was shown previously that the combination of nanosilver and antibiotics could enhance the antibacterial performance depending on the bacterial

strains, type of antibiotics, concentration of antibiotics, and nanosilver concentration [13–17]. However, no study on the effect of antibiotics and nanosilver that are incorporated into hydroxyapatite matrix on antibacterial activity has been studied. It is thought that the impregnation of antibiotics in nanosilver phosphate-doped hydroxyapatite could also provide the improvement in antibacterial performance of hydroxyapatite, but the mechanism and the effect might be different.

In this study, nanosilver phosphate-doped hydroxyapatite which was prepared by low temperature coconversion process was, thus, impregnated with two types of antibiotics including gentamicin and vancomycin. Materials properties and antibacterial performance including phase composition, microstructure, total drug loading, antibacterial activity, and cytotoxic potential of antibiotic impregnated nanosilver phosphate-doped hydroxyapatite sample were determined and compared to antibiotics impregnated only and nanosilver phosphate loaded only samples.

2. Materials and Method

2.1. Materials. Raw materials used in this study were calcium sulfate hemihydrate (Lafarge Prestia Co., Ltd, Thailand) and pregelatinized starch (Thaiwah Co., Ltd, Thailand). These materials were supplied in the form of powders and used without further sieving. Antibiotics used were gentamicin sulfate (T.P Drug Laboratories (1969) Co., Ltd) and vancomycin hydrochloride (CJ CheilJedang Corporation, Korea), abbreviated as CN and VC, respectively.

2.2. Sample Preparation. Calcium sulfate hemihydrate powders was mixed with pregelatinized starch powders using a mechanical blender and loaded into a three dimensional printing machine (Z400, Z Corporation) to print 7 mm in diameter spherical specimens. Solutions containing 1 M of disodium hydrogen phosphate (Fluka) and two concentration of silver nitrate (BDH) (0.001 and 0.005 M) were prepared, designated HA_001 and HA_005, respectively. Ammonium (BDH) was then added dropwise to the solution until clear solutions were obtained. The fabricated 3DP beads were then immersed in the solution and kept at 80°C for 24 hours to transform to nanosilver phosphate-doped hydroxyapatite by low temperature phosphorization reaction. Samples were then taken out, rinsed by distilled water, and oven-dried. They were then loaded with two types of antibiotics, using vacuum-assisted method similarly to previous studies [1, 2].

2.3. Characterization

2.3.1. Microstructure, Phase Composition and Total Silver Content. XRD characterization was carried out using X-ray diffractometer (JDX 3530, JEOL, Japan) with Co K-alpha radiation in the range of 10–80° 2θ with step angle of 0.02 degree. JCPDS files were used to identify the peaks of main compositions in sample. Microstructures of nanosilver phosphate loaded hydroxyapatite samples were examined using a transmission electron microscope (JEOL JEM-2010)

and a scanning electron microscope (JSM-5410, JEOL, Japan). In the case of TEM analysis, all samples were grinded into powders and then dispersed onto continuous carbon film grids prior to observation. Total silver content in each sample was determined by acid digestion technique using an atomic absorption spectrometry (AAS) (Analyst 200, Perkin Elmer).

2.3.2. Total Antibiotic Loading. The total antibiotics concentration in the sample beads were determined by dissolving them in 2.4 M hydrochloric acid and analyzed by using UV-VIS spectrophotometer (Jasco V-530) in relation to the previously constructed calibration curve.

2.3.3. Minimum Inhibitory Concentration. Silver nitrate solution was employed to represent the silver ions that were expected to be released from nanosilver phosphate particles. Minimum Inhibitory Concentration (MIC) of silver nitrate and each antibiotic used against two bacterial strains (gram negative *P. aeruginosa* ATCC 27853 and gram positive *S. aureus* ATCC 25923) was determined by the broth macrodilution method. Bacterial inoculum was prepared by transferring 3–5 colonies of bacterial isolate from a fresh (18–24 h) nutrient agar plate to 5 mL of sterile nutrient broth (NB). It was incubated at 35°C ± 2°C for 4–6 h (become visibly turbid) and the culture was adjusted to a 0.5 McFarland standard (≈1.5 × 10⁸ CFU/mL). Tenfold serial dilution of the inoculum suspension was made by adding 1.0 mL of the inoculum suspension to 9.0 mL of NB to achieve 1.5 × 10⁶ CFU/mL and gently mixing by the vortex mixture. Serial 2-fold dilution of the silver nitrate or antibiotic solution was made in the series of tubes and 0.5 mL of the prepared inoculum suspension was added to each tube and incubated at 35°C ± 2°C for 16–18 h. The growth of bacteria was shown as the visual turbidity and the MIC value was determined from the final silver nitrate or antibiotic concentration of the lowest concentration of nonturbid tube.

2.3.4. Antimicrobial Activity. All the samples were sterilized by ethylene oxide gas prior to the tests. Antimicrobial performance tests were carried out by modified agar diffusion assay against two bacterial strains (gram negative *P. aeruginosa* ATCC 27853 and gram positive *S. aureus* ATCC 25923). These two strains were selected to represent gram negative and gram positive strains that are commonly found in bone infection areas [18, 19]. Bacterial strains were inoculated on each agar plate. The sample beads were submerged in simulated body fluid (SBF) at 37°C for 15 days and the beads were withdrawn and placed in a new SBF at every 24 hours. Each eluate was placed in the bored holes in the agar plates and incubated at 37°C. Antibiotic assay was performed by measuring inhibition zone by a vernier caliper.

2.3.5. Cytotoxic Potential. All the samples were sterilized by ethylene oxide gas and incubated in 1 mL of DMEM (Biowhittaker) completed medium at 37°C. The eluates were drawn at 24, 48, and 72 hours with replenishment of a new medium after each eluate aspiration. This was devised to study and compare the effect of the releasing behavior

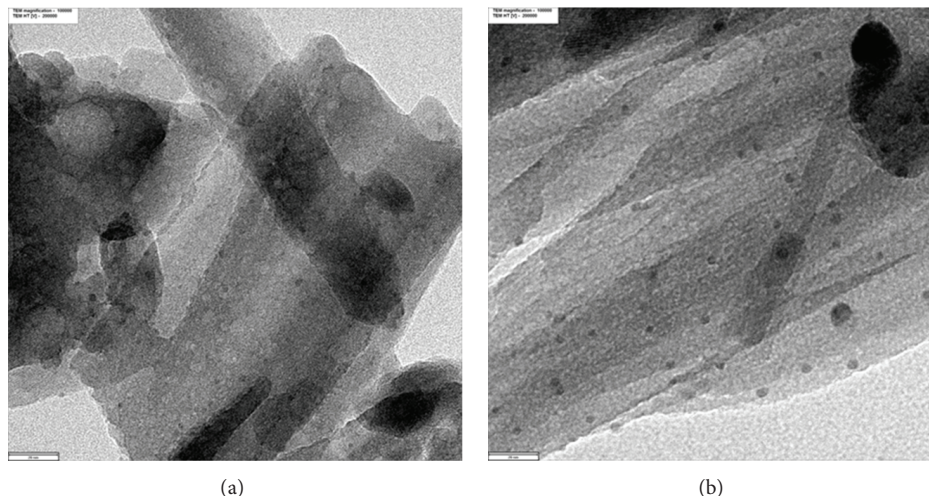


FIGURE 1: TEM micrographs showing microstructure of nanosilver phosphate-doped hydroxyapatite. (a) HA001; (b) HA005. Scale bar = 20 nm.

of each sample on the cytotoxic potential at each period by the replenishment of a new medium after each eluate aspiration similar to the antimicrobial activity test. By this way, the media which contained released antibiotics and silver ions from the previous extraction period was discarded and the concentration of antibiotics or silver ions in the solution would be changed accordingly with extraction periods depending on the releasing characteristic. The elutes were then added to each tissue culture dish which contained 1×10^5 human osteoblast cells per one milliliter of DMEM medium and incubated for 24 hours. After incubation, $100 \mu\text{L}$ of 0.5 mg mL^{-1} MTT (Sigma-Aldrich) was added in each well and incubated for another 2 hours. Dimethyl sulfoxide was then added and transferred to a 96-well plate. Optical density was measured at the wavelength of 570 nm using a microplate reader (Easys Model UVM 340) to quantify the cell viability. Thermanox (Nunc) cover slip was used as negative control (NC) while polyurethane film containing 0.1% Zinc diethyldithiocarbamate (ZDEC): RM-A for ISO 10993 cytotoxicity testing (Hatano) was used as positive control (PC). Reagent control (RC) was the well which contained no samples. Hydroxyapatite sample (HA) which was fabricated by similar process, but without antibiotics or nanosilver phosphate loading, was also tested as a control sample.

2.3.6. Statistical Analysis. The differences in properties amongst samples were analyzed using an analysis of variance (ANOVA) and Tukey post hoc testing. A value of $P < 0.05$ was considered significant.

3. Results

3.1. Phase Composition and Microstructure. Figure 1 shows the typical microstructures of fabricated nanosilver phosphate-doped hydroxyapatite samples, HA_001 and HA_005. It was observed that both samples similarly

comprised the nanosized crystals of hydroxyapatite with the distribution of spherical-shaped silver phosphate nanoparticles within the cluster. Particle sizes of silver phosphate particles in both samples were estimated from the images to be less than 5 nm. SEM images showed that as-fabricated nanosilver phosphate-doped hydroxyapatite sample was porous comprising numerous pores (Figures 2(a) and 2(b)). No significant difference in the microstructure between samples could be detected. Figure 3 shows the XRD pattern of sample fabricated by low temperature coconversion technique. HA_005 showed the characteristic peaks of hydroxyapatite and silver phosphate. HA_001 also showed the characteristic peaks of hydroxyapatite, but silver phosphate peaks were not clearly observed. In all samples, hydroxyapatite peaks were similarly broad while the silver phosphates peaks were sharp. Total silver content in each sample was determined by an atomic absorption technique and observed to be 0.09 and 0.42% for HA_001 and HA_005, respectively. After impregnation by antibiotic, the microstructure of the gentamicin impregnated samples appeared relatively unchanged (Figures 2(c) and 2(d)). In contrast, the surface of vancomycin impregnated samples was extensively coated by vancomycin (Figures 2(e) and 2(f)). This was owing to the greater gelation ability of vancomycin at high concentration compared to gentamicin.

3.2. Total Antibiotics Loading. Figure 4 shows the total antibiotics loading in the nanosilver phosphate-doped hydroxyapatite at different silver content. It could be seen that drug loading in pure hydroxyapatite samples was greater than those of nanosilver phosphate-doped samples for both type of antibiotics. In the case of gentamicin, the drug content in HA_CN_001 was not significantly different to HA_CN, but approximately twice greater than that of HA_CN_005. In contrast, the drug content in HA_VC_001 was lower than those of HA_VC and HA_VC_005.

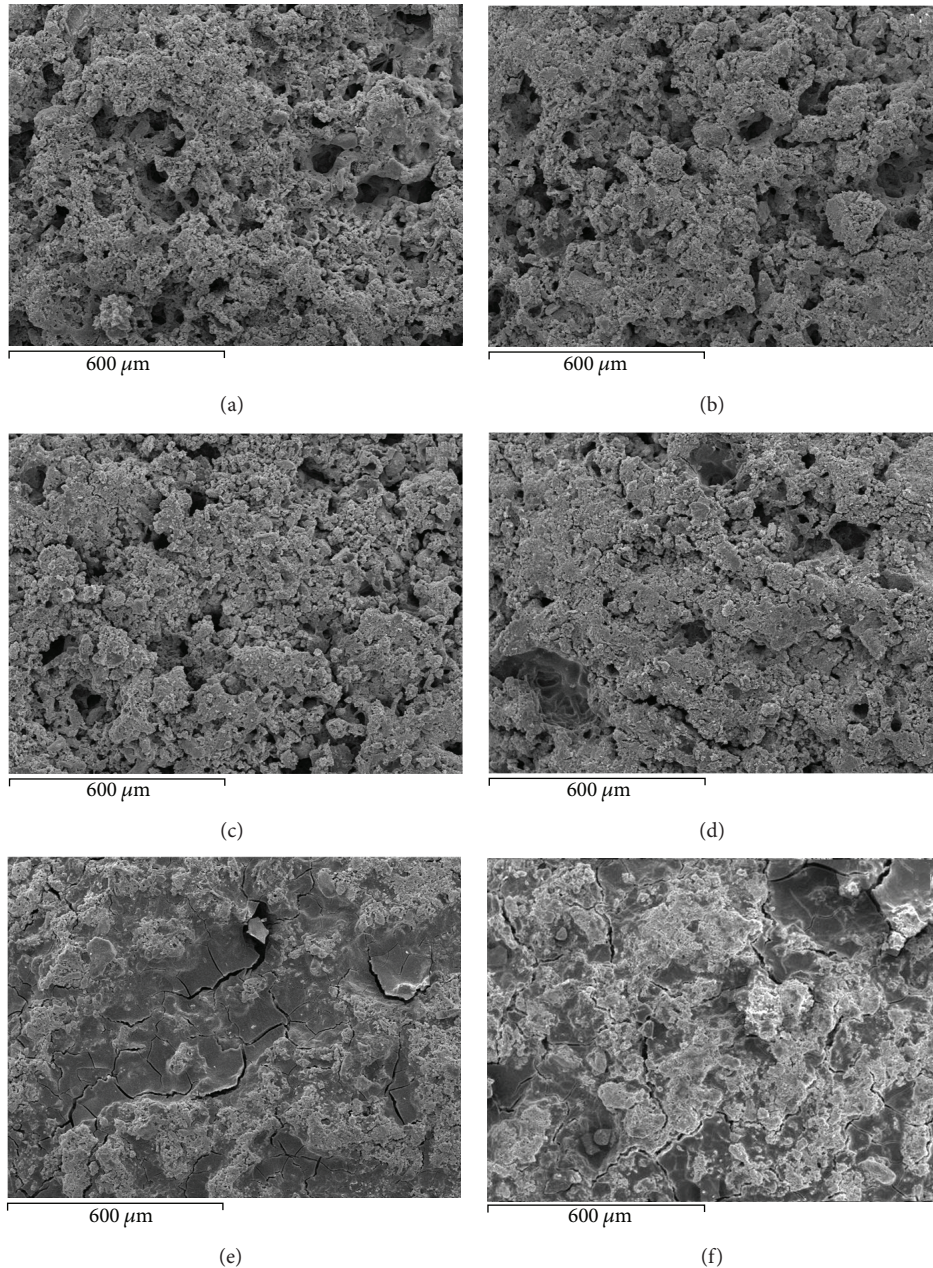


FIGURE 2: SEM images showing microstructure of nanosilver phosphate-doped hydroxyapatite and antibiotic impregnated nanosilver phosphate-doped hydroxyapatite samples: (a) HA_001; (b) HA_005; (c) HA_CN_001; (d) HA_CN_005; (e) HA_VC_001; (f) HA_VC_005. Scale bar = 600 μm .

3.3. Minimum Inhibition Concentration. Table 1 shows the MIC values for each antibiotic and silver nitrate (in the form of silver ions) against two bacterial strains. Gentamicin displayed the lowest MIC values, whereas vancomycin showed the highest values against *S. aureus*. In the case of *P. aeruginosa*, MIC value was not obtained for vancomycin since it is not active against gram negative bacteria. Silver ions showed lower MIC value than that of gentamicin.

3.4. Antibacterial Performance against *P. aeruginosa*. Figure 5 shows the antimicrobial performance of the samples against

P. aeruginosa. In the case of vancomycin impregnated samples (Figure 5(a)), no inhibition zone was seen for HA_VC sample since vancomycin was known to be inactive against gram negative strains [20]. In contrast, vancomycin impregnated nanosilver phosphate samples (HA_VC_001 and HA_VC_005) showed inhibition zone. However, the sizes of the inhibition zone at the same period were observed to be similar to those of the hydroxyapatite samples containing similar content of nanosilver phosphate such as HA_VC_001 versus HA_001 or HA_VC_005 versus HA_005. In the case of gentamicin impregnated samples (Figure 5(b)), all gentamicin impregnated samples showed inhibition zone.

TABLE I: Minimum inhibition concentration of the employed bacterial strains against each antibiotics and silver nitrate solution.

Antibiotics	Minimum inhibition concentration (g/mL)	
	<i>P. aeruginosa</i> ATCC 27853	<i>S. aureus</i> ATCC 25923
Vancomycin (VC)	No inhibition (>125)	0.975
Gentamicin (CN)	1.5625	0.0977
Ag ⁺ (AgNO ₃)	0.3125	0.3125

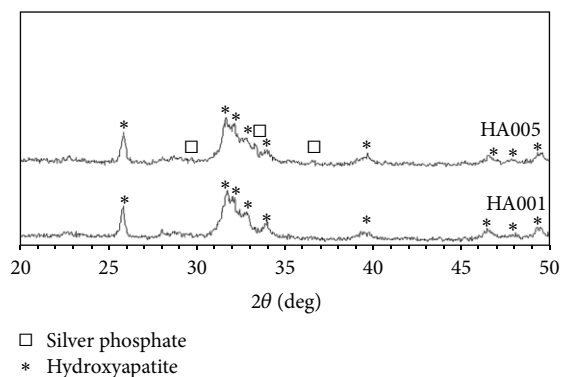


FIGURE 3: Phase composition of fabricated nanosilver phosphate-doped hydroxyapatite by low temperature phosphorization technique.

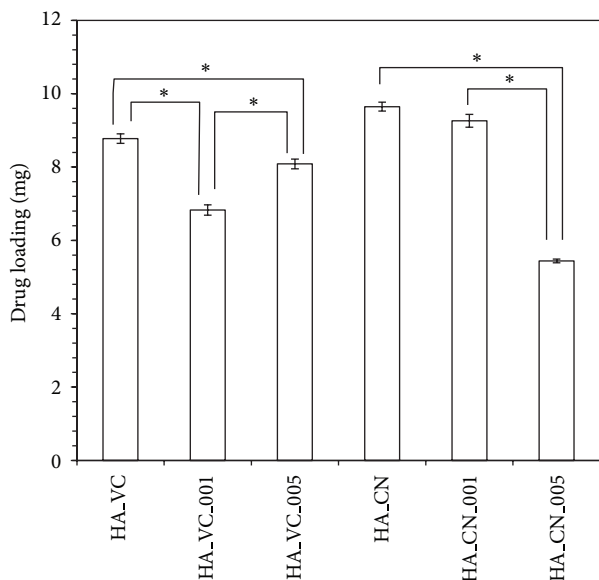


FIGURE 4: Total antibiotics content in the hydroxyapatite and nanosilver phosphate-doped hydroxyapatite samples (error bars = standard deviation, $n = 2$). * $P < 0.05$.

The inhibition zones of samples containing both gentamicin and nanosilver phosphate were significantly greater than those of samples containing nanosilver phosphate alone and exhibited decreasing trends with extraction periods, whereas the inhibition zone size of nanosilver phosphate-doped samples was relatively constant throughout the extraction periods. HA_001, HA_VC_001 and HA_CN_001 samples displayed antibacterial duration for about 7 days while HA_005,

HA_VC_005 and HA_CN_005 samples which contained large amount of nanosilver phosphate displayed longer antibacterial duration for about 15 days.

3.5. Antibacterial Performance against *S. aureus*. In the case of *S. aureus*, inhibition zones were seen for all samples. HA_001 showed limited antibacterial activity at day 2 extraction only while HA_005 displayed inhibition zone for only 5 days. The sizes of inhibition zone were also significantly lower than those of antibiotics impregnated nanosilver phosphate-doped samples. In the case of vancomycin impregnated samples (Figure 6(a)), HA_VC_005 showed the longest antibacterial duration followed by HA_VC and HA_VC_001, respectively. In contrast, both HA_CN_001 and HA_CN_005 showed about two times longer antibacterial duration than HA_CN sample (Figure 6(b)). The inhibition zones of samples containing both antibiotics and nanosilver phosphate displayed decreasing trends with extraction periods, whereas the inhibition zone size of nanosilver phosphate-doped samples was relatively constant throughout the extraction periods.

3.6. Cytotoxic Potential. Cytotoxic potential test (Figure 7) indicated that no cytotoxic potential at all extraction periods was observed for HA, HA_VC, and HA_VC_001 samples. However, HA_VC_005 sample showed cytotoxic potential (cell viability lower than 70%) even at day 3 extraction. In the case of gentamicin impregnated samples, HA_CN and HA_CN_005 samples displayed cytotoxic potential at day 1 extraction, whereas cytotoxic potential was observed until day 2 extraction for HA_CN_001 sample. In the case of nanosilver phosphate-doped hydroxyapatite alone, HA_001 sample displayed cytotoxic potential only at day 1 extraction, but no cytotoxic potential was observed at day 2 and longer extraction periods. HA_005 sample showed cytotoxic potential at all extraction periods, but cell viability tended to increase at longer extraction periods. The cell viability of the positive control sample remained low (less than 4%) at all extraction periods.

4. Discussion

A combination of a three dimensional printing technique and low temperature phosphorization process was previously shown to provide a simple mean to direct fabricate low crystalline nanostructure hydroxyapatite which is close to those of bone [21, 22]. This manufacturing route was subsequently developed to possess the antibacterial performance by employing either antibiotics impregnation or nanosilver compound incorporation [1, 2, 12, 23]. In this study, the

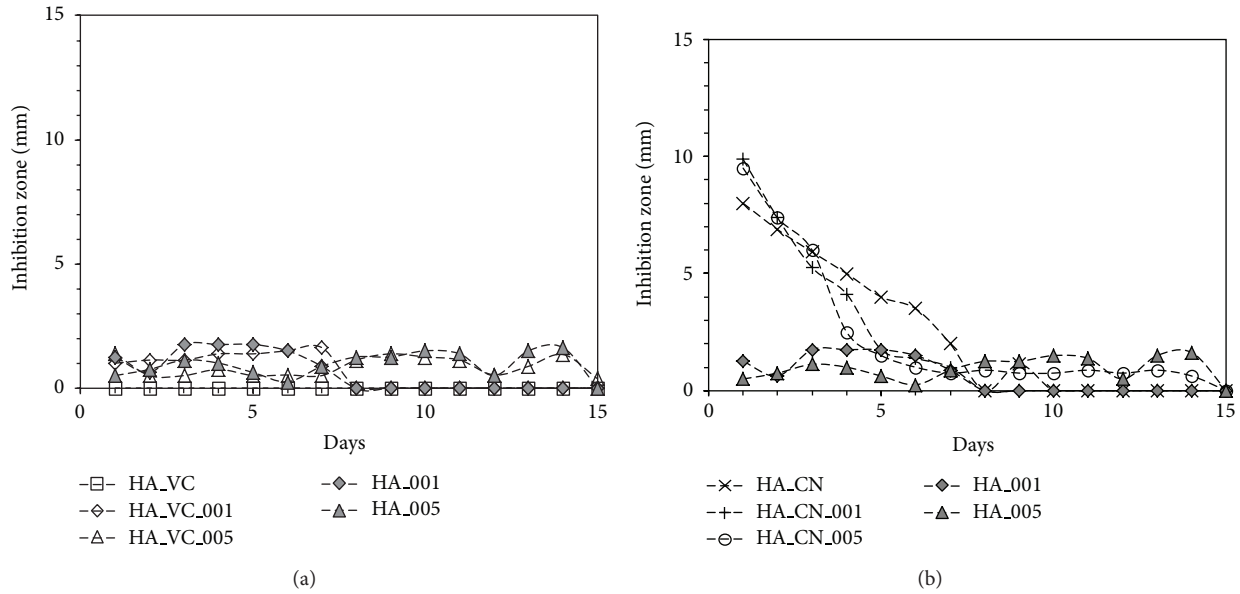


FIGURE 5: Antibacterial profile of VC (a) and CN (b) impregnated hydroxyapatites and nanosilver phosphate-doped hydroxyapatites against *P. aeruginosa* ($n = 2$).

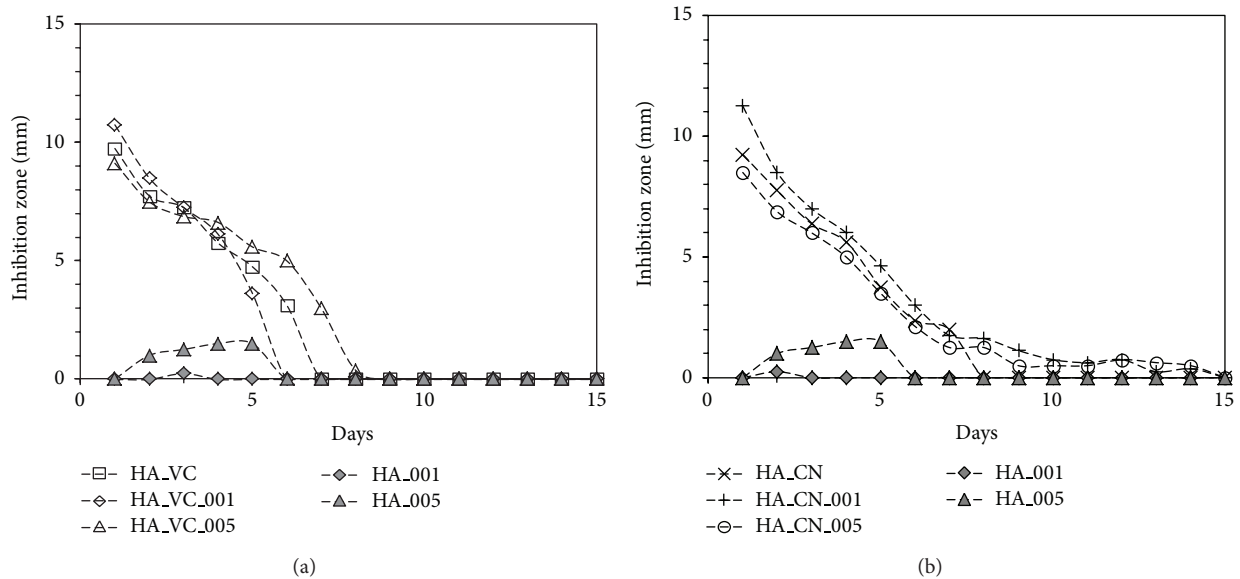


FIGURE 6: Antibacterial profile of VC (a) and CN (b) impregnated hydroxyapatites and nanosilver phosphate-doped hydroxyapatites against *S. aureus* ($n = 2$).

impregnation of antibiotics in nanosilver phosphate-doped hydroxyapatite was further developed to further provide the improvement in antibacterial performance of hydroxyapatite.

From XRD analysis, the characteristic peaks of nanosilver phosphate-doped hydroxyapatite were found to be broad and overlapped indicating the low crystallinity and nanosized crystals of the materials similar to those of bone mineral [24, 25]. Only silver phosphate peaks were observed without any other metallic silver bands. SEM and TEM analysis showed that the fabricated 3DP nanosilver phosphate-doped hydroxyapatite was highly porous and

comprised the distribution of nanosized silver phosphate particles in the structure of nanosized hydroxyapatite crystals. After impregnation by antibiotics, difference in loading efficiency was observed. This difference in drug loading efficiency for both antibiotics could be related to the microstructure of the samples as a result of the fabrication process. The increase in degree of nanosilver phosphate incorporation in the sample tended to decrease the adsorption sites for the drugs in the samples due to the greater number and size of formed silver phosphate particles which could obstruct the diffusion of antibiotics solution into the samples. In

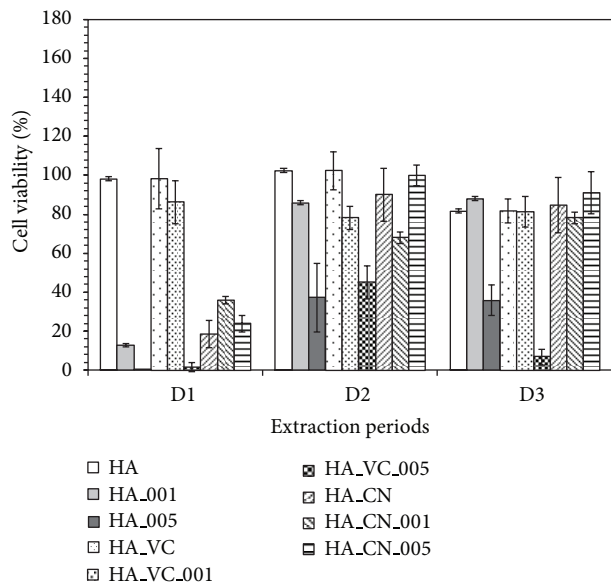


FIGURE 7: Cell viability of antibiotics impregnated nanosilver phosphate-doped hydroxyapatite samples using serial extraction technique (error bars = standard deviation, $n = 3$).

the case of vancomycin impregnated samples, the reincrease in antibiotics content in HA_VC.005 was noted. It was thought that this might be related to the greater gelling tendency of vancomycin on the sample surface than that of gentamicin. However, further investigation is needed to clarify this observation.

In term of antibacterial activity, no enhancement was observed from the combination of nanosilver phosphate and vancomycin against *P. aeruginosa*. However, some improvement in antibacterial duration for HA_VC.005 (7 days) when testing against *S. aureus* compared to HA_VC (6 days) or HA_005 (5 days) was noted. The combination of nanosilver phosphate and gentamicin seemed to give greater enhancement in antibacterial activity than vancomycin. This is possible due to the greater spectrum of activity, lower molar mass and lower minimum inhibitory concentration (MIC) of gentamicin [26]. MIC determination in Table 1 also confirmed that vancomycin has higher MIC values than both gentamicin and silver ions. In the case of *P. aeruginosa*, 21% and 814% increase in inhibition zone size at day 1 of both gentamicin impregnated nanosilver phosphate-doped samples (9.5–9.87 mm) compared to HA_CN (8 mm) and nanosilver phosphate-doped samples alone (0.87–1.25 mm), respectively, was observed. However, no improvement in antibacterial duration was observed. This improvement was thought to be the additional effect since the increase in the inhibition zone size was resulted from the sum of those of HA_CN and HA_001 or HA_005 samples. In the case of *S. aureus*, the enhancement in both initial inhibition zone size at day 1 and the antibacterial duration was seen for HA_CN_001, but not for HA_CN_005. A 22% increase in inhibition zone size at day 1 of HA_CN_001 (11.25 mm) compared to HA_CN (9.25 mm) was observed. The antibacterial duration

increased from 7 days for HA_CN to 14 days for HA_CN_001. Therefore, the synergic effect resulting from the combination of gentamicin and nanosilver phosphate in HA_CN_001 was observed against *S. aureus*. The absence in enhancement of HA_CN_005 was thought to be due to its low gentamicin loading (Figure 4) which might be not sufficient to produce an improvement when combined with nanosilver phosphate. The antibacterial activity of nanosilver particles was generally attributed to its small size that could attach or penetrate the cell membrane of bacteria and disrupt the integrity of bacterial membrane [27, 28]. The possible mechanism of synergic antibacterial effect of nanosilver particles and antibiotics combination was hypothesized to be due to the binding of drug molecules onto the nanosilver which increasing the destruction and penetration into the cell wall of bacteria [16, 17]. However, in this study, nanosilver phosphate particles were incorporated into hydroxyapatite structure and could not attach and penetrate the cell membrane by themselves but only release silver ions to produce the antibacterial activity [27]. Therefore, the degree of bactericidal performance of nanosilver phosphate-doped hydroxyapatite was expected to be different from that of nanosilver phosphate particles. In this case, silver ions which were released from nanosilver phosphate-doped hydroxyapatite would prevent the DNA of bacteria from unwinding [17]. This would result in the difference in antibacterial activity enhancement caused by antibiotics impregnated nanosilver phosphate-doped hydroxyapatite as prepared in this study and the direct combination of nanoparticles and antibiotics as reported previously [13–17].

Cytotoxic potential of antibiotics impregnated samples and nanosilver phosphate-doped samples alone could be related to the amount of released silver and type of antibiotics. It was reported previously that vancomycin was less toxic to osteoblasts than gentamicin and required greater concentration to induce cytotoxicity [29, 30]. Therefore, HA_VC was less cytotoxic than HA_CN and HA_001 was less cytotoxic than HA_005. When the extraction periods increased, lower concentrations of both antibiotics and silver were released from the samples so the level of cytotoxic of the samples diminished with increasing numbers of extraction periods [31–33]. In the case of samples containing both nanosilver phosphate and antibiotics, HA_VC_005 samples showed cytotoxic potential even at day 3, whereas HA_VC and HA_VC_001 did not showed cytotoxic at all periods. This could be related to the cytotoxic potential of silver ions that was released from HA_005 samples which also showed cytotoxic potential at all periods. In the case of HA_VC_001, the noncytotoxic potential was possibly due to the lower level of released silver ions and the non-cytotoxic potential of vancomycin. In the case of gentamicin impregnated nanosilver phosphate-doped hydroxyapatite, HA_CN_001 showed the lower cell viability than HA_CN and HA_CN_005. One might expect that HA_CN_005 would show the greatest cytotoxic potential since it contained greater amount of silver phosphate similarly to that of HA_VC_005 sample. Unlike vancomycin, gentamicin was observed to be cytotoxic to osteoblasts. Thus, the content of gentamicin in the samples that could be released and resulted in cytotoxic

potential should also be taken into account. It was found that the gentamicin loading in HA_CN_001 was similar to that of HA_CN while that of HA_CN_005 was about twice lower (Figure 4). Therefore, the greater cytotoxic potential of HA_CN_001 was thought to be due to the combination of high content of gentamicin and nanosilver phosphate compared to the cytotoxic potential of gentamicin only in HA_CN and lower gentamicin content and higher silver phosphate content in HA_CN_005.

5. Conclusion

The combined use of nanosilver phosphate and antibiotics could enhance the antibacterial performance of the hydroxyapatite samples. Synergic enhancement was found for gentamicin impregnated nanosilver phosphate-doped hydroxyapatite against *S. aureus*, but additive effect was observed against *P. aeruginosa*. Limited enhancement was observed for vancomycin impregnated nanosilver phosphate-doped hydroxyapatite against *S. aureus*, but no improvement was seen against *P. aeruginosa*. These behaviors were related to the antibiotics and nanosilver phosphate content in the samples, type of antibiotics used, and bacterial strains tested.

Conflict of Interests

The authors declare that there is no conflict of interests regarding the publication of this paper.

Acknowledgments

Lafarge Prestia Co., Ltd. is thanked for the supply of calcium sulfate and Thaiwah Co., Ltd, Thailand, for the supply of pregelatinized starch. Cluster and Program Management Office, National Science and Technology Development Agency is acknowledged for financial support. W. Chokevivat (MTEC) was thanked for cytotoxic potential study.

References

- [1] F. Thammarakcharoen and J. Suwanprateeb, "The effect of bead size on drug loading and releasing characteristic of antibiotic loaded 3DP calcium phosphate bead," in *Proceedings of the Pure and Applied Chemistry International Conference*, pp. 473–476, 2011.
- [2] P. Phanphiriya, F. Thammarakcharoen, W. Chokevivat, and J. Suwanprateeb, "Antimicrobial performance and cytotoxicity of antibiotics impregnated hydroxyapatite for osteomyelitis treatment," *Advanced Materials Research*, vol. 506, pp. 513–516, 2012.
- [3] Y. Shinto, A. Uchida, F. Korkusuz, N. Araki, and K. Ono, "Calcium hydroxyapatite ceramic used as a delivery system for antibiotics," *Journal of Bone and Joint Surgery B*, vol. 74, no. 4, pp. 600–604, 1992.
- [4] Y. Yamashita, A. Uchida, T. Yamakawa, Y. Shinto, N. Araki, and K. Kato, "Treatment of chronic osteomyelitis using calcium hydroxyapatite ceramic implants impregnated with antibiotic," *International Orthopaedics*, vol. 22, no. 4, pp. 247–251, 1998.
- [5] A. Ślósarczyk, J. Szymura-Oleksiak, and B. Mycek, "The kinetics of pentoxifylline release from drug-loaded hydroxyapatite implants," *Biomaterials*, vol. 21, no. 12, pp. 1215–1221, 2000.
- [6] F. Chai, J.-C. Hornez, N. Blanchemain, C. Neut, M. Descamps, and H. F. Hildebrand, "Antibacterial activation of hydroxyapatite (HA) with controlled porosity by different antibiotics," *Biomolecular Engineering*, vol. 24, no. 5, pp. 510–514, 2007.
- [7] C. Marambio-Jones and E. M. V. Hoek, "A review of the antibacterial effects of silver nanomaterials and potential implications for human health and the environment," *Journal of Nanoparticle Research*, vol. 12, no. 5, pp. 1531–1551, 2010.
- [8] S. Sarkar, A. D. Jana, S. K. Samanta, and G. Mostafa, "Facile synthesis of silver nano particles with highly efficient antimicrobial property," *Polyhedron*, vol. 26, no. 15, pp. 4419–4426, 2007.
- [9] Y. Li, L. Li, J. Li et al., "Antibacterial properties of nanosilver PLLA fibrous membranes," *Journal of Nanomaterials*, vol. 2009, Article ID 168041, 5 pages, 2009.
- [10] C.-T. Dinh, T.-D. Nguyen, F. Kleitz, and T.-O. Do, "Large-scale synthesis of uniform silver orthophosphate colloidal nanocrystals exhibiting high visible light photocatalytic activity," *Chemical Communications*, vol. 47, no. 27, pp. 7797–7799, 2011.
- [11] J. J. Buckley, A. F. Lee, L. Olivi, and K. Wilson, "Hydroxyapatite supported antibacterial Ag₃PO₄ nanoparticles," *Journal of Materials Chemistry*, vol. 20, no. 37, pp. 8056–8063, 2010.
- [12] J. Suwanprateeb, F. Thammarakcharoen, K. Wasoontarat, W. Chokevivat, and P. Phanphiriya, "Preparation and characterization of nanosized silver phosphate loaded hydroxyapatite by single step co-conversion process," *Materials Science and Engineering C*, vol. 32, pp. 2122–2128, 2012.
- [13] K. I. Wolska, K. Grzes, and A. Kurek, "Synergy between novel antimicrobials and conventional antibiotics or bacteriocins," *Polish Journal of Microbiology*, vol. 61, pp. 95–104, 2012.
- [14] S. Ruden, K. Hilpert, M. Berditsch, P. Wadhvani, and A. S. Ulrich, "Synergistic interaction between silver nanoparticles and membrane-permeabilizing antimicrobial peptides," *Antimicrobial Agents and Chemotherapy*, vol. 53, no. 8, pp. 3538–3540, 2009.
- [15] G. Geoprincy, P. Saravanan, N. Nagendra Gandhi, and S. Renganathan, "A novel approach for studying the combined antimicrobial effects of silver nanoparticles and antibiotics through agar over layer method and disk diffusion method," *Digest Journal of Nanomaterials and Biostructures*, vol. 6, no. 4, pp. 1557–1565, 2011.
- [16] A. M. Fayaz, K. Balaji, M. Girilal, R. Yadav, P. T. Kalaichelvan, and R. Venketesan, "Biogenic synthesis of silver nanoparticles and their synergistic effect with antibiotics: a study against gram-positive and gram-negative bacteria," *Nanomedicine: Nanotechnology, Biology, and Medicine*, vol. 6, no. 1, pp. e103–e109, 2010.
- [17] P. Li, J. Li, C. Wu, Q. Wu, and J. Li, "Synergistic antibacterial effects of β -lactam antibiotic combined with silver nanoparticles," *Nanotechnology*, vol. 16, no. 9, pp. 1912–1917, 2005.
- [18] P. J. Carek, L. M. Dickerson, and J. L. Sack, "Diagnosis and management of osteomyelitis," *American Family Physician*, vol. 63, no. 12, pp. 2413–2420, 2001.
- [19] P. D. P. Lew and P. F. A. Waldvogel, "Osteomyelitis," *The Lancet*, vol. 364, no. 9431, pp. 369–379, 2004.

- [20] O. S. Kluin, H. C. van der Mei, H. J. Busscher, and D. Neut, "A surface-eroding antibiotic delivery system based on poly-(trimethylene carbonate)," *Biomaterials*, vol. 30, no. 27, pp. 4738–4742, 2009.
- [21] J. Suwanprateeb, W. Suvannapruk, and K. Wasoontarat, "Low temperature preparation of calcium phosphate structure via phosphorization of 3D-printed calcium sulfate hemihydrate based material" *Journal of Materials Science: Materials in Medicine*, vol. 21, no. 2, pp. 419–429, 2010.
- [22] J. Suwanprateeb, F. Thammarakcharoen, K. Wasoontarat, and W. Suvannapruk, "Influence of printing parameters on the transformation efficiency of 3D-printed plaster of paris to hydroxyapatite and its properties," *Rapid Prototyping Journal*, vol. 18, pp. 490–499, 2012.
- [23] J. Suwanprateeb, F. Thammarakcharoen, K. Wasoontarat, W. Chokeyivat, and P. Phanphiriya, "Single step preparation of nanosilver loaded calcium phosphate by low temperature co-conversion process," *Journal of Materials Science: Materials in Medicine*, vol. 23, pp. 2091–2100, 2012.
- [24] R.-J. Chung, "Study of hydroxyapatite nano composites with photoluminescence properties," *Biomedical Engineering*, vol. 23, no. 2, pp. 107–112, 2011.
- [25] F. Peters, K. Schwarz, and M. Epple, "The structure of bone studied with synchrotron X-ray diffraction, X-ray absorption spectroscopy and thermal analysis," *Thermochimica Acta*, vol. 361, no. 1-2, pp. 131–138, 2000.
- [26] S. Alvarez, M. Jones, and S. L. Berk, "In vitro activity of fosfomycin, alone and in combination, against methicillin-resistant *Staphylococcus aureus*," *Antimicrobial Agents and Chemotherapy*, vol. 28, no. 5, pp. 689–690, 1985.
- [27] J. R. Morones, J. L. Elechiguerra, A. Camacho et al., "The bactericidal effect of silver nanoparticles," *Nanotechnology*, vol. 16, no. 10, pp. 2346–2353, 2005.
- [28] M. J. Hajipour, K. M. Fromm, A. A. Ashkarran et al., "Antibacterial properties of nanoparticles," *Trends in Biotechnology*, vol. 30, pp. 499–511, 2012.
- [29] V. Antoci Jr., C. S. Adams, N. J. Hickok, I. M. Shapiro, and J. Parvizi, "Antibiotics for local delivery systems cause skeletal cell toxicity in vitro," *Clinical Orthopaedics and Related Research*, no. 462, pp. 200–206, 2007.
- [30] C. R. Rathbone, J. D. Cross, K. V. Brown, C. K. Murray, and J. C. Wenke, "Effect of various concentrations of antibiotics on osteogenic cell viability and activity," *Journal of Orthopaedic Research*, vol. 29, no. 7, pp. 1070–1074, 2011.
- [31] W. Chen, Y. Liu, H. S. Courtney et al., "In vitro anti-bacterial and biological properties of magnetron co-sputtered silver-containing hydroxyapatite coating," *Biomaterials*, vol. 27, no. 32, pp. 5512–5517, 2006.
- [32] B. Singh, A. K. Dubey, S. Kumar, N. Saha, B. Basu, and R. Gupta, "In vitro biocompatibility and antimicrobial activity of wet chemically prepared $\text{Ca}_{10-x}\text{Ag}_x(\text{PO}_4)_6(\text{OH})_2$ ($0.0 \leq x \leq 0.5$) hydroxyapatites," *Materials Science and Engineering C*, vol. 31, no. 7, pp. 1320–1329, 2011.
- [33] G. Gosheger, J. Hardes, H. Ahrens et al., "Silver-coated megaendoprostheses in a rabbit model—an analysis of the infection rate and toxicological side effects," *Biomaterials*, vol. 25, no. 24, pp. 5547–5556, 2004.

Research Article

Iron Oxide Magnetic Nanoparticles: Characterization and Toxicity Evaluation by *In Vitro* and *In Vivo* Assays

Alina Mihaela Prodan,^{1,2} Simona Liliana Iconaru,³ Carmen Steluta Ciobanu,³
Mariana Carmen Chifiriuc,⁴ Mihai Stoicea,² and Daniela Predoi³

¹ Carol Davila University of Medicine and Pharmacy, 8 Eroii Sanitari, Sector 5, 050474 Bucharest, Romania

² Emergency Hospital Floreasca, Bucharest 5, Calea Floreasca Nr 8, Sector 1, 014461 Bucarest, Romania

³ National Institute of Materials Physics, 105 bis Atomistilor, P.O. Box MG 07, 077125 Bucuresti-Magurele, Romania

⁴ Microbiology Department, Faculty of Biology, University of Bucharest, Aleea Portocalelor 1-3, 60101 Bucharest, Romania

Correspondence should be addressed to Daniela Predoi; dpredoi@gmail.com

Received 21 August 2013; Revised 4 October 2013; Accepted 5 October 2013

Academic Editor: In-Kyu Park

Copyright © 2013 Alina Mihaela Prodan et al. This is an open access article distributed under the Creative Commons Attribution License, which permits unrestricted use, distribution, and reproduction in any medium, provided the original work is properly cited.

The aim of this study was to evaluate the biological properties of iron oxide nanoparticles (IO-NPs) obtained in the aqueous suspension. The iron oxide nanoparticles were characterized by scanning electron microscopy (SEM) and transmission electron microscopy (TEM). The biocompatibility of the iron oxide was demonstrated by the *in vitro* quantification of HeLa cells viability using propidium iodide (PI) and fluorescein diacetate (FdA) and the MTT colorimetric assay. The toxicity of small size iron oxide nanoparticles was also evaluated by means of histological examination on male Brown Norway rats after intraperitoneal injection. At the tested concentrations, the nanoparticles proved to be not cytotoxic on HeLa cells. The rat's behavior, as well as the histopathological aspect of liver, kidney, lung, and spleen tissues at 48 h after intraperitoneal injection did not present any modifications. The *in vivo* and *in vitro* assays suggested that the IO-NPs could be further used for developing new *in vivo* medical applications.

1. Introduction

Nowadays, finding new approaches for solving pressing problems in the field of medical science is the focus of research institutes everywhere. The most studied materials with promising potential in the field of biomedical applications are those with magnetic properties. Magnetic materials, especially iron oxides nanoparticles, are known since ancient times to have many spectacular properties, but in the last decade the properties that they possess at nanometric scale have been the starting point of great potential applications such as drug delivery, magnetic cell separation, tumor labeling and cell labeling. The most common forms of iron oxides, magnetite and maghemite (Fe_3O_4 , $\gamma\text{-Fe}_2\text{O}_3$), are studied due to the outstanding properties they exhibit at nanometric scale (high specific surface area, superparamagnetism, etc.) [1–5]. The nanometric dimensions of these materials makes them ideal candidates for surface engineering and functionalization. Surface enhancement and functionalization facilitate

the use of these nanomaterials in biomedical applications, for example, as contrast agents for magnetic resonance imaging (MRI) [6, 7], tissue-specific release of therapeutic agents, targeted drug delivery in tumor therapy [8], hyperthermia, cell labeling [9], magnetic cell sorting [10], and magnetic field assisted radionuclide therapy [11].

In the past few years, superparamagnetic iron oxide nanoparticles with controlled and enhanced surface chemistry properties have been used successfully as contrast agents for magnetic resonance imaging *in vivo* [12, 13]. The new direction of research aims to develop new compounds based on iron oxide nanoparticles for *in vivo* biomedical applications. Recent studies in the field of malignant tumors are focused on developing a new drug delivery systems based on iron oxide nanoparticles in order to avoid damaging the healthy cells around the tumor mass in the process of cancerous cell destruction. These types of nanosystems based on iron oxide nanoparticles have the ability to heat up,

delivering toxic amounts of thermal energy to tumors, or as chemotherapy and radiotherapy enhancement agents, where a controlled degree of tissue warming leads to an effective cell destruction [14, 15].

In agreement with Pisanic II et al. [16], magnetic nanoparticles could be used as tools in a wide variety of biomedical applications. On the other hand, Pisanic II et al. showed that failure to fully and properly evaluate nanostructures on an individual case-by-case basis may lead to lack of parameter control in *in vitro* experiments, as well as incorrect assumptions concerning their biocompatibility and biosafety of their *in vivo* use [16]. In order to improve the knowledge on cytotoxicity of iron oxide nanoparticles, we performed an *in vivo* toxicity study (48 h) by administration by intraperitoneal injection of γ -Fe₂O₃ dispersion at concentrations of 0.7 mL/kg, 1.7 mL/kg, and 3.7 mL/kg.

The aim of this study was to develop iron oxide nanoparticles by an adapted coprecipitation method [17–22] with controllable parameters and enhanced biocompatible properties for *in vivo* applications. Scanning electron microscopy (SEM) and transmission electron microscopy (TEM) studies have been conducted to obtain information about the size, structure, and morphology of IO-NPs. The biocompatibility of the iron oxide was evaluated using *in vitro* and *in vivo* assays, consisting in the quantification of HeLa cells viability and the histological evaluation of the nanoparticles effects on the male Brown Norway rat's tissues.

2. Experimental Section

2.1. Materials. Ferrous chloride tetrahydrate (FeCl₂·4H₂O), ferric chloride hexahydrate (FeCl₃·6H₂O), sodium hydroxide (NaOH), and chlorhydric acid (HCl) were purchased from Merck. Deionized water was used in the synthesis of nanoparticles and for rinsing the clusters.

2.2. Synthesis of Iron Oxide Ferrofluid. Iron oxide nanoparticles were prepared by coprecipitation [17–22]. Ferrous chloride tetrahydrate (FeCl₂·4H₂O) in 2 M HCl and ferric chloride hexahydrate (FeCl₃·6H₂O) were mixed at 100°C (Fe²⁺/Fe³⁺ = 1/2). The mixture was dropped into 200 mL of NaOH (2 mol·L⁻¹) solution under vigorous stirring for about 30 min. The precipitate of magnetite (black precipitate immediately formed) was converted into γ -Fe₂O₃ particles by repeated treatment with HNO₃ (2 mol·L⁻¹) and FeNO₃ (0.3 mol·L⁻¹) solutions [23]. The acidic precipitate was isolated by decantation on a magnet, separated by centrifugation (6000 rpm), then washed in acetone, and dispersed in deionized water at pH = 2.5. The final ion concentration was 0.38 mol·L⁻¹. For biological investigations, the pH was adjusted to 7 using aqueous ammonia. The iron content of the suspensions was determined by redox-titration [23].

2.3. Characterization of Nanoparticles. The morphology of the obtained material was studied using a Quanta Inspect F scanning electron microscope (SEM), operating at 25 kV in vacuum. The elemental local analysis was performed using an energy dispersive spectroscopy (EDS) detector

from EDAX. The operating conditions were an accelerating voltage between 2 and 25 keV (depending of the signal/noise ratio) for samples tilted at 25° in order to get the optimal take off angle (30°) allowing a dead time around 20–30% and a collecting time of 90–120 s. Transmission electron microscopy (TEM) images for these samples were recorded using a FEI Tecnai 12 equipped with a low dose digital camera from Gatan. The specimen for TEM imaging was prepared by ultramicrotomy in order to obtain a thin section of about 60 nm. The powder was embedded in an epoxy resin (polaron 612) before microtomy.

2.4. Cytotoxicity Assay. Quantification of cell viability was performed using propidium iodide (PI) and fluorescein diacetate (FdA). Briefly, 5 × 10⁴ HeLa cells were seeded in each well of a 24-well plate and after 24 h, the monolayers were treated with a suspension of γ -Fe₂O₃ (200 μL) nanoparticles diluted 100 times. The effects on cellular viability were evaluated after 48 h by adding 100 μL PI (0.1 mg/mL) and 100 μL FdA (0.1 mg/mL) and fluorescence studies have been performed using Observer D1 Carl Zeiss microscope. The cell viability was established by the ratio between viable (green) and dead cells (red) counted on several microscopic fields [24].

The cell viability was determined by MTT colorimetric assay developed by Mosmann for *in vitro* cytotoxicity and cell proliferation measurements [25]. It was reported that the mitochondrial enzyme succinate-dehydrogenase within viable cells is able to cleave the MTT salt into formazan, a blue colored product. The amount of formazan produced, read on scanning multiwell spectrophotometer, is proportional to the number of viable cells present [25–27]. The cells were cultured in the medium (2.5 × 10⁵ cells/mL) containing iron oxide nanoparticles for 12, 24, and 72 hours periods. Culture medium without iron oxide nanoparticles served as control in each experiment. The different final concentrations of the suspension of iron oxide nanoparticles were prepared in cell growth medium. Concentration ranges were 10, 20, and 30 μg/mL. The medium from each well was removed by aspiration, the cells were washed with 200 μL phosphate buffer saline solution (PBS)/well, and then 50 μL of 1 mg/mL MTT solution was added on each well. After 2 h of incubation, the MTT solution from each well was removed by aspiration. A volume of 50 μL isopropanol was added and the plate was shaken to dissolve formazan crystals. The optical density at 595 nm, for each well, was then determined using a Tecan multiplate reader (Tecan GENios, Grödic, Germany). The percent of viable cells cultured on the iron oxide nanoparticles was calculated in comparison with a control sample; the cells cultured on uncoated culture plastic vessels, being considered to have a viability of 100%.

2.5. Animals. Male Brown Norway rats (weighing ~300 ± 10 g) were purchased from the National Institute of Research and Development for Microbiology and Immunology “Cantacuzino,” Bucharest. The rats were housed in an environment controlled for temperature (22 ± 2°C), light (12 h light/dark cycles), and humidity (60 ± 10%). The animals were maintained under specific pathogen free-conditions in accordance with NIH Guide for the Care and Use of laboratory Animals.

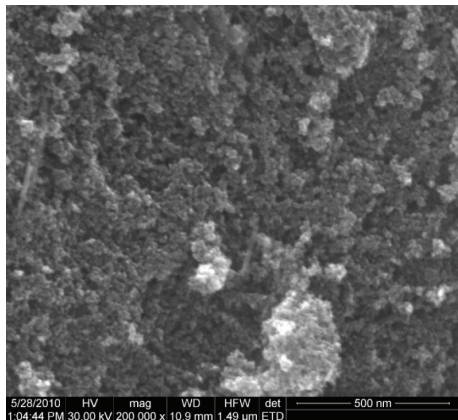


FIGURE 1: Scanning electron microscopy image of the synthesized iron oxide sample.

2.6. Histological Examination. For the analysis of iron oxide toxicity *in vivo*, the rats ($n = 4$ per group) were treated with normal saline and iron oxide (at concentrations of 0.7 mL/kg, 1.7 mL/kg, and 3.7 mL/kg) via intraperitoneal injection. The final iron concentration in iron oxide solution prepared by coprecipitations was $0.38 \text{ mol}\cdot\text{L}^{-1}$. For histopathological examinations, selected organs (liver, kidney, lung and spleen) were removed from the rats and fixed in 10% formalin. The organs were prepared as paraffin-embedded glass slides stained with hematoxylin and eosin. The morphological changes were observed by microscopic examination [28].

3. Results and Discussion

SEM analysis was used to confirm the morphology of the synthesized iron oxide sample (Figure 1). The obtained results using scanning electron microscopy analysis clearly show that the IO-NPs have spherical shape. Detailed structural information and the growth direction of the maghemite, $\gamma\text{-Fe}_2\text{O}_3$, were obtained from TEM and HRTEM micrographs.

Figure 2(a) shows TEM picture of iron oxide nanoparticles (IO-NPs), clearly showing that the product is entirely composed of crystals with a relatively uniform, spherical morphology. Grain size distribution was determined by measuring the mean diameter, D , of about 500 particles on the micrographs (Figure 2(b)). TEM images indicate a very uniform size distribution of iron oxide nanoparticles. The average grain size of the monodisperse nanoparticles is $10 \pm 0.3 \text{ nm}$. Figure 2(c) shows the selected area electron diffraction (SAED) pattern recorded from an area containing a large number of nanoparticles and the high-resolution TEM picture. The rings in the SAED pattern can be indexed as the (220), (311), (400), (422), (511), and (440) reflections of the cubic maghemite in agreement with the XRD results [29].

Despite the great potential of iron nanoparticles to be used for different industrial and medical applications, data about their toxicity are still scarce [30]. Bearing in mind that *in vitro* tests represent a first step of biomedical application investigation [31], we have studied the toxicity of the obtained nanoparticles on HeLa cells. It has been previously

established that the optimum size of magnetic nanoparticles to promote an effective biodistribution is ranging from 10 to 100 nm [32]. From this point of view, the obtained nanoparticles meet this criterium, with a diameter of 10 nm. The results have shown that the obtained nanoparticles were not cytotoxic on the HeLa cells after 48 h exposure to a suspension of $\gamma\text{-Fe}_2\text{O}_3$ (200 μL) nanoparticles diluted 100 times (Figure 3(b)), as revealed by the absence of dead, red cells stained with propidium iodide (Figure 3). The low cytotoxicity of iron nanoparticles has been reported also by other authors and has been explained by the fact that the nanoparticles are not degraded within the timescale of the cellular assay (48 h) [33].

To examine the cytotoxicity of the iron oxide nanoparticles, the MTT assay was used. The HeLa cells were treated on/in a medium containing different concentrations (10, 20, and 30 $\mu\text{g}/\text{mL}$) of the suspension of iron oxide nanoparticles. Cell viability was determined at 12 h, 24 h, and 72 h after treatment and the test results are shown in Figure 4. We can see that the cell viability decreased when the concentration and time period increased. These results are in agreement with previous studies presented by Kouchesfehiani et al. [34]. The toxic effect was taken into consideration when the survival rate was below 80%. The graph shows the mean \pm s.d. of normalized values on three independent experiments.

The *in vivo* toxicity study (48 h) was performed with $\gamma\text{-Fe}_2\text{O}_3$ dispersion administered by intraperitoneal injection at concentrations of 0.7 mL/kg, 1.7 mL/kg, and 3.7 mL/kg. The rats were observed after 48 h from each administration and their behavior was evaluated. All animals survived the administration of $\gamma\text{-Fe}_2\text{O}_3$ on all tested concentrations and did not show any sign of discomfort (lethargy, nausea, vomiting or diarrhea) during the whole duration of the experiment. The histopathological assessment of the selected tissues including liver, kidney, lung, and spleen was conducted.

At 48 h after the intraperitoneal injection no significant macroscopic histopathological changes were observed in the case of liver and kidney for all tested concentrations in the treated group compared with the control.

In Figure 5, the microscopic observations of the rat liver injected with different $\gamma\text{-Fe}_2\text{O}_3$ concentrations after 48 h are shown. The microscopic observations of the rat kidney injected with different $\gamma\text{-Fe}_2\text{O}_3$ concentrations after 48 h are presented in Figure 6.

Pathological sections of liver after injection with a 0.7 mL/kg dose of iron oxide nanoparticles (Figure 5(b)) show that the architecture of the liver was not affected by IO-NPs (0.7 mL/kg). Hepatocytes with discreet anisokaryosis, formation of chromocenters and nucleoli, and focal intrahepatocyte cholestasis (HE, 600x) were found in the liver of both the IO-NPs (0.7 mL/kg) treated and control groups (Figure 5(a)) with no significant difference between them. Greaves in histopathology of preclinical toxicity studies [35] showed that laboratory animals under conventional housing can undergo liver changes. On the other hand, he showed that granulomas are common spontaneous lesions in the liver. The liver changes may occur due to multiple causes such as drugs, bacterial, fungal, parasitic or viral infections, and liver or systemic disorders and are usually asymptomatic [36].

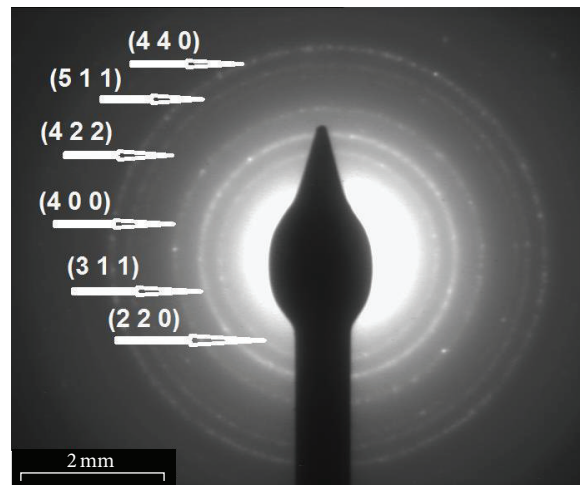
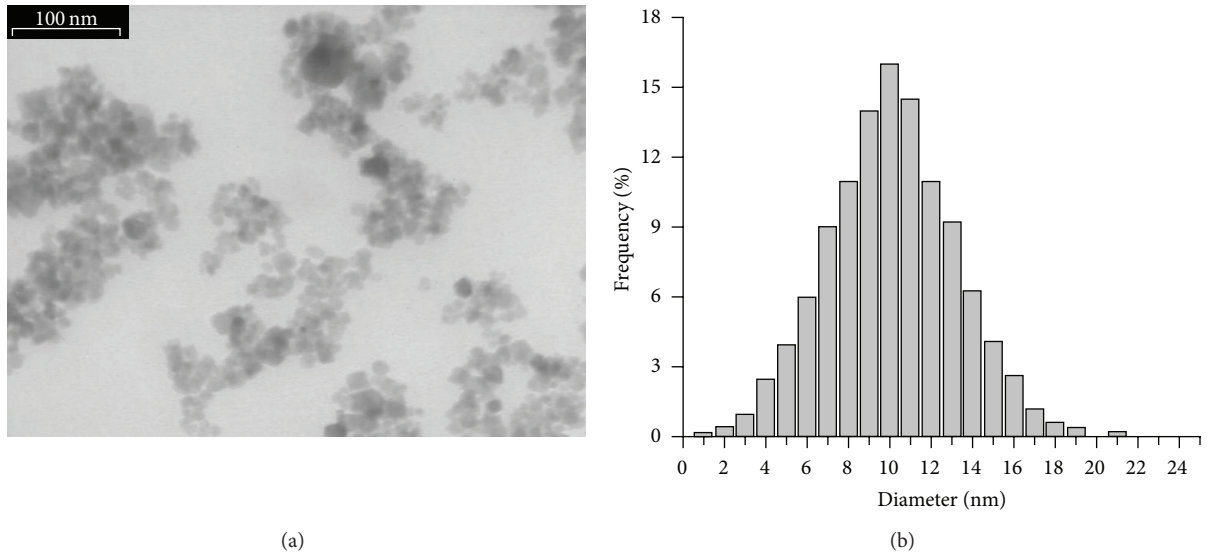


FIGURE 2: Bright field TEM picture showing a homogeneous distribution of iron oxide nanoparticles (a), size distribution of IO-NPs (b), and SAED pattern from a region including a large number of nanoparticles (c).

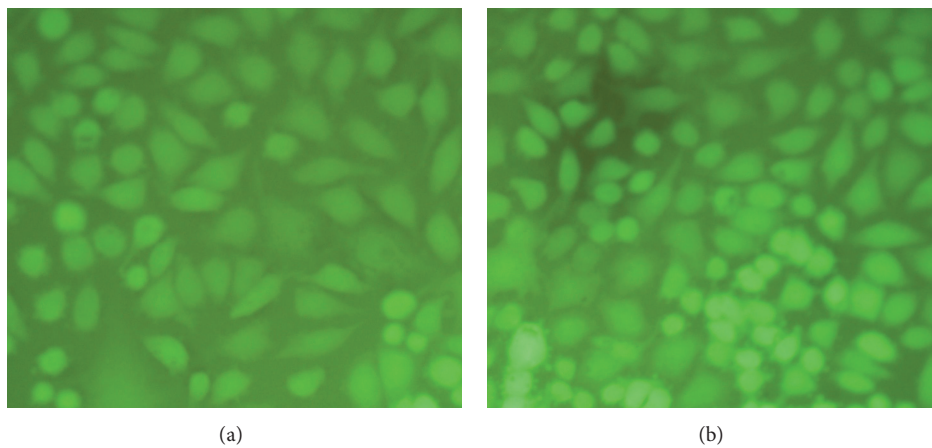


FIGURE 3: Inverted microscope image of HeLa cells after 48 h exposure to a suspension of $\gamma\text{-Fe}_2\text{O}_3$ (200 μL) nanoparticles diluted 100 times (b). Control cells cultured in free medium were run in parallel to the treated groups (a) ($\times 200$).

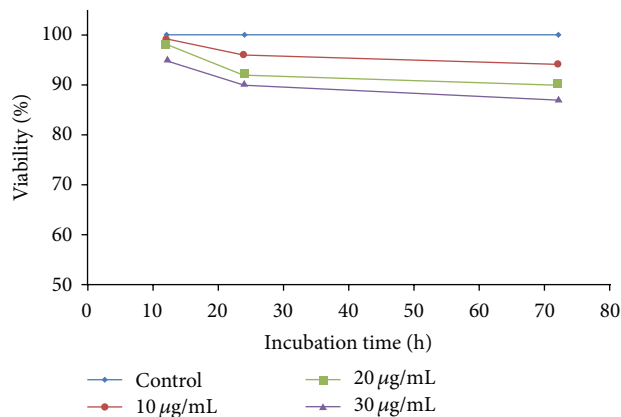


FIGURE 4: Effect of different concentrations of iron oxide nanoparticles on HeLa cells viability.

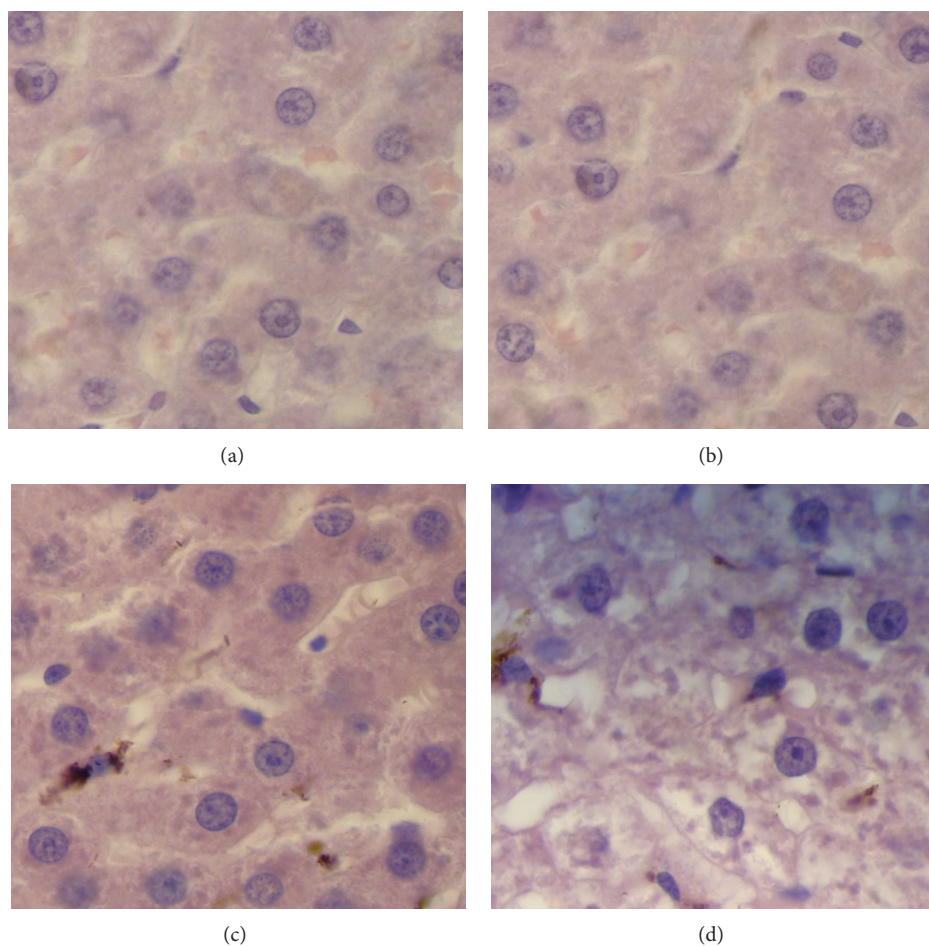


FIGURE 5: Light optical image of the liver after 48 h exposure to $\gamma\text{-Fe}_2\text{O}_3$ nanoparticles at concentrations of 0.7 mL/kg (b), 1.7 mL/kg (c), and 3.7 mL/kg (d). The reference sample is also presented (a).

The liver examination after the injection of 1.7 mL/kg dose of iron oxide nanoparticles (Figure 5(c)) indicates hepatocytes with moderate anisokaryosis, formation of chromocenters and nucleoli, and moderate granular cytoplasmic degeneration. The microgranular brown pigment deposits in Kupffer cells (HE, 600x) were also observed in the liver after

injection with 1.7 mL/kg dose of iron oxide nanoparticles (Figure 5(c)). After injection with 3.7 mL/kg dose of iron oxide nanoparticles (Figure 5(d)) were noticed hepatocytes with moderate anisokaryosis, formation of chromocenters and nucleoli. The granulovacuolar cytoplasmic degeneration and microgranular brown pigment deposits in Kupffer

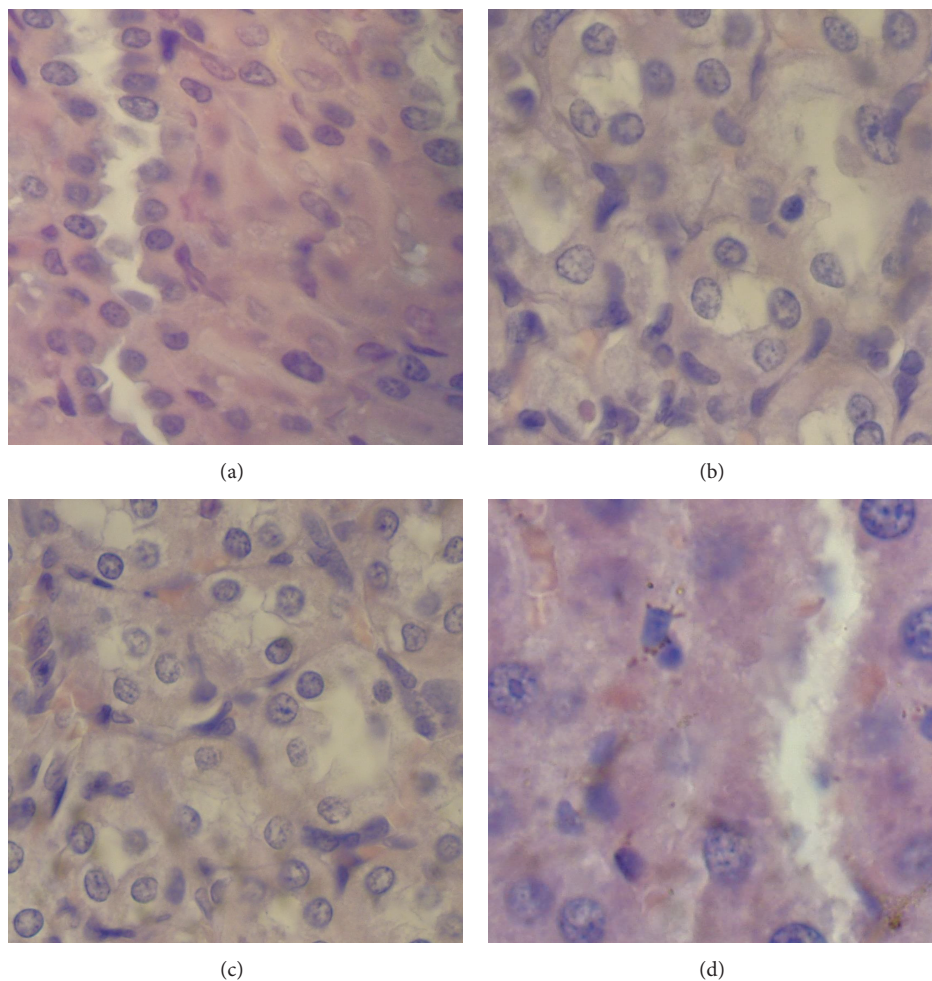


FIGURE 6: Light optical image of the kidney after 48 h exposure to $\gamma\text{-Fe}_2\text{O}_3$ nanoparticles at concentrations of 0.7 mL/kg (b), 1.7 mL/kg (c), and 3.7 mL/kg (d). The reference sample is also presented (a).

cells and hepatocytes (HE, 600x) were also distinguished (Figure 5(d)).

The pathological micrographs of kidneys in rats after injection with 0.7 mL/kg dose of iron oxide nanoparticles (Figure 6(b)) show that the kidney has preserved the architecture of the control specimen (Figure 6(a)) with no significant differences. The tubular cells with moderate anisokaryosis and anisochromia with formation of chromocenters and minimal granular cytoplasmic degeneration (HE, 600x) are also presented in Figure 6(b).

The specimen injected with a solution of 1.7 mL/kg iron oxide (Figure 6(c)) preserves the architecture, tubular cells with moderate anisokaryosis, and anisochromia with formation of chromocenters, moderate granulovacuolar cytoplasmic degeneration with focal clear cells, and moderate vascular congestion (HE, 400x). For the specimen injected with a solution containing 3.7 mL/kg iron oxide (Figure 6(d)) were observed tubular cells with pronounced architectural distortions, enlarged nuclei with irregular contours, formation of prominent nucleoli, marked granular cytoplasmic degeneration and discreet deposition of microgranular brown pigment in the renal interstitium (HE, 600x).

On the other hand, the microscopic observations of the rat lung and spleen injected with different $\gamma\text{-Fe}_2\text{O}_3$ concentrations after 48 h are presented in Figures 7 and 8.

In Figure 7, the pathological micrographs of lungs in rats after the injection with doses containing 0.7 mL/kg, 1.7 mL/kg, and 3.7 mL/kg of iron oxide nanoparticles and the pathological micrographs of the control specimen (Figure 7(a)) are presented. After injection with 0.7 mL/kg (Figure 6(b)) dose of iron oxide nanoparticles, the lung parenchyma of the rats shows preserved alveolar architecture with rare macrophages in the alveolar septa, discreet anisokaryosis, and anisochromia of type II pneumocytes with rare nucleoli. The focal ectatic capillaries in the alveolar septa are also presented. We can see that the pathological micrographs of lung in rats after injection with 0.7 mL/kg dose of iron oxide nanoparticles (Figure 7(b)) show that the lung has preserved the architecture of the control specimen (Figure 7(a)) with no significant differences. For the specimen injected with a solution containing 1.7 mL/kg iron oxide (Figure 7(c)), we observed that the lung parenchyma shows preserved alveolar architecture with rare macrophages in the alveolar septa, discreet anisokaryosis, and anisochromia of

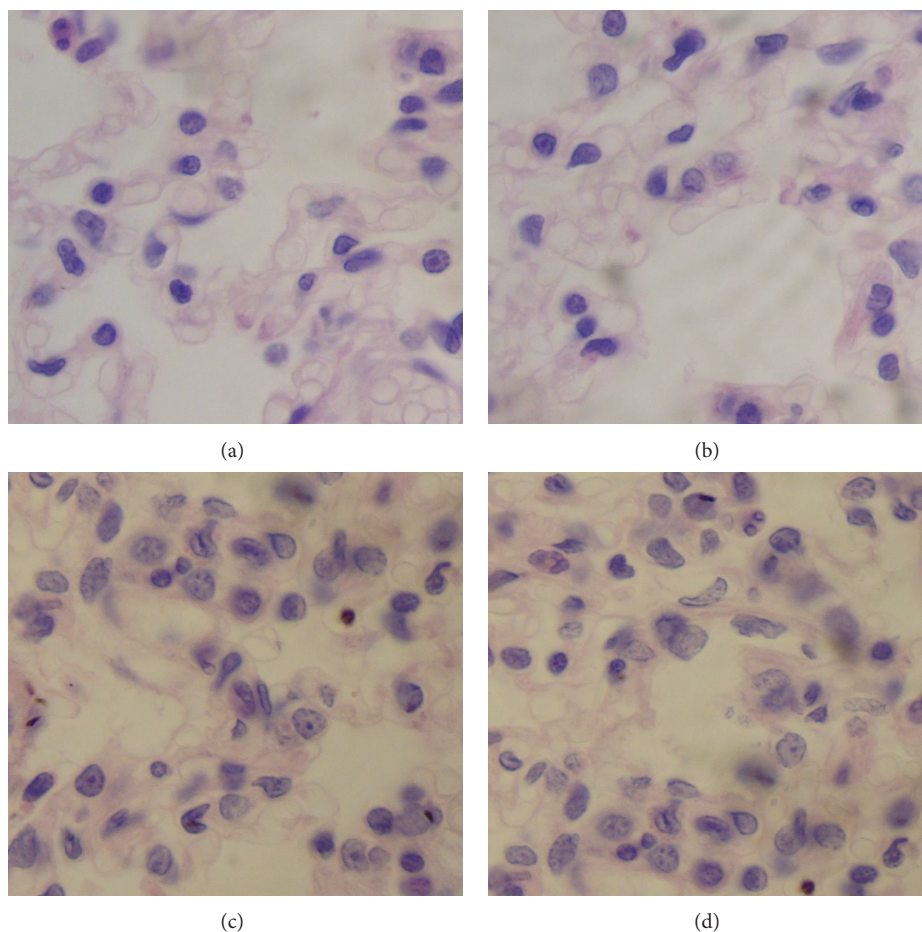


FIGURE 7: Light optical image of the lung after 48 h exposure to $\gamma\text{-Fe}_2\text{O}_3$ nanoparticles at concentrations of 0.7 mL/kg (b), 1.7 mL/kg (c), and 3.7 mL/kg (d). The reference sample is also presented (a).

type II pneumocytes, with rare chromocenters and nucleoli. The focal ectatic capillaries in the alveolar septa are also presented. Lung parenchyma of the specimen injected with a solution of 3.7 mL/kg iron oxide (Figure 7(d)) shows preserved alveolar architecture with rare macrophages in the alveolar septa, discreet anisokaryosis, and anisochromia of type II pneumocytes, with rare chromocenters and nucleoli. In the lung parenchyma it is also observed focal ectatic capillaries in the alveolar septa.

Pathological sections of spleen after injection with a 0.7 mL/kg and 1.7 mL/kg dose of iron oxide nanoparticles (Figures 8(b)-8(c)) show that the architecture of the spleen was not affected by IO-NPs compared with the architecture of the control specimen (Figure 8(a)). After injection with 0.7 and 1.7 mL/kg dose of iron oxide nanoparticles, there were noticed splenic red pulp with discreet nuclear contour irregularities, discreet anisochromia with focal chromocenter formation, and rare nucleoli. After injection with a 3.7 mL/kg dose of iron oxide nanoparticles (Figure 8(d)), we observed the splenic red pulp with increased number of monocytes, with nuclear contour irregularities. The discreet anisochromia with focal chromocenter formation were also remarked in the splenic pulp after injection with a 3.7 mL/kg dose of iron oxide nanoparticles.

In the present study, we have established that the tested IO-NPs did not induce any morphological alterations such as an increase of granulomas or tissue damage to the liver and kidneys. The lack of morphological modifications to the liver and kidneys could be explained by the low amount of IO-NPs. For low concentrations of IO-NPs, the histopathological investigations performed after injection showed that the architecture of the liver and kidneys was not affected and no significant differences between the control groups and injected groups were observed. These results are in agreement with previous studies conducted by Wang et al. [32–37] which ascertained that the toxicity apparently depends on the type of nanoparticles and their concentration. Furthermore, Wang et al. showed that some metal nanoparticles as well as Zn nanoparticles are highly toxic in acute assessments. Previous studies realized by Dekkers et al. [38] showed that metal oxide nanoparticles, like some forms of silica (SiO_2), induce toxicity after subacute assessments.

Hillyer and Albrecht, in gastrointestinal persorption and tissue distribution of differently sized colloidal gold nanoparticles studies [39], show that the acute and subacute *in vivo* intraperitoneal administration studies are very important, allowing us to find the potential toxicological effects that iron oxide nanoparticles may have in key organs (gastrointestinal

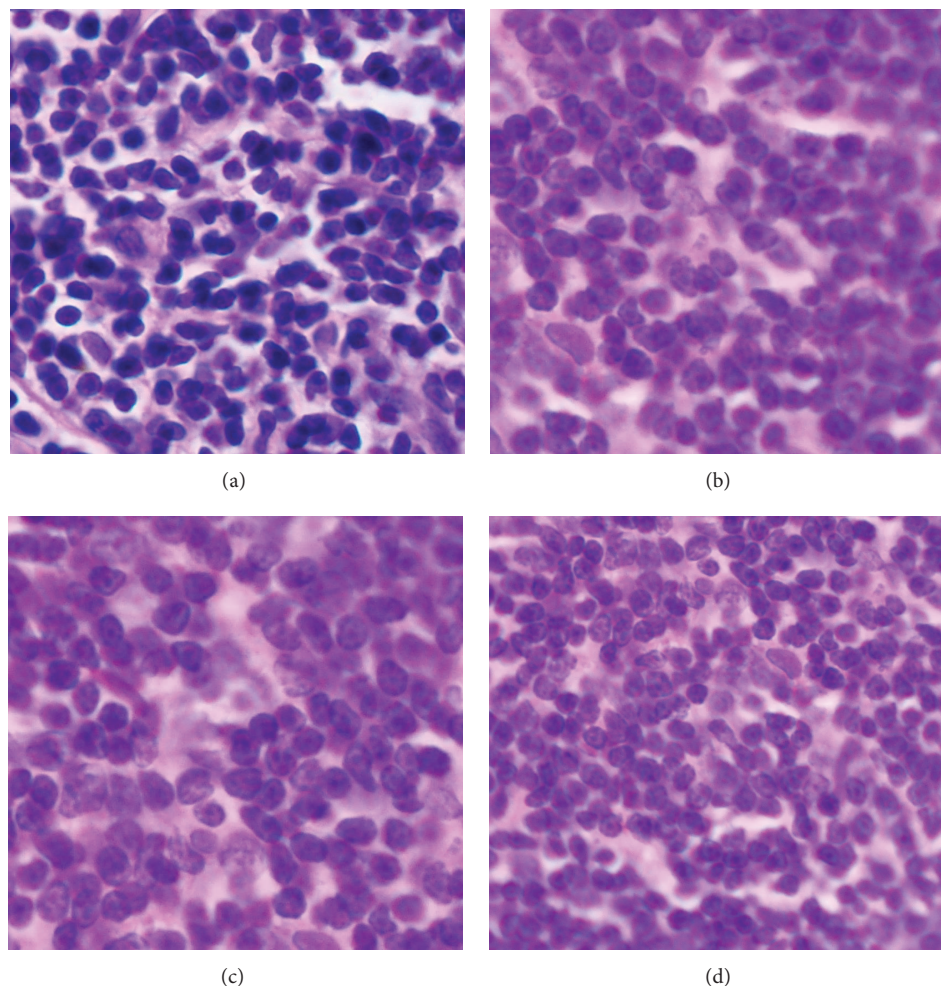


FIGURE 8: Light optical image of the spleen after 48 h exposure to $\gamma\text{-Fe}_2\text{O}_3$ nanoparticles at concentrations of 0.7 mL/kg (b), 1.7 mL/kg (c), and 3.7 mL/kg (d). The reference sample is also presented (a).

tract, liver, kidneys, and spleen) and the cardiovascular system. On the other hand, Kim et al. [40] showed that the study of the possibility of iron oxide nanoparticles to cross the intestinal barrier as well as their effects in blood serum, and the possible alteration to urinary parameters (potassium, sodium, and osmolality) is very important in order to understand the toxicity effects of these particles. Understanding the potential risks associated with exposure to iron oxide nanoparticles used for a great variety of medical applications is crucial. It is very important to design functionalized iron oxide nanoparticles that can be effectively internalized and which can meet the demands of a particular application without compromising on cellular toxicity.

4. Conclusions

The toxicity of the uniform, spherical obtained nanoparticles with 10 ± 0.3 nm in size has been investigated by *in vitro* and *in vivo* assays. At the tested concentrations, the nanoparticles

proved to be not cytotoxic on HeLa cells and did not modify the rat's behavior or the histopathological aspect of liver, kidney, lung, and spleen tissues. Intraperitoneal injection of $\gamma\text{-Fe}_2\text{O}_3$ nanoparticles at several concentrations showed a normal macroscopic histopathological behavior of liver, kidney, lung, and spleen after 48 h for each concentration in the treated group compared with the control. Therefore, the preserved architecture of the control or slightly pathological changes of liver, kidney, lung, and spleen joint were induced by the low-dose of IO-NPs. The results of the present study suggested that the Fe_2O_3 nanoparticles could be used for future therapeutic alternative treatment strategies.

Acknowledgments

The financial and encouragement support provided by the Ministry of Educations of the Romania, Project no. C2-06 under program CEA-IFA, POSDRU/107/1.5/S/76813 (DocInvest), and by the scholarship of the French government via the cultural section of the French Embassy.

References

- [1] S. Laurent, D. Forge, M. Port et al., "Magnetic iron oxide nanoparticles: synthesis, stabilization, vectorization, physic-chemical characterizations and biological applications," *Chemical Reviews*, vol. 108, no. 6, pp. 2064–2110, 2008.
- [2] S. Mornet, S. Vasseur, F. Grasset, and E. Duguet, "Magnetic nanoparticle design for medical diagnosis and therapy," *Journal of Materials Chemistry*, vol. 14, no. 14, pp. 2161–2175, 2004.
- [3] A. M. Prodan, S. L. Iconaru, C. M. Chifriuc et al., "Magnetic properties and biological activity evaluation of iron oxide nanoparticles," *Journal of Nanomaterials*, vol. 2013, Article ID 893970, 7 pages, 2013.
- [4] E. Katz and I. Willner, "Integrated nanoparticle-biomolecule hybrid systems: synthesis, properties, and applications," *Angewandte Chemie*, vol. 43, no. 45, pp. 6042–6108, 2004.
- [5] S. Laurent, S. Dutz, U. O. Häfeli, and M. Mahmoudi, "Magnetic fluid hyperthermia: focus on superparamagnetic iron oxide nanoparticles," *Advances in Colloid and Interface Science*, vol. 166, no. 1-2, pp. 8–23, 2011.
- [6] C. H. Cunningham, T. Arai, P. C. Yang, M. V. McConnell, J. M. Pauly, and S. M. Conolly, "Positive contrast magnetic resonance imaging of cells labeled with magnetic nanoparticles," *Magnetic Resonance in Medicine*, vol. 53, no. 5, pp. 999–1005, 2005.
- [7] S. A. Anderson, R. K. Rader, W. F. Westlin et al., "Magnetic resonance contrast enhancement of neovasculature with alpha(v)beta(3)-targeted nanoparticles," *Magnetic Resonance in Medicine*, vol. 44, no. 3, pp. 433–439, 2000.
- [8] B. Polyak and G. Friedman, "Magnetic targeting for site-specific drug delivery: applications and clinical potential," *Expert Opinion on Drug Delivery*, vol. 6, no. 1, pp. 53–70, 2009.
- [9] R. Weissleder, H.-C. Cheng, A. Bogdanova, and A. Bogdanov Jr., "Magnetically-labeled cells can be detected by MR imaging," *Journal of Magnetic Resonance Imaging*, vol. 7, no. 1, pp. 258–263, 1997.
- [10] E. A. Schellenberger, F. Reynolds, R. Weissleder, and L. Josephson, "Surface-functionalized nanoparticle library yields probes for apoptotic cells," *ChemBioChem*, vol. 5, no. 3, pp. 275–279, 2004.
- [11] A. R. Jalilian, A. Panahifar, M. Mahmoudi, M. Akhlaghi, and A. Simchi, "Preparation and biological evaluation of [67Ga]-labeled- superparamagnetic nanoparticles in normal rats," *Radiochimica Acta*, vol. 97, no. 1, pp. 51–56, 2009.
- [12] C. Corot, P. Robert, J.-M. Idée, and M. Port, "Recent advances in iron oxide nanocrystal technology for medical imaging," *Advanced Drug Delivery Reviews*, vol. 58, no. 14, pp. 1471–1504, 2006.
- [13] C. Fan, W. Gao, Z. Chen et al., "Tumor selectivity of stealth multi-functionalized superparamagnetic iron oxide nanoparticles," *International Journal of Pharmaceutics*, vol. 404, no. 1-2, pp. 180–190, 2011.
- [14] Q. A. Pankhurst, J. Connolly, S. K. Jones, and J. Dobson, "Applications of magnetic nanoparticles in biomedicine," *Journal of Physics D*, vol. 36, no. 13, pp. R167–R181, 2003.
- [15] R. K. Gilchrist, W. D. Shorey, R. C. Hanselman, J. C. Parrott, and C. B. Taylor, "Selective inductive heating of lymph," *Annals of Surgery*, vol. 146, pp. 596–606, 1957.
- [16] T. R. Pisanic II, J. D. Blackwell, V. I. Shubayev, R. R. Fiñones, and S. Jin, "Nanotoxicity of iron oxide nanoparticle internalization in growing neurons," *Biomaterials*, vol. 28, no. 16, pp. 2572–2581, 2007.
- [17] R. Massart, "Magnetic fluids and process for obtaining them," US Patent 4329241, 1982.
- [18] R. Massart, "Preparation of aqueous magnetic liquids in alkaline and acidic media," *IEEE Transactions on Magnetics*, vol. 17, pp. 1247–1248, 1981.
- [19] R. Massart, J. Roger, and V. Cabuil, "New trends in chemistry of magnetic colloids: polar and non polar magnetic fluids, emulsions, capsules and vesicles," *Brazilian Journal of Physics*, vol. 25, no. 2, pp. 135–141, 1995.
- [20] D. Predoi and C. Valsangiacom, "Thermal studies of magnetic spinel iron oxide in solution," *Journal of Optoelectronics and Advanced Materials*, vol. 9, no. 6, pp. 1797–1799, 2007.
- [21] D. Zins, V. Cabuil, and R. Massart, "New aqueous magnetic fluids," *Journal of Molecular Liquids*, vol. 83, no. 1–3, pp. 217–232, 1999.
- [22] D. Predoi, "A study on iron oxide nanoparticles coated with dextrin obtained by coprecipitation," *Digest Journal of Nanomaterials and Biostructures*, vol. 2, no. 1, pp. 169–173, 2007.
- [23] S. Mornet, F. Grasset, J. Portier, and E. Duguet, "Maghemite@silica nanoparticles for biological applications," *European Cells and Materials*, vol. 3S2, article 110, 2002.
- [24] A. M. Grumezescu, E. Andronescu, A. Fica, C. Bleotu, and M. C. Chifriuc, "Chitin based biomaterial for antimicrobial therapy: fabrication, characterization and in vitro profile based interaction with eukaryotic and prokaryotic cells," *Biointerface Research in Applied Chemistry*, vol. 2, p. 446, 2012.
- [25] T. Mosmann, "Rapid colorimetric assay for cellular growth and survival: application to proliferation and cytotoxicity assays," *Journal of Immunological Methods*, vol. 65, no. 1-2, pp. 55–63, 1983.
- [26] F. Denizot and R. Lang, "Rapid colorimetric assay for cell growth and survival: modifications to the tetrazolium dye procedure giving improved sensitivity and reliability," *Journal of Immunological Methods*, vol. 89, no. 2, pp. 271–277, 1986.
- [27] H. Wan, R. L. Williams, P. J. Doherty, and D. F. Williams, "The cytotoxicity evaluation of Kevlar and silicon carbide by MTT assay," *Journal of Materials Science*, vol. 5, no. 6-7, pp. 441–445, 1994.
- [28] B. Su, S. L. Xiang, J. Su et al., "Diallyl disulfide increases histone acetylation and P21^{WAF1} expression in human gastric cancer cells *in vivo* and *in vitro*," *Biochemical Pharmacology*, vol. 1, no. 7, pp. 1–10, 2012.
- [29] C. S. Ciobanu, S. L. Iconaru, E. Gyorgy et al., "Biomedical properties and preparation of iron oxide-dextran nanostructures by MAPLE technique," *Chemistry Central Journal*, vol. 6, article 17, 2012.
- [30] O. Krystofova, J. Sochor, O. Zitka et al., "Effect of magnetic nanoparticles on tobacco BY-2 cell suspension culture," *International Journal of Environmental Research and Public Health*, vol. 10, no. 1, pp. 47–71, 2013.
- [31] L. L. C. Estevanato, J. R. Da Silva, A. M. Falqueiro et al., "Co-nanoencapsulation of magnetic nanoparticles and selol for breast tumor treatment: in vitro evaluation of cytotoxicity and magnetohyperthermia efficacy," *International Journal of Nanomedicine*, vol. 7, pp. 5287–5299, 2012.
- [32] M. L. B. Carneiro, E. S. Nunes, R. C. A. Peixoto et al., "Free Rhodium (II) citrate and rhodium (II) citrate magnetic carriers as potential strategies for breast cancer therapy," *Journal of Nanobiotechnology*, vol. 9, article 11, 2011.
- [33] L. Gu, R. H. Fang, M. J. Sailor, and J.-H. Park, "In vivo clearance and toxicity of monodisperse iron oxide nanocrystals," *ACS Nano*, vol. 6, no. 6, pp. 4947–4954, 2012.

- [34] H. M. Kouchesfehani, S. rKiani, A. A. Rostami, and R. Fakheri, "Cytotoxic effect of iron oxide nanoparticles on mouse embryonic stem cells by MTT assay," *Iranian Journal of Toxicology*, vol. 7, no. 21, pp. 849–853, 2013.
- [35] P. Greaves, "Liver and pancreas," in *Histopathology of Preclinical Toxicity Studies*, pp. 457–503, Academic Press, Elsevier, New York, NY, USA, 2007.
- [36] A. Shiga, Y. Ota, Y. Ueda et al., "Study on the pathogenesis of foreign body granulomatous inflammation in the livers of sprague-dawley rats," *Journal of Toxicologic Pathology*, vol. 23, no. 4, pp. 253–260, 2010.
- [37] B. Wang, W. Feng, M. Wang et al., "Acute toxicological impact of nano- and submicro-scaled zinc oxide powder on healthy adult mice," *Journal of Nanoparticle Research*, vol. 10, no. 2, pp. 263–276, 2008.
- [38] S. Dekkers, P. Krystek, R. J. B. Peters et al., "Presence and risks of nanosilica in food products," *Nanotoxicology*, vol. 5, no. 3, pp. 393–405, 2011.
- [39] J. F. Hillyer and R. M. Albrecht, "Gastrointestinal persorption and tissue distribution of differently sized colloidal gold nanoparticles," *Journal of Pharmaceutical Sciences*, vol. 90, no. 12, pp. 1927–1936, 2001.
- [40] Y. S. Kim, J. S. Kim, H. S. Cho et al., "Twenty-eight-day oral toxicity, genotoxicity, and gender-related tissue distribution of silver nanoparticles in Sprague-Dawley rats," *Inhalation Toxicology*, vol. 20, no. 6, pp. 575–583, 2008.

Research Article

Electrospun Hyaluronan-Gelatin Nanofibrous Matrix for Nerve Tissue Engineering

Hau-Min Liou,¹ Lih-Rou Rau,¹ Chun-Chiang Huang,¹ Meng-Ru Lu,¹
and Fu-Yin Hsu^{1,2}

¹ Institute of Bioscience and Biotechnology, National Taiwan Ocean University, Keelung 20224, Taiwan

² Department of Life Sciences, National Taiwan Ocean University, Keelung 20224, Taiwan

Correspondence should be addressed to Fu-Yin Hsu; fyhsu5565@gmail.com

Received 23 July 2013; Revised 25 September 2013; Accepted 26 September 2013

Academic Editor: In-Kyu Park

Copyright © 2013 Hau-Min Liou et al. This is an open access article distributed under the Creative Commons Attribution License, which permits unrestricted use, distribution, and reproduction in any medium, provided the original work is properly cited.

Schwann cells play a critical role in the repair of the peripheral nerve. The goal of this study was to fabricate electrospun gelatin (Gel) and hyaluronan-gelatin (HA-Gel) composite nanofibers to provide a suitable growth environment for Schwann cells. The fiber diameters of Gel, 0.5 HA-Gel, 1 HA-Gel, and 1.5 HA-Gel were 130 ± 30 nm, 294 ± 87 nm, 362 ± 129 nm, and 224 ± 54 nm, respectively. The biological performance of Gel and HA-Gel was evaluated using an *in vitro* culture of RT4-D6P2T rat Schwann cells. We found that the cell attachment and proliferation rates were not significantly different on these matrices. However, the Schwann cells displayed better organized F-actin on HA-Gel than on Gel. Moreover, the expression levels of several genes, including Nrg1, GFAP, and P0, were significantly higher on HA-Gel than on Gel. In addition, the levels of Nrg1 and P0 protein expression were also higher on the HA-Gel than on Gel. These results indicate that the hyaluronan-gelatin composite nanofibrous matrix could potentially be used in peripheral nerve repair.

1. Introduction

Regeneration of the nervous system is a major challenge. However, the peripheral nervous system has a better intrinsic ability to repair and regenerate axons after axonal damage due to the ability of Schwann cells to enhance the environment for regeneration [1]. For the treatment of peripheral nerve injury, nerve autografts or direct end-to-end surgical reconnection is used to repair nerve injury. Unfortunately, direct end-to-end surgical reconnection only can repair small gaps in the nerve, because the tension introduced into the nerve cable would inhibit nerve regeneration for longer nerve gaps [2]. A nerve autograft harvested from another site in the body is used in these cases and is considered the “gold standard” for repair of the longer nerve damage gaps without immunological rejection problems. However, a nerve autograft has several disadvantages, including neuroma, hypofunction at the donor nerve graft site, and nerve site mismatch. Allografts and xenografts are possible replacements for autografts. Nevertheless, the major clinical problems are the risk of immune repulsion and disease transmission [3]. Thus, a nerve graft

made of natural and synthetic materials is a promising alternative for promoting successful nerve regeneration.

Gelatin is obtained by the partial hydrolysis of native collagen in an alkaline or acidic environment. Gelatin exhibits excellent biocompatibility and biodegradability properties; thus, it has been widely used for nerve repair [4]. Hyaluronan is a naturally biopolymer composed of repeating disaccharide units of glucuronic acid and N-acetylglucosamine. It is the major constituent of the extracellular matrix (ECM) of connective tissues and has many important biological functions. Because of its excellent biocompatibility, nonimmunogenicity, and specific biological functions, hyaluronan is used in a variety of clinical therapies, including supplementing joint fluid in arthritis and facilitating wound healing and regeneration [5, 6]. Furthermore, hyaluronan is known to prevent perineural scar formation, which improves peripheral nerve regeneration [7].

Tissue engineered scaffolds are another choice for implantation to facilitate neural repair. Fibrous scaffolds have become very popular in tissue engineering because they mimic the physical architecture of the ECM. The architecture

TABLE 1: Oligonucleotide primer for real-time PCR amplification.

Gene	Primer sequence: sense/antisense
GFAP	5'-GGTGTGGAGTGCCTTCGTAT-3' 5'-TACGATGTCCTGGGAAAAGG-3'
NGF	5'-CCAAGCACTGGAACCTACTACTGC-3' 5'-CTGCTGAGCACACACACGCAG-3'
Nrg1	5'-GGCAGTCAGCCCCTTTGTG-3' 5'-TGCAGGGTTGTGATGAAAGGA-3'
p75	5'-CATCTCTGTGGACAGCCAGA-3' 5'-CTCTACCTCCTCAGCTTGG-3'
P0	5'-CTGCACTGCTCCTTCTGGT-3' 5'-CCTTGGCATAGTGAAGATTG-3'
S100	5'-ATAGCACCTCCGTTGGACAG-3' 5'-TCGTTTGCACAGAGGACAAG-3'
18S rRNA	5'-GGCCCGAAGCGTTTACTT-3' 5'-CGGCCGTCCCTCTTAATC-3'

of the ECM plays an important role in regulating cell behavior with biochemical signals and topographical cues [8, 9].

Electrospinning is an easy method to fabricate ultrafine fibers with submicrometer to nanometer diameters. Electrospun fibrous matrices exhibit certain special characteristics, such as a high specific surface area, a high aspect ratio, and a high porosity surface area. Most importantly, the topological structure of electrospun matrices mimics the architecture of the ECM and could enhance cell attachment, migration, proliferation, and differentiation [10].

Schwann cells are a major component of the peripheral nerve system and play an important role in Wallerian degeneration and the subsequent axon regeneration in peripheral nerve injury [11]. After Wallerian degeneration, the Schwann cells begin to proliferate and migrate to the lesion, forming longitudinally oriented cell strands called the bands of Büngner; thereafter, Schwann cells secrete a number of neurotrophic factors such as nerve growth factor and cytokines that support the survival of injured neurons [12], secrete extracellular matrix components, such as laminin and collagen type IV, for axonal growth, and produce neurite promoting factors to guide the growing axon [13, 14]. Thus, the aim of the present study was to investigate whether a hyaluronan-gelatin electrospun matrix has potential as a neurograft for peripheral nerve repair.

2. Materials and Methods

2.1. Reagents. Dulbecco's Modified Eagle Medium (DMEM), fetal bovine serum (FBS), and trypsin were purchased from GIBCO (Grand Island, NY, USA). Gelatin type A (Gel) was purchased from the Sigma-Aldrich Chemical Company (St. Louis, MO, USA). Sodium hyaluronan was purchased from NovaMatrix (Drammen, Norway). The RT4-D6P2T rat Schwann cells were purchased from BCRC (Bioresource Collection and Research Center, Taiwan). The other chemicals used were of reagent grade unless otherwise stated.

2.2. Preparation of Hyaluronan-Gelatin Composite Nanofibrous Matrix (HA-Gel). To allow complete evaporation of the solvent, the solvent used in this study was a mixture of formic acid and 1,1,1,3,3,3-hexafluoro-2-propanol (HFIP) at a volume/volume ratio of 3/7. The gelatin powder was dissolved in the solvent mixture to a concentration of 12% (w/v). Various concentrations of sodium hyaluronan (0%, 0.5%, 1%, and 1.5% w/v) were added to the gelatin solution and dissolved by vortexing until the solution was clear. For the electrospinning process, the polymer solution was placed in a plastic syringe fitted with an 18 G needle and attached to a syringe pump that provided a steady flow rate of 8.5 μ L/min. The electrospinning voltage of 2.3 kV/cm was applied using a high-voltage power supply (Glassman High Voltage, Inc.).

2.3. Characterization of the Electrospun Nanofibers. The fiber morphology and diameter of the HA-Gels were determined by a field emission scanning electron microscope (SEM; model S-4800, Hitachi, Tokyo, Japan). Briefly, the electrospun matrices were sputter-coated with gold and visualized by SEM at an accelerating voltage of 5 kV. The fiber diameter was analyzed using image analysis (ImageJ software 1.42, National Institutes of Health, USA). The average fiber diameter and standard deviation were calculated from 100 random measurements.

2.4. Cell Culture on HA-Gel. Because the HA-Gels readily dissolved in aqueous media, it was necessary to cross-link them before using them for cell culture. The electrospun matrices were cross-linked by treatment with N-(3-dimethylaminopropyl)-N-ethylcarbodiimide hydrochloride (EDC). The matrix was immersed in 1% EDC solution in 95% ethanol for 2 hrs and then washed repeatedly with 0.01 M PBS to remove the residual EDC. Finally, the electrospun matrices were sterilized by exposure to ultraviolet light in a sterile hood overnight. The electrospun matrices were placed in 24-well tissue culture plates containing a suspension of RT4-D6P2T rat Schwann cells (BCRC no. 60508) (5×10^4 cells/well) in DMEM supplemented with 10% (v/v) FBS, 100 U/mL of penicillin, and 100 μ g/mL of streptomycin. The cultures of cell-seeded electrospun matrices were harvested at 1, 2, 3, and 4 hrs for cell attachment assays and on days 1, 3, and 6 days for cell proliferation assays. Cell viability was determined using the MTT assay. At each time point, three samples were used to measure the number of cells attached to the electrospun matrices. The experiments were performed in triplicate.

2.5. Fluorescent Staining of the Cytoskeleton. The morphology of cells with their F-actin cytoskeleton fluorescently stained with fluorescein isothiocyanate (FITC)-conjugated phalloidin and nuclei stained with DAPI was examined. After 1 or 4 hrs of cell culture, cells were fixed with 3.7% (v/v) paraformaldehyde in PBS for 10 min, followed by 2 times washing with PBS and permeabilization with 0.1% (v/v) Triton X-100 in PBS for 5 min. After washing with PBS, the samples were blocked with 1% bovine serum albumin in PBS for 1 hr. After blocking, the samples were stained with 6.4 μ M FITC-conjugated phalloidin for 20 min. Cell nuclei were stained

TABLE 2: Sample notation, average diameter of hyaluronan-gelatin composite nanofibers.

Sample notation	Gelatin concentration (mg/mL)	Hyaluronan concentration (mg/mL)	Average diameter Standard deviation (nm)	1st quartile; 3rd quartile (nm)
Gel	12	0	130 ± 30	109; 144
0.5 HA-Gel	12	0.5	294 ± 87	230; 352
1 HA-Gel	12	1	362 ± 129	282; 422
1.5 HA-Gel	12	1.5	224 ± 54	179; 256

with 4',6-diamidino-2-phenylindole (DAPI). After staining, the samples were washed with PBS and observed under a fluorescence microscope (TS100, Nikon) and a laser scanning confocal microscope (LSCM, Zeiss LSM 510 META).

2.6. Quantitative Real-Time PCR. Real-time PCR was used to determine the levels of neuregulin 1 (Nrg1), S100, nerve growth factor (NGF), low-affinity nerve growth factor receptor (p75), glial fibrillary acidic protein (GFAP), and myelin protein zero (P0) mRNA and 18S ribosomal RNA (as the internal control). Table 1 shows the sequences of the oligonucleotides that were used as PCR primers. Briefly, the reaction is followed by the manufacture protocol of SYBR Green PCR Master Mix Kit (Protech SA-SQGLR-V2). The real-time PCR conditions for the promoter region were 15 mins at 94°C, 1 min at 62.5°C, and 15 s at 94°C. Real-time PCR reactions were performed using an iQ5 Gradient Real-Time PCR system (Bio-Rad). The levels of RNA expression were calculated using the $2^{-\Delta\Delta C_t}$ method.

2.7. Immunoblotting Analysis. Cells were seeded on substrates at 3×10^4 cells/cm² in medium. Immunoblotting to detect the Schwann cell-specific proteins neuregulin 1 (Nrg1), myelin protein zero (P0), and CD44 was performed after day 3 and day 6 of culturing. Cells were collected and lysed in lysis buffer. The supernatants were obtained by centrifugation at 4°C, 15,000 ×g for 10 min. The concentration of protein was analyzed using a Bradford Coomassie assay. The proteins (30 μg/μL) were fractionated by electrophoresis and electrotransferred to polyvinylidene difluoride film (PVDF). Blocking was performed using 5% (w/v) nonfat milk, and then the primary antibody was applied to the membrane overnight at 4°C. Antibodies specific to CD44 (Santa Cruz Biotechnology-INC. sc-9960), Nrg1 (Santa Cruz Biotechnology-INC. sc-28916), P0 (Santa Cruz Biotechnology-INC. sc-18531), and nucleophosmin B23 (Invitrogen 325200) were used. After incubation with a HRP-conjugated secondary antibody, the immunoreactive bands were detected using enhanced chemiluminescence detection (Millipore WBKLS0500). The immunoreactive bands were analyzed by ImageJ software (National Institutes of Health, USA). Nucleophosmin B23 was used as the internal control.

2.8. Statistical Analyses. Statistical analyses were performed using SPSS v.11 software. For each condition, the diameters of at least 100 randomly chosen fibers were measured. The fiber diameters were analyzed using a one-way ANOVA with Tukey's post hoc test. The cell viability, gene expression, and

immunoblotting were analyzed with the nonparametric Mann-Whitney *U* test. Differences at $P < 0.05$ were considered statistically significant.

3. Results

3.1. Fabrication of Hyaluronan-Gelatin Electrospun Nanofibers. Formic acid is a good solvent for hyaluronan and gelatin. However, gelatin and hyaluronan/gelatin which dissolved in a formic acid solution cannot be fabricated into nanofibrous matrices by electrospinning. In a previous study, hexafluoropropanol was found to be a suitable solvent to dissolve hyaluronan/collagen [15]. To obtain hyaluronan-gelatin nanofibers (HA-Gel), we used the cosolvent method by mixing formic acid and HFIP.

Figure 1 shows that the synthetic product was a three-dimensional nonwoven nanofibrous hyaluronan-gelatin matrix with interconnected pores. The fiber diameters were 130 ± 30 nm, 294 ± 87 nm, 362 ± 129 nm, and 224 ± 54 nm for Gel, 0.5 HA-Gel, 1 HA-Gel, and 1.5 HA-Gel, respectively. These dimensions are similar to those of the native fibrous proteins in the ECM. We found that the diameters of the fibers in the HA-Gel matrix were significantly different from those in the Gel matrix ($P < 0.05$, one-way ANOVA with Tukey's post hoc test) (Table 2). In addition, the diameters of the fibers gradually increased and then decreased as the concentration of hyaluronan was gradually increased.

The Gel and HA-Gel fibers cross-linked with EDC are shown in Figure 2. The Gel and HA-Gel fibers still maintained their morphology. However, the fibers appeared to be more rubbery and were fused at fiber junctions.

3.2. Cell Attachment and Proliferation. Cellular functions, including spreading, proliferation, and differentiation, are sensitive to the composition and surface topography of the matrix. To test the effects of the hyaluronan/gelatin weight ratios of the nanofibrous matrix on cell morphology, we incubated the RT4-D6P2T rat Schwann cells on hyaluronan and gelatin matrices with different weight ratios. The morphologies of the Schwann cells that adhered to the different matrices were investigated by staining the actin cytoskeleton with FITC-phalloidin and visualizing the cells with a fluorescence microscope (shown in Figure 3) and a laser scanning confocal microscope (shown in Figure 4). We found that most of the Schwann cells cultured on the HA-Gel matrix appeared to have spread during the 4 hr attachment period. However, it was obvious that the cells cultured on the Gel matrix remained round after 4 h (Figure 3(e) and Figure 4(e)). The attachment and proliferation of the Schwann cells on the Gel

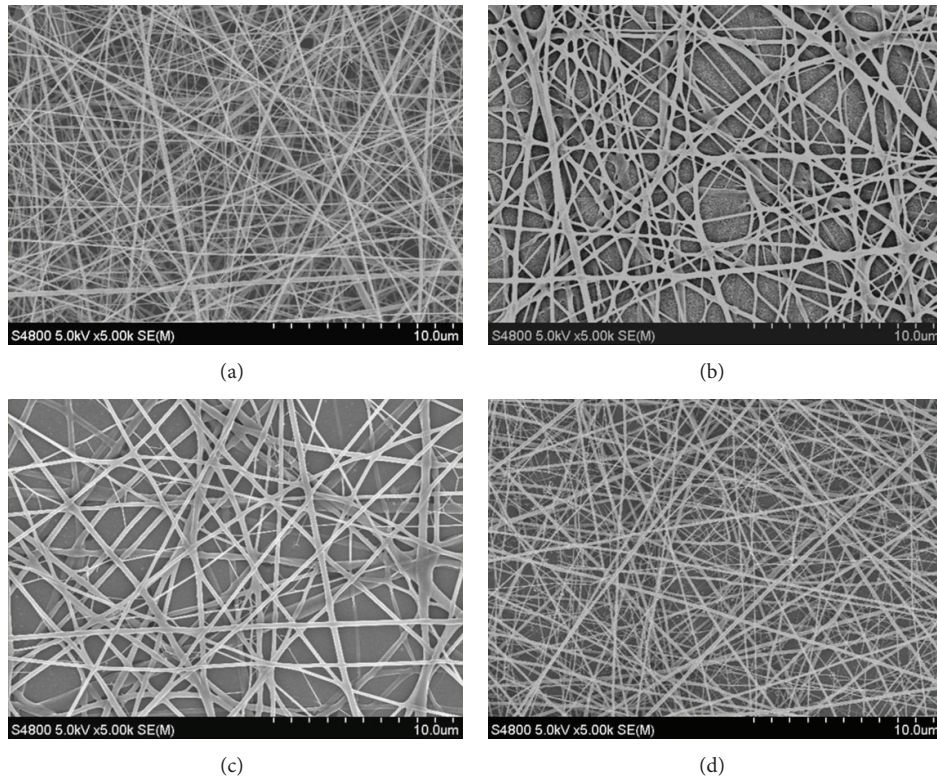


FIGURE 1: Scanning electron microscopy images of as-electrospun HA-Gel matrix at a magnification of 5000x. (a) Gel, (b) 0.5 HA-Gel, (c) 1 HA-Gel, and (d) 1.5 HA-Gel. The scale bar represents 10 μm .

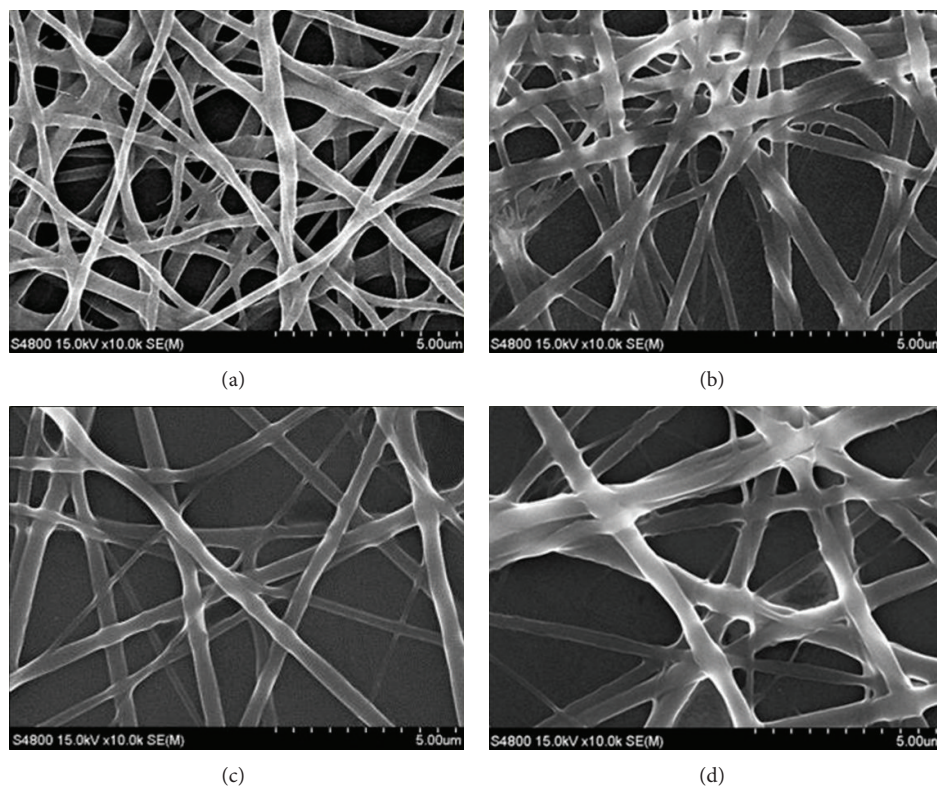


FIGURE 2: Scanning electron microscopy images of electrospun HA-Gel matrix after EDC treatment at a magnification of 10000x. (a) Gel, (b) 0.5 HA-Gel, (c) 1 HA-Gel, and (d) 1.5 HA-Gel. The scale bar represents 5 μm .

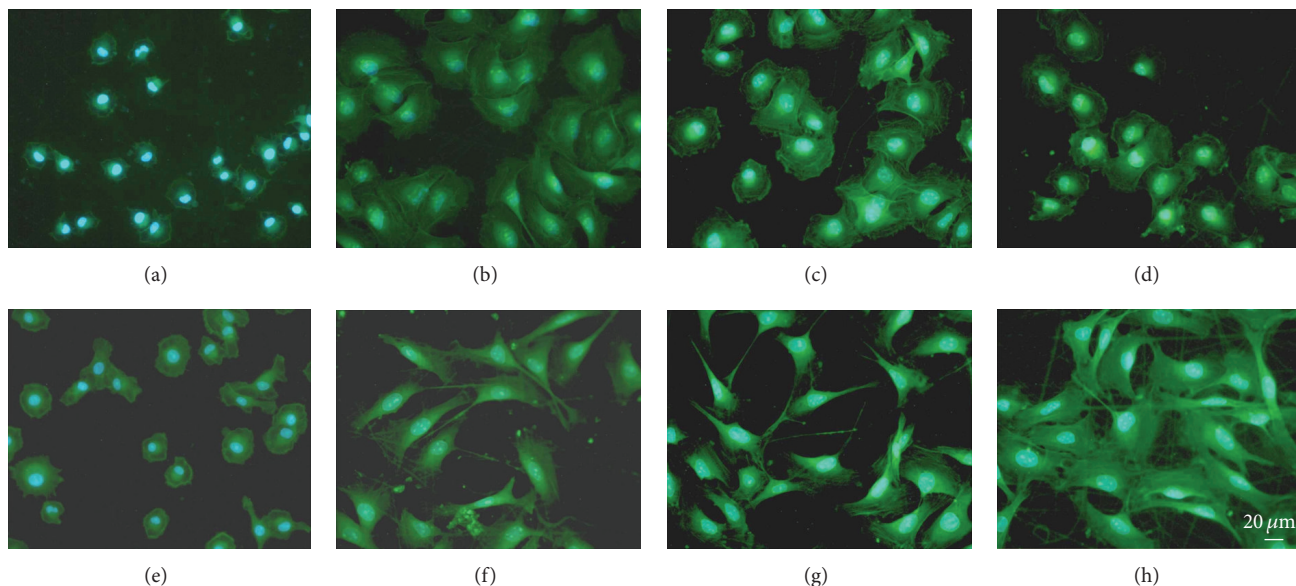


FIGURE 3: Fluorescence micrographs of F-actin stained RT4-D6P2T Schwann cell grown on an electrospun matrix of Gel ((a), (e)), 0.5 HA-Gel ((b), (f)), 1 HA-Gel ((c), (g)), and 1.5 HA-Gel ((d), (h)) for 1 hr ((a), (b), (c), and (d)) or 4 hrs ((e), (f), (g), and (h)). Cytoskeletal F-actin was stained green with FITC, and cell nuclei were stained blue with DAPI. (Scale bar = 20 μm .)

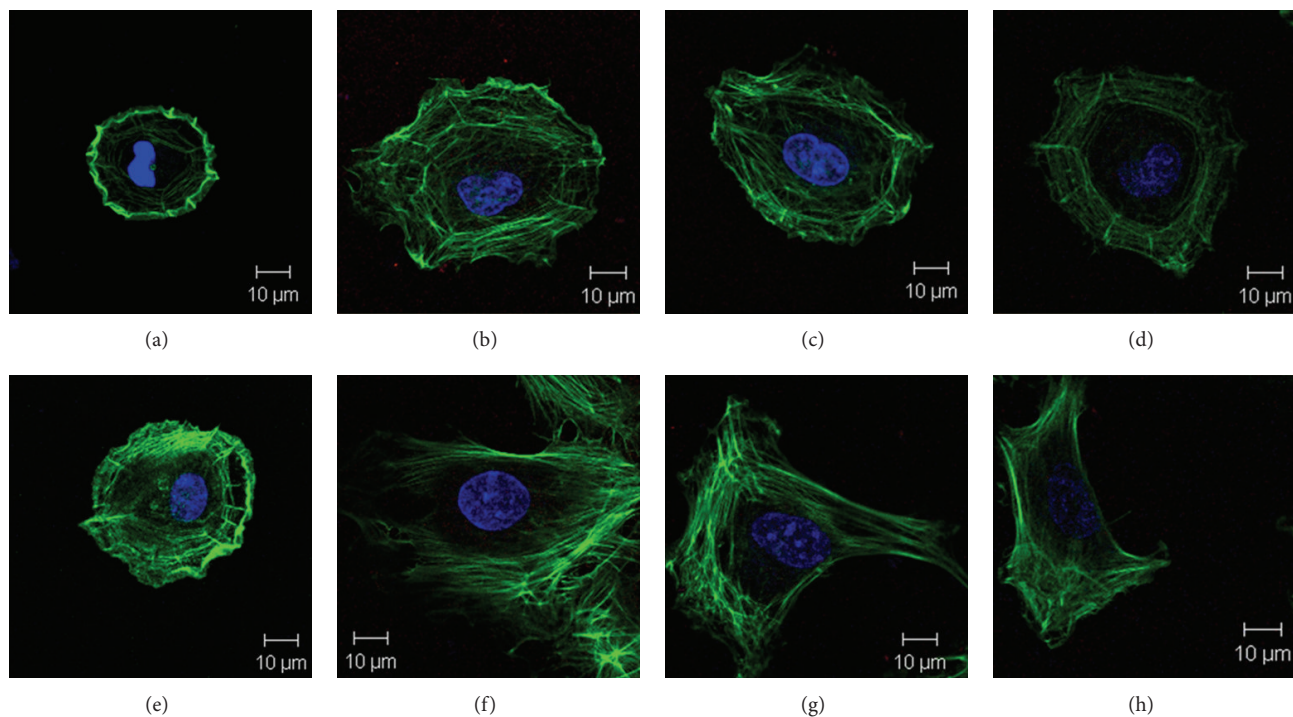


FIGURE 4: Confocal micrographs of F-actin stained RT4-D6P2T Schwann cell on an electrospun matrix of Gel ((a), (e)), 0.5 HA-Gel ((b), (f)), 1 HA-Gel ((c), (g)), and 1.5 HA-Gel ((d), (h)) for 1 hour ((a), (b), (c), and (d)) and 4 hours ((e), (f), (g), and (h)). Cytoskeletal F-actin was stained green with FITC, and cell nuclei were stained blue with DAPI. (Scale bar = 10 μm .)

and HA-Gel matrices were quantified using the MTT assay. There were no significant differences in attachment or proliferation among the cells cultured on 0.5 HA-Gel, 1 HA-Gel, or 1.5 HA-Gel ($P > 0.05$) (as shown in Figure 5).

3.3. Real-Time PCR Analysis. The expression levels of Schwann cell-specific genes were analyzed using real-time

PCR for *Nrg1*, *S100*, *NGF*, *p75*, *GFAP*, and *P0* and 18S ribosomal RNA (as shown in Figure 6). On day 3, the Schwann cells displayed insignificantly increased gene expression levels of *Nrg1*, *S100*, *NGF*, *p75*, *GFAP*, and *P0* when grown on 0.5 HA-Gel, 1 HA-Gel, or 1.5 HA-Gel relative to those obtained from cells grown on Gel ($P > 0.05$). However, on day 6, the Schwann cells showed significantly higher gene expression

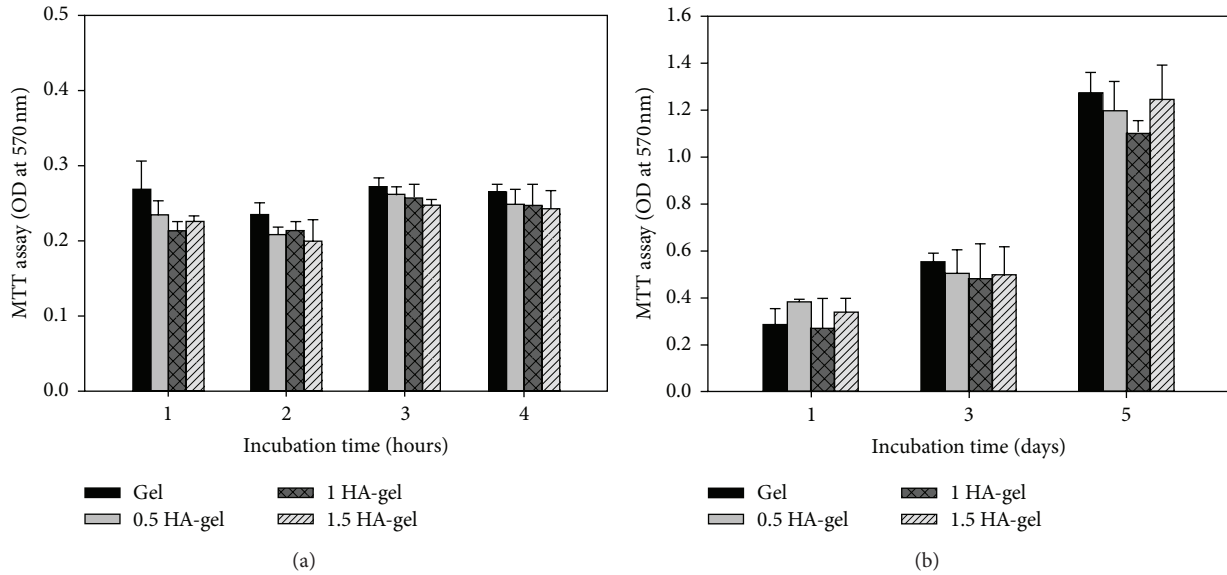


FIGURE 5: Quantification of RT4-D6P2T Schwann cells on Gel and HA-Gel matrices. The MTT assay was used to quantify cell attachment and proliferation on Gel and HA-Gel. (a) The attachment of RT4-D6P2T Schwann cells on various matrices after culturing for up to 4 hrs. (b) The viability of RT4-D6P2T Schwann cells on various matrices after culturing for up to 6 days. The data are presented as the means \pm SD, $n = 4$. No statistically significant differences in cell attachment or proliferation on the HA-Gel and Gel were found.

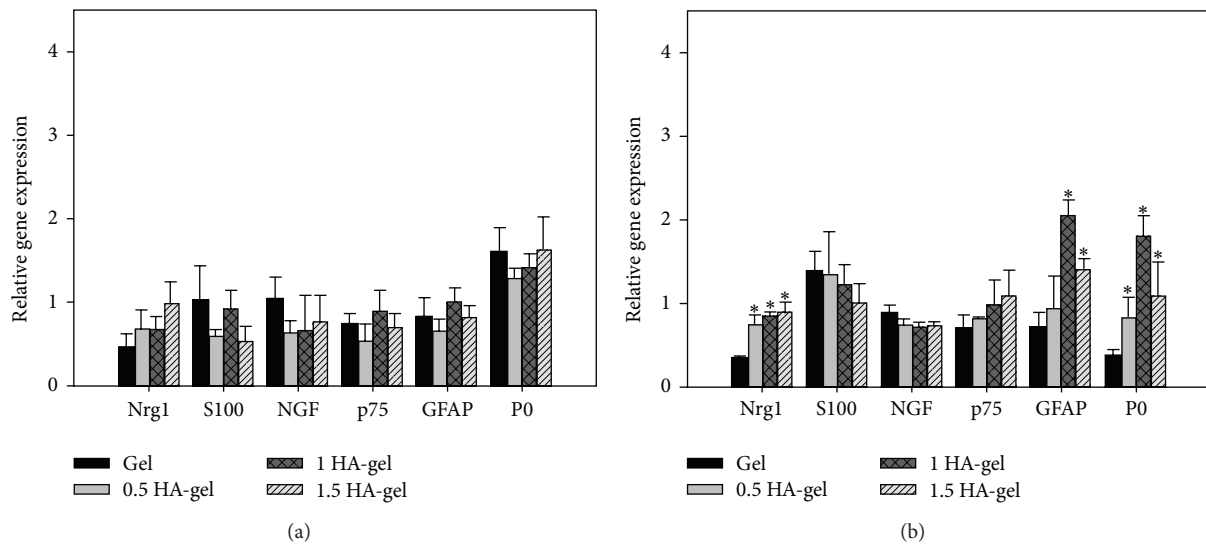


FIGURE 6: Real-time PCR analyses of the nerve-associated genes expressed by RT4-D6P2T Schwann cells on various matrices after culturing for (a) 3 days or (b) 6 days. The data are shown as the fold change relative to those obtained from cells grown on the culture dish surface. The data are presented as the means \pm SD ($n = 4$). (*) denotes significant difference between HA-Gel and Gel ($P < 0.05$).

levels of Nrg1, GFAP, and P0 when grown on 0.5 HA-Gel, 1 HA-Gel, or 1.5 HA-Gel compared to cells grown on Gel ($P < 0.05$) (as shown in Figure 6).

3.4. Western Blot Analysis. The CD44 levels expressed on day 3 and day 6 by the RT4-D6P2T rat Schwann cells grown on the different matrices were not significantly different ($P > 0.05$). The levels of Nrg1 and P0 were higher in the cells grown on 0.5 HA-Gel, 1 HA-Gel, or 1.5 HA-Gel than in the cells grown on Gel on day 6 ($P < 0.05$) (as shown in Figure 7).

However, the levels of Nrg1 and P0 on day 3 and day 6 were not significantly different among the cells grown on 0.5 HA-Gel, 1 HA-Gel, or 1.5 HA-Gel ($P > 0.05$).

4. Discussion

Sponge forms of gelatin, hyaluronan, and their composites have been widely used to fabricate scaffolds for tissue engineering [16–18]. However, the physical structure of the sponge form of these matrices is not acceptable for the tissue

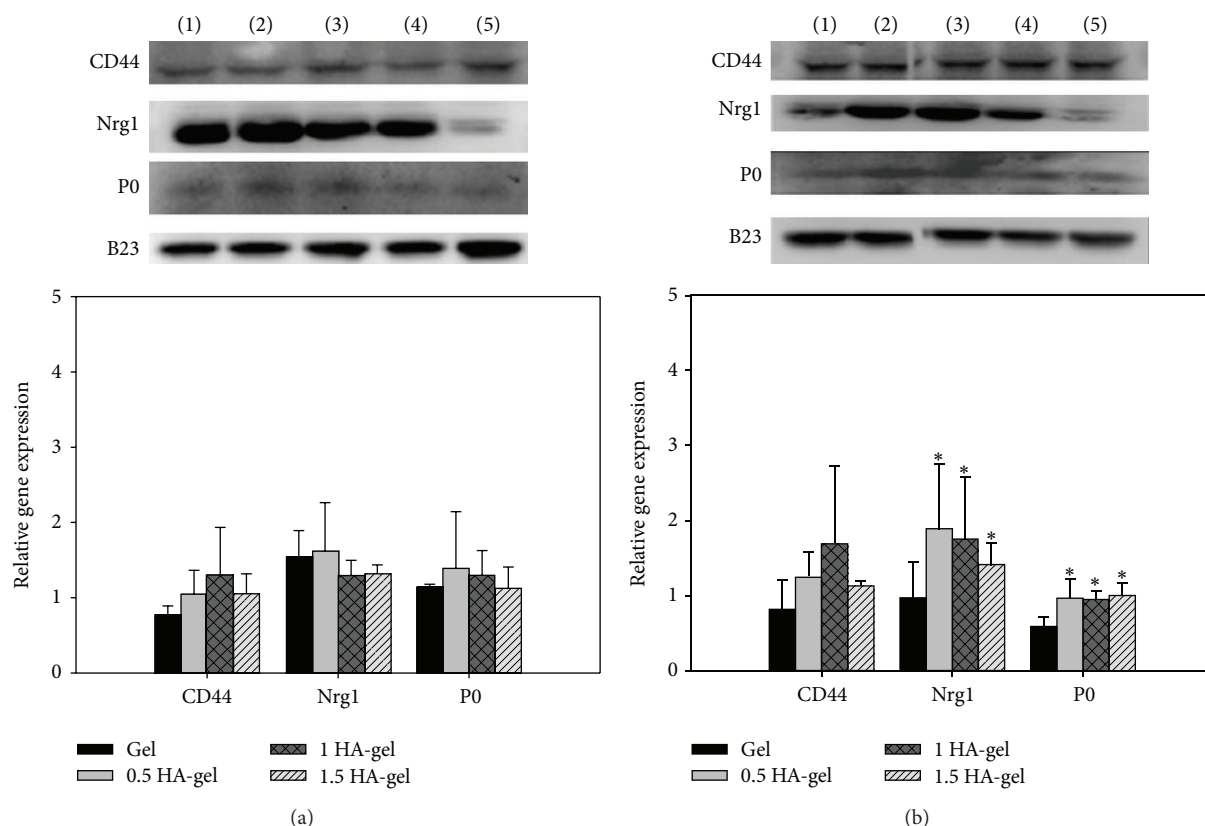


FIGURE 7: Western blot analysis of CD44, Nrg1, and P0 proteins in RT4-D6P2T Schwann cells cultured for (a) 3 or (b) 6 days. Densitometric quantification of the protein bands was performed by normalizing with B23. The data are shown as the fold change relative to those obtained from cells grown on the culture dish surface. The data are presented as the means \pm SD ($n = 3$). (*) denotes significant difference between HA-Gel and Gel ($P < 0.05$). (1) Gel, (2) 0.5 HA-Gel, (3) 1 HA-Gel, (4) 1.5 HA-Gel, and (5) culture dish.

regeneration. A porous and nanofibrous biodegradable matrix that mimics a natural ECM is the optimal scaffold for tissue engineering [19]. It is widely accepted that cell adhesion and most cellular activities, including spreading, migration, proliferation, gene expression, and cytoskeletal function, are sensitive to the nanotopography [20] and molecular composition of the matrix [15]. Xu et al. demonstrated that there were stronger interactions between the cells and the nanofibers [21]. Consequently, most researchers believe that a nanofibrous matrix may promote cell growth more effectively than a sponge substrate.

Several methods have been used to fabricate the fibrous matrix, but the electrospinning is a simple and effective fabrication technique to produce nano-/microfibers. The morphology and diameter of electrospun fibers are dependent on many processing parameters, including the molecular weight of the polymer, the concentration (or viscosity), the conductivity, the applied voltage, and the feeding rate of the polymer solution. In our previous study, we found that increasing the concentration of hyaluronan would increase the charge density on the surface of the electrospinning jet, which would induce higher electrostatic forces and result in the formation of smaller diameter fibers [15]. On the other hand, the diameter of the electrospun fibers increases with increasing concentrations of a polymer solution. A combination of the aforesaid

factors might explain why the mean fiber diameters increased at lower hyaluronan concentrations and decreased at higher hyaluronan concentrations.

Hyaluronan is found in all vertebrate tissues and is important for the organization of pericellular and extracellular matrices [22]. Hyaluronan plays a crucial role in tissue hydration and lubrication and in the regulation of cell functions, including cell attachment, cell mitosis, cell migration, tumor development, metastasis, cell apoptosis, and inflammation [23, 24]. The function of hyaluronan depends upon its interaction with the cell surface receptors, including the receptor for hyaluronan-mediated motility (RHAMM), cluster determinant 44 (CD44), lymphatic vessel endothelial hyaluronan receptor (LYVE-1), hyaluronan receptor for endocytosis (HARE), liver endothelial cell clearance receptor (LEC receptor), and toll-like receptor 4 (TLR4) [25, 26]. Hyaluronan has been shown to influence the interaction of glial cells with axons, to reduce the formation of scar tissue and to provide a suitable environment for tissue repair [27–29]. Wang et al. found that hyaluronan played a vital role in the biological processes involved in the deposition and remodeling of the fibrin extracellular matrix to increase the level of myelination of axons after 4 weeks *in vivo* [30]. Sherman noted that the CD44 transmembrane glycoprotein plays a key role in Schwann cell-neuron interaction. The reduction of CD44 expression

in vitro decreased Schwann cell-neurite adhesion and caused the apoptosis of Schwann cells [31].

The peripheral nerve repair process depends on Schwann cells, which synthesize and secrete important substances such as neuregulin-1 (Nrg1), GFAP, and P0. Nave proposed that Nrg1 is essential for every developmental stage of Schwann cells and for the myelination of axons [32]. Nrg1 is an epidermal growth factor-like ligand that interacts with the tyrosine kinase ErbB receptor to regulate many aspects of neural development. Moreover, Ghatak et al. demonstrated that ErbB2 can be activated by HA through CD44-mediated mechanisms to promote the proliferation and differentiation of Schwann cells [33].

GFAP is an intermediate filament protein that functions as a scaffold for cytoskeletal assembly and maintenance [34]. GFAP also plays a vital role in Schwann cell proliferation and the upregulation of Schwann cell-specific cytoskeletal constituents after nerve damage [35]. Myelin protein zero (P0) is the major adhesive and structural protein of the myelin sheath of peripheral nerves [36]. P0 is expressed by myelinating Schwann cells and is necessary for normal myelin structure and function [37]. Some studies have demonstrated that P0 promoted the regeneration of injured axons [38]. From the results of real-time Q-PCR and western blotting, we found that Nrg1, GFAP, and P0 gene expression and Nrg1 and P0 protein expression were enhanced at day 6 when Schwann cells were cultured on HA-Gel. We speculate that the HA-Gel enhanced myelination via the interaction of the surface CD44 receptors of Schwann cells with hyaluronan.

5. Conclusion

Schwann cells grown on hyaluronan-gelatin nanofibrous matrices showed better organized F-actin stress fibers, higher levels of Nrg1, GFAP, and P0 mRNA, and higher levels of Nrg1 and P0 protein compared to those grown on the gelatin nanofibrous matrix. These findings suggest that the hyaluronan-gelatin nanofibrous matrix could potentially be used in the repair of injured peripheral nerves.

Conflict of Interests

The authors declare that there is no conflict of interests regarding the publication of this paper.

References

- [1] T. A. Ferguson and Y. J. Son, "Extrinsic and intrinsic determinants of nerve regeneration," *Journal of Tissue Engineering*, vol. 2, no. 1, 2011.
- [2] C. E. Schmidt and J. B. Leach, "Neural tissue engineering: strategies for repair and regeneration," *Annual Review of Biomedical Engineering*, vol. 5, pp. 293–347, 2003.
- [3] T. E. Trumble and F. G. Shon, "The physiology of nerve transplantation," *Hand Clinics*, vol. 16, no. 1, pp. 105–122, 2000.
- [4] R. E. Gámez Sazo, K. Maenaka, W. Gu, P. M. Wood, and M. B. Bunge, "Fabrication of growth factor- and extracellular matrix-loaded, gelatin-based scaffolds and their biocompatibility with Schwann cells and dorsal root ganglia," *Biomaterials*, vol. 33, no. 33, pp. 8529–8539, 2012.
- [5] J. M. Medina, A. Thomas, and C. R. Denegar, "Knee osteoarthritis: should your patient opt for hyaluronic acid injection?" *Journal of Family Practice*, vol. 55, no. 8, pp. 669–675, 2006.
- [6] E. Nyman, F. Huss, T. Nyman, J. Junker, and G. Kratz, "Hyaluronic acid, an important factor in the wound healing properties of amniotic fluid: in vitro studies of re-epithelialisation in human skin wounds," *Journal of Plastic Surgery and Hand Surgery*, vol. 47, no. 2, pp. 89–92, 2013.
- [7] G. Y. Özgenel, "Effects of hyaluronic acid on peripheral nerve scarring and regeneration in rats," *Microsurgery*, vol. 23, no. 6, pp. 575–581, 2003.
- [8] J. Taipale and J. Keski-Oja, "Growth factors in the extracellular matrix," *FASEB Journal*, vol. 11, no. 1, pp. 51–59, 1997.
- [9] F. Berthiaume, P. V. Moghe, M. Toner, and M. L. Yarmush, "Effect of extracellular matrix topology on cell structure, function, and physiological responsiveness: hepatocytes cultured in a sandwich configuration," *FASEB Journal*, vol. 10, no. 13, pp. 1471–1484, 1996.
- [10] C. Li, C. Vepari, H.-J. Jin, H. J. Kim, and D. L. Kaplan, "Electrospun silk-BMP-2 scaffolds for bone tissue engineering," *Biomaterials*, vol. 27, no. 16, pp. 3115–3124, 2006.
- [11] M. G. Burnett and E. L. Zager, "Pathophysiology of peripheral nerve injury: a brief review," *Neurosurgical Focus*, vol. 16, no. 5, article E1, 2004.
- [12] S. S. Scherer and J. Salzer, "Axon-Schwann cell interaction during peripheral nerve degeneration and regeneration," in *Glial Cell Development*, pp. 299–330, Oxford University Press, London, UK, 2003.
- [13] J. Hu, J. Zhou, X. Li, F. Wang, and L. Hezuo, "Schwann cells promote neurite outgrowth of dorsal root ganglion neurons through secretion of nerve growth factor," *Indian Journal of Experimental Biology*, vol. 49, no. 3, pp. 177–182, 2011.
- [14] A. I. Gravvanis, A. A. Lavdas, A. Papalois, D. A. Tsoutsos, and R. Matsas, "The beneficial effect of genetically engineered Schwann cells with enhanced motility in peripheral nerve regeneration: review," *Acta Neurochirurgica*, vol. 100, pp. 51–56, 2007.
- [15] F.-Y. Hsu, Y.-S. Hung, H.-M. Liou, and C.-H. Shen, "Electrospun hyaluronate-collagen nanofibrous matrix and the effects of varying the concentration of hyaluronate on the characteristics of foreskin fibroblast cells," *Acta Biomaterialia*, vol. 6, no. 6, pp. 2140–2147, 2010.
- [16] L. Hong, I. Peptan, P. Clark, and J. J. Mao, "Ex vivo adipose tissue engineering by human marrow stromal cell seeded gelatin sponge," *Annals of Biomedical Engineering*, vol. 33, no. 4, pp. 511–517, 2005.
- [17] Y. C. Chen, W. Y. Su, S. H. Yang, A. Gefen, and F. H. Lin, "In situ forming hydrogels composed of oxidized high molecular weight hyaluronic acid and gelatin for nucleus pulposus regeneration," *Acta Biomaterialia*, vol. 9, no. 2, pp. 5181–5193, 2013.
- [18] Y. Liu, X. Z. Shu, S. D. Gray, and G. D. Prestwich, "Disulfide-crosslinked hyaluronan-gelatin sponge: growth of fibrous tissue in vivo," *Journal of Biomedical Materials Research A*, vol. 68, no. 1, pp. 142–149, 2004.
- [19] H. M. Lin, Y. H. Lin, and F. Y. Hsu, "Preparation and characterization of mesoporous bioactive glass/polycaprolactone nanofibrous matrix for bone tissues engineering," *Journal of Materials Science: Materials in Medicine*, vol. 23, no. 11, pp. 2619–2630, 2012.

- [20] K. S. Park, K. J. Cha, I. B. Han et al., "Mass-producible nano-feathered polystyrene surfaces for regulating the differentiation of human adipose-derived stem cells," *Macromolecular Bioscience*, vol. 12, no. 11, pp. 1480–1489, 2012.
- [21] C. Xu, R. Inai, M. Kotaki, and S. Ramakrishna, "Electrospun nanofiber fabrication as synthetic extracellular matrix and its potential for vascular tissue engineering," *Tissue Engineering*, vol. 10, no. 7-8, pp. 1160–1168, 2004.
- [22] T. Laurent, "The biology of hyaluronan. Introduction," *Ciba Foundation Symposium*, vol. 143, pp. 1–20, 1989.
- [23] B. P. Toole and M. G. Slomiany, "Hyaluronan: a constitutive regulator of chemoresistance and malignancy in cancer cells," *Seminars in Cancer Biology*, vol. 18, no. 4, pp. 244–250, 2008.
- [24] C. Cencetti, D. Bellini, C. Longinotti, A. Martinelli, and P. Maricardi, "Preparation and characterization of a new gellan gum and sulphated hyaluronic acid hydrogel designed for epidural scar prevention," *Journal of Materials Science: Materials in Medicine*, vol. 22, no. 2, pp. 263–271, 2011.
- [25] J. B. Park, H.-J. Kwak, and S.-H. Lee, "Role of hyaluronan in glioma invasion," *Cell Adhesion & Migration*, vol. 2, no. 3, pp. 202–207, 2008.
- [26] M. A. Solis, Y.-H. Chen, T. Y. Wong, V. Z. Bittencourt, Y.-C. Lin, and L. L. H. Huang, "Hyaluronan regulates cell behavior: a potential niche matrix for stem cells," *Biochemistry Research International*, vol. 2012, Article ID 346972, 11 pages, 2012.
- [27] L. S. Sherman, T. A. Rizvi, S. Karyala, and N. Ratner, "CD44 enhances neuregulin signaling by Schwann cells," *Journal of Cell Biology*, vol. 150, no. 5, pp. 1071–1083, 2000.
- [28] Y. T. Wei, W. M. Tian, X. Yu et al., "Hyaluronic acid hydrogels with IKVAV peptides for tissue repair and axonal regeneration in an injured rat brain," *Biomedical Materials*, vol. 2, no. 3, pp. S142–S146, 2007.
- [29] Z. Z. Khaing and C. E. Schmidt, "Advances in natural biomaterials for nerve tissue repair," *Neuroscience Letters*, vol. 519, no. 2, pp. 103–114, 2012.
- [30] K. K. Wang, I. R. Nemeth, and B. R. Seckel, "Hyaluronic acid enhances peripheral nerve regeneration in vivo," *Microsurgery*, vol. 18, no. 4, pp. 270–275, 1998.
- [31] L. S. Sherman, T. A. Rizvi, S. Karyala, and N. Ratner, "CD44 enhances neuregulin signaling by Schwann cells," *Journal of Cell Biology*, vol. 150, no. 5, pp. 1071–1083, 2000.
- [32] K.-A. Nave and J. L. Salzer, "Axonal regulation of myelination by neuregulin 1," *Current Opinion in Neurobiology*, vol. 16, no. 5, pp. 492–500, 2006.
- [33] S. Ghatak, S. Misra, and B. P. Toole, "Hyaluronan constitutively regulates ErbB2 phosphorylation and signaling complex formation in carcinoma cells," *Journal of Biological Chemistry*, vol. 280, no. 10, pp. 8875–8883, 2005.
- [34] P. A. Coulombe and P. Wong, "Cytoplasmic intermediate filaments revealed as dynamic and multipurpose scaffolds," *Nature Cell Biology*, vol. 6, no. 8, pp. 699–706, 2004.
- [35] D. Triolo, G. Dina, I. Lorenzetti et al., "Loss of glial fibrillary acidic protein (GFAP) impairs Schwann cell proliferation and delays nerve regeneration after damage," *Journal of Cell Science*, vol. 119, no. 19, pp. 3981–3993, 2006.
- [36] D. D'Urso, P. J. Brophy, S. M. Staugaitis et al., "Protein zero of peripheral nerve myelin: biosynthesis, membrane insertion, and evidence for homotypic interaction," *Neuron*, vol. 4, no. 3, pp. 449–460, 1990.
- [37] D. M. Menichella, E. J. Arroyo, R. Awatramani et al., "Protein Zero is necessary for E-cadherin-mediated adherens junction formation in Schwann cells," *Molecular and Cellular Neuroscience*, vol. 18, no. 6, pp. 606–618, 2001.
- [38] L. B. Spiryda, "Myelin protein zero and membrane adhesion," *Journal of Neuroscience Research*, vol. 54, no. 2, pp. 137–146, 1998.

Research Article

Investigation of the *In Vitro* Degradation of a Novel Polylactide/Nanohydroxyapatite Composite for Artificial Bone

Jianghong Huang,^{1,2} Jianyi Xiong,^{1,2} Jianquan Liu,^{1,2} Weimin Zhu,^{1,2} and Daping Wang^{1,2}

¹ State Key Department of Orthopedics, The Second People's Hospital of Shenzhen, Shenzhen, Guangdong 518035, China

² Key Laboratory of Tissue Engineering, Shenzhen, Guangdong 518035, China

Correspondence should be addressed to Daping Wang; dapingwang1972@163.com

Received 22 April 2013; Revised 7 August 2013; Accepted 20 September 2013

Academic Editor: Anchal Srivastava

Copyright © 2013 Jianghong Huang et al. This is an open access article distributed under the Creative Commons Attribution License, which permits unrestricted use, distribution, and reproduction in any medium, provided the original work is properly cited.

We prepared the poly-L-lactic acid (PLLA)/nanohydroxyapatite (n-HA) composite and investigated the *in vitro* degradation of pure PLLA material and PLLA/n-HA composites in order to identify a suitable and ideal artificial bone tissue repair material. The water uptake, weight loss, and changes in the PBS pH value and in the mechanical properties of material were measured during the processes that PLLA and PLLA/n-HA biological composites were degraded in PBS. We also performed electron microscopic scanning of the material fracture surface and observed the microscopic morphologies of materials during the degradation process. We found that the degradation rate of the PLLA/n-HA material was slower than the PLLA material, and there was a little degradation of the PLLA/n-HA material at early stages. The PLLA/n-HA material also maintained the initial mechanical strength better than the pure PLLA material. The PLLA/n-HA material is thus a better material for artificial bone than the pure PLLA material.

1. Introduction

The quest for an ideal artificial bone tissue repair material is a hot topic in the bone tissue engineering research field. Polylactic acid is biomedical synthetic material that is most commonly used in bone tissue repair, and it has good biocompatibility, degradability, and processing controllability. However, polylactic acid still has defects such as poor hydrophilicity, generation of acidic degradation products, and insufficient retention time for its mechanical strength [1–3]. Nanohydroxyapatite (n-HA) is a type of bone graft substitute material that has similar physicochemical and biological properties as the human skeleton and can be absorbed by the body and gradually transformed into autologous bone component. n-HA is strongly hydrophilic and is a mildly basic material. Moreover, it can be degraded via the solution-mediated process (dissolved in physiological solutions) and the cell-mediated process (phagocytosis). The calcium and phosphate ions released after degradation participate in the local bone tissue calcification or enter the calcium and phosphorus pools of the body, and they can be subsequently utilized or discharged physiologically. However, as a scaffold material for tissue engineering, the mechanic characteristics of n-HA

are weak and cannot match the mechanical strength of human bone. In addition, the degradation of the n-HA is slow [4–6]. PLLA/n-HA composites can be generated using the poly-L-lactic acid (PLLA) as a base material and n-HA particles as reinforcement substances, thus fully utilizing the advantages of the two materials as biomedical engineering materials [7, 8]. The paper focused on the *in vitro* degradation characteristics of pure PLLA and PLLA/n-HA composites in order to provide the ideal bone tissue repair material for bone tissue engineering.

2. Materials and Methods

2.1. Preparation of Composites

2.1.1. Preparation of PLLA. L-lactide (LLA) with high purity (99.95%) was prepared by a combination of distillation technology and washing-recrystallization with lactic acid. PLLA was synthesized via ring-opening polymerization using prepared L-lactide at 140°C for 24 hours. The solution spinning method was used to obtain sheets of the PLLA material (Figure 1).



FIGURE 1: Sheets of the PLLA material.

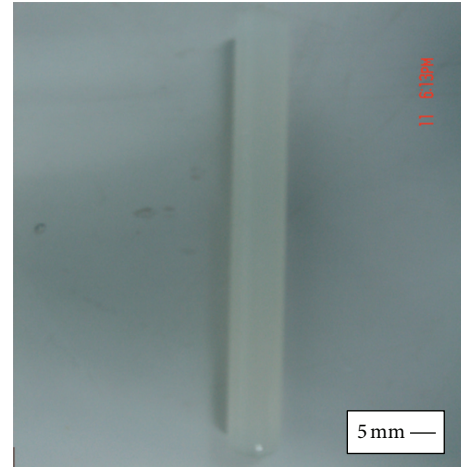


FIGURE 2: n-HA powder.

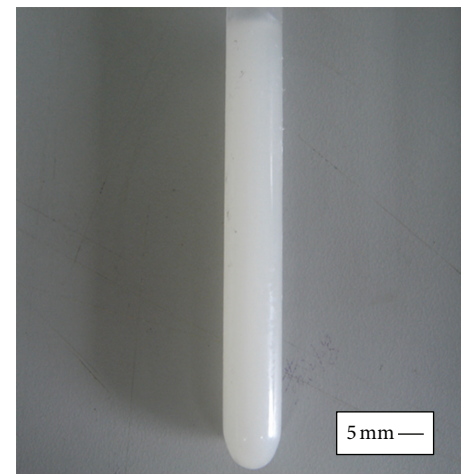
2.1.2. Preparation of n-HA Powder. n-HA was generated from $\text{Ca}(\text{NO}_3)_2$ and NH_4PO_3 via sol flocculation. During the chemosynthesis of n-HA, aqua ammonia was used to adjust the PH value to 8~13. With dispersant agent and appropriate agitator, the n-HA deposit was separated out of the solution. With series of processes including scouring, filtering, drying, sinter-roasting, and milling, the n-HA powder has been prepared (Figure 2).

2.1.3. Preparation of PLLA/n-HA Artificial Bone. The PLLA/n-HA composite was jointly developed by the Tissue Engineering Laboratory of the Second People's Hospital of Shenzhen and the Powder Metallurgy Research Institute of Central South University. The PLLA/n-HA composite was prepared via melt blending method, which includes 2 steps. Firstly, the PLLA was heated into viscous flow state at 160°C . Then n-HA was mixed with PLLA. The PLLA/n-HA artificial bone material was processed into cylinders (with a length of 10 mm, diameter of 5 mm, and height of 5 mm) (Figure 3) and preserved in vacuum packaging.

2.2. Preparation of the In Vitro Degradation Medium, Phosphate Buffered Saline (PBS). The preparation of PBS solution was carried out according to the following steps:



(a)



(b)

FIGURE 3: Sample strips after being mold-pressed: (a) PLLA; (b) PLLA/n-HA.

- (1) prepare 1/15 mol/L KH_2PO_4 , that is, 9.078 g KH_2PO_4 per liter of water;
- (2) prepare 1/15 mol/L $\text{Na}_2\text{HPO}_4 \cdot 2\text{H}_2\text{O}$, that is, 11.876 g $\text{Na}_2\text{HPO}_4 \cdot 2\text{H}_2\text{O}$ per liter of water;
- (3) mix 18.2% (volume fraction) of the KH_2PO_4 solution and 81.8% of the $\text{Na}_2\text{HPO}_4 \cdot 2\text{H}_2\text{O}$ solution;
- (4) adjust the pH of the PBS solution to be about 7.4 by using acid/base solution.

2.3. In Vitro Degradation Experiments. We used the compression molding method to prepare strips of PLLA and PLLA/n-HA composite materials ($10 \text{ mm} \times 5 \text{ mm} \times 5 \text{ mm}$ with a n-HA content of 20 wt%) (Figure 3). The prepared biological material was cleaned with deionized water and placed in a 40°C vacuum oven. After being sufficiently dried, the sample stripes were weighed, and the weight was recorded as m_0 . The weighted and dry strips were divided into two categories based on the material composition (PLLA and PLLA/n-HA). Each category of material was further divided into 10 groups

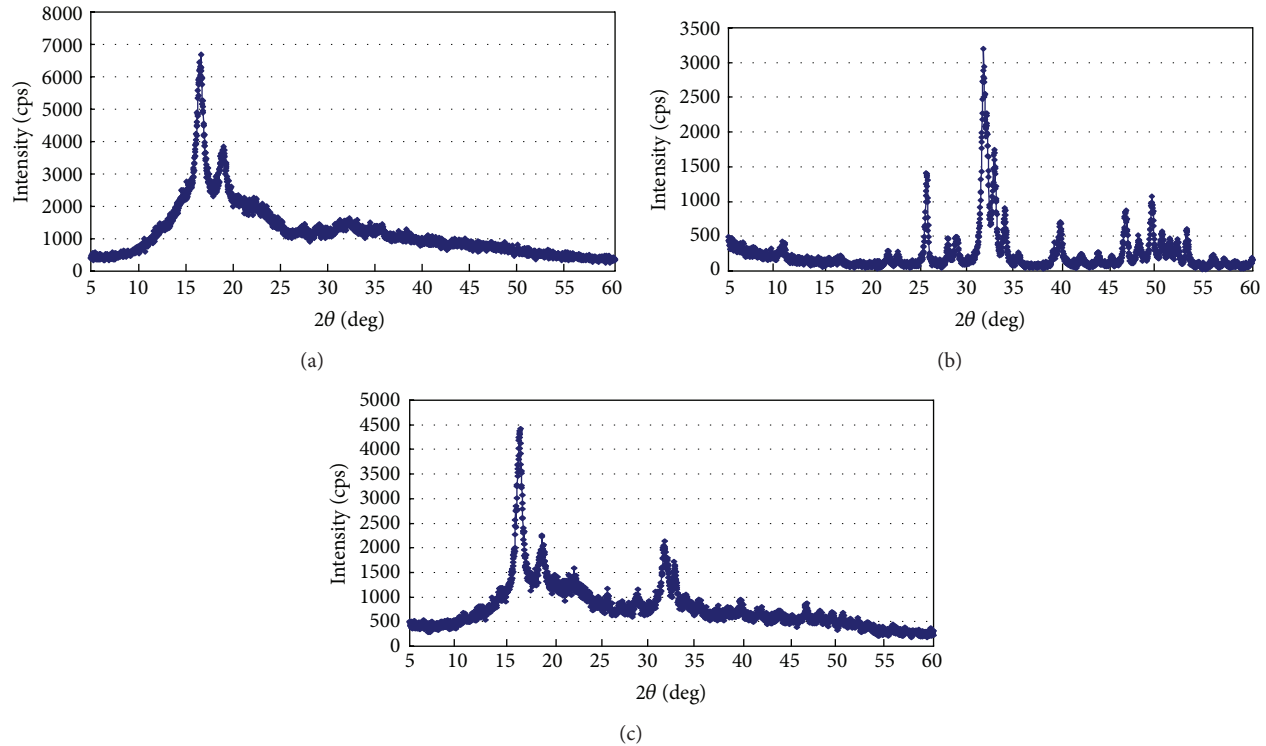


FIGURE 4: (a) XRD curves of PLLA; (b) XRD curves of HA powder; (c) XRD curves of PLLA/n-HA composite.

based on the degradation time (2 weeks, 4 weeks, 6 weeks, 8 weeks, 10 weeks, 12 weeks, 14 weeks, 16 weeks, 18 weeks, and 20 weeks), and each group contained three samples.

All the samples were placed in clean glass bottles containing PBS, which were then sealed and placed in an electric thermostatic shaker. The shaker temperature was $37 \pm 0.5^\circ\text{C}$, and the vibration speed was 100 rpm.

2.4. Evaluation Indicators

2.4.1. Assessing the PLLA, n-HA Powder, and PLLA/n-HA Composite Using X-Ray Diffraction (XRD). The crystal structure of PLLA, n-HA, and PLLA/n-HA composite was measured by X-ray diffraction system (D/max 2550, Japan). The scanning range is from 0 to 80 degree and the scanning speed is $8.0^\circ/\text{min}$. Data were acquired using a $\text{CuK}\alpha_1$ source at 40 kV and 300 mA.

2.4.2. Assessing the PLLA/n-HA Composite Using Transmission Electron Microscope (TEM). The PLLA/n-HA composite was cut into blocks measuring about 1 mm wide, 1 mm long, and 1 mm thick. The blocks and n-HA powder were post-fixed in 1% osmium tetroxide for 2 h at 4°C . They were rinsed in distilled water for several times, dehydrated in graded series (20~100%) of ethanol and then in propylene oxide, infiltrated with Epon 812, and finally polymerized in pure Epon 812 for 48 h at 65°C . Ultrathin sections were cut on an ultramicrotome using diamond knives, collected on copper

grids, and stained with 4% uranyl acetate and Reynolds, lead citrate. Sections were observed under a transmission electron microscope.

2.4.3. Calculation of the Biological Material Water Uptake Ratio and Weight Loss Ratio. One group was taken for each type of material at various degradation time points (2 weeks, 4 weeks, 6 weeks, 8 weeks, 10 weeks, 12 weeks, 14 weeks, 16 weeks, 18 weeks, and 20 weeks). The sample weight was measured in accordance with the following steps.

The weight of the sample before degradation is called the initial weight (m_0). After a certain period of degradation, the samples were removed, blotted gently with paper to remove the water on the surface, and weighed to get the wet weight (m_1). The degraded experimental samples were vacuum-dried for 24 h at 40°C , and the residual weight (m_2) was then obtained. The sample water uptake ratio (m_A) and the weight loss ratio (m_L) were calculated as follows [9]:

$$m_A (\%) = \frac{100 (m_1 - m_2)}{m_2} \quad (1)$$

$$m_L (\%) = \frac{100 (m_0 - m_2)}{m_0} \quad (2)$$

2.4.4. pH of the PBS Solution. A digital pH meter (pHS-25 pH meter with digital display, Shanghai REX Instrument Factory) was used to measure the pH value of the PBS solution at different degradation stages.

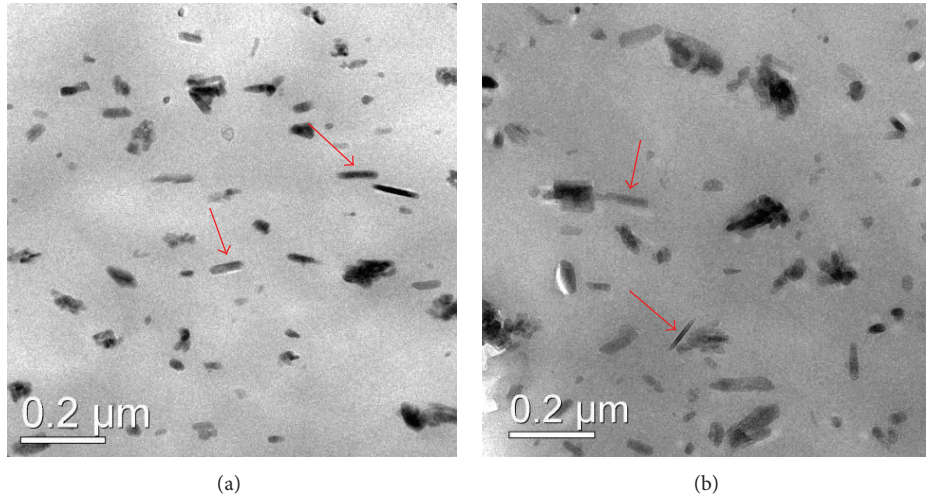


FIGURE 5: (a) TEM micrograph of the n-HA powder; (b) TEM micrograph of PLLA/n-HA composites.

2.4.5. Measurement of Flexural Strength and Modulus. The flexural strength and modulus of each dried sample strip were measured using the three-point bending method on a universal testing machine (Instron-1121, UK).

2.4.6. Scanning Electron Microscopy (SEM) Morphological Features of the Fracture Surface. After measuring the flexural strength, the fracture surface of the sample strip was sprayed with gold, and SEM (field emission scanning electron microscope, Tescan, Czech) was used to observe the changes in the bending fracture microscopic morphology of samples in the degradation process.

3. Results

3.1. XRD Analysis of the PLLA, n-HA Powder, and PLLA/n-HA Composite. Figure 4 shows the XRD curves of PLLA, n-HA, and PLLA/n-HA composite. From Figure 4(a), we can see that PLLA shows its most intense diffraction peaks at 2θ values of 16.6 and 18.96, which is in agreement with 2013 international center for diffraction data (PDF no. 54-1917). Figure 4(b) shows the XRD curve of n-HA. n-HA shows its most intense diffraction peaks at 2θ values of 31.74, 32.12, and 32.9, which coincides with 2013 international center for diffraction data (PDF no. 9-432). Figure 4(c) shows XRD curve of PLLA/n-HA composite. PLLA/n-HA composite shows its most intense diffraction peaks at 2θ values of 16.6 and 18.96, which is in agreement with the PLLA data in PDF no. 54-1917. In addition, PLLA/n-HA shows its most intense diffraction peaks at 2θ values of 31.74, 32.12, and 32.9, which coincides with the n-HA data in PDF no. 9-432.

3.2. TEM Analysis of the n-HA Morphology in the PLLA/n-HA Composite. Results of TEM showed that n-HA presents needle-like structure, which is similar to human bone components (Figure 5(a)). In addition, n-HA was distributed evenly in n-HA/PLLA composite (Figure 5(b)).

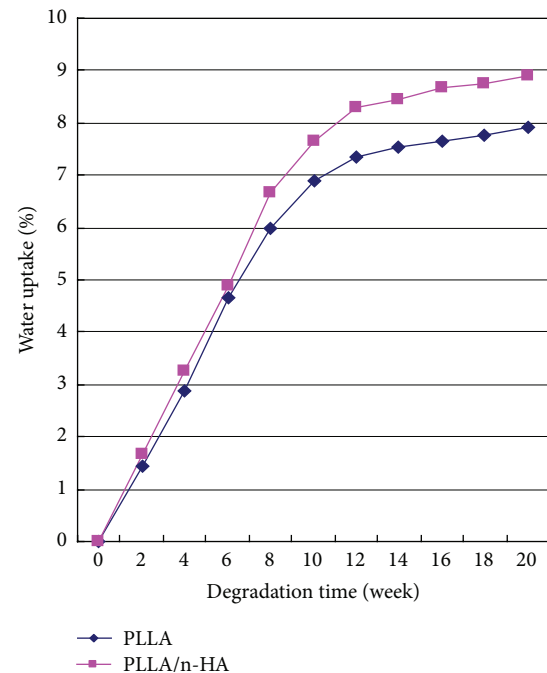


FIGURE 6: Variation of water uptake of biomaterials with degradation time.

3.3. Changes in the Material Water Uptake Ratio and Weight Loss Ratio. Figure 6 showed that with the extension of the degradation time, the water uptake ratios of the two samples were gradually increased, but the rate of increase in the water uptake ratio became slower. During the entire degradation period, the water uptake ratios of the PLLA/n-HA samples were significantly higher than those of the PLLA samples.

As seen from the curves in Figure 7, the weight loss ratios of the PLLA and PLLA/n-HA materials were relatively low before the 6th week of degradation, and they were 1.038% and 0.698%, respectively. After 6 weeks of degradation, with the rapid increase of the water uptake ratio, the weight loss ratio

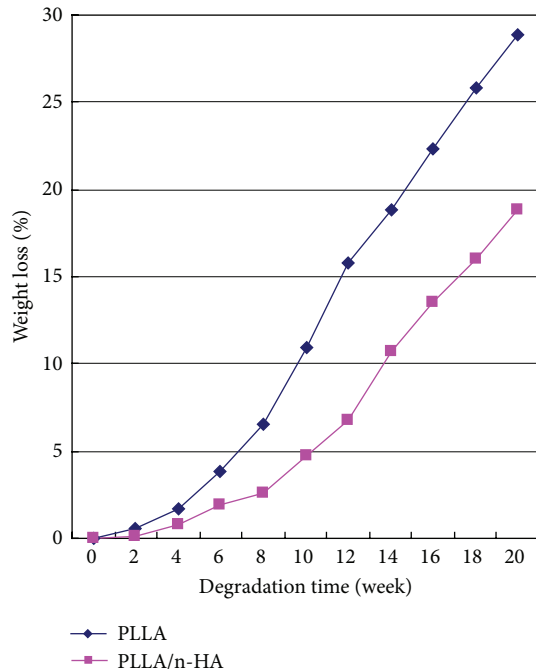


FIGURE 7: Change of sample weight loss as a function of degradation time.

of the pure PLLA material was also increased sharply and showed a linear upward trend with the degradation time. In contrast, the weight loss ratio of PLLA/n-HA composite did not increase with the degradation time until the degradation time reached 10 weeks, and the extent of increase was smaller than the pure PLLA material.

3.4. pH Changes of the PBS Solution. Figure 8 showed the curve that the pH value of the PBS solution changed with the degradation time. It demonstrated that prior to 4 weeks of degradation, the decrease in the pH value was small for all PBS solution. After 4 weeks, the pH value of the PBS solutions containing the PLLA samples began to show the phenomenon of accelerated decrease. This phenomenon became even more significant after the pH value dropped below 6. At the 10th week, the pH value was reduced to about 3. After 10 weeks, the decrease in the pH value became slow and basically stopped decreasing. Before the degradation time reached six weeks, the pH value of the PBS solution containing the PLLA/n-HA sample almost showed no changes. And between 6~12 weeks, the pH value of the buffer was slightly decreased with the extension of degradation time. After 12 weeks, the decrease in the buffer pH was intensified. The pH value at 16 weeks was about 4.2, and after 16 weeks, the decrease in the pH value started to slow down.

3.5. Changes in the Material Mechanical Properties in the Degradation Process. Figures 9 and 10, respectively, demonstrate the curves by which the bending strength and bending modulus of each sample of biological material changes with the degradation time in the process of degradation. As

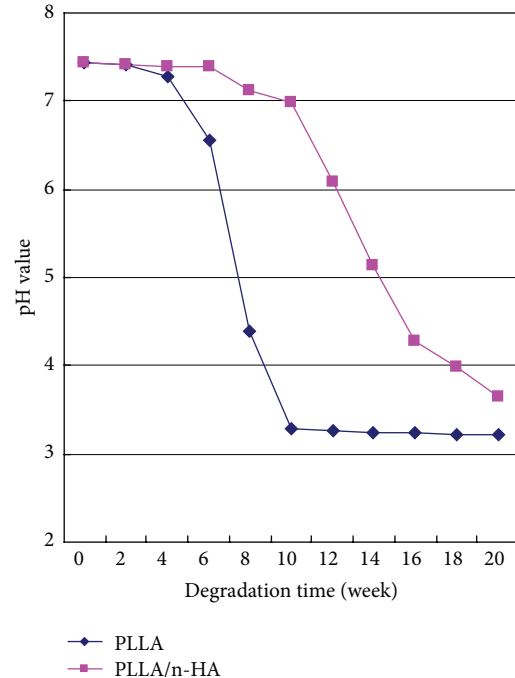


FIGURE 8: Effect of degradation time on pH value of PBS.

seen from Figure 9, in the early stages of degradation (0~6 weeks), the strengths of all materials showed little reduction. The strength of the pure PLLA material decreased abruptly between 6~12 weeks, and the decrease of strength was alleviated after 12 weeks. The strength of the PLLA/n-HA composite started to show significant decrease after eight weeks and lasted until the end of the degradation experiment. The curves in Figure 10 that depicted the changes of material flexural over the degradation time revealed similar changes as the curves in Figure 9.

3.6. Analysis of the Fracture Morphology of Biological Materials in the Degradation Process. Figure 11 shows the SEM images of the morphologies of the bending fracture of the pure PLLA biological material in the degradation process ($\times 8000$). Figure 12 shows the SEM images of the morphologies of the bending fracture of the PLLA/n-HA composite biomaterial in the degradation process ($\times 8000$).

Before degradation, the fractures of each biological material sample showed dense structures. After 4 weeks of degradation, the fracture surface of the pure PLLA material did not show significant changes, and the fracture surface was smooth without cracks (Figure 11(b)). After 6 weeks of degradation, a small amount of cracks could be observed in the middle of the fracture, although the fracture edge still showed compact structures (Figure 11(c)). It might be related to that fact that the polymeric material first underwent autocatalytic degradation. After 8 weeks of degradation, the cracks extended to peripheral areas and a large number of the small holes could be observed in the fracture surface (Figure 11(d)), which might be caused by the degradation of the interior of the material. This suggested that the PLLA

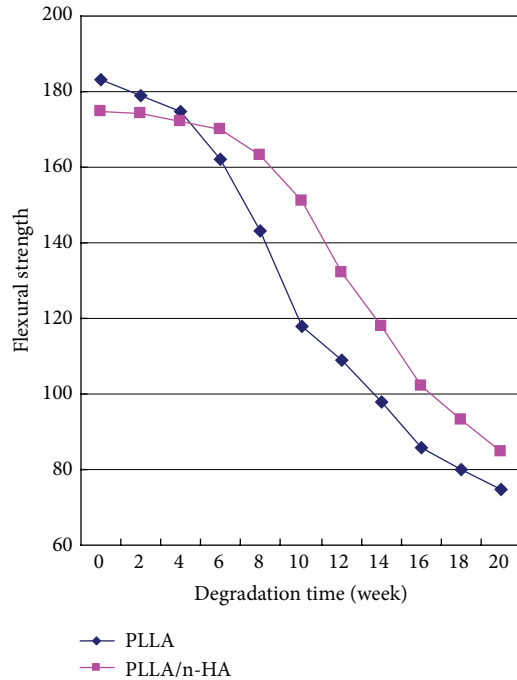


FIGURE 9: Variations of bending strength of biomaterials with degradation time.

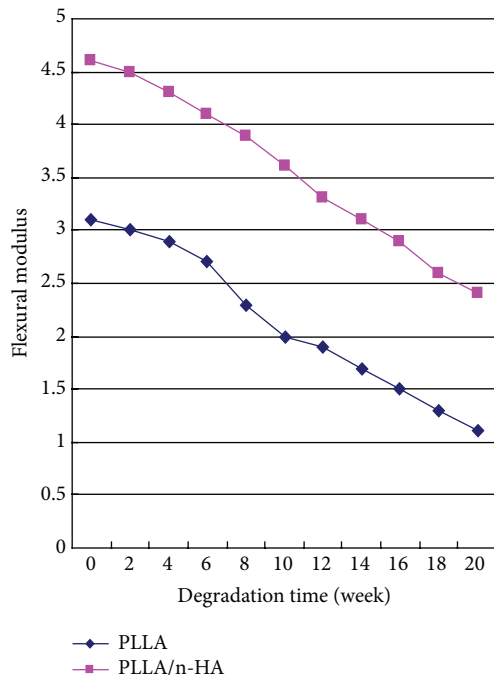


FIGURE 10: Effects of the degradation time on the bending modulus of biomaterials.

materials had undergone partial degradation. After 12 weeks of degradation, the cracks of the material expanded to form slits, providing passage for the water molecules, thus accelerating the degradation of the PLLA materials. Many holes generated by the degradation process could be observed in

the material fracture surface (Figure 11(e)). When the degradation time was further extended, the slits continued to expand, and 18 weeks later, the PLLA material had collapsed, and the material was destructed as a whole (Figure 11(f)).

Figure 12 shows the SEM images of the fracture surfaces of the PLLA/n-HA material. Compared with the morphology of the fracture surface of the pure PLLA material, the fracture surface of the PLLA/n-HA material showed dense structures with only a small amount of cracks prior to 10 weeks of degradation. After 14 weeks, the fracture surface showed a large number of mesh-like holes, accompanied by the generation of large cracks. In addition, exposed HA particles could also be clearly seen, suggesting the occurrence of the degradation and absorption of the PLLA/n-HA materials. With the extension of the degradation time, the PLLA/n-HA material underwent accelerated degradation, and criss-cross cracks appeared on the fracture surface, although exposed HA particles were not found. It suggested that with the progress of the degradation, HA particles were already dissolved in the PBS solution. After 20 weeks, the fracture surface presented more depression, widened and deepened cracks, and loose structures. Large amounts of degradation fragments could not be decomposed in a timely manner and were thus filled into the cracks in the interior of the materials. The composite materials showed significant degradation.

4. Discussion

The biggest advantage of biomedical polymeric materials is its biodegradability and bioresorbability. Biocomposite materials not only keep the features of the component materials, but also can acquire new properties that individual component materials do not have. Therefore, the comprehensive properties of the composite materials are better than those of the original component materials [10]. Biodegradability refers to the process that the polymeric chains of solid-state polymeric materials or devices are broken by the complex physiological environment *in vivo*, leading to the generation of large quantities of small molecule fragments and the complete destruction of the polymeric materials or devices. Bioresorbability refers to the process that solid-state polymeric materials or devices are biodegraded *in vivo* and that the resulting degradation products are absorbed or excreted via metabolism.

Besides the general characteristics such as good biocompatibility and the lack of antigenicity, rejection reaction, teratogenicity, carcinogenicity, and toxicity and side effects, biodegradable polymeric composites that can be used as an artificial bone tissue repair materials also need to have other features as follows: (1) moderate degradation rate, that is, the degradation rate of the artificial bone tissue repair material must match the rate of bone healing, (2) appropriate biomechanical properties, that is, the biomechanical properties of the implanted artificial bone tissue repair material have to match the mechanical properties of the implant site [11].

Hydroxyapatite (HA), whose chemical formula is $\text{Ca}_{10}(\text{PO}_4)_6(\text{OH})_2$, is the major inorganic component of human bone. Sixty percent of HA in bone is needle-like and less than 100 nm in size [12]. TEM results demonstrated

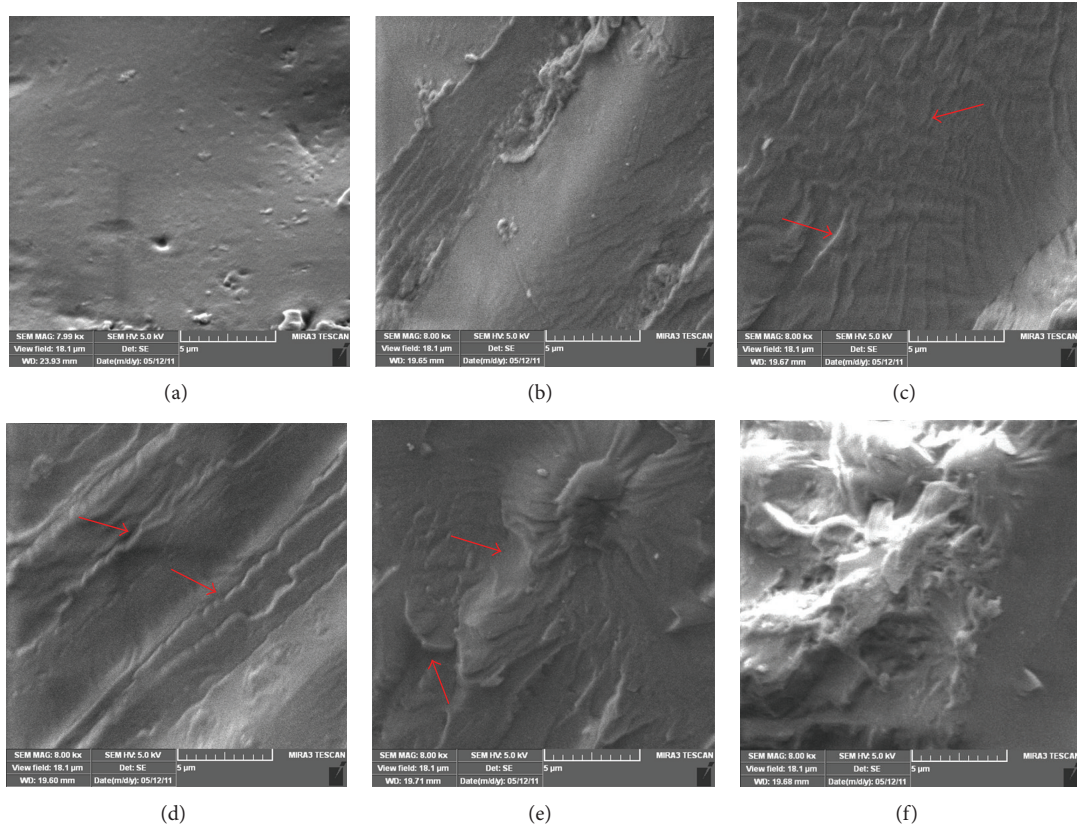


FIGURE 11: SEM images of fracture surfaces of degraded PLLA biomaterials ($\times 8000$) ((a)-0 w; (b)-4 w; (c)-6 w; (d)-8 w; (e)-12 w; (f)-18 w). (a) and (b) smooth fracture surface without substantial cracks; (c) Surfaces showed a small amount of cracks as red arrows indicated, and the fracture edges still had compact structure; (d) the cracks in material surface extended to the peripheral area, and a large number of small holes appeared in the fracture surface as red arrows indicated; (e) the cracks of the material expanded to form slits, and the fracture surface was covered with holes as red arrows indicated; (f) materials had collapsed, and the material was destructed as a whole.

that the n-HA in this study was 50~200 nm in size and showed needle-like appearance, which was close to that of human bone. Results of XRD showed that PLLA and n-HA manufactured in this study are of good degree of crystallization. Furthermore, both PLLA and n-HA keep the integrated structure of crystal in the PLLA/n-HA composite.

Several methods have been used to prepare the PLLA/n-HA composite, such as coating method [13], solvent casting/particulate leaching [14], supercritical CO_2 foaming [15], solution blending method [16], and melt blending method. Organic solvent is often used in the preparation of composites via the above methods except melt blending method. Besides its unfavorable effect on grafted tissues, organic solvent may inactivate biological growth factors and negatively influence cell adherence and proliferation. In order to avoid the negative effect of organic solvent, melt blending method was used in this study.

Varila et al. compared *in vitro* the reactivity of the composites in simulated body fluid, Tris-buffered solution, and phosphate buffered saline (PBS). They concluded that degradation of the composites containing the bioactive glasses was faster in PBS than in the two other solutions [17]. Furthermore, PBS was often used as *in vitro* degradation system in other studies [9, 18–26]. In consistent with previous

studies, PLLA/n-HA was put into PBS to observe the water uptake ratio, weight loss ratio, and other biological properties.

There are multiple interfaces between the respective components of the PLLA/n-HA composite material. The interfaces exposed in the medium present the “suction effect” due to the capillary action. As a result, water molecules are prone to diffuse along the interfaces and enter into the inside of the material. Therefore, the water uptake ratio of the PLLA/n-HA composite material is higher than that of the non-interfaced and closely combined pure PLLA material. In addition, the hydrophilic n-HA particles are more conducive for absorption and lead to the increase in the water uptake ratio of the composite material.

As compared to the pure polymeric materials, composite materials have a slower degradation rate. The specific reasons might include the following aspects. First, micropores among the pure PLLA material molecules provide channels for the penetration of water molecules, so that water molecules can easily get access to the interior of the material and accelerate the material degradation. Second, as to the PLLA/n-HA composite material, although the water uptake of the composite material is greater than that of the pure PLLA material, the basic ions released by HA into the PBS buffer can neutralize the acidic substances generated in the PLLA

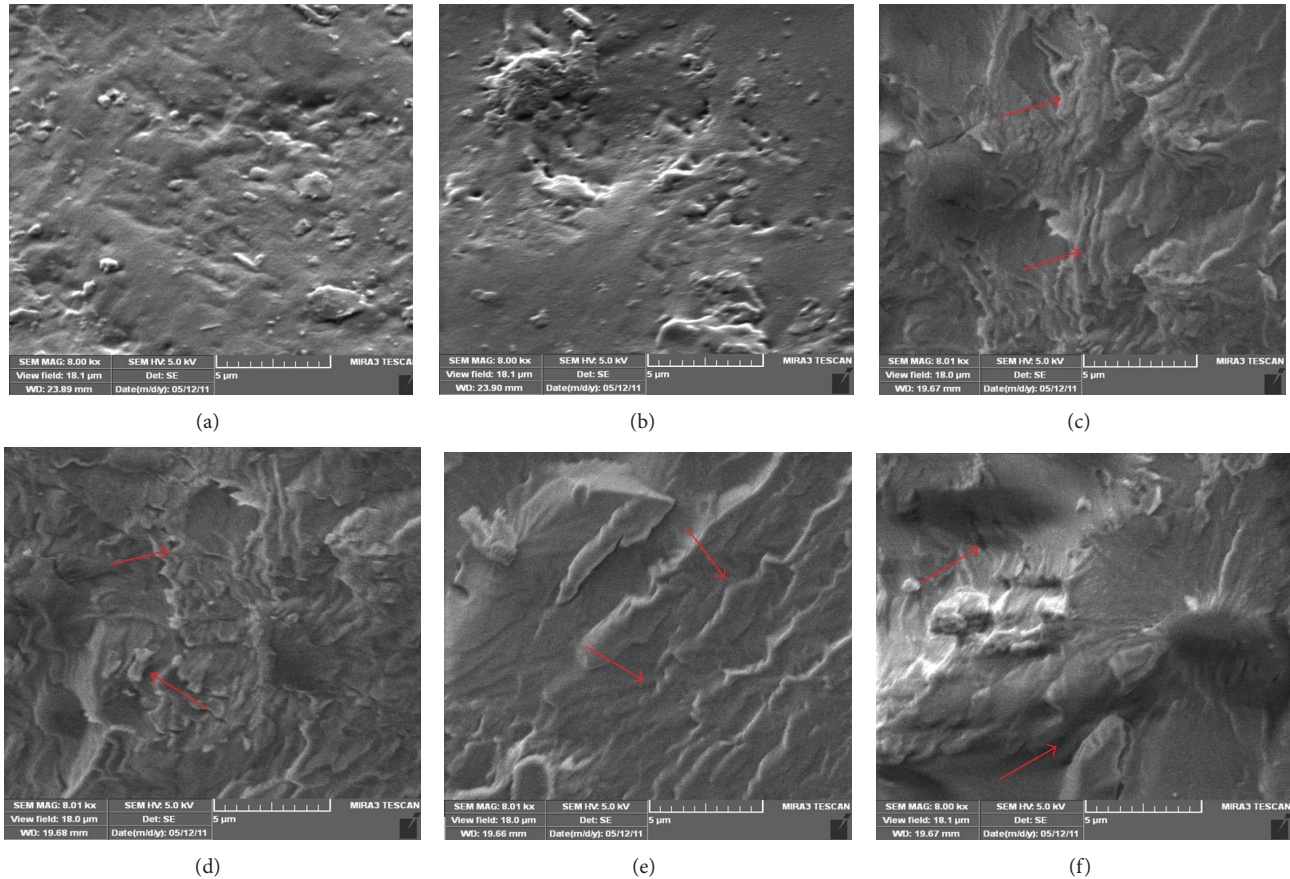


FIGURE 12: SEM images of fracture surfaces of degraded PLLA/n-HA biomaterials ($\times 8000$) ((a)-0 w; (b)-6 w; (c)-10 w; (d)-14 w; (e)-18 w; (f)-20 w). (a) and (b) No significant changes on the fracture surface, which had no substantial cracks; (c) The fracture showed compact structure with only a small number of cracks as red arrows indicated; (d) Fracture surface showed a large number of mesh-like holes, accompanied by the generation of large cracks as red arrows indicated; (e) Criss-cross cracks on the fracture surface as red arrows indicated; (f) Fracture surface showed more depression, widened and deepened cracks as red arrows indicated, loose structure, and significant degradation.

degradation process, slowing the autocatalytically accelerated degradation of the polymeric material in acidic environment and inhibiting the degradation of the polymeric material. As compared to the pure PLLA biological material, the degradation rate of the PLLA/n-HA composite material in the initial stages of degradation is slower, thus delaying the degradation of the PLLA/n-HA composite. Therefore, the weight loss of the composite material is smaller than that of the pure polymer materials in the same period.

The incorporation of n-HA particles successfully reduces the acidity caused by the acidic products of polylactic acid degradation generated in the early phase of degradation. It thus can reduce or avoid the aseptic inflammation caused by the acidic substance, and it can improve the biocompatibility of the polymeric biomaterial. In addition, in the early phase of degradation, due to the slowing down of the degradation rate, the PLLA/n-HA composite material can maintain high initial mechanical strength and provide sufficient supporting effect for new bone tissue. In the late phase of degradation, the degradation of the PLLA/n-HA composite material accelerates, which is conducive to new bone tissue ingrowth in order to achieve good therapeutic effect. Therefore, the prepared

polymeric PLLA/n-HA composite material has wide application prospect and practical value.

The ions released from the dissolution of n-HA in the PLLA/n-HA composite material are basic and can neutralize the acidic degradable substances generated during the PLLA degradation process. The autocatalytic degradation effect of acids on the polymeric material can be alleviated, thus slowing down the degradation rate. In the early phases of degradation, the composite material can still maintain relatively high strength. After 6 weeks of degradation, the decrease rate in the composite material flexural strength and modulus accelerated. After 10 weeks of degradation, the composite material had a flexural strength of 151 MPa, equivalent to that of the fresh adult bone (160 MPa), and it could still provide a good supporting role for the newly generated bone tissue. Thus, the PLLA/n-HA composite material prepared by the addition of n-HA can maintain relatively high flexural strength and modulus in the early and middle phases of degradation. After 16 weeks of degradation, it was still able to maintain a flexural strength of 100 MPa, higher than the minimum flexural strength of the human bones (96 MPa), thus providing a reliable support for the regeneration of new

bone tissue. In addition, the improvement in the acidic environment can reduce or avoid the occurrence of inflammatory reaction caused by the acidic degradation products. In the late phase of degradation, due to the degradation of the polymeric substance in the composite material, the amount of composite material is gradually reduced, leaving space for new generated bone tissue.

Changes in the material fracture surface morphology revealed that the degradation rate of the PLLA/n-HA material was slower than that of the PLLA material. Most importantly, before the degradation time reached 14 weeks, there was little degradation of the PLLA/n-HA material, and its mechanical strength loss was also small. It thus is able to maintain a high mechanical strength and provide a good supporting role for new bone tissue. This is mainly related to the following reasons. (1) The addition of n-HA particles neutralizes the acidic products generated during the degradation process of polymeric materials and slows down the PLLA autocatalytic degradation. (2) It also effectively reduces the inflammatory response caused by the acidic products and improves the biocompatibility of the composite materials.

The *in vitro* degradation characteristics of our PLLA/n-HA composite material as mentioned above might be beneficial for its application in bone tissue repair. However, since the body's osteogenic process is very complicated, investigation of the physicochemical properties of *in vitro* degradation alone cannot confirm its value in application. It is thus necessary to carry out a series of follow-up experiments focusing on the *in vivo* bone tissue repair and construction, coupling with the bone growth factors and co-culture with osteoblasts *in vitro*.

Acknowledgments

The authors acknowledge the Shenzhen Key Laboratory Enhancement Projects (CXB201104220049A), Shenzhen-Hong Kong Innovation Circle Project Fund (JSE201007190007A), Shenzhen Second People's Hospital Seeding Plan for providing the funding source for this work.

References

- [1] C. Zhang, Q. Feng, T. Zhang, J. Chen, C. Lu, and H. Wu, "In vitro biologic evaluation on nano-hydroxyapatite/poly (L-lactic acid) biocomposites fabricated using in-situ growth method," *Sheng Wu Yi Xue Gong Cheng Xue Za Zhi*, vol. 29, no. 2, pp. 307–310, 2012.
- [2] H. K. Moon, Y. S. Choi, J.-K. Lee, C.-S. Ha, W.-K. Lee, and J. A. Gardella Jr., "Miscibility and hydrolytic behavior of poly(trimethylene carbonate) and poly(L-lactide) and their blends in monolayers at the air/water interface," *Langmuir*, vol. 25, no. 8, pp. 4478–4483, 2009.
- [3] X. Niu, Q. Feng, M. Wang, X. Guo, and Q. Zheng, "Porous nano-HA/collagen/PLLA scaffold containing chitosan microspheres for controlled delivery of synthetic peptide derived from BMP-2," *Journal of Controlled Release*, vol. 134, no. 2, pp. 111–117, 2009.
- [4] S. Ishii, J. Tamura, T. Furukawa et al., "Long-term study of high-strength hydroxyapatite/poly(L-lactide) composite rods for the internal fixation of bone fractures: a 2-4-year follow-up study in rabbits," *Journal of Biomedical Materials Research B*, vol. 66, no. 2, pp. 539–547, 2003.
- [5] L. MacArini, P. Milillo, A. Mocci, R. Vinci, and G. C. Ettore, "Poly-L-lactic acid—hydroxyapatite (PLLA-HA) bioabsorbable interference screws for tibial graft fixation in anterior cruciate ligament (ACL) reconstruction surgery: MR evaluation of osteointegration and degradation features," *Radiologia Medica*, vol. 113, no. 8, pp. 1185–1197, 2008.
- [6] M. Ngiam, S. Liao, A. J. Patil et al., "Fabrication of mineralized polymeric nanofibrous composites for bone graft materials," *Tissue Engineering A*, vol. 15, no. 3, pp. 535–546, 2009.
- [7] F. Peng, X. Yu, and M. Wei, "In vitro cell performance on hydroxyapatite particles/poly(L-lactic acid) nanofibrous scaffolds with an excellent particle along nanofiber orientation," *Acta Biomaterialia*, vol. 7, no. 6, pp. 2585–2592, 2011.
- [8] F. Peng, J. R. Olson, M. T. Shaw, and M. Wei, "Influence of pretreatment on the surface characteristics of PLLA fibers and subsequent hydroxyapatite coating," *Journal of Biomedical Materials Research B*, vol. 88, no. 1, pp. 220–229, 2009.
- [9] H. Zhao, L. Ma, Y. Gong, C. Gao, and J. Shen, "A polylactide/fibrin gel composite scaffold for cartilage tissue engineering: fabrication and an *in vitro* evaluation," *Journal of Materials Science*, vol. 20, no. 1, pp. 135–143, 2009.
- [10] D. D. Wright-Charlesworth, J. A. King, D. M. Miller, and C. H. Lim, "In vitro flexural properties of hydroxyapatite and self-reinforced poly(L-lactic acid)," *Journal of Biomedical Materials Research A*, vol. 78, no. 3, pp. 541–549, 2006.
- [11] G. Sui, X. Yang, F. Mei et al., "Poly-L-lactic acid/hydroxyapatite hybrid membrane for bone tissue regeneration," *Journal of Biomedical Materials Research A*, vol. 82, no. 2, pp. 445–454, 2007.
- [12] M. A. Malik, D. A. Puleo, R. Bizios, and R. H. Doremus, "Osteoblasts on hydroxyapatite, alumina and bone surfaces *in vitro*: morphology during the first 2 h of attachment," *Biomaterials*, vol. 13, no. 2, pp. 123–128, 1992.
- [13] T. Tian, D. Jiang, J. Zhang, and Q. Lin, "Fabrication of bioactive composite by developing PLLA onto the framework of sintered HA scaffold," *Materials Science and Engineering C*, vol. 28, no. 1, pp. 51–56, 2008.
- [14] T. Kasuga, Y. Ota, M. Nogami, and Y. Abe, "Preparation and mechanical properties of polylactic acid composites containing hydroxyapatite fibers," *Biomaterials*, vol. 22, no. 1, pp. 19–23, 2001.
- [15] C. Delabarde, C. J. G. Plummer, P.-E. Bourban, and J.-A. E. Månson, "Biodegradable polylactide/hydroxyapatite nanocomposite foamscaffolds for bone tissue engineering applications," *Journal of Materials Science*, vol. 23, no. 6, pp. 1371–1385, 2012.
- [16] X. Deng, J. Hao, and C. Wang, "Preparation and mechanical properties of nanocomposites of poly(D,L-lactide) with Ca-deficient hydroxyapatite nanocrystals," *Biomaterials*, vol. 22, no. 21, pp. 2867–2873, 2001.
- [17] L. Varila, T. Lehtonen, and J. Tuominen, "In vitro behaviour of three biocompatible glasses in composite implants," *Journal of Materials Science*, vol. 23, no. 10, pp. 2425–2435, 2012.
- [18] S. Zhou, B. Song, and X. Li, "In vitro degradation and release profiles for poly-dl-lactide film containing paracetamol," *Journal of Materials Science*, vol. 18, no. 8, pp. 1623–1626, 2007.
- [19] S. Kobayashi and K. Sakamoto, "Effect of hydrolysis on mechanical properties of tricalcium phosphate/poly-L-lactide composites," *Journal of Materials Science*, vol. 20, no. 1, pp. 379–386, 2009.

- [20] M. Mehdikhani-Nahrkhalaji, M. H. Fathi, V. Mortazavi, S. B. Mousavi, B. Hashemi-Beni, and S. M. Razavi, "Novel nanocomposite coating for dental implant applications *in vitro* and *in vivo* evaluation," *Journal of Materials Science*, vol. 23, no. 2, pp. 485–495, 2012.
- [21] T. Niemelä, H. Niiranen, and M. Kellomäki, "Self-reinforced composites of bioabsorbable polymer and bioactive glass with different bioactive glass contents. Part II: *in vitro* degradation," *Acta Biomaterialia*, vol. 4, no. 1, pp. 156–164, 2008.
- [22] N. A. Weir, F. J. Buchanan, J. F. Orr, and G. R. Dickson, "Degradation of poly-L-lactide. Part I: *in vitro* and *in vivo* physiological temperature degradation," *Proceedings of the Institution of Mechanical Engineers H*, vol. 218, no. 5, pp. 307–319, 2004.
- [23] S. Chen, Y. Hao, and W. Cui, "Biodegradable electrospun PLLA/chitosan membrane as guided tissue regeneration membrane for treating periodontitis," *Journal of Materials Science*, vol. 48, no. 19, pp. 6567–6577, 2013.
- [24] J. Russias, E. Saiz, R. K. Nalla, and A. P. Tomsia, "Microspheres as building blocks for hydroxyapatite/poly(lactide) biodegradable composites," *Journal of Materials Science*, vol. 41, no. 16, pp. 5127–5133, 2006.
- [25] L. M. Ehrenfried, M. H. Patel, and R. E. Cameron, "The effect of tri-calcium phosphate (TCP) addition on the degradation of poly(lactide-co-glycolide) (PLGA)," *Journal of Materials Science*, vol. 19, no. 1, pp. 459–466, 2008.
- [26] Z. Zhou, Q. Yi, X. Liu, L. Liu, and Q. Liu, "*In vitro* degradation behaviors of poly-L-lactide/bioactive glass composite materials in phosphate-buffered solution," *Polymer Bulletin*, vol. 63, no. 4, pp. 575–586, 2009.

Research Article

A Study on the Effect of Plasma Treatment for Waste Wood Biocomposites

MiMi Kim, Heung Soo Kim, and Joong Yeon Lim

Department of Mechanical, Robotics and Energy Engineering, Dongguk University-Seoul, 26 Pil-dong 3-ga, Jung-gu, Seoul 100-715, Republic of Korea

Correspondence should be addressed to Joong Yeon Lim; jylim@dongguk.edu

Received 12 June 2013; Accepted 3 July 2013

Academic Editor: Il-Kwon Oh

Copyright © 2013 MiMi Kim et al. This is an open access article distributed under the Creative Commons Attribution License, which permits unrestricted use, distribution, and reproduction in any medium, provided the original work is properly cited.

The surface modification of wood powder by atmospheric pressure plasma treatment was investigated. The composites were manufactured using wood powder and polypropylene (wood powder: polypropylene = 55 wt% : 45 wt%). Atmospheric pressure plasma treatment was applied under the condition of 3 KV, 17 ± 1 KHz, 2 g/min. Helium was used as the carrier gas and hexamethyl-disiloxane (HMDSO) as the monomer to modify the surface property of the waste wood biocomposites by plasma polymerization. The tensile strengths of untreated waste wood powder (W3) and single species wood powder (S3) were about 18.5 MPa and 21.5 MPa while those of plasma treated waste wood powder (PW3) and plasma treated single species wood powder (PS3) were about 21.2 MPa and 23.4 MPa, respectively. Tensile strengths of W3 and S3 were improved by 14.6% and 8.8%, respectively. From the analyses of mechanical properties and morphology, we conclude that the interfacial bonding of polypropylene and wood powder can be improved by atmospheric pressure plasma treatment.

1. Introduction

Governmental regulations and growing environmental awareness worldwide have triggered a paradigm shift towards designing materials compatible with the environment [1]. Biocomposites are most actively investigated as environment friendly materials [2]. Biofibers or natural fibers have been generally used as reinforcements for biocomposites. The matrices of biocomposites are biodegradable or nonbiodegradable polymers that can be extracted from natural resources instead of existing oil resources [3].

Wood plastics composites (WPCs) are made of wood powder. Composites are made by combining two materials to obtain better performance than either of the original ones while the original phases of these materials are retained [4]. Strong interfacial adhesion between fibers and matrices, however, is very important in making composites with high mechanical properties. For production of WPCs, the two materials that are to be combined must be treated by coupling agents because of the incompatibility between the hydrophilic wood powder and the hydrophobic polymer. However, the high prices of coupling agents have reduced

the productivity of WPCs. Moreover, coupling agents are chemical materials that are not environment friendly. Therefore, new technologies have been developed to produce environment friendly materials from biomass resources. The interfacial adhesion in biocomposites can be enhanced by two types of methods: one type modifies the base polymers and another type treats the biodegradable fillers to increase their hydrophobic properties. The latter type includes methods such as corona treatment, plasma treatment, heating, and so forth [5]. Plasma treatment changes the chemical structure and surface properties of hydrophilic natural fibers to give them hydrophobic properties, which would enhance their interfacial adhesion with the base polymer [6, 7].

For mass production of biocomposites, atmospheric pressure plasma was used in this study instead of vacuum plasma. Biocomposites production in an atmospheric pressure plasma is a dry process that has many advantages such as low contamination, energy savings, and enhanced interfacial adhesion [8, 9]. It also removes foreign matters by making chemical reactions only on surfaces of polymer while preserving the basic physical properties of the polymer [10]. Plasma processes, which have been usually carried out

in vacuum, are now carried out at atmospheric pressure, and these atmospheric pressure plasma processes have become very popular because of their reduced production cost and shortened process time. Recently, the application of atmospheric pressure plasma processes has been extended. Plasma processes in vacuum, on the other hand, take a long time because of the less numbers of electrons and ions in vacuum plasma than in atmospheric pressure plasma, and they also have difficulty in providing stable and uniform modification.

In this study, we tried to make biocomposites with increased interfacial adhesion between the wood powder and the polypropylene (PP) of hydrophobic thermoplastic polyolefin polymers by modifying the surfaces of the hydrophilic wood powder particles. To achieve this objective, a lab scale chamber was made. A screw was inserted in the chamber to move the wood powder. Electrodes were installed outside the chamber so that the wood powder could move and plasma processes could be carried out by rotating the screw. Continuity and good productivity were achieved.

The surfaces of the wood powder particles are modified by plasma processes as follows. First, electrons and gas molecules collide in the plasma. When an electron collides with a molecule XY, an electron escapes from the molecule XY and the molecule becomes ionized. Sometimes, the bond of the molecule XY is broken, and the molecule divides into X and Y. The divided molecules X and Y are then likely to interact with the many unbounded electrons. These molecules are called radicals or chemically-active species. Through the chemical reactions of the ionized electrons in collisions in the plasma, wood powder becomes coated and the dispersion components on the surfaces are increased. Then, the surfaces of the wood powder particles are modified to have hydrophobicity. To investigate such effects of surface modification, experiments were carried out for waste wood powder and single species wood powder. If the interfacial adhesion of waste wood powder with polypropylene is enhanced by surface modification, the strength of the waste wood biocomposites would increase and the waste wood powder could be used as a recycled raw material of biocomposites.

2. Experimental Procedure

2.1. Materials. Two types of wood powder were used: one was a single species powder of spruce and the other was a waste wood powder of crushed, construction waste wood chips. Wood powder was extracted from a 60–80 mesh sieve. Before wood powder was treated by plasma, it was dried in vacuum at moisture content of less than 1%. Hexamethyldisiloxane (HMDSO) was used in the plasma treatment to modify the surface properties of the wood powder to make it hydrophobic. We used H1501 Polypropylene (LG Chem.) of less than 3 mm in diameter, 0.9 g/cm^3 in density, and 17 g/10 min in melting index.

2.2. Contact Angle. A series of experiments were conducted to select the monomer that would be used to modify the hydrophilic wood powder surface into a hydrophobic surface.

A film type of polyethylene terephthalate (PET) was produced using a press. The plasma treatment was conducted using a vacuum plasma. The monomer used in the experiment was evaporated and then used to modify the PET film surface. Ten microliters of water and glycerol droplets was dropped on the processed film using the sessile drop method, and then the contact angle was measured. All contact angle measurements were repeated three times to obtain the mean value and the deviation.

2.3. Atmospheric Pressure Plasma Treatment. In the atmospheric pressure plasma treatment for the modification of the wood powder surface, helium was used to make the plasma generation atmosphere and as the carrier gas. Wood powder, injected through a hopper, was moved by a screw inserted at the chamber. The plasma generated between the two types of electrodes surrounding the chamber treated the wood powder being moved by the screw. At this time, the plasma treatment condition was 3 kV at $17 \pm 1 \text{ kHz}$. Figure 1 shows schematic of the atmospheric pressure plasma treatment.

2.4. Composite Processing. For the mechanical mixing of wood powder and polypropylene, pellets were produced at 210°C at 180 rpm using a twin screw extruder. The wood powder content in the biocomposites was fixed at 55 wt%. The dispersion of the wood powder in PP was increased by carrying out the extrusion process three times. The pellets produced were dried for 24 hours at 60°C , and then, the specimens whose mechanical properties were to be evaluated were injected by the injection molding machine.

2.5. Mechanical Properties. The tensile test was conducted at 5 mm/min at room temperature using a 100 kN load according to ASTM D638, while the flexural test was conducted at 3.4 mm/min at room temperature using a 100 kN load according to ASTM D790. Five specimens were tested for each experiment. The average value of the measurements was calculated and used for analysis.

3. Results and Discussion

3.1. Surface Free Energy. The intermolecular forces acting on the surface of the polymer can be divided into three categories: primary (chemical) force, quasi-chemical (hydrogen bond) force, and secondary (Van der Waals) force. The secondary force is again subdivided into Keesom force, Debye force, and London dispersion force, which is much larger than the other two Van der Waals forces. Surface tension is surface free energy per unit area, thermodynamically. Interfacial tension is created by cohesion and adhesion, which are the results of intermolecular forces at the interface of two different molecules. Since the free energy of a solid surface cannot be measured directly, unlike that of a liquid, it is calculated indirectly using a liquid whose surface tension is known.

Surface energy can be expressed in Young-Dupre' equation as follows.

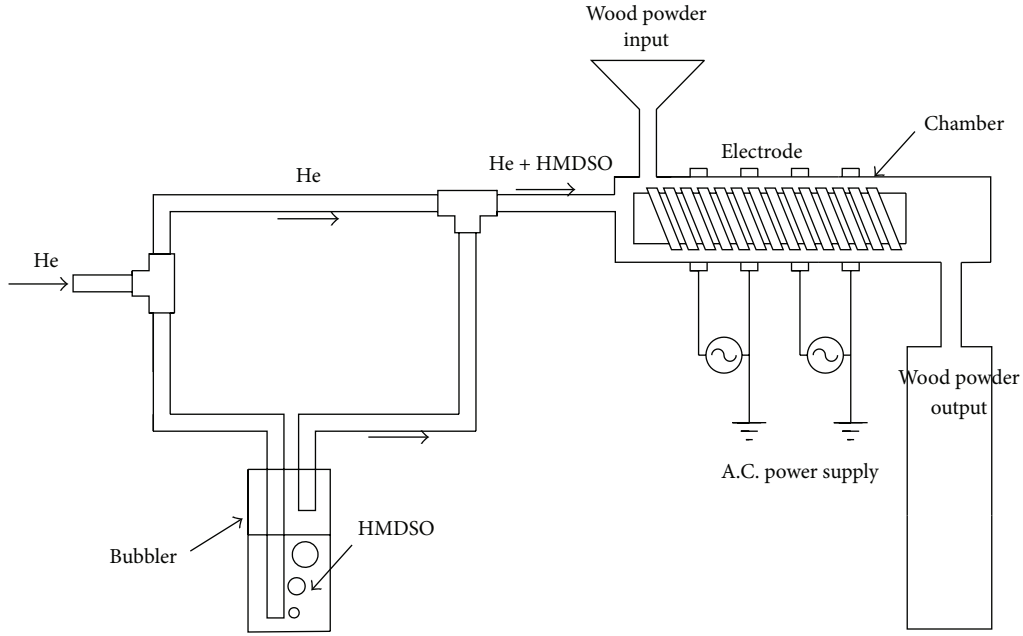


FIGURE 1: Schematic of atmospheric pressure plasma treatment.

Young equation:

$$\gamma_{SV} = \gamma_{SL} + \gamma_{LV} \cos \theta. \quad (1)$$

Dupre equation:

$$W_A = \gamma_{LV} + \gamma_{SV} - \gamma_{SL}. \quad (2)$$

Young-Dupre equation:

$$W_A = \gamma_{LV} (1 + \cos \theta). \quad (3)$$

In addition, it can be expressed as the sum of polar components and dispersion components. Consider the following:

$$\gamma_{SL} = \gamma_{SV} + \gamma_{LV} - 2(\gamma_S^d \gamma_{LV}^d)^{1/2} - 2(\gamma_S^p \gamma_{LV}^p)^{1/2}. \quad (4)$$

Contact angle is a measure that represents the wettability of a solid surface. It can be calculated by measuring the contact angle of a water droplet on the PET film surface-modified by plasma treatment. In general, a low contact angle indicates high wettability (hydrophilic property), and a high contact angle represents low wettability (hydrophobic property). Figure 2 shows equilibrium contact angle of a solid/liquid surface.

Table 1 provides the measured contact angle and surface energy of the PET film. Experimental results showed that the plasma-treated film had a low contact angle and a high surface energy but that the polar components were much higher than the dispersion components. These results confirm the modification of the film surface into that having the hydrophilic property.

This experiment aims to modify the hydrophilic surface of wood powder into a hydrophobic surface. The suitable monomer is hexamethyl-disiloxane (HMDSO). The polar

TABLE 1: Contact angle and surface energy of PET film.

Monomer	Contact angle (°)		Surface energy (dyne/cm)		
	Water	Glycerol	Total	Dispersion	Polar
Oxygen/PET	8	9	73.73	12.78	60.96
Benzene/PET	58.8	65	49.17	1.08	47.37
CH ₄ /PET	55.7	47.6	59.56	2.14	57.42
Acrylic acid/PET	35.7	47.7	71.94	1.72	70.22
HMDSO/O ₂ (1:9)/PET	28	41	75.74	2.54	73.21
HMDSO/O ₂ (2:8)/PET	56.5	60	47.25	4.32	42.93
HMDSO/O ₂ (3:7)/PET	66	68.8	38.03	4.39	33.64
HMDSO/O ₂ (4:6)/PET	72	73	32.39	4.57	27.81
HMDSO/O ₂ (5:5)/PET	73.5	73.5	30.64	5.43	25.21
HMDSO/PET	105	76	74.77	71.68	3.09

component among the surface energy of the film after HMDSO plasma treatment was very low, which was also verified by measurement of the contact angle. However, oxygen mixing ratio also plays an important role in plasma treatments using HMDSO. The values of the plasma-treated polar component and dispersion component obtained by mixing HMDSO and oxygen at a mixing ratio of 1:9 showed the opposite of those when treated using HMDSO alone. As a result, it was found that HMDSO was most effective when modifying a surface to have hydrophobic property, but the results depend on the amount of oxygen input.

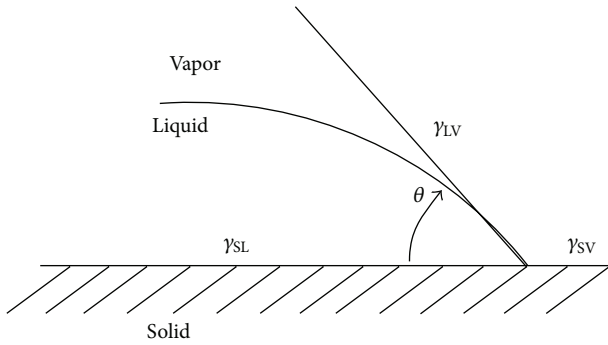
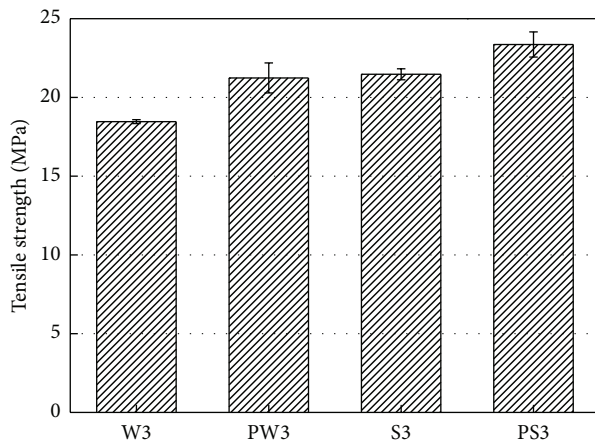


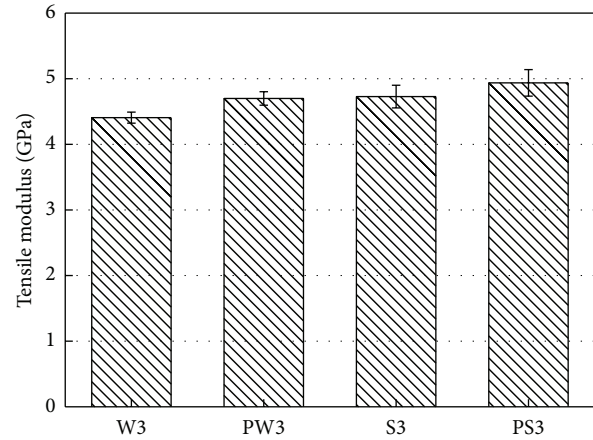
FIGURE 2: Equilibrium contact angle of solid/liquid surface.



W3-waste wood powder
 PW3-waste wood powder by plasma treatment
 S3-single species wood powder
 PS3-single species wood powder by plasma treatment

FIGURE 3: Tensile strength of composites.

3.2. Tensile Strength. Figures 3 and 4 show the effect of plasma treatment on the tensile strength and tensile modulus of the composites according to the type of wood powder. The tensile strength of the composites formed from the single species wood powder was 21.5 MPa, which is 16.2% higher than that of the composites formed from the waste wood powder (18.5 MPa). The reason why the tensile strength of the composites made of the waste wood powder was lower than that of the composites made of the single species wood powder was due to the foreign matters in the waste wood powder. These foreign matters come from the surface overlay, coating and adhesives of living wood waste and construction waste woods, which are the raw materials of waste wood powder. The foreign matters make recycling waste wood difficult. The strength of waste wood powder should be improved to broaden its application. The surface of waste wood powder can be modified to increase the strength of waste wood composites. The experimental results showed that the tensile strength of waste wood powder after surface modification by the atmospheric pressure plasma treatment was 21.2 MPa, which is an increase of 14.6% from that of the



W3-waste wood powder
 PW3-waste wood powder by plasma treatment
 S3-single species wood powder
 PS3-single species wood powder by plasma treatment

FIGURE 4: Tensile modulus of composites.

TABLE 2: Flexural strength and flexural modulus of composites.

	W3	PW3	S3	PS3
Flexural strength (MPa)	36.0	39.5	41.1	42.6
Flexural modulus (GPa)	3.8	4.0	4.3	4.5

nontreated waste wood powder. The plasma-treated single species wood powder also showed an increase in tensile strength. These results confirm that atmospheric pressure plasma treatment is effective in the surface modification of wood powder. The tensile modulus of the single species wood powder was higher than that of the waste wood powder. They were also increased by plasma treatment.

3.3. Flexural Strength. The flexural strength and flexural modulus of the composites according to the type of wood powder are summarized in Table 2. The flexural strength of the composite made from the single species wood powder was 41.1 MPa, which is 14.2% higher than that of the composite made from the waste wood powder (36.0 MPa). It was also observed that the flexural strength of the composite made from the waste wood powder with surface modification by atmospheric pressure plasma treatment was 39.5 MPa, which is an increase of 9.7% from that made from the nontreated waste wood powder. In addition, flexural moduli also increased in the single species wood powder.

3.4. SEM Images. Figures 5 and 6 present the cross-sections of the composites observed by SEM. In the case of the composite made of the nontreated wood powder, voids were observed at the interface between the wood powder and polymer. However, voids were not observed at the interface in the case of the composite made of the plasma-treated wood powder. These results showed that the hydrophilic surface of the wood powder was modified into a hydrophobic surface, which

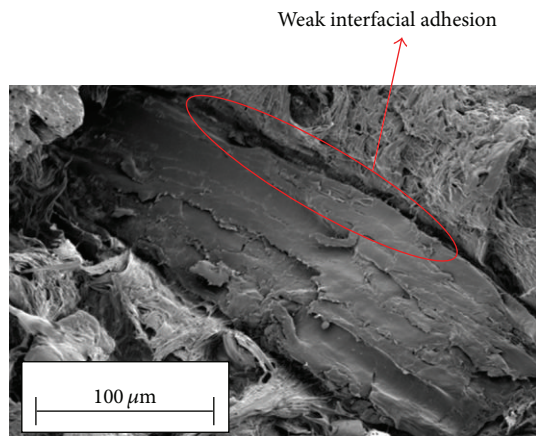


FIGURE 5: SEM micrograph of nontreated composites' cross-section.

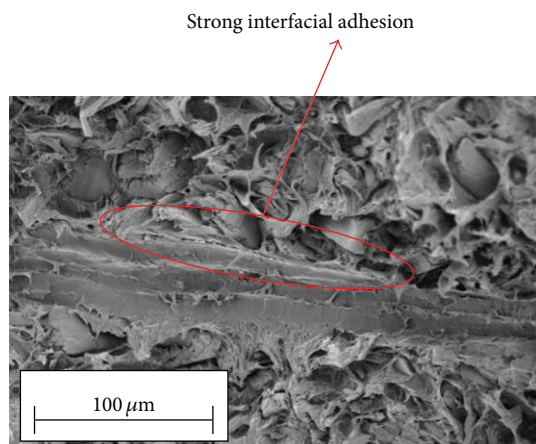


FIGURE 6: SEM micrograph of plasma-treated composites' cross-section.

helped to improve the interfacial adhesion with polymer, which is hydrophobic. The experimental results of tensile and flexural strengths also provided the same tendency.

4. Conclusion

The strengths of waste wood biocomposites were investigated for recycling waste wood. The surfaces of the wood powders were modified to enhance their interfacial adhesion with polypropylene by atmospheric pressure plasma treatment. Several important observations were made from the tensile and flexural strength tests as follows.

- (1) Although the total energy of the surfaces was high by the atmospheric pressure plasma treatment using monomers, the surfaces were modified into hydrophobic or hydrophilic surfaces depending on polar or dispersed components.
- (2) The most efficient monomer for the modification of the hydrophilic wood powders was HMDSO, which had the lowest polar component (3.09 dyne/cm) in

the surface energy calculated by measurement of the contact angle.

- (3) Tensile strengths of the composites made of the waste wood powder and single species wood powder were 18.5 MPa and 21.5 MPa, respectively. The tensile strength of the single species wood powder composites was 16.2% higher than that of the waste wood powder composites. Foreign matters on the wood powder surface decreased the tensile strength of the waste wood powder composites. This is why plasma treatment is required for recycling waste wood.
- (4) When the surface of the waste wood powder was modified by atmospheric pressure plasma treatment, the tensile strength increased by 14.6% from 18.5 MPa to 21.2 MPa and the flexural strength also increased by 9.7%, from 36.0 MPa to 39.5 MPa. In the case of the single species wood powder, the tensile strength increased by 8.8% and flexural strength increased by 3.6%. These results confirm that surface modification by atmospheric pressure plasma treatment is effective for increasing the strength of both single species wood powder and waste wood powder.
- (5) Through surfaces' modification by plasma treatment, the mechanical properties of the waste wood powder became similar to those of the single species wood powder without modification. Therefore, it is expected that waste wood powder can be recycled as raw biomaterials by various treatment processes.

Acknowledgments

This research was supported by the Ministry of Land, Infrastructure and Transport and the Korea Agency for Infrastructure Technology Advancement.

References

- [1] A. K. Mohanty, M. A. Khan, and G. Hinrichsen, "Surface modification of jute and its influence on performance of biodegradable jute-fabric/Biopol composites," *Composites Science and Technology*, vol. 60, no. 7, pp. 1115–1124, 2000.
- [2] S.-Y. Park, G.-S. Han, H.-S. Kim, H.-S. Yang, and H.-J. Kim, "Evaluation of the impact on manufacturing temperature and time in the production process of bio-composites," *Mokchae Konghak*, vol. 33, no. 1, pp. 29–37, 2005.
- [3] T. Takayama, K. Komabayasi, M. Itou, and Y. Miyake, "Development of Bio-based plastics for injection molding," *SAE International Journal of Materials and Manufacturing*, vol. 2, no. 1, pp. 12–17, 2009.
- [4] C.-H. Kim, K.-J. Kim, and T.-J. Eom, "Properties of WPC prepared with various size and amount of wood particle," *Palpu Chongi Gisul/Journal of Korea Technical Association of the Pulp and Paper Industry*, vol. 40, no. 3, pp. 59–64, 2008.
- [5] B.-H. Lee, H.-S. Kim, S.-W. Choi, and H.-J. Kim, "Improvement of interfacial adhesion for surface treated rice husk flour-filled polypropylene bio-composites," *Mokchae Konghak*, vol. 34, no. 3, pp. 38–45, 2006.

- [6] T. S. Lee, S. G. Lee, and K. H. Song, "Natural fiber reinforced biocomposites and biodegradation," *Fashion Information and Technology*, vol. 7, pp. 10–21, 2010.
- [7] S. Singh, D. Y. Sasaki, J. Cesarano III, and A. J. Hurd, "Nanometer pores in ultrathin silica films prepared by self-assembly of organic spacers in an alkylsiloxane monolayer," *Thin Solid Films*, vol. 339, no. 1-2, pp. 209–215, 1999.
- [8] J. Lai, B. Sunderland, J. Xue et al., "Study on hydrophilicity of polymer surfaces improved by plasma treatment," *Applied Surface Science*, vol. 252, no. 10, pp. 3375–3379, 2006.
- [9] V. Kotal, V. Svorcik, P. Slepicka et al., "Gold coating of poly(ethyleneterephthalate) modified by argon plasma," *Plasma Process and Polymers*, vol. 4, no. 1, pp. 69–76, 2007.
- [10] S.-H. Seo, S. Chang, Y.-E. Yoo, and J. D. Chung, "Surface characteristics of polymer material treated by atmospheric pressure plasma," *Korean Journal of Air-Conditioning and Refrigeration Engineering*, vol. 22, no. 5, pp. 282–288, 2010.

Research Article

Water Absorption and Diffusion Characteristics of Nanohydroxyapatite (nHA) and Poly(hydroxybutyrate-co-hydroxyvalerate-) Based Composite Tissue Engineering Scaffolds and Nonporous Thin Films

Naznin Sultana^{1,2} and Tareef Hayat Khan³

¹ Department of Mechanical Engineering, The University of Hong Kong, Pokfulam Road, Hong Kong

² IJN-UTM Cardiovascular Engineering Centre (CEC), Faculty of Biosciences and Medical Engineering, Universiti Teknologi Malaysia, 81310 UTM Johor Bahru, Johor, Malaysia

³ KALAM, Faculty of Built Environment, Universiti Teknologi Malaysia, 81310 UTM Johor Bahru, Johor, Malaysia

Correspondence should be addressed to Naznin Sultana; naznin@biomedical.utm.my

Received 15 March 2013; Revised 10 April 2013; Accepted 10 April 2013

Academic Editor: In-Kyu Park

Copyright © 2013 N. Sultana and T. H. Khan. This is an open access article distributed under the Creative Commons Attribution License, which permits unrestricted use, distribution, and reproduction in any medium, provided the original work is properly cited.

Water uptake characteristics of poly(hydroxybutyrate-co-hydroxyvalerate) (PHBV-) based composite tissue engineering (TE) scaffolds incorporating nanosized hydroxyapatite (nHA) have been investigated. The water absorption of these composite scaffolds obeyed the classical diffusion theory for the initial period of time. The diffusion coefficients of the composite scaffolds during the water absorption were much faster than those for the nonporous thin films, suggesting that the water uptake process depends on the presence of porosity and porous microstructure of the composite scaffolds. The incorporation of nHA increased the water uptake of both the composite scaffolds and thin films. It was also observed that the equilibrium uptake increased with the incorporation of nHA. This increase in the water uptake was largely due to the nHA particle aggregates in the microstructure of both composite scaffolds and thin films. The activation energy for diffusion was also determined using the Arrhenius equation for both porous scaffolds and thin films and the results suggested that the activation energy for scaffolds was lower than that for thin films.

1. Introduction

Through the combination of cell biology, biomaterials, and engineering, tissue engineering (TE) seeks to provide a solution to replace, repair, or regenerate tissues/organs [1, 2]. To overcome the limitations of the autogenous and allogenic bone graft, development of new synthetic scaffolds has received increasing interest. In TE, the biomaterial based scaffolds are the most important aspects [3, 4]. A number of approaches such as phase separation, selective laser sintering, and electrospinning are being used for fabricating scaffolds for bone regeneration. Biodegradable polymers, including poly(caprolactone), poly(L-lactic acid) (PLLA), and poly(hydroxybutyrate-co-hydroxyvalerate) (PHBV), have been processed into 3D scaffolds with the development of TE [5].

Both PLLA and PHBV possess good biocompatibility with tissue and blood and are regarded as good candidates as biodegradable polymer matrix of composite scaffolds [6]. Blending of PHBV with PLLA can shorten the degradation time and rate of PHBV which has much longer degradation time [7, 8]. Several biodegradable polymer-hydroxyapatite (HA) composites have been developed as bone substitute material or bone TE scaffolds [9–11]. As HA is a natural component of bones and possesses the osteoconductive properties, polymer-HA composite scaffold is a promising system for bone tissue regeneration as it can mimic the composition and structure with the mineral phase of the bone.

By guiding new tissue growth *in vivo* and *in vitro*, scaffolds play an important role in TE. The scaffolds possess 3D macroporous and interconnected network with

the macropore diameter of a few hundreds of micrometers to allow cell invasion. The water uptake properties of composite scaffolds for tissue TE are of importance as the primary mechanism of the polymer degradation inside body is hydrolysis. The ingress of water into polymer-based scaffolds can have both adverse and beneficial effects on the properties of the scaffolds. Hydrolysis and microcrack can be formed due to water exposure. On the other hand, breakdown of three-dimensional scaffolds can occur due to excessive water uptake. Several studies have been performed for dental application to study the characteristics of polymeric systems and composites [12, 13]. However, the water uptake and diffusion characteristics of TE scaffolds have been rarely assessed and reported.

Previously, we reported the fabrication, characterization, and *in vitro* biological evaluation of PHBV/PLLA-based scaffolds [14]. The aim of the present study was to determine the water uptake and diffusion characteristics of 100/0 PHBV/PLLA, 50/50 PHBV/PLLA blend, and 10% nHA incorporated 50/50 PHBV/PLLA composite scaffolds. For comparison, solvent-cast thin films were also used in the study. The effect of incorporation of HA, porosity, and microstructures of the composite scaffolds on the diffusion coefficient, equilibrium uptake, and temperature dependence was also investigated.

2. Experimental

2.1. Materials and General Methods. PHBV with 6% of 3-hydroxyvalerate was purchased from Sigma-Aldrich. In order to blend with PHBV, PLLA with viscosity 1.6 dL g^{-1} (Medisorb 100L 1A) was purchased from Lakeshore Biomaterials (Birmingham, AL). The nHA nanoparticles were produced in-house which were used for producing composite scaffolds and composite thin films [15]. Figure 1 shows the SEM micrograph of nanosized HA. The freeze-dried HA powders used in this investigation consisted of tiny agglomerates of HA nanocrystallites. The particle size of the HA powders was found to be in the range of 20–30 nm. Chloroform and acetic acid were analytical grade.

2.2. Fabrication of Scaffolds and Solvent Cast Films. Pure 100/0 PHBV/PLLA, 50/50 PHBV/PLLA, and 10% nHA in 50/50 PHBV/PLLA tissue engineering scaffolds with 10% (w/v) polymer concentration were fabricated using the emulsion freezing/freeze-drying technique described elsewhere [16]. Briefly, to produce polymer scaffolds, 1g polymer or polymer blend was dissolved in 5 mL chloroform and then 5 mL acetic acid was added. The emulsion was then homogenized and kept frozen at -18°C in a freezer for overnight to induce phase separation. Then the frozen emulsion was freeze-dried using a freeze-drying vessel (Labconco, USA). Similarly, to produce 10% nHA in 50/50 PHBV/PLLA composite scaffolds, 0.1g nHA was added in the emulsion and homogenized prior to the phase-separation process. Non-porous thin films with the same compositions were fabricated using solvent casting technique.

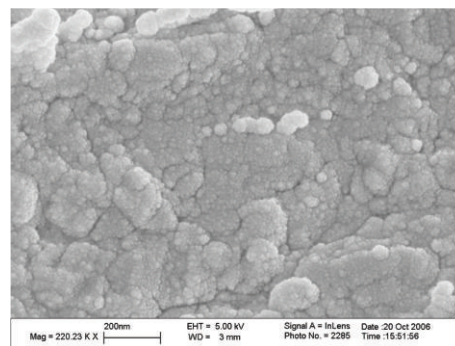


FIGURE 1: SEM micrograph of nanosized HA particles synthesized in-house through a nanoemulsion process.

2.3. Preparation of Polymer and Composite Specimens. Rectangular shape specimens ($20 \text{ mm} \times 5 \text{ mm} \times 0.5 \text{ mm}$) were cut with sharp razor blade from three types of polymer and composite scaffolds, namely, PHBV scaffolds (10% w/v), 50/50 PHBV/PLLA (10% w/v) blend scaffolds, and 10% nHA in PHBV/PLLA (10% w/v) composite scaffolds. Rectangular specimens of ($20 \text{ mm} \times 5 \text{ mm} \times 0.5 \text{ mm}$) were also prepared from solvent-cast films of the same compositions. The porous microstructure, morphology, and pore sizes of the scaffolds specimens were studied using a scanning electron microscopy (SEM; Stereoscan 440, UK). In order to determine the presence and distribution of nHA nanoparticles in composite scaffolds, energy dispersive X-ray spectrometry (EDX, INCA 300, UK) was performed. The skeletal density and the porosity of the scaffolds were measured using equations described elsewhere [16]. The wettability of the scaffolds was measured by measuring contact angles using a contact angle measuring machine (SL200B, Shanghai Salon Tech Inc., Ltd., China). With distilled water as liquid, the sessile drop method was employed. The contact angle of the water drop on the scaffold specimen was determined at room temperature using proprietary software. At least three measurements were conducted at different locations of the scaffold specimen. As the mean \pm standard deviation, the contact angle was expressed.

2.4. Water Absorption. The specimens were placed in an oven at 37°C for 48 hours and then weighed to an accuracy of $\pm 0.0001 \text{ g}$ on a balance. The specimens were then placed into 100 mL of distilled water at 37°C . During the first day of immersion, the specimens were removed at intervals of 2, 5, 10, 15 min, and so forth, blotted dry on filter paper to remove excess water, weighed, and returned to the water. Following the first day, the samples were weighed daily, until the uptake slowed. Until there was no significant change in weight, the uptake of water was recorded. When equilibrium was attained, the samples were then transferred to a drying oven at 37°C . Similarly, the experiment was repeated at 25°C and at 50°C .

2.5. *Diffusion Coefficients.* For the earlier stages of uptake (usually where $M_t/M_\infty \leq 0.5$), classical diffusion theory predicts [1, 17] the following:

$$\frac{M_t}{M_\infty} = 2 \left(\frac{Dt}{\pi l^2} \right)^{1/2}, \quad (1)$$

where M_t is the mass uptake at time t , M_∞ is the mass uptake at equilibrium, $2l$ is the thickness of the specimen, D is the diffusion coefficient, and t is the water uptake time. A plot of M_t/M_∞ against $t^{1/2}$ should provide a straight line for earlier stages of water uptake. Diffusion coefficients can be calculated from the slope of the straight line.

The temperature dependence of the diffusion coefficient is given by the Arrhenius equation:

$$\ln D = \ln D_0 - \frac{Q}{R} \left(\frac{1}{T} \right), \quad (2)$$

where T is the absolute temperature ($^\circ\text{K}$), Q is the activation energy for diffusion (J/mol or eV/atom), and D_0 is a temperature independent constant (preexponential) (m^2/s), R is the gas constant ($8.314 \text{ J/mol}\cdot\text{K}$ or $8.62 \times 10^{-5} \text{ eV/atom}$).

3. Results and Discussion

Several assumptions were used for this study. They were as follows.

- (i) Distilled water was in infinite supply.
- (ii) Polymer and composite films and scaffolds were surrounded by water.

3.1. *Morphological Observation.* Figure 2 shows the morphologies of thin films of 100/0 PHBV/PLLA, 50/50 PHBV/PLLA, and 10% nHA incorporated 50/50 PHBV/PLLA. Some micropores were observed in 50/50 PHBV/PLLA thin film due to the immiscibility of PHBV and PLLA. Figure 3 shows the morphologies of 100/0 PHBV/PLLA, 50/50 PHBV/PLLA, and 10% nHA in 50/50 PHBV/PLLA scaffolds. It was observed that highly porous scaffold specimens consisted of many micropores. Pore structure and size depended on the phase separation process used in the fabrication technique. Scanning electron microscopy (SEM) and energy dispersive X-ray spectroscopy showed the distribution of HA nanoparticles in the pore walls of the scaffolds, and some particle agglomeration was also observed (Figure 4). The average pore diameter of the 100/0 PHBV/PLLA scaffold was higher than that of 10% nHA incorporated 50/50 PHBV/PLLA scaffold as incorporation of nHA perturbed the phase separation process slightly (Table 1). As the scaffolds were prepared from same polymer emulsion concentration, 10% (w/v), the porosity did not change significantly in the scaffolds. The contact angle was much higher in 100/0 PHBV/PLLA scaffold than 50/50 PHBV/PLLA and 10% nHA in PHBV/PLLA scaffolds as PHBV polymer is well known for its hydrophobic nature. Blending with PLLA and incorporation of nHA increased the hydrophilicity of the composite scaffolds.

TABLE 1: Average pore diameter, porosity, and contact angle of the scaffold.

Scaffold	Average pore diameter (μm)	Porosity %	Contact angle
100/0 PHBV/PLLA	290	75 ± 2.0	103 ± 1.6
50/50 PHBV/PLLA	271	77 ± 1.5	98 ± 2.5
10% nHA in 50/50 PHBV/PLLA	250	72 ± 3.0	83 ± 1.5

3.2. *Diffusion Study of Solvent-Cast Thin Films.* Figure 5 shows the water uptake curve of 100/0 PHBV/PLLA thin film at 37°C as M_t/M_∞ versus the square root of immersion time. The specimens were immersed in distilled water. The maximum uptake at equilibrium was 1.4%. The diffusion coefficients were calculated from the initial linear region of the curves.

In order to observe the temperature dependence of the diffusion coefficients of 100/0 PHBV/PLLA thin film, the experiment was performed at three different temperatures, namely, at 25°C , 37°C , and 50°C . Water uptake study was also performed for 50/50 PHBV/PLLA thin film and 10% HA in 50/50 PHBV/PLLA thin film following the same procedure mentioned above. The calculated diffusion coefficients are given in Table 2. It can be seen that diffusion coefficient is significantly higher at high temperature of 50°C than that of 25°C , 37°C .

In order to study the temperature dependence of diffusion coefficients, Arrhenius plot was constructed for 10% HA in 50/50 PHBV/PLLA thin films as shown in Figure 6. From the slope of the curve, activation energy can be calculated which is referred to as the energy required to produce the diffusive motion of one mole of atoms. The activation energy calculated from the slope of the best fit linear curve was $76 \pm 20 \text{ KJ/mole}$ with the regression coefficient, r^2 value of 0.94. The activation energy of 100/0 PHBV/PLLA and 50/50 PHBV/PLLA thin film was $99.8 \pm 21.9 \text{ KJ/mole}$ and $112 \pm 45 \text{ KJ/mole}$, respectively.

3.3. *Diffusion Study of Scaffolds.* Figure 7 is the plot of water uptake as M_t/M_∞ versus square root of immersion time at 37°C for 100/0 PHBV/PLLA scaffolds. The diffusion coefficients were calculated from the initial linear regions of the curves. In order to study the temperature dependence of diffusion coefficients of the scaffolds, the experiment was performed at three different temperatures, namely, at 25°C , 37°C , and 50°C .

Table 3 shows the diffusion coefficients of 100/0 PHBV/PLLA scaffolds at 25°C , 37°C , and 50°C , which were 51.75×10^{-12} , 67.60×10^{-12} , and $165 \times 10^{-12} \text{ m}^2/\text{s}$, respectively. It was observed that the initial water uptake of HA incorporated composite scaffold was much higher than that of polymer blend scaffolds, and the diffusion coefficients were also higher. The value of diffusion coefficient was lower at low temperature and relatively high at high temperature. Figure 8 shows the Arrhenius plot which represents the temperature dependence of the diffusion coefficients of 10% HA in 50/50 PHBV/PLLA scaffolds. From the slope of the best

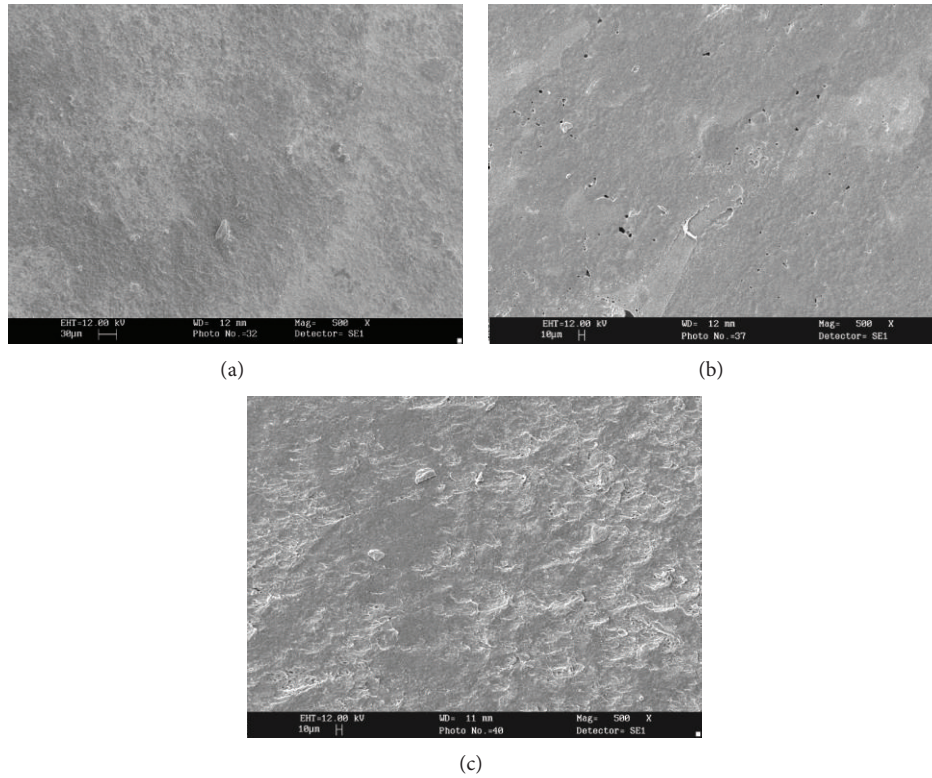


FIGURE 2: SEM micrographs of thin films of different compositions. (a) 100/0 PHBV/PLLA thin film; (b) 50/50 PHBV/PLLA thin film; (c) 10% nHA in 50/50 PHBV/PLLA blend film.

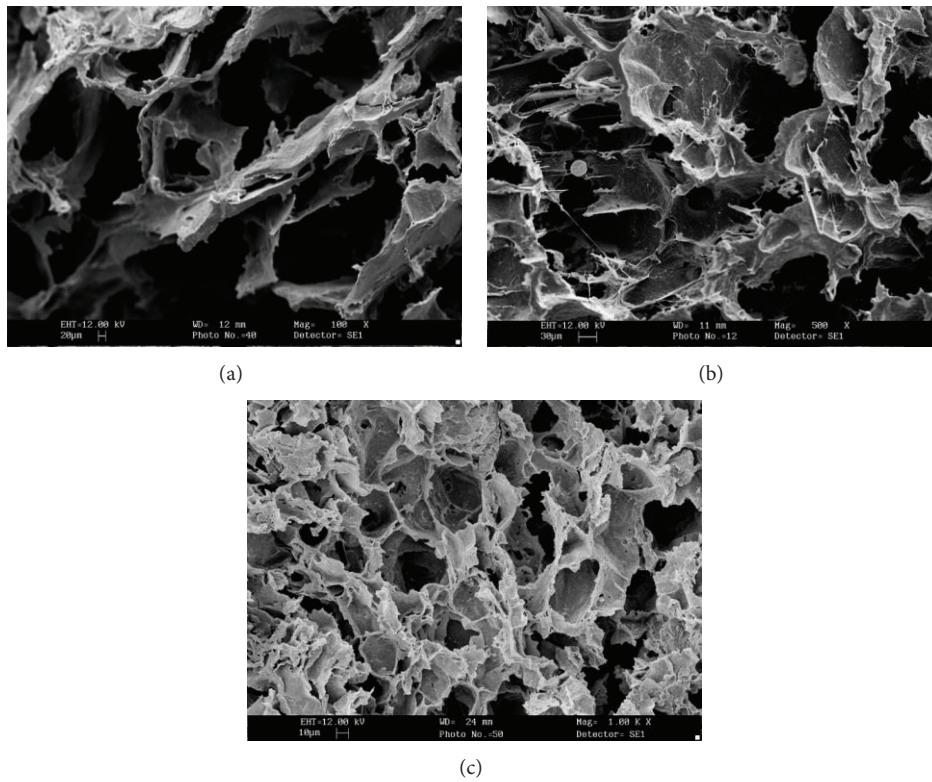


FIGURE 3: SEM micrographs of scaffolds of different compositions. (a) 100/0 PHBV/PLLA scaffold; (b) 50/50 PHBV/PLLA scaffold; (c) 10% nHA in 50/50 PHBV/PLLA scaffold.

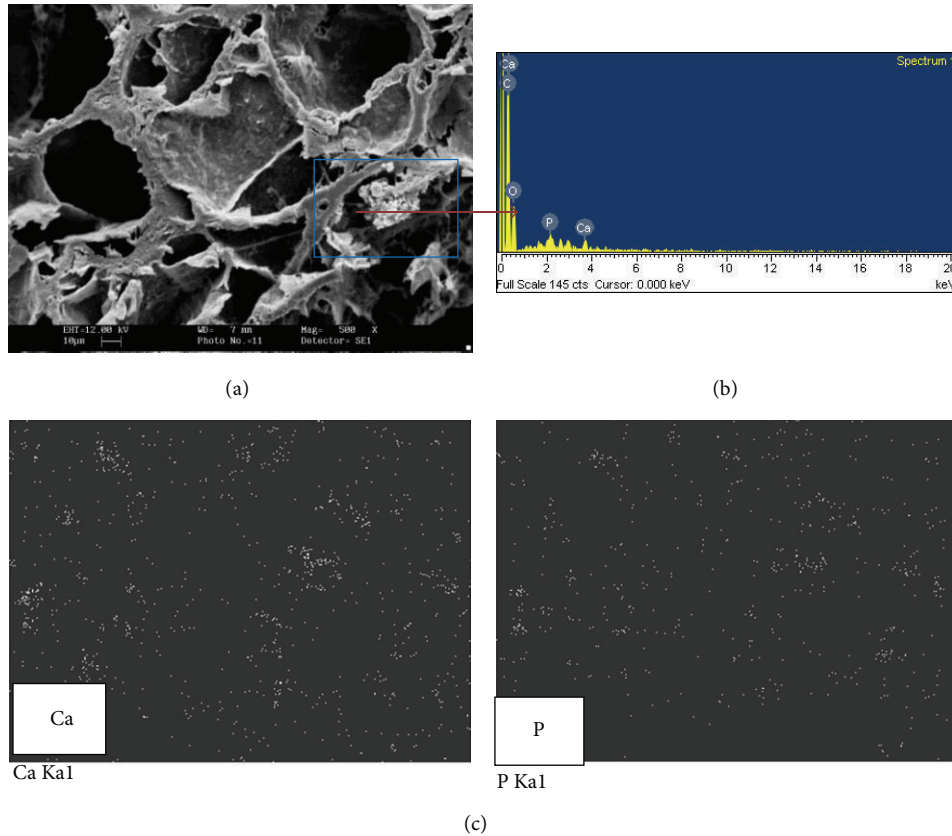


FIGURE 4: SEM micrographs of (a) 10% nHA in 50/50 PHBV/PLLA composite scaffold; (b) EDX spectrum; (c) Mapping of Ca and P.

fit linear line, the activation energy was calculated, which was 100.9 ± 5.3 KJ/mole. The activation energies were found 120.3 ± 45 KJ/mole for 50/50 PHBV/PLLA scaffold and 83.5 ± 53 KJ/mole for 100/0 PHBV/PLLA scaffolds, respectively.

Table 4 shows the comparison between the amounts of water uptake (g/g) at equilibrium between the different compositions of thin films and scaffolds. Among the different compositions of thin films and scaffolds, the amount (g/g) of equilibrium water uptake of 10% nHA in 50/50 PHBV/PLLA films and scaffolds was higher than that of 100/0 PHBV/PLLA and 50/50 PHBV/PLLA thin films and scaffolds. This result was opposite to other studies where the uptake of HA/polymer composite films was slower than the pure polymeric film as the polymers were very much hydrophilic and water uptake was high for the polymer itself [12]. In the present study, it was also observed that water uptake increased significantly with the increasing porosity. The scaffolds which were more than 70% porous, absorbed more water at the same condition than that of dense films. Besides, the incorporation of HA increased the water uptake in both composite thin film and composite scaffold.

Water uptake can occur by the materials in terms of “absorbed water” that means the amount of water absorbed from media which mainly depends on the hydrophilicity of material. Capillary water is termed as liquid water that is “drawn in” through pores or capillaries of the materials. Moreover, the amount of water absorbed is related to the

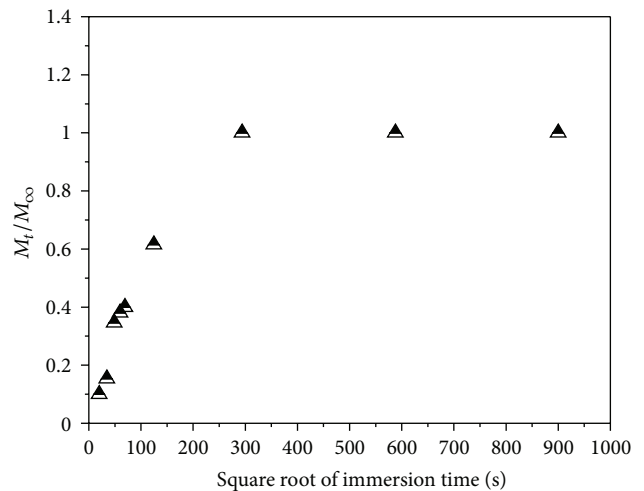


FIGURE 5: Water uptake curve for 100/0 PHBV/PLLA thin film at 37°C in the form of M_t/M_∞ versus square root of immersion time.

porosity and the amount of available liquid water at the surface of the material. For this reason, porous material can uptake and store more water whereas the nonporous (dense) material can store a limited amount of water (Table 4). It can be seen from the plots of M_t/M_∞ versus square root of time (Figures 5 and 7) that the plots are almost linear for both the

TABLE 2: Diffusion coefficients of thin films at 25°C, 37°C, and 50°C.

Temperature (°C)	100/0 PHBV/PLLA thin films (m ² /s)	50/50 PHBV/PLLA thin films (m ² /s)	10% nHA in 50/50 PHBV/PLLA thin films (m ² /s)
25	$3.8 \times 10^{-13} \pm 1.5 \times 10^{-13}$	$2.12 \times 10^{-13} \pm 0.65 \times 10^{-13}$	$2.3 \times 10^{-13} \pm 0.7 \times 10^{-13}$
37	$11.3 \times 10^{-13} \pm 1.0 \times 10^{-13}$	$3.215 \times 10^{-13} \pm 0.47 \times 10^{-13}$	$11.6 \times 10^{-13} \pm 0.9 \times 10^{-13}$
50	$59.3 \times 10^{-13} \pm 12.0 \times 10^{-13}$	$59.8 \times 10^{-13} \pm 3.53 \times 10^{-13}$	$22.9 \times 10^{-13} \pm 0.8 \times 10^{-13}$

TABLE 3: Diffusion coefficients of scaffolds at 25°C, 37°C, and 50°C.

Temperature (°C)	100/0 PHBV/PLLA scaffolds (m ² /s)	50/50 PHBV/PLLA scaffolds (m ² /s)	10% nHA in 50/50 PHBV/PLLA scaffolds (m ² /s)
25	$51.7 \times 10^{-12} \pm 1.1 \times 10^{-12}$	$0.16 \times 10^{-11} \pm 0.06 \times 10^{-11}$	$0.2 \times 10^{-11} \pm 0.05 \times 10^{-11}$
37	$67.6 \times 10^{-12} \pm 3.2 \times 10^{-12}$	$3.58 \times 10^{-11} \pm 0.7 \times 10^{-11}$	$1.3 \times 10^{-11} \pm 0.5 \times 10^{-11}$
50	$165 \times 10^{-12} \pm 9.1 \times 10^{-12}$	$6.92 \times 10^{-11} \pm 2 \times 10^{-11}$	$5.4 \times 10^{-11} \pm 1.35 \times 10^{-11}$

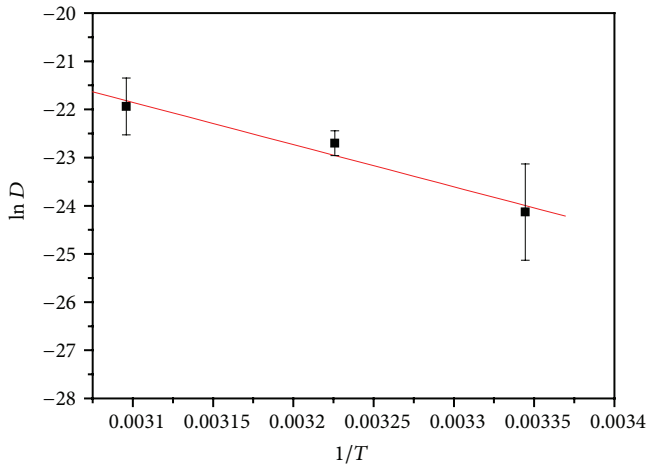
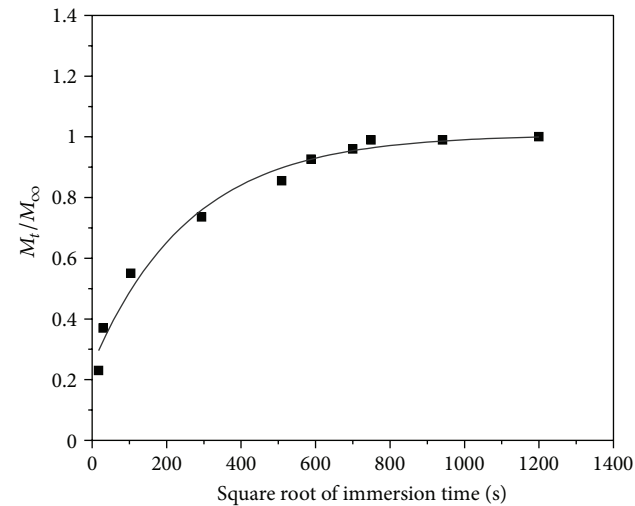
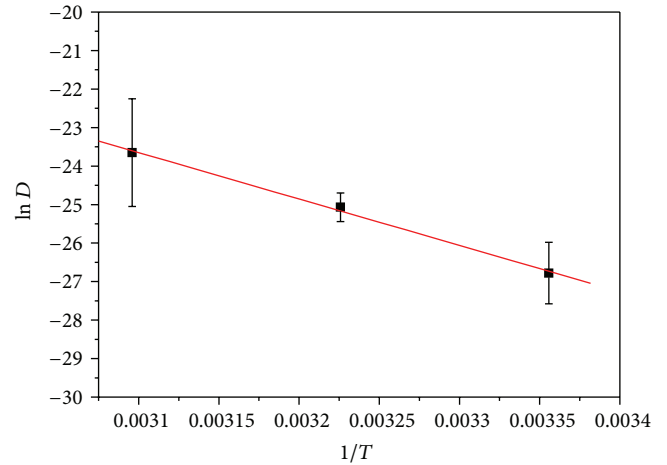
FIGURE 6: Arrhenius plot of 10% HA in 50/50 PHBV/PLLA thin films (the graph is plotted as logarithm of diffusion coefficients (D) versus the reciprocal of absolute temperature, T).FIGURE 7: Water uptake curve for 100/0 PHBV/PLLA scaffolds at 37°C in the form of M_t/M_∞ versus square root of immersion time.

TABLE 4: Comparison of equilibrium water uptake between thin films and scaffolds at 37°C.

Compositions of films and scaffold specimens	Equilibrium water uptake for thin films (g/g)	Equilibrium water uptake for scaffolds (g/g)
100/0 PHBV/PLLA	0.01	1.24
50/50 PHBV/PLLA	0.03	1.35
10% nHA in 50/50 PHBV/PLLA	0.09	2.97

FIGURE 8: Arrhenius plot of 10% HA in 50/50 PHBV/PLLA scaffolds (the graph is plotted as logarithm of diffusion coefficients (D) versus the reciprocal of absolute temperature, T).

thin films and scaffolds in the initial period of time. As Fick's second law is applicable for both the thin films and scaffolds for the initial period of time, it can be stated that the initial stage is diffusion controlled. Similar results were obtained by several studies of polymeric composite materials for dental applications [12, 18, 19].

It was also found that the water uptake of PHBV/PLLA scaffold was lower than 10 wt% nHA incorporated PHBV/PLLA scaffold. For the scaffold specimens, when all the

pores were assumed to be filled with water, the equilibrium water uptake of polymer blend scaffold and composite scaffold specimens were found to be 1.35 g/g and 2.97 (g/g), respectively (Table 4). Moreover, water uptake of composite scaffold specimen decreased after few days. The reason might be the starting of dissolution of nHA within the composite scaffold. The initial increase of water uptake of the composite films and scaffolds may be due to hydrophilic nature of the nanosized nHA particles or the inclusions of HA nanoparticle aggregates. The nHA nano-particles may appear as loosely embedded aggregates in the polymer matrix. As a result, additional amount of water at the interface between the agglomerates and the matrix can be accommodated.

The calculated diffusion coefficients expressed are given in Tables 2 and 3 during water absorption. The values of diffusion coefficients are available in the literature for other conventional composites [18, 20]. The diffusion coefficients were higher in scaffolds than thin films. This behaviour can occur during the initial uptake of water through the pores of the scaffolds which can cause the formation of water clusters. Surface area to volume ratio and thickness can also have effects on this.

Temperature and composition are the two most important factors which can affect the diffusion coefficient [21]. Between these two factors, temperature has the most profound influence on the coefficients and diffusion rates. The diffusion coefficients are related to temperature according to Arrhenius equation. From Arrhenius plots of thin film and scaffold (Figures 6 and 8), it can be seen that the plot is almost linear. These results can further confirm that water uptake of thin films is controlled by diffusion process. From the plots of M_t/M_∞ versus square root of immersion time, it is also possible to estimate when a plateau region can be established and how long the diffusion phenomena can be observed. It was also found by other studies that after saturation, many other properties should be taken into account such as structure and surface chemistry.

4. Conclusions

- (1) The amount of water absorption or uptake depends mainly on the hydrophilicity and porosity of the materials. For this reason, PHBV/PLLA and 10% HA in PHBV/PLLA scaffolds and thin films absorbed more water than that of 100/0 PHBV/PLLA scaffolds and thin films as PHBV is more hydrophobic than PLLA and HA. The water uptake of the scaffolds was much higher than that of thin films because the scaffolds had high porosity.
- (2) For thin films and scaffold, Arrhenius plot was almost linear. For the initial period of time, water uptake of the thin films was controlled by diffusion process. It was possible to estimate when a plateau region could be established and how long the diffusion phenomena could be observed.
- (3) After saturation, many other properties should be taken into account such as structure and surface chemistry. 10% HA in 50/50 PHBV/PLLA scaffolds

showed decrease in water uptake after saturation due to dissolution of HA and also degradation of amorphous part of PLLA/PHBV polymer.

- (4) The diffusion coefficients were higher in porous scaffolds than thin films as the rate of diffusion increased with decreasing density of atomic packing. Porosity and surface to volume ratio had a profound effect on the water uptake of scaffolds.

Conflict of Interests

The authors, hereby, declare that they do not have any conflict of interests.

Acknowledgments

N. Sultana thanks The University of Hong Kong (HKU) for providing her with a research studentship. This work was supported by a GRF Grant (HKU 7182/05E) from the Research Grants Council of Hong Kong. Assistance provided by technical staff in the Department of Mechanical Engineering, Faculty of Engineering, is acknowledged. Authors also thank Universiti Teknologi Malaysia, Ministry of Higher Education (MOHE), RMC, IJN-UTM Cardiovascular Engineering Centre, and FRGS Grant (vot: 4F126), GUP Tier 1 (03 H13, 05H07) for financial supports.

References

- [1] E. Bell, *Tissue Engineering: Current Perspectives*, Birkhäuser, Boston, Mass, USA, 1993.
- [2] R. P. Lanza, R. S. Langer, and J. Vacanti, *Principles of Tissue Engineering*, Elsevier/Academic Press, Amsterdam, The Netherlands, 2007.
- [3] Z. Li, Y. Su, B. Xie et al., "A tough hydrogel-hydroxyapatite bone-like composite fabricated *in situ* by the electrophoresis approach," *Journal of Materials Chemistry B*, vol. 1, no. 12, pp. 1755–1764, 2013.
- [4] J. Lacroix, J. Lao, and E. Jallot, "Green and safe *in situ* templating of bioactive glass scaffolds for bone tissue engineering," *Journal of Materials Chemistry B*, vol. 1, no. 13, pp. 1782–1785, 2013.
- [5] S. Lalan, I. Pomerantseva, and J. P. Vacanti, "Tissue engineering and its potential impact on surgery," *World Journal of Surgery*, vol. 25, no. 11, pp. 1458–1466, 2001.
- [6] C. Bastioli, *Handbook of Biodegradable Polymers*, Rapra Technology, Shrewsbury, UK, 2005.
- [7] E. Blümm and A. J. Owen, "Miscibility, crystallization and melting of poly(3-hydroxybutyrate)/poly(l-lactide) blends," *Polymer*, vol. 36, no. 21, pp. 4077–4081, 1995.
- [8] N. Sultana and M. Wang, "PHBV/PLLA-based composite scaffolds containing nano-sized hydroxyapatite particles for bone tissue engineering," *Journal of Experimental Nanoscience*, vol. 3, no. 2, pp. 121–132, 2008.
- [9] P. X. Ma, R. Zhang, G. Xiao, and R. Franceschi, "Engineering new bone tissue *in vitro* on highly porous poly(α -hydroxyl acids)/hydroxyapatite composite scaffolds," *Journal of Biomedical Materials Research*, vol. 54, pp. 284–293, 2001.
- [10] B. D. Ratner, *BioMaterials Science: An Introduction to Materials in Medicine*, Elsevier Academic Press, San Diego, Calif, USA, 2004.

- [11] N. Sultana and T. H. Khan, "Factorial study of compressive mechanical properties and primary *in vitro* osteoblast response of PHBV/PLLA scaffolds," *Journal of Nanomaterials*, vol. 2012, Article ID 656914, 8 pages, 2012.
- [12] M. Braden, "Water absorption characteristics of dental micro-fine composite filling materials. II. Experimental materials," *Biomaterials*, vol. 5, no. 6, pp. 373–375, 1984.
- [13] S. Deb, M. Braden, and W. Bonfield, "Water absorption characteristics of modified hydroxyapatite bone cements," *Biomaterials*, vol. 16, no. 14, pp. 1095–1100, 1995.
- [14] N. Sultana and M. Wang, "PHBV/PLLA-based composite scaffolds fabricated using an emulsion freezing/freeze-drying technique for bone tissue engineering: surface modification and *in vitro* biological evaluation," *Biofabrication*, vol. 4, no. 1, Article ID 015003, 2012.
- [15] W. Y. Zhou, M. Wang, W. L. Cheung, B. C. Guo, and D. M. Jia, "Synthesis of carbonated hydroxyapatite nanospheres through nanoemulsion," *Journal of Materials Science: Materials in Medicine*, vol. 19, no. 1, pp. 103–110, 2008.
- [16] N. Sultana and M. Wang, "Fabrication of HA/PHBV composite scaffolds through the emulsion freezing/freeze-drying process and characterisation of the scaffolds," *Journal of Materials Science: Materials in Medicine*, vol. 19, no. 7, pp. 2555–2561, 2008.
- [17] J. Crank and G. S. Park, Eds., *Diffusion in Polymers*, Academic Press, New York, NY, USA, 1977.
- [18] M. Braden and R. L. Clarke, "Water absorption characteristics of dental microfine composite filling materials. I. Proprietary materials," *Biomaterials*, vol. 5, no. 6, pp. 369–372, 1984.
- [19] C. Santos, R. L. Clarke, M. Braden, F. Guitian, and K. W. M. Davy, "Water absorption characteristics of dental composites incorporating hydroxyapatite filler," *Biomaterials*, vol. 23, no. 8, pp. 1897–1904, 2002.
- [20] J. Crank and G. S. Park, *Diffusion in Polymers*, Academic Press, London, UK, 1968.
- [21] R. E. Smallman and A. H. W. Ngan, *Physical Metallurgy and Advanced Materials*, Butterworth-Heinemann; Elsevier, Amsterdam, The Netherlands, 2007.